UNIVERSITÀ
degli STUDI
di CATANIA

Study of the $^{18}O + {}^{48}Ti$ scattering at 275 MeV and Monte Carlo simulations and experimental characterization of the MAGNEX focal plane detector for the NUMEN project

A DISSERTATION PRESENTED
BY
GIUSEPPE ANTONIO BRISCHETTO
TO
THE DEPARTMENT OF PHYSICS "ETTORE MAJORANA"

IN PARTIAL FULFILLMENT OF THE REQUIREMENTS
FOR THE DEGREE OF
DOCTOR OF PHILOSOPHY
IN THE SUBJECT OF
PHYSICS

UNIVERSITÀ DEGLI STUDI DI CATANIA
CATANIA, ITALIA
DECEMBER 2022

Thesis tutors:
Prof. Francesco Cappuzzello
Ph.D. Luciano Pandola

Giuseppe Antonio Brischetto

Study of the ^{18}O + ^{48}Ti scattering at 275 MeV and Monte Carlo simulations and experimental characterization of the MAGNEX focal plane detector for the NUMEN project

Abstract

In the last years neutrinoless double beta ($0\nu\beta\beta$) decay has attracted much interest from the scientific community since its observation would represent the first experimental evidence of physics beyond the Standard Model. The NUMEN project proposed at the Laboratori Nazionali del Sud of the Istituto Nazionale di Fisica Nucleare (INFN-LNS) an innovative method to deduce data-driven information on the nuclear matrix elements involved in the half-life of $0\nu\beta\beta$ decay. Such a method is based on the measurement of heavy-ion induced Double Charge Exchange (DCE) nuclear reaction cross-sections, which are typically very low (few tens of nb). In the perspective of a systematic study of all the isotopes relevant for $0\nu\beta\beta$, an upgrade of the K800 Superconducting Cyclotron and of the MAGNEX magnetic spectrometer is foreseen to increase the maximum beam intensity of two orders of magnitude. The upgrade of MAGNEX involves the construction of a new Focal Plane Detector (FPD), constituted by a M-THGEM-based gas tracker and a wall of ΔE E telescope detectors, based on the SiC-CsI(Tl) technology, for the Particle IDentification (PID). In this context, an intense R&D activity was performed, that has required the realization of extensive tests and simulations of the detectors.

The purpose of this Thesis is twofold. First of all, it contributes to the development of the multi-channel approach proposed by NUMEN for the analysis of the reaction mechanism and nuclear structure details of the network of nuclear reactions involving nuclei relevant for $0\nu\beta\beta$ decay. In this context, the study of the elastic and inelastic scattering channels plays a central role since it gives access to the initial state interaction. The analysis of such channels in the case

Thesis tutors:
Prof. Francesco Cappuzzello
Ph.D. Luciano Pandola

Giuseppe Antonio Brischetto

of the ^{18}O + ^{48}Ti collision at 275 MeV incident energy is here presented for the first time. The data reduction procedure and the theoretical analysis performed in the PhD period are described. The second pillar of this Thesis consists in the study of the future MAGNEX FPD. One of the most important results obtained in the PhD activity is the realization of a Monte Carlo simulation tool capable of describing the response of the future FPD to the events of interest. In this work, such a tool was used to optimize the rotation angle of the towers of telescopes constituting the PID wall and to test a proposal of a PID strategy. Furthermore, the characterization tests, performed during the PhD period, on the tracker prototype based on M-THGEM are discussed. Two kinds of M-THGEM, differing for the holes pattern, were tested. The detector was characterized by measuring the currents flowing through the electrodes, varying the applied voltages, the gas pressure, and the rate of incident particles. Important quantities such as the gas gain and the ion backflow were determined.

Contents

Introduction **1**

1 The scientific context **6**
- 1.1 Neutrinoless double beta decay . . . 8
- 1.2 The Nuclear Matrix Elements of $0\nu\beta\beta$ . . . 10
- 1.3 Double Charge Exchange reactions and $0\nu\beta\beta$ . . . 13
- 1.4 The NUMEN project . . . 14
  - 1.4.1 The phases of the project . . . 16
  - 1.4.2 The multi-channel approach . . . 19

2 The present MAGNEX facility **28**
- 2.1 The scattering chamber . . . 30
- 2.2 The MAGNEX magnetic elements . . . 34
  - 2.2.1 Trajectory reconstruction . . . 36
- 2.3 The present Focal Plane Detector . . . 38
  - 2.3.1 The gas tracker . . . 39
  - 2.3.2 The silicon stopping wall . . . 42
  - 2.3.3 Principle of operation . . . 43

3 The ^{18}O + ^{48}Ti elastic and inelastic scattering **51**
- 3.1 Data reduction . . . 52
  - 3.1.1 Calibration . . . 53
  - 3.1.2 Particle Identification . . . 60
  - 3.1.3 Final phase-space parameters . . . 62

3.1.4 Application of the ray-reconstruction technique to the experimental data . . . 63
3.1.5 Excitation energy spectrum . . . 71
3.1.6 Cross section angular distribution . . . 71
3.2 Determination of the Initial State Interaction . . . 77
3.2.1 Optical Potential . . . 78
3.2.2 Optical Model results . . . 80
3.2.3 Coupling to the inelastic scattering channels . . . 82
3.2.4 The ^{18}O + ^{48}Ti scattering at 54 MeV . . . 84

4 The future MAGNEX focal plane detector 95
4.1 The gas tracker . . . 97
4.1.1 The drift region . . . 99
4.1.2 The electron multiplication stage . . . 99
4.1.3 The readout anode . . . 100
4.1.4 The working principle . . . 101
4.2 The wall of SiC-CsI(Tl) telescope detectors . . . 102
4.2.1 The silicon carbide ΔE detectors . . . 104
4.2.2 The cesium iodide E detectors . . . 108
4.3 Concept validation and commissioning . . . 109

5 The simulation tool of the future Focal Plane Detector 121
5.1 The Geant4 toolkit . . . 123
5.1.1 Geant4 structure . . . 123
5.2 Main aspects of the FPD simulation tool . . . 124
5.2.1 The first part of the simulation tool: COSY INFINITY . . . 125
5.2.2 The second part of the simulation tool: the Geant4 application . . . 127
5.3 Results . . . 134
5.3.1 The elastic scattering of ^{20}Ne as examplifying case . . . 135
5.3.2 Study of the towers rotation angle . . . 137
5.3.3 Proposal of a particle identification strategy . . . 137
5.3.4 Ionization processes in the gas tracker . . . 142

6 The characterization of the gas tracker prototype **148**
6.1 The gas tracker prototype 149
6.2 Layout of the M-THGEM 149
6.3 The characterization test set-up 156
6.4 Current-voltage characterization of the gas tracker prototype . . . 158
6.4.1 Current-induction voltage characterization 161
6.4.2 Current-drift voltage characterization 164
6.4.3 Current-THGEM voltage characterization 166
6.4.4 Gain 166
6.4.5 Ion backflow 169
6.4.6 Rate characterization 172
6.5 Track reconstruction test 174
6.5.1 Charge distribution and arrival time measurement 174
6.5.2 Horizontal and vertical angles reconstruction 175
6.6 Conclusions 178

Conclusions **183**

Appendix A Electrical configurations and gas pressures explored for the characterization tests of the prototype **187**

List of Figures

1.1 Nuclear mass for isobars as a function of the atomic number Z with (a) even and (b) odd mass number A. Figure from Ref. [11]. . . . 9
1.2 Example of the $2\nu\beta\beta$- and the $0\nu\beta\beta$-decay spectra. 10
1.3 Nuclear structure calculations of the $0\nu\beta\beta$ Nuclear Matrix Elements (NMEs) for different nuclei. Abbreviations: EDF, energy-density functional; IBM, interacting boson model; QRPA, quasi-particle random phase approximation, SM, shell-model. Figure from Ref. [25] 12
1.4 Sketch of the nuclear channels involved in the routes connecting the initial partition to the final DCE one in a typical NUMEN experiment with $^{18}O^{8+}$ ion beam. The ^{48}Ti target case is here illustrated. 19

2.1 Target ladder: in parenthesis the thicknesses of the several targets are indicated in $\mu g/cm^2$. 31
2.2 Interior of the scattering chamber. (a) The four slits that define the MAGNEX angular acceptance and the Faraday Cup (FC). (b) The collimation system and the monitor detector. 33
2.3 The MAGNEX magnetic spectrometer at the LNS-INFN in Catania. (a) From the left to the right: the scattering chamber, the quadrupole (red) magnet, the dipole (blue) magnet and the Focal Plane Detector chamber. (b) Panoramic view of the MAGNEX experimental hall. 35

2.4 Schematic drawings of the MAGNEX FPD, showing the gas tracker and silicon stopping wall in: (a) lateral view (y-z plane) and (b) top view (x-z plane). 40
2.5 Picture of: (a) the vacuum chamber that hosts the gas tracker, opened on one side and showing the Mylar window; (b) the silicon detector columns. Figure from Ref. [31] 41
2.6 Scheme of the segmented anode (bottom view). The six anodic strips of corresponding to the six Drift Chambers DC_i are shown. Each strip is further segmented in pads (in gray) that are tilted of $\theta_{tilt} = 59.2°$. In green the positions of the proportional wires are shown. The sizes are expressed in mm. Figure from Ref. [57] . . . 43
2.7 Scheme of the electronics and read-out of the detectors signals at the MAGNEX FPD. 46

3.1 Linear correlation between the response of a pad (pad_i) with the response of a reference one (pad_ref). Each point corresponds to the pads response to the signal (2, 5, 8 and 10 V) generated by a pulse generator and sent onto the wires in the case of DC_3. Figure from Ref. [31]. 54
3.2 Examples of charge distributions on DC1: a) presence of spurious signals distant from the main avalanche. Threshold values obtained using the standard COG method and the optimized algorithm (green dashed and red solid line, respectively); b) time variation of the pedestal level above the stored values; c) two ions trajectories piling-up in the multiplexer. Figure from Ref. [72]. . . 57
3.3 Ion track through the FPD. Blue and orange dots are the experimentally measured and the extrapolated positions of the ion, respectively. Red line is the implemented linear fit. (a) Track projection onto the x-z (horizontal) plane. (b) Track projection onto the y-z (vertical) plane. Figure from Ref. [31]. 58
3.4 (a) y_1 distribution of unidentified events. The minima, indicated by the red dashed lines, correspond to the mechanical wires (see text) shown in panel (b). 59

3.5 Typical ΔE_{tot}^{corr} E_{resid} plot for a single silicon detector at $\theta_{opt} = 15°$. (b) x_{foc} E_{resid} plot for the ions selected with the graphical cut in (a). 61
3.6 Final phase-space parameters for the selected $^{18}O^{8+}$ events belonging to the ^{18}O + ^{48}Ti scattering at 275 MeV incident energy and $\theta_{opt} = 15°$. In (a) and (b) the θ_{foc}-xf_fit and yf_fit-xf_fit correlation plots are shown, respectively. 64
3.7 Sketches of the target and the projectile/ejectile energies involved in the nuclear reactions from the ^{18}O + ^{48}Ti collision at 275 MeV of incident energy. Panels (a) and (b) indicate the true scale geometry and the zero thickness hypothesis described in the text, respectively. 66
3.8 (a) Horizontal final phase-space representation in terms of the θ_{foc} x_{foc} parameters for both the experimental and simulated data at $\theta_{opt} = 15°$. (b) Vertical final phase-space representation in terms of the y_{foc} x_{foc} parameters for both the experimental and simulated data at $\theta_{opt} = 15°$. Figure from Ref. [43]. 67
3.9 The ϕ_i vs. $\theta_i + \theta_{opt}$ correlation plot for the ^{18}O + ^{48}Ti scattering at 275 MeV incident energy and $\theta_{opt} = 15°$. The graphical contour indicates the effective solid angle acceptance of MAGNEX. 69
3.10 The θ_{lab} E_x correlation plot for the ^{18}O + ^{48}Ti scattering at 275 MeV incident energy and $\theta_{opt} = 15°$. 70
3.11 Excitation energy spectrum for the ^{18}O +^{48} Ti elastic and inelastic scattering at 275 MeV in the angular range $11° \sim \theta_{lab} < 12°$. The coloured lines show the result of the multiple-fit procedure and identify different states of projectile and target, as well as a structure due to the Al backing, as explained in the legend. The asterisk refers to the transition where the 2_1^+ excited state of the ^{18}O at 1.982 MeV is populated. 72

3.12 (a) Geometrical representation of the MAGNEX solid angle acceptance. (b) Differential solid angle evaluation: the nominal and the effective MAGNEX solid angle acceptance are shown with the green and red lines, respectively. The solid angle of a singular angular bin (hatched region) is defined by the intersection of the circular ring enclosed in the (θ_{lab} $\Delta\theta_{lab}/2$; $\theta_{lab} + \Delta\theta_{lab}/2$) interval and the red contour. 75
3.13 Cross-section angular distribution for the ^{18}O + ^{48}Ti elastic scattering at 275 MeV. The three explored angular ranges are highlighted with different colors and marker. The Rutherford differential cross-section is also shown (red line). 76
3.14 Experimental cross section angular distribution of the ^{18}O +^{48}Ti elastic scattering at 275 MeV incident energy in terms of the ratio with the Rutherford cross section. The theoretical calculations for the elastic transition in OM (blue dashed line) and CC (red solid line) are also shown. The theoretical curves are folded with the experimental angular resolution. 81
3.15 Coupling scheme adopted for the DWBA (blue dashed arrows) and CC (red solid arrows) theoretical calculations of the ^{18}O +^{48}Ti elastic and inelastic scattering at 275 MeV incident energy. On the right, the excitation energies of the considered states are reported. 82
3.16 Experimental cross section angular distribution of the ^{18}O +^{48}Ti inelastic scattering to the 2_1^+ excited state of the ^{48}Ti (top panel) and of the structure centered at 2.2 MeV (bottom panel). The DWBA (blue dashed line) and CC (red solid line) theoretical calculations for both the inelastic channels are also shown. The theoretical curves are folded with the experimental angular resolution. 85
3.17 Experimental cross section angular distribution of ^{18}O +^{48}Ti elastic scattering at 54 MeV in terms of the ratio with the Rutherford cross section. The OM (blue dashed line) and CC (red solid line) theoretical calculations are also shown. 86

3.18 Angular distributions of differential cross-section for the inelastic transitions towards the 2_1^+ state of (top panel) target and (bottom panel) projectile induced by the ^{18}O + ^{48}Ti collision at 54 MeV. The DWBA (blue dashed line) and CC (red solid line) calculations are also shown. 88

4.1 CAD Drawing of MAGNEX FPD. The Mylar window (yellow), the gas tracker (red) and the PID wall (green) are highlighted. 97
4.2 Drawing of the new gas tracker for the MAGNEX FPD. Figure from Ref. [111]. 98
4.3 Schematic drawing of (a) two- and (b) three-layer M-THGEM device. Figure from Ref. [110]. 100
4.4 CAD drawing of one of the module of the anode for the new gas tracker. Figure from Ref. [111]. 101
4.5 Sketch of a SiC-CsI(Tl) telescope for the PID wall of the MAGNEX FPD. Figure from Ref. [4]. 104
4.6 Pictures of: (a) the SiC detector, (b) the Hamamatsu S3590 photodiode, (c) the CsI(Tl) tile housing 20 crystals. 105
4.7 Drawing of a *tower* for the PID wall of the MAGNEX FPD. Each tower is composed by 20 SiC-CsI(Tl) telescopes. Figure from Ref. [4]. 106
4.8 Sketch of the PID wall of the MAGNEX FPD. Figure from Ref. [4]. 107
4.9 Energy spectrum measured with a CsI(Tl) scintillator before (blue) and after (orange) a dose equivalent to several years of NUMEN experiments. 111
4.10 ΔE E_{resid} correlation plot measured with a SiC-CsI(Tl) telescope placed in the MAGNEX scattering chamber. Figure from Ref. [109]. 113
4.11 (a) The ΔE E_{resid} correlation plot measured with the SiC-CsI(Tl) telescope placed in the silicon stopping wall. (b) Distribution of the ejectiles close to oxygen as a function of their atomic number Z. Figure from Ref. [109]. 115

4.12 (a) The x_{foc} E_{resid} correlation plot for oxygen ions selected in the plot in Fig. 4.11.a. (b) Distribution of oxygen ejectiles as a function of their mass number A. Figure from Ref. [109]. 116

5.1 GEANT simulation of the MAGNEX magnetic spectrometer: trajectories with different colors correspond to different kinetic energies. Figure from Ref. [3]. 126

5.2 Snapshots from the Geant4 application. (a) The Focal Plane Detector: the Mylar window (orange), the gas tracker (grey) and the SiC-CsI wall are shown. (b) A telescope detector: the SiC active volume (red), the CsI crystal (blue) and the epoxy resin (light grey) are visible. The SiC dead substrate (green) behind the SiC active volume is barely distinguishable. (c) Details of the CsI scintillator: the CsI crystal (blue) is embedded in the epoxy resin (light grey). 129

5.3 Simulation of a ^{20}Ne ion at 700 MeV kinetic energy crossing the Mylar window (orange) and the gas tracker (grey) and stopping in a telescope. The ion track is clearly recognizable. The yellow points represent the enery releases in the gas, while the red lines are the trajectories of primary electrons with energies above the production threshold. 131

5.4 A typical ΔE_{SiC}^{corr} E_{CsI} correlation plot for a single SiC-CsI(Tl) telescope. The ^{20}Ne + ^{197}Au elastic scattering at 700 MeV bombarding energy was simulated. 136

5.5 The typical ΔE_{SiC}^{corr} E_{CsI} correlation plots of a single SiC-CsI(Tl) telescope for (a) $\theta_{tilt} = 0°$ and (b) $\theta_{tilt} = 35°$. 138

5.6 The elastic scattering of ^{18}O, ^{19}F and ^{20}Ne onto a ^{197}Au target at 700 MeV bombarding energy: (a) a typical ΔE_{SiC}^{corr} n_{phot} correlation plot for a single SiC-CsI(Tl) telescope is shown. The corresponding ΔE_{SiC}^{corr} and n_{phot} spectra are illustrated in (b) and (c), respectively. 140

5.7 The identification procedure of the $^{20}O^{8+}$ ejectiles: (a) a typical ΔE_{SiC}^{corr} n_{phot} matrix for a single SiC-CsI(Tl) telescope. The graphical cut to select the oxygen ions is reported. (b) A typical x_{foc} n_{phot} correlation plot for a single SiC-CsI(Tl) telescope for the oxygen ions selected with the graphical cut shown in (a). The graphical cut to select the $^{20}O^{8+}$ isotopes is also represented. 141
5.8 (a) ΔE_{SiC}^{corr} n_{phot} matrix of Fig. 5.7.a under the condition $45.8° < \theta_{foc} < 57.3°$. (b) x_{foc} n_{phot} correlation plot of Fig. 5.7.b under the identical condition on θ_{foc}. The same graphical contours as in Fig. 5.7 are reported. 143
5.9 Simulation of 10 trajectories of ^{20}Ne ions at 700 MeV kinetic energy in the gas tracker: in (a) the full 3D tracks are shown; in (b) and (c) the projections of the tracks onto the x-z and the y-z planes are shown, respectively. Each point corresponds to an energy release in the gas. The points far away from the ions trajectories are due δ-rays. 145

6.1 Picture of the gas tracker prototype. 150
6.2 Pictures of the two types of M-THGEMs: (a) the FULL M-THGEM and (b) the ROW M-THGEM. In (c) and (d) are shown a magnification of a small area of the FULL M-THGEM and of the ROW M-THGEM, respectively. 151
6.3 Schematic drawing of the gas tracker prototype illustrating the operation principles. 153
6.4 Electric field in the region of the holes for ROW a), b) and for FULL c), d) obtained with COMSOL Multiphysics software. The blue field lines start from a plane parallel to the M-THGEM foils placed in the middle of the central hole, while the red field lines in a) originate from the cathode. 155
6.5 Top-view drawing of the TEBE facility at INFN-LNS. 157
6.6 Scheme of the biasing and measuring systems based on CAEN SY5527 and PICO. 159

6.7 Biasing scheme of the detector with an illustration of the measured currents. 160
6.8 Measured currents as a function of time in a typical run. From the top to the bottom of the figure, the current of anode, top layer of the M-THGEM, bottom layer of the M-THGEM and cathode electrodes are shown. The two abrupt changes in the current at $\rightarrow$ 80 and $\rightarrow$160 s correspond to the opening and closure of the shutter in front the α-particle source, respectively. The measurement was performed with $P = 30$ mbar, $V_{ind} = 40$ V, $V_{THGEM} = 200$ V, and $V_{drift} = 1000$ V. 162
6.9 Current-induction voltage characterization for FULL at $P = 30$ mbar, $V_{THGEM} = 220$ V and $V_{drift} = 1000$ V. 163
6.10 Current-drift voltage characterization for FULL at $P = 30$ mbar, $V_{ind} = 70$ V and $V_{THGEM} = 240$ V (top) and for ROW at $P =$ 30 mbar, $V_{ind} = 120$ V and $V_{THGEM} = 220$ V (bottom). 165
6.11 Current-THGEM voltage characterization for ROW at $P = 10$ mbar, $V_{ind} = 50$ V, and $V_{drift} = 200$ V. The absolute values of the measured currents are plotted. 167
6.12 Gain as a function of V_{THGEM} for different configurations listed in Table A.3. 168
6.13 Gain for ROW and FULL as a function of V_{THGEM} for ^{18}O beam data (black) and α-particle source data (green) at $P = 20$ mbar. See Table A.3 for electrical configurations. 169
6.14 IBF for the ROW and FULL as a function of V_{drift} for different gas pressures, using ^{18}O beam and α-particle source. See Table A.2 for electrical configurations. 170
6.15 IBF for different gas pressures as a function of the gain for α-particle source data. See Table A.3 for electrical configurations. . 171
6.16 IBF as a function of the gain for one symmetric and two asymmetric configurations for the FULL at $P = 10$ mbar, $V_{ind} = 70$ V and $V_{drift} = 600$ V. Sym: $V_{TH1} = V_{TH2} = V_{TH3} = 120$ - 210 V; Asym 1: $V_{TH1} = V_{TH2} = 150$ - 190 V, $V_{TH3} = 200$ V; Asym 2: $V_{TH1} = 200$ V, $V_{TH2} = V_{TH3} = 150$ - 195 V. 172

6.17 Anodic current as a function of the rate of incident particles for the FULL (circles) and ROW (squares) at $P = 20$ mbar, $V_{ind} = 50$ V and $V_{THGEM} = 190$ V for ROW and $V_{ind} = 100$ V and $V_{THGEM} = 205$ V for FULL, at $V_{drift} = 400$ V (magenta), 800 V (green) and 1000 V (blue). The data were obtained with ^{18}O beam and α-particle source. 173
6.18 Signals generated on the strip-segmented anode by a typical α-particle track: (a) The charge induced on each strip. The five-gaussian fit function is also shown. (b) The arrival time measured by each strip with respect to the first one fired. 176
6.19 Distribution of the (a) vertical and (b) horizontal reconstructed angles. 177
6.20 Difference between the measured third horizontal coordinate (x_3^{meas}) and the same coordinate reconstructed from the fit on the other four horizontal positions (x_3^{rec}). 178

Introduction

In the last years, neutrinoless double beta ($0\nu\beta\beta$) decay has attracted much interest from the scientific community, as testified by the numerous experiments born to observe it for the first time. Indeed, such a phenomenon represents a fundamental tool to unveil some of the mysteries that surround one of the most elusive particles of the Universe: the neutrino. If $0\nu\beta\beta$ decay will be observed, it allows not only to reveal that it is a Majorana particle, but also to access the neutrino absolute mass scale. In addition, since such a phenomenon violates the lepton number conservation law, it would represent the first experimental evidence of physics beyond the Standard Model.

In order to determine the neutrino mass from the $0\nu\beta\beta$ experiments, the knowledge of the Nuclear Matrix Elements (NMEs) of the process is required. Such NMEs are not physical observables, but are evaluated through theoretical calculations, giving rise to a scenario where the different nuclear structure models show large discrepancies. In order to resolve such ambiguities, the NUMEN (NUclear Matrix Elements for Neutrinoless double beta decay) project [1] was proposed at the Laboratori Nazionali del Sud of the Istituto Nazionale di Fisica Nucleare (INFN-LNS), aiming to access useful information for the determination of the NMEs through an experimental approach. The core of such an approach is the measurement of the cross-section of Double Charge Exchange (DCE) nuclear reactions induced by heavy ions on the isotopes candidates as double beta emitters. Indeed, the NMEs of DCE and $0\nu\beta\beta$ processes share the same initial and final nuclear states and have transition operators with similar structure. Since the DCE reactions have very low cross-sections (typically of the order of few tens of nb), only a few of the relevant cases, characterized by special favorable condi-

tions, were analyzed. However, in order to reach its main goal, the project aims to build a systematics, exploring all isotopes of interest for $0\nu\beta\beta$ studies. This requires the use of ion beams with intensity much higher than the one currently deliverable at INFN-LNS. To this aim, a radical restyling has already been initiated involving the two main tools used to perform the DCE measurements: the K800 Superconducting Cyclotron [2] and the MAGNEX large acceptance magnetic spectrometer [3]. At the end of the upgrade, the heavy-ion beams available at INFN-LNS will have a maximum intensity of about 10^{13} particle-per-second (pps). With such a high intensity, the expected rate of reaction products at the MAGNEX focal plane rises up by more than two orders of magnitude. Therefore, a specific upgrade of the MAGNEX Focal Plane Detector (FPD) is mandatory [4]. The new gas tracker is based on Multi-layer THGEM (M-THGEM), a technology able to withstand rates higher than requested and to provide sub-millimetric position resolution. The wall of silicon stopping detectors will be replaced by a wall of solid state ΔE E telescopes, dedicated to Particle IDentification (PID). Each telescope is composed by a thin (100 μm) silicon carbide (SiC) stage followed by a thallium-doped cesium iodide (CsI(Tl)) crystal used as stopping detector (5 mm).

The purpose of this Thesis is two-fold: on the one hand it consists in working on the development of the ambitious multi-channel approach proposed by NUMEN [5], on the other hand it concerns the study of the future MAGNEX FPD. The first pillar of this work involves the data reduction and the theoretical analysis of the ^{18}O + ^{48}Ti elastic and inelastic scatterings at 275 MeV incident energy. The analysis of such reaction channels was performed in order to access the initial state interaction and the strength of the couplings with the low-lying excited states of projectile and target. Both these ingredients are essential to the analysis of all the other direct reactions generated in the ^{18}O + ^{48}Ti collision, thus being a fundamental building block for the multi-channel description of the entire reaction network.

The second pillar of this Thesis is based on the delevopment of a simulation tool and on the realization of tests on the tracker prototype. The latter were fundamental to characterize the detector response in terms of the currents flowing through the electrodes, with the final goal to deduce two important quantities, namely the gain and the ion backflow. The simulation tool allows to describe the

reaction kinematics, the motion of the ejectiles through the magnetic elements of MAGNEX and their interaction with the gas tracker and the PID wall. The development of such a tool is of high relevance for the NUMEN project, since it is critical in several applications. Indeed, it has been used in the design phase to optimize the layout and the arrangement of the detectors. Morevover, it allows to predict the PID performance and the sensitivity of the future FPD, as well as its overall efficiency. In order to develop a realiable simulation and correctly interpret its results, a deep knowledge of the MAGNEX spectrometer characteristics is needed. For this purpose, the above-mentioned data analysis of the ^{18}O + ^{48}Ti scattering was fundamental, because it gave me the chance to understand the MAGNEX response to real events. The typical correlation plots produced in the analysis of the experimental data were compared to the simulated ones.

In Chapter 1, the scientific context of the NUMEN project is presented, describing the fundamental aspects of $0\nu\beta\beta$ decay and the link between such a process and DCE reactions. Moreover, the important theoretical and experimental challenges that the project needs to face in order to reach its ambitious goals are discussed.

In Chapter 2, a description of the present MAGNEX facility is given, focusing on the set-up arranged for the measurement of the ^{18}O + ^{48}Ti scattering at 275 MeV incident energy. The ray-reconstruction technique is briefly described, together with the main characteristics of the present FPD and its working principle.

In Chapter 3, the study of the ^{18}O + ^{48}Ti scattering at 275 MeV incident energy is presented. In the first part, the several phases that compose the data reduction procedure are described. The excitation energy spectra and the cross-section angular distributions for the elastic and some inelastic transitions are shown. The second part is devoted to the theoretical analysis of such reaction channels, with the final aim to deduce the initial state interaction for the system under study. Theoretical calculations were performed in Optical Model (OM), Distorted-Wave Born Approximation (DWBA) and Coupled Channel (CC) formalisms. The comparison between such calculations and the experimental data highlights that the couplings to the low-lying excited states of projectile and target are significant for the scrutinized system. A further test of the adopted approach was carried out by performing the theoretical analysis of the experimental data on the ^{18}O +

^{48}Ti scattering at 54 MeV incident energy reported in literature. Also in this case, OM, DWBA and CC calculations were performed and compared to experimental data. The results confirm the reliability of the adopted theoretical framework.

Chapter 4 presents the future MAGNEX FPD, describing the new gas tracker and the wall of ΔE E telescope detectors. The main characteristics of the SiC detectors and of the CsI(Tl) scintillators are reported. The results of some of the tests performed by the NUMEN collaboration on such detectors are briefly described.

In Chapter 5, the Monte Carlo simulation tool of the future FPD, developed for this work, is presented. The main aspects of such a tool are described, highlighting the importance of the integration between the COSY INFINITY software, devoted to the transport of the ejectiles through MAGNEX, and the specific Geant4 application, developed to simulate the interaction between the ejectiles and the FPD. The optimization of the rotation angle of the towers constituting the PID wall and a proposal of a PID strategy are presented.

Chapter 6 reports the characterization tests on the prototype of gas tracker for the future FPD. Such tests were performed by irradiating the detector with a radioactive α-particle source and an ^{18}O beam. Two kinds of M-THGEM, differing for the hole patterns, were tested and compared. The characterization of the tracker in terms of measured currents induced on the detector electrodes as a function of the applied voltages, gas pressure and rate of incident particles is presented. The obtained gain and ion backflow are shown. In addition, the results of a track reconstruction test performed with a strip-segmented anode are described.

Introduction References

[1] F. Cappuzzello et al. "The NUMEN project: NUclear Matrix Elements for Neutrinoless double beta decay". In: *European Physical Journal A* 54.5 (2018). cited By 106. DOI: 10.1140/epja/i2018-12509-3.

[2] D. Rifuggiato, L. Calabretta, and G. Cuttone. "Cyclotrons and their applications. Proceedings, 17th International Conference, Cyclotrons 2004". In: *Part. Accel. Soc. Japan (2004) 541 p* (2004). Ed. by Akira Goto.

[3] F. Cappuzzello et al. "The MAGNEX spectrometer: results and perspectives". In: *Eur. Phys. J. A* 52.6 (2016), p. 167. DOI: 10.1140/epja/i2016-16167-1.

[4] F. Cappuzzello et al. "The NUMEN Technical Design Report". In: *International Journal of Modern Physics A* 36 (2021), p. 2130018. DOI: 10.1142/S0217751X21300180.

[5] F. Cappuzzello et al. "Shedding light on nuclear aspects of neutrinoless double beta decay by heavy-ion double charge exchange reactions". In: *Progress in Particle and Nuclear Physics* 128 (2023), p. 103999. ISSN: 0146-6410. DOI: https://doi.org/10.1016/j.ppnp.2022.103999.

1

The scientific context

Contents

1.1 Neutrinoless double beta decay **8**
1.2 The Nuclear Matrix Elements of $0\nu\beta\beta$ **10**
1.3 Double Charge Exchange reactions and $0\nu\beta\beta$ **13**
1.4 The NUMEN project **14**
1.4.1 The phases of the project 16
1.4.2 The multi-channel approach 19

The Standard Model (SM) is a theory of wide success, capable to describe accurately the results of many experiments that probe the properties of the elementary particles and of their interactions up to energies of the order of TeV. However, in the last years the discovery of new phenomena brought into question some of its assumptions.

In the SM, it is assumed that the neutrino mass is zero; notwithstanding, in 1998 the Super-Kamiokande experiment observed for the first time the neutrino flavour oscillations [6] and few years later, the Sudbury Neutrino Observatory managed to solve the solar neutrino problem, reaching the conclusion that the electronic neutrino deficit is due to flavour oscillations [7]. Both the experiments demonstrated unequivocally that neutrino is massive. Similarly to quark oscillations, the flavour

oscillations of neutrino can be introduced in the SM. In such a theory, neutrino is generated in a weak interaction in one of the three flavour eigenstates $(\nu_e, \nu_\mu, \nu_\tau)$. Since these eigenstates are different from the mass eigenstates (ν_1, ν_2, ν_3), a neutrino in a flavour eigenstate is in a superposition of mass eigenstates, which can be described in terms of the Pontecorvo-Maki-Nakagawa-Sakata (PMNS) matrix $U_{\alpha i}$, where $\alpha = e, \mu, \tau$ and $i = 1, 2, 3$.

Since the oscillation phenomenon is sensible only to the difference of squared masses, the neutrino absolute mass scale is still unkown. Morever, other aspects of the neutrino properties must be further investigated, such as the Majorana or Dirac nature of such a particle [8], the mass hierarchy, the mass-generation mechanism, the CP-transformation properties.

Among the processes that could open a physics scenario beyond the SM, neutrinoless double beta ($0\nu\beta\beta$) decay is of utmost importance, because, if observed, it would reveal that neutrino is a Majorana particle and that the lepton-number conservation law can be violated. This would represent a possible explanation of the creation of matter in our universe [9]. For these reasons, $0\nu\beta\beta$ decay has attracted the interest of the scientific community from both the experimental and theoretical sides.

Since $0\nu\beta\beta$ decay involves transitions between atomic nuclei, a central role is assumed by nuclear physics, which comes into play through the Nuclear Matrix Elements (NMEs) of the process [10, 11]. NMEs are not physical observables, thus can be only determined by calculations. Such calculations strongly depend on the unavoidable truncations of the model space adopted by the different nuclear structure models in order to describe the many-body nature of the involved nuclear states. The NUMEN project proposes a data-driven approach to determine information useful to put constraints on such calculations [1, 5, 12].

In this Chapter, the main features of the $0\nu\beta\beta$ are desribed. Then, the NUMEN project is introduced, highlighting the challenging theoretical and experimental goals that such a project wants to achieve.

1.1 Neutrinoless double beta decay

The double beta decays involves transitions where a parent nucleus (A, Z) transforms into a daughter one (A, $Z \mp 2$) changing the atomic number Z by two units and keeping constant the mass number A. If the atomic number increases (decreases), the double beta decay is referred to as $\beta^-\beta^-$ ($\beta^+\beta^+$). The first idea of double beta decay was proposed by M. Goeppert-Mayer in 1935 [13] as a second-order effect of Fermi theory of beta decay. In such a decay, two electrons (positrons) and two antineutrinos (neutrinos) are emitted by the nucleus:

$$(A, Z) \propto (A, Z + 2) + 2e^- + 2\bar{\nu}_e \tag{1.1}$$

$$(A, Z) \propto (A, Z \quad 2) + 2e^+ + 2\nu_e \tag{1.2}$$

This process, today known as two-neutrino double beta ($2\nu\beta\beta$) decay, is allowed by the SM and has been observed for twelve isotopes, exhibiting a typical half-life longer than 10^{19} years [14, 15].

The double beta decay is measurable only for some nuclei; indeed, if the (A,Z) nucleus can decay through a single beta transition into the (A,$Z + 1$) nucleus, the double beta decay is practically impossible to observe, because the first-order process dominates (see Fig. 1.1.a). However, for some nuclei the first-order decay is energetically forbidden due to the mass staggering between even-even and odd-odd nuclei generated by the nucleon pairing correlation, while the transition toward the (A,$Z + 2$) is allowed (see Fig. 1.1.b). Therefore, the candidates to double beta decay are even-even 0^+ nuclei.

In 1937, Majorana proposed the equivalence between neutrino and antineutrino [8]; on this basis Furry suggested the existence of $0\nu\beta\beta$ decay [16], following the idea of Goeppert-Mayer:

$$(A, Z) \propto (A, Z + 2) + 2e^- \tag{1.3}$$

$$(A, Z) \propto (A, Z \quad 2) + 2e^+ \tag{1.4}$$

In this decay, the lepton-number conservation is violated by two units because two leptons are created without the corresponding anti-leptons. This process has

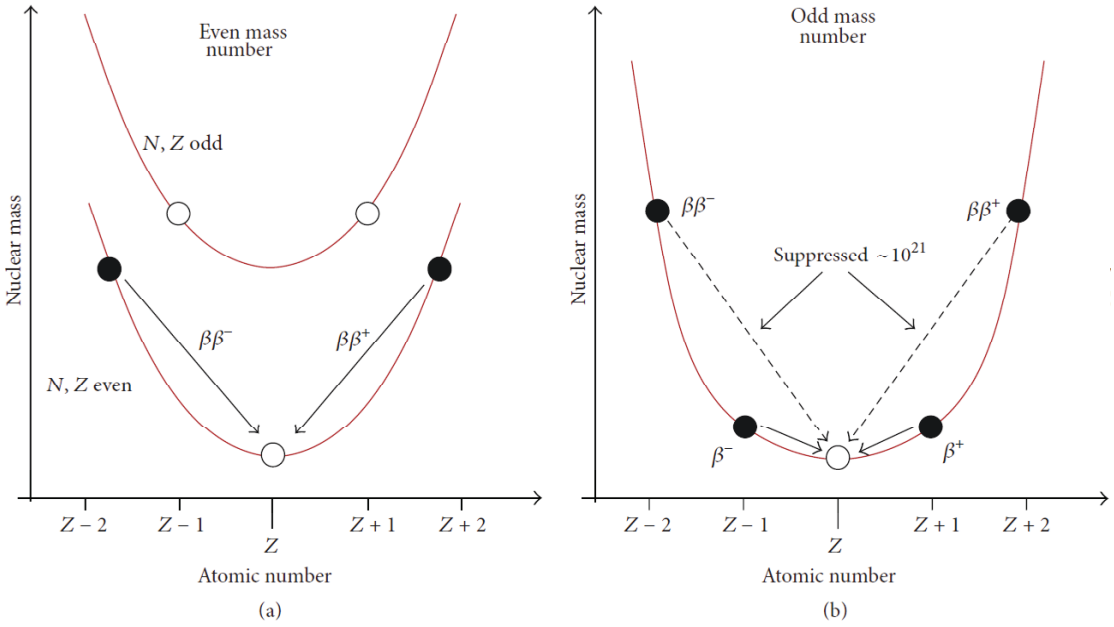

Figure 1.1: Nuclear mass for isobars as a function of the atomic number Z with (a) even and (b) odd mass number A. Figure from Ref. [11].

not been observed yet. The most recent estimate of the lower limit of the $0\nu\beta\beta$ half-life is 1.8 ± 10^{26} years for ^{76}Ge [17], 2.2 ± 10^{25} years for ^{130}Te [18], while for ^{136}Xe the measured limits are 3.5 ± 10^{25} [19] and 1.07 ± 10^{26} [20] years.

The half-life of the $0\nu\beta\beta$ decay can be expressed as the product of three terms [21]:

$$\left[T_{0\nu}^{1/2}\right]^{-1} = G_{0\nu} \sqrt{M_{0\nu}}^{2} m_{\beta\beta}^{2} \tag{1.5}$$

where $G_{0\nu}$ is the phase-space integral of the two emitted electrons, $m_{\beta\beta}$ is the effective neutrino mass and $M_{0\nu}$ is the nuclear matrix element. The $G_{0\nu}$ factor can be calculated with high accuracy [22, 23]. The effective neutrino mass $m_{\beta\beta}$ is defined by the following formula

$$m_{\beta\beta} = \left| m_1 \sqrt{U_{e1}}^{2} + m_2 \sqrt{U_{e2}}^{2} e^{i(\alpha_2 - \alpha_1)} + m_3 \sqrt{U_{e3}}^{2} e^{i(-\alpha_1 - 2\delta)} \right| \tag{1.6}$$

where m_i $(i = 1, 2, 3)$ are the three neutrino mass eigenvalues, U_{ei} are three coefficients of the PMNS matrix, δ and α_i are the Dirac and Majorana phases, respectively. Since $M_{0\nu}$ is the quantity of interest for the NUMEN project, it is

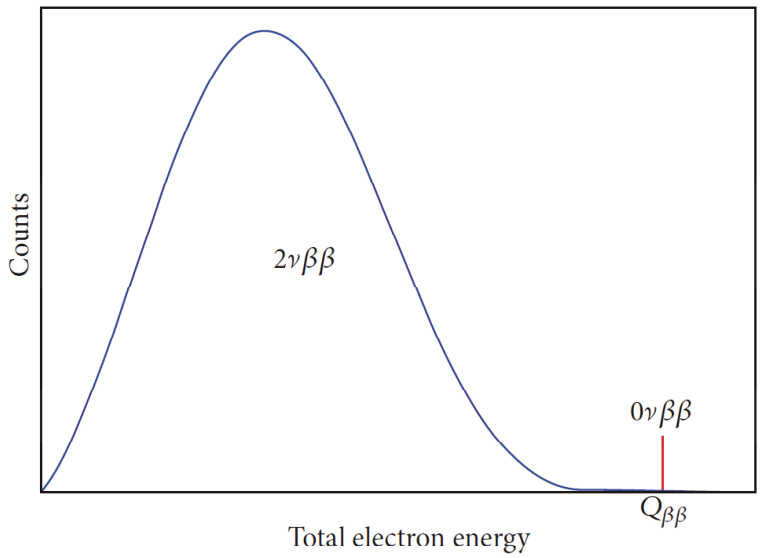

Figure 1.2: Example of the $2\nu\beta\beta$- and the $0\nu\beta\beta$-decay spectra.

discussed in detail in the next section.

In the $0\nu\beta\beta$ experiments, the most important quantities are the kinetic energies of the two emitted electrons. Indeed, for $0\nu\beta\beta$ the sum of these two quantities is equal to the Q-value ($Q_{\beta\beta}$) of the process. Therefore, in the search for $0\nu\beta\beta$ decay, one is interested in finding a mono-energetic peak at $Q_{\beta\beta}$ in the spectrum of the summed kinetic energies of the two electrons, as shown in Fig. 1.2.

The candidate nuclei to $0\nu\beta\beta$ decay are 35, but not all of them can be used for the experiments because of isotopic abundances, costs and experimental constraints of the material. In Table 1.1 the most relevant $0\nu\beta\beta$ candidates are listed.

1.2 The Nuclear Matrix Elements of $0\nu\beta\beta$

The Nuclear Matrix Element (NME) $M_{0\nu}$ in Eq. 1.5 represents the probability amplitude for the transition from the initial ϕ_i to the final ϕ_f nuclear wave function through the $\hat{O}^{0\nu\beta\beta}$ operator, namely

$$M_{0\nu} = \langle \phi_f \underbrace{\hat{O}^{0\nu\beta\beta}}_{\surd} \underbrace{\phi_i}_{\surd} | \tag{1.7}$$

Table 1.1: The most used $0\nu\beta\beta$ candidates, together with the corresponding $Q_{\beta\beta}$ (from Ref. [24]).

Isotope	$Q_{\beta\beta}$ (MeV)
^{48}Ca	4.263
^{76}Ge	2.093
^{82}Se	2.998
^{96}Zr	3.348
^{100}Mo	3.305
^{116}Cd	2.813
^{130}Te	2.527
^{136}Xe	2.459
^{150}Nd	3.371

It is usually decomposed in the following way:

$$M_{0\nu} = M_{0\nu}^{GT} + \frac{g_V^2}{g_A^2} M_{0\nu}^{F} + M_{0\nu}^{T} \tag{1.8}$$

where $M_{0\nu}^{GT}$, $M_{0\nu}^{F}$ and $M_{0\nu}^{T}$ are the Gamow-Teller, Fermi and rank-two Tensor components, respectively, while g_V and g_A are the vector and axial coupling constants of the weak interaction.

As mentioned, NMEs are evaluated by using state-of-the-art calculations (QRPA, Nuclear Shell Model, Interacting Boson Model, Energy-Density Functional, etc.), which mainly differs for the adopted model spaces; indeed, they typically propose different truncation schemes of the nuclear wave functions according to the relevant degrees of freedom. Although accurate information coming from Single Charge Exchange and transfer reactions were used to constrain the theoretical calculations, the discrepancy between different nuclear structure models are quite large, typically by a factor 2 or 3, as shown in Fig. 1.3.

Since the square of the NME enters in the expression of the half-life of $0\nu\beta\beta$ decay (see Eq. 1.5), an accurate value of $M_{0\nu}$ is fundamental to deduce information the neutrino effective mass $m_{\beta\beta}$ if a $0\nu\beta\beta$ half-life would be measured.

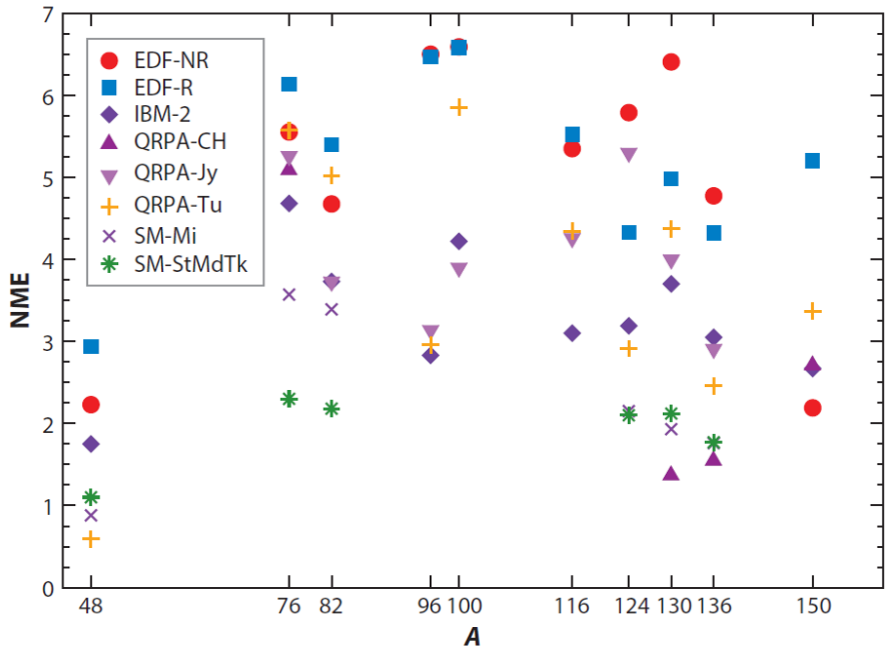

Figure 1.3: Nuclear structure calculations of the $0\nu\beta\beta$ Nuclear Matrix Elements (NMEs) for different nuclei. Abbreviations: EDF, energy-density functional; IBM, interacting boson model; QRPA, quasi-particle random phase approximation, SM, shell-model. Figure from Ref. [25]

1.3 Double Charge Exchange reactions and $0\nu\beta\beta$

In order to check the importance of specific model space components, valuable information can be deduced from the experimental data. For example, the analysis of single-charge exchange nuclear reactions [26–28] is a powerfool tool to determine the Gamow-Teller strength, from which the nuclear response to the first-order spin-isospin operator can be derived. However, the information obtained from these experiments were not sufficient to constrain the theoretical models, so that the discrepancies remained almost unaltered.

In this context, the Double Charge Exchange (DCE) reactions are probably the most interesting approach due to the similiraties to $0\nu\beta\beta$. In the DCE reactions the atomic number of the projectile and target nuclei changes by two units leaving unchanged the mass number, namely

$$a(N_a, Z_a) + A(N_A, Z_A) \propto\ b(N_a \mp 2, Z_a \equiv 2) + B(N_A \equiv 2, Z_A \mp 2) \tag{1.9}$$

Although the DCE and $0\nu\beta\beta$ are mediated by the strong and the weak interactions respectively, they share important properties:

- the initial and final many-body nuclear wave functions are the same;
- the $0\nu\beta\beta$ and DCE operators both present a Fermi, a Gamow-Teller and a rank-two tensor component, even though with different relative weights;
- a large linear momentum transfer ($\rightarrow$100 MeV/c) in the virtual intermediate channel is available for both processes;
- both processes occur in the same nuclear medium, therefore the DCE experimental data could provide valuable information about the need of possible renormalization of the coupling constants due to in-medium nuclear effects, foreseen for $0\nu\beta\beta$. Indeed, such effects are expected to influence also the DCE reactions.

The measurement of DCE reactions is very challenging from the experimental point of view: firstly, they are characterized by very low cross-sections (typically of the order of tens of nb [29]). Therefore, in order to collect a significant statistics

long acquisition time or high-intensity beams are needed. Moreover, the physical background due to all competitive processes, generated in the collision between projectile and target, is even 7-8 orders of magnitude more intense than the typical DCE cross-section. Therefore, a very high rejection factor is needed for the measurement of DCE reactions. To identify the reaction of interest it is essential to measure with high accuracy and resolution both the energy spectra and the angular distributions at very forward angles. In addition, the contributions of multi-nucleon transfer reactions leading to the same final states as DCE must be quantified. The measurement of DCE reactions represent the core of the NUMEN project, which is presented in the following section.

1.4 The NUMEN project

The NUMEN (NUclear Matrix Elements for Neutrinoless double beta decay) project at Laboratori Nazionali del Sud of the Instituto Nazionale di Fisica Nucleare (INFN-LNS) proposes an innovative method to deduce data-driven information about the NMEs of the $0\nu\beta\beta$ decay for all isotopes of interest [1]. The key aspect of the project is the measurement of DCE reaction cross-sections induced by heavy-ions. Such experimental measurements are performed by using the K800 Superconducting Cyclotron (SC) [2] and the MAGNEX large acceptance magnetic spectrometer [3] installed at INFN-LNS. The latter can guarantee the high resolution and sensitivity needed to measure rare processes as the DCE reactions, identifying the transition of interest among the large background due to more intense reaction channels.

The most important and ambitious goal of NUMEN is the access to the $0\nu\beta\beta$ NMEs through an approach based on experimental data. This requires a deep study of the reaction mechanism, to understand if it can be described as the product of a reaction dynamics and a nuclear structure terms, with the latter factorized in a projectile and a target parts. Therefore, the development of a coherent microscopic theory of the DCE reaction is a indispensable part of the project. In order to verify if the DCE NMEs are related to the $0\nu\beta\beta$ ones as a smooth function of the projectile energy and of the mass of the system, an experimental campaign exploring all the relevant isotopes for $0\nu\beta\beta$ decay at several

beam energy is needed, with the final purpose to build a complete systematics. As mentioned before, the typical DCE cross-sections are very low, therefore the build up of such a systematic dataset requires beam intensities significantly higher than those currently available at the INFN-LNS. For this reason, a radical restyling of the SC and of MAGNEX is ongoing in order to increase the maximum beam intensity of more than two orders of magnitude.

Another important goal of NUMEN is the validation of the nuclear structure theories involved in the calculation of the $0\nu\beta\beta$ NMEs. Indeed, as mentioned, the DCE and $0\nu\beta\beta$ NMEs contain the same intial and final nuclear wave functions and transition operators with similar structure. Therefore, if a nuclear structure model with a certain truncation scheme of the nuclear many-body wavefunction does not allow an accurate description of the experimental DCE cross-sections, then that model space is unsuitable for the description of the wavefunctions involved in the $0\nu\beta\beta$ decay. Thus, once determined the expression of the wavefunctions, these can be used for the $0\nu\beta\beta$ NMEs calculations. To this aim, the reaction dynamics component must be accurately determined. Therefore, NUMEN is developing a fully quantum scattering description of the DCE reaction mechanism [5].

In addition, NUMEN could give precious information about the isotopes used for the $0\nu\beta\beta$ research, because the ratio of the absolute cross-sections measured in the DCE experiments with different isotopes offers a model independent estimate of the corresponding NMEs ratio. Consequently, the sensitivity of different $0\nu\beta\beta$ experiments can be compared. This procedure allows to reduce the impact of possible systematic errors because they largely cancel out in the ratio. This kind of analysis could give key indications on which isotopes may be the best candidates for the discovery of the process.

The ambitious goals of NUMEN put numerous challenges that require the development and the use of innovative techniques on both the theoretical and experimental sides. In particular, the use of high intensity beams demands the R&D of state-of-the-art technologies in several fields, as will be shown in the next subsection.

1.4.1 The phases of the project

The NUMEN project was proposed in 2015 with a long-range time perspective. It plans to perform an intense experimental campaign on all the isotopes relevant for $0\nu\beta\beta$. NUMEN is organized in four phases, briefly described in the following.

Phase 1: The pilot experiment

In 2013, the $^{18}O + ^{40}Ca$ collision at 275 MeV bombarding energy was studied at the INFN-LNS. The $^{40}Ca(^{18}O,^{18}Ne)^{40}Ar$ DCE reaction cross-section was measured, as well as those of the following competing channels: the $^{40}Ca(^{18}O,^{18}F)^{40}K$ single charge exchange, the $^{40}Ca(^{18}O,^{20}Ne)^{38}Ar$ two-proton transfer and the $^{40}Ca(^{18}O,^{16}O)^{42}Ca$ two-neutron transfer. A complete description of the experimental set-up and data-reduction methods is reportef in Ref. [30]. This work provided for the first time high resolution and statistically relevant experimental data of DCE cross-sections in a wide range of transferred momenta. Moreover, it proved the feasibility of the NUMEN project, showing that it is possible to deduce information on the $0\nu\beta\beta$ nuclear wavefunctions by studying DCE reactions.

Phase 2: Preliminary experimental campaign and R&D activity

The Phase 2 of the project concerned the realization of an experimental campaign limited to some of the isotopes of interest, chosen as a compromise between the relevance of such isotopes for the $0\nu\beta\beta$ experiments and technical issues. The system analyzed during the Phase 2 are listed in Table 1.2. For each experiment, a wide net of nuclear reactions was measured, which included: elastic and inelastic scattering, one- and two-nucleon transfer, single and double charge exchange. The (^{18}O,^{18}Ne) and (^{20}Ne,^{20}O) reactions were used as probes for the $\beta^+\beta^+$ and $\beta^-\beta^-$ transitions, respectively. In the NUMEN Phase 2, important progresses were obtained in the theoretical description of SCE and DCE reaction mechanisms, developing new formalisms and carrying out numerical calculations [36, 44–48].

As mentioned, in order to perform a systematic study over all isotopes of interest for $0\nu\beta\beta$ experiments, beams with intensity much higher than those currently available at INFN-LNS are required. For this reason, the NUMEN project has driven the ongoing upgrade of the whole INFN-LNS research infrastructure, which

Table 1.2: Nuclear systems investigated during the Phase 2 of the NUMEN project. Table from Ref. [31]

Collision	Beam energy(AMeV)	References
^{18}O + ^{116}Sn	15.3	[32]
^{20}Ne + ^{116}Cd	15.3	[33–36]
^{20}Ne + ^{130}Te	15.3	[29, 32]
^{20}Ne + ^{76}Ge	15.3	[37]
^{18}O + ^{76}Se	15.3	[38, 39]
^{18}O + ^{12}C	15.3	[40, 41]
^{18}O + ^{48}Ti	15.3	[42, 43]
^{18}O + ^{12}C	22.0	-

in particular involves the K800 Superconducting Cyclotron and MAGNEX [49]. It is foreseen that at the end of the upgrade process the maximum beam current at the target will be increased by three orders of magnitude, going from the present 10^{10} particle-per-second (pps) to 10^{13} pps. This goal can be reached only through radical changes of the technologies used for the beam extraction and transport, for the target realization and for the detection of the ejectiles. In particular, concerning the latter, the most important upgrades involve:

- the increase of the maximum magnetic rigidity accepted by MAGNEX;
- the replacement of the present gas tracker, based on multiplication wires, with a system using Multi-layer THGEM;
- the replacement of the present wall of silicon stopping detectors with a wall of ΔE E telescope detectors characterized by high radiation-hardness properties;
- the introduction of an array of detectors around the target for the measurement of γ-rays emitted in the de-excitation of the nuclear states populated in the DCE reactions;
- the use of a new front-end and readout electronics capable to manage the high number of channels and the high rate of events.

Therefore, in order to achieve the goals designated by NUMEN, a substantial transformation of the present MAGNEX Focal Plane Detector (FPD) (see Sect. 2.3) is needed. The mentioned changes require the development of innovative technologies, especially in the field of detectors capable to cope with high counting rates and high radiation doses. For these reasons, during the Phase 2 an intense R&D activity was carried out, that led to technological developments in various fields. The main results of the R&D and the technologies selected for the upgrade have been recently published in a Technical Design Report [4]. In this context, extensive test activities and the development of reliable simulations are essential tools to evaluate if a solution meets all the specific requirements and to search for the optimal technical configurations. Both these aspects are central topics of this work; indeed, as will be shown in Chapt. 6, characterization tests of the first gas tracker prototype for the future MAGNEX FPD were performed. The development of a Monte Carlo simulation tool that allows to study the response of the future MAGNEX FPD to the event of interest is described in Chapt. 5.

Phase 3: The upgrade of the facility

The NUMEN Phase 3 started in June 2020 with the beginning of the disassambling operations of SC, beamlines and MAGNEX. Contemporary, the assembling of the new experimental setup has started. The end of these operations and the restart of the experimental activity is foreseen in 2025 for low energy beams from the Tandem Van der Graaf accelerator and in 2027 for SC beams.

This phase is also dedicated to the completion of the Phase 2 experiments data analysis: all of them are concluded or in advanced status. Moreover, tests of new prototypes and specific experiments will be performed in other laboratories (i. e. Institute of Physics of the University of Sao Paulo in Brazil, INFN-Laboratori Nazionali di Legnaro in Italy, iThemba Lab in South Africa, Institute of Nuclear Physics of Orsay in France) in order to continue the R&D activity and characterize the detectors.

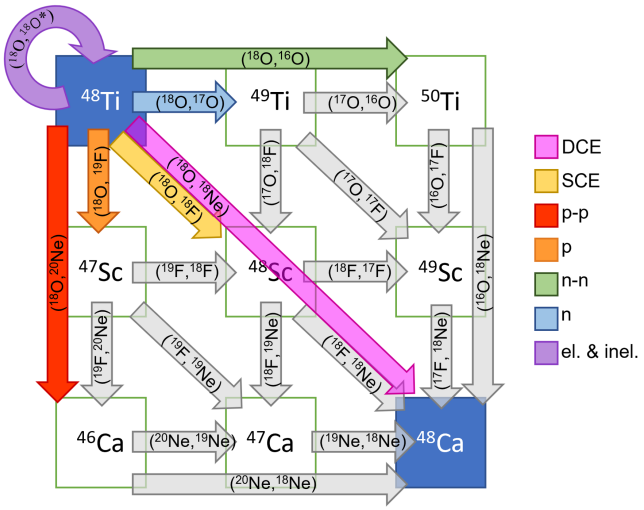

Figure 1.4: Sketch of the nuclear channels involved in the routes connecting the initial partition to the final DCE one in a typical NUMEN experiment with $^{18}O^{8+}$ ion beam. The ^{48}Ti target case is here illustrated.

Phase 4: The experimental campaign with high-intensity beam

In the Phase 4 of the project a systematic experimental campaign will be performed with high-intensity beams (up to 10^{13} pps), investigating all the isotopes of interest for the $0\nu\beta\beta$ decay studies, such as ^{48}Ca, ^{76}Ge, ^{82}Se, ^{96}Zr, ^{100}Mo, ^{106}Cd, ^{110}Pd, ^{116}Cd, ^{110}Sn, ^{124}Sn, ^{128}Te, ^{130}Te, ^{136}Xe, ^{148}Nd, ^{150}Nd, ^{154}Sm, ^{160}Gd, ^{198}Pt. In the Phase 4 the absolute DCE cross-sections will be determined, together with their uncertainties. Hopefully, thanks to upgraded theoretical methods, the NMEs of $0\nu\beta\beta$ decay will be accessed.

1.4.2 The multi-channel approach

One key aspect of the analysis of the DCE reaction cross-section is that several different channels lead to the same final state populated by the direct DCE mechanism [5]. The latter, called Majorana DCE [12], is the most interesting from the theoretical point of view due to its analogy with the $0\nu\beta\beta$ decay. A scheme of the routes connecting the initial to the final DCE partition is illustrated in Fig. 1.4, where the Majorana DCE mechanism is represented by a magenta arrow.

In order to obtain a full description of the DCE reaction mechanism, the contri-

butions coming from all the competing channels must be evaluated. This requires the study of a wide network of nuclear reactions; in fact, several characteristics of the reaction mechanism and of the structure of the colliding nuclei are required to disentangle the many DCE contributions. In particular:

- the initial and final state interactions account for the distorsion of the incoming and outgoing wavefunctions involved in nuclear reactions, thus being essential in the description of all the reaction channels. The gateway to the initial and final state interaction is the study of elastic and inelastic scattering, which allow to determine the average nucleus-nucleus potential and the strength of the couplings with the low-lying excited states.

- The analysis of one-nucleon transfer reactions allows to evaluate the spectroscopic amplitudes, which describe the single-particle configurations in nuclear states.

- The study of two-nucleon transfers can give access to important many-body properties of the nuclear matter, such as the pairing interaction.

- The contribution to the DCE cross-section originated by two sequential single charge exchange reactions must be evaluated. Therefore, the measurement of single charge exchange processes is particularly important.

The studies reported in literature on heavy-ion direct reactions are usually focused on one or few reaction channels at a time. This implies that the information deduced from data analysis cannot be fully constrained and fundamental parameters must be taken from theoretical calculations or from other experiments carried out in similar conditions if any. The analysis of a large set of reaction channels measured under the same experimental conditions allows to reduce the number of free parameters, putting strong constraints to the theoretical models.

In this framework, the analysis of the ^{18}O + ^{48}Ti elastic and inelastic scattering described in Chapt. 3 finds its place, with the main aim to provide the initial state interaction for the system of interest. It is important to remark that ^{48}Ti is not a $0\nu\beta\beta$ candidate, but it is the daughter nucleus of the $\beta^-\beta^-$ decay of ^{48}Ca. Therefore, in this case the ^{48}Ti - ^{48}Ca system is investigated along the $\beta^+\beta^+$

direction. Since NMEs are time invariant-quantities (i.e. they are equal in a DCE reaction and its inverse), the analysis of both the $\beta^-\beta^-$ and $\beta^+\beta^+$ directions in the DCE transition allows to validate the method of deducing the NMEs from the measured DCE cross-sections.

Chapter References

[1] F. Cappuzzello et al. "The NUMEN project: NUclear Matrix Elements for Neutrinoless double beta decay". In: *European Physical Journal A* 54.5 (2018). cited By 106. DOI: 10.1140/epja/i2018-12509-3.

[2] D. Rifuggiato, L. Calabretta, and G. Cuttone. "Cyclotrons and their applications. Proceedings, 17th International Conference, Cyclotrons 2004". In: *Part. Accel. Soc. Japan (2004) 541 p* (2004). Ed. by Akira Goto.

[3] F. Cappuzzello et al. "The MAGNEX spectrometer: results and perspectives". In: *Eur. Phys. J. A* 52.6 (2016), p. 167. DOI: 10.1140/epja/i2016-16167-1.

[4] F. Cappuzzello et al. "The NUMEN Technical Design Report". In: *International Journal of Modern Physics A* 36 (2021), p. 2130018. DOI: 10.1142/S0217751X21300180.

[5] F. Cappuzzello et al. "Shedding light on nuclear aspects of neutrinoless double beta decay by heavy-ion double charge exchange reactions". In: *Progress in Particle and Nuclear Physics* 128 (2023), p. 103999. ISSN: 0146-6410. DOI: https://doi.org/10.1016/j.ppnp.2022.103999.

[6] Y. Fukuda et al. "Evidence for Oscillation of Atmospheric Neutrinos". In: *Phys. Rev. Lett.* 81 (8 Aug. 1998), pp. 1562–1567. DOI: 10.1103/PhysRevLett.81.1562.

[7] A. B. McDonald. "Nobel Lecture: The Sudbury Neutrino Observatory: Observation of flavor change for solar neutrinos". In: *Rev. Mod. Phys.* 88 (3 July 2016), p. 030502. DOI: 10.1103/RevModPhys.88.030502.

[8] E. Majorana. "Teoria simmetrica dell'elettrone e del positrone". In: *Il Nuovo Cimento (1924-1942)* 14 (1937), pp. 171–184.

[9] Matteo Agostini et al. *Toward the discovery of matter creation with neutrinoless double-beta decay*. 2022. DOI: 10.48550/ARXIV.2202.01787.

[10] J. Menéndez *et al.* "Is it possible to study neutrinoless $\beta\beta$ decay by measuring double Gamow-Teller transitions?" In: *J. Phys.: Conf. Ser.* 1056, 012037 (July 2018), p. 012037. DOI: 10.1088/1742-6596/1056/1/012037.

[11] S. Dell'Oro et al. "Neutrinoless Double Beta Decay: 2015 Review". In: *Advances in High Energy Physics* 2016.2162659 (2016), p. 37. DOI: 10.1155/2016/2162659.

[12] H. Lenske et al. "Heavy ion charge exchange reactions as probes for nuclear β-decay". In: *Progress in Particle and Nuclear Physics* 109 (2019), p. 103716. ISSN: 0146-6410. DOI: 10.1016/j.ppnp.2019.103716.

[13] M. Goeppert-Mayer. "Double Beta-Disintegration". In: *Phys. Rev.* 48 (6 Sept. 1935), pp. 512–516. DOI: 10.1103/PhysRev.48.512.

[14] M. G. Inghram and J. H. Reynolds. "Double Beta-Decay of ^{130}Te". In: *Phys. Rev.* 78 (6 June 1950), pp. 822–823. DOI: 10.1103/PhysRev.78.822.2.

[15] S. R. Elliott, A. A. Hahn, and M. K. Moe. "Direct evidence for two-neutrino double-beta decay in ^{82}Se". In: *Phys. Rev. Lett.* 59 (18 Nov. 1987), pp. 2020–2023. DOI: 10.1103/PhysRevLett.59.2020.

[16] W. H. Furry. "On Transition Probabilities in Double Beta-Disintegration". In: *Phys. Rev.* 56 (12 Dec. 1939), pp. 1184–1193. DOI: 10.1103/PhysRev.56.1184.

[17] M. Agostini et al. "Final Results of GERDA on the Search for Neutrinoless Double-β Decay". In: *Phys. Rev. Lett.* 125 (25 Dec. 2020), p. 252502. DOI: 10.1103/PhysRevLett.125.252502.

[18] D. Q. Adams and et al. "Search for Majorana neutrinos exploiting millikelvin cryogenics with CUORE". In: *Nature* 604 (2022), pp. 53–58. DOI: 10.1038/s41586-022-04497-4.

[19] G. Anton et al. “Search for Neutrinoless Double-β Decay with the Complete EXO-200 Dataset”. In: *Phys. Rev. Lett.* 123 (16 Oct. 2019), p. 161802. DOI: 10.1103/PhysRevLett.123.161802.

[20] A. Gando et al. “Search for Majorana Neutrinos Near the Inverted Mass Hierarchy Region with KamLAND-Zen”. In: *Phys. Rev. Lett.* 117 (8 Aug. 2016), p. 082503. DOI: 10.1103/PhysRevLett.117.082503.

[21] F. T. Avignone, S. R. Elliott, and J. Engel. “Double beta decay, Majorana neutrinos, and neutrino mass”. In: *Rev. Mod. Phys.* 80 (2 Apr. 2008), pp. 481–516. DOI: 10.1103/RevModPhys.80.481.

[22] S. Stoica and M. Mirea. “New calculations for phase space factors involved in double-β decay”. In: *Phys. Rev. C* 88 (3 Sept. 2013), p. 037303. DOI: 10.1103/PhysRevC.88.037303.

[23] Du šan Štefánik et al. “Reexamining the light neutrino exchange mechanism of the $0\nu\beta\beta$ decay with left- and right-handed leptonic and hadronic currents”. In: *Phys. Rev. C* 92 (5 Nov. 2015), p. 055502. DOI: 10.1103/PhysRevC.92.055502.

[24] R. Saakyan. “Two-Neutrino Double-Beta Decay”. In: *Annual Review of Nuclear and Particle Science* 63.1 (2013), pp. 503–529. DOI: 10.1146/annurev-nucl-102711-094904.

[25] M. J. Dolinski, A. W.P. Poon, and W. Rodejohann. “Neutrinoless Double-Beta Decay: Status and Prospects”. In: *Annual Review of Nuclear and Particle Science* 69.1 (2019), pp. 219–251. DOI: 10.1146/annurev-nucl-101918-023407.

[26] H. Akimune et al. “GT strengths studied by (^{3}He, t) reactions and nuclear matrix elements for double beta decays”. In: *Physics Letters B* 394.1 (1997), pp. 23–28. ISSN: 0370-2693. DOI: https://doi.org/10.1016/S0370-2693(96)01659-0.

[27] D. Frekers. “Nuclear reactions and the double beta decay”. In: *Progress in Particle and Nuclear Physics* 64.2 (2010). Neutrinos in Cosmology, in Astro, Particle and Nuclear Physics, pp. 281–284. ISSN: 0146-6410. DOI: https://doi.org/10.1016/j.ppnp.2009.12.029.

[28] C. J. Guess et al. "The ^{150}Nd(^{3}He,t) and ^{150}Sm(t,^{3}He) reactions with applications to $\beta\beta$ decay of ^{150}Nd". In: *Phys. Rev. C* 83 (6 June 2011), p. 064318. DOI: 10.1103/PhysRevC.83.064318.

[29] V. Soukeras et al. "Measurement of the double charge exchange reaction for the ^{20}Ne + ^{130}Te system at 306 MeV". In: *Results in Physics* 28 (2021), p. 104691. ISSN: 2211-3797. DOI: https://doi.org/10.1016/j.rinp.2021.104691.

[30] F. Cappuzzello et al. "Heavy-ion double charge exchange reactions: A tool toward $0\nu\beta\beta$ nuclear matrix elements". In: *Eur. Phys. J.* A51.11 (2015), p. 145. DOI: 10.1140/epja/i2015-15145-5.

[31] A. Spatafora. "Experimental and theoretical multi-channel study of direct nuclear reactions: a tool to provide data driven information on neutrino-less double-beta decay". PhD thesis. Università degli studi di Catania, 2022.

[32] D. Carbone et al. "Initial state interaction for the ^{20}Ne + ^{130}Te and ^{18}O + ^{116}Sn systems at 15.3 AMeV from elastic and inelastic scattering measurements". In: *Universe* 7.3 (2021). cited By 1. DOI: 10.3390/universe7030058.

[33] D. Carbone et al. "Analysis of two-nucleon transfer reactions in the ^{20}Ne + ^{116}Cd system at 306 MeV". In: *Physical Review C* 102.4 (2020). cited By 6. DOI: 10.1103/PhysRevC.102.044606.

[34] S. Calabrese et al. "Analysis of the background on cross section measurements with the MAGNEX spectrometer: The (20Ne, 20O) Double Charge Exchange case". In: *Nuclear Instruments and Methods in Physics Research, Section A: Accelerators, Spectrometers, Detectors and Associated Equipment* 980 (2020). cited By 0. DOI: 10.1016/j.nima.2020.164500.

[35] S. Burrello et al. "Multichannel experimental and theoretical constraints for the ^{116}Cd(^{20}Ne,^{20} F)^{116}In charge exchange reaction at 306 MeV". In: *Phys. Rev. C* 105 (2 Feb. 2022), p. 024616. DOI: 10.1103/PhysRevC.105.024616.

[36] J. L. Ferreira et al. "Multinucleon transfer in the ^{116}Cd(^{20}Ne,^{20} O)^{116}Sn double charge exchange reaction at 306 MeV incident energy". In: *Phys. Rev. C* 105 (1 Jan. 2022), p. 014630. DOI: 10.1103/PhysRevC.105.014630.

[37] A. Spatafora et al. "^{20}Ne+^{76}Ge elastic and inelastic scattering at 306 MeV". In: *Phys. Rev. C* 100 (3 Sept. 2019), p. 034620. DOI: 10.1103/PhysRevC.100.034620.

[38] L. La Fauci et al. "^{18}O +^{76} Se elastic and inelastic scattering at 275 MeV". In: *Phys. Rev. C* 104 (5 Nov. 2021), p. 054610. DOI: 10.1103/PhysRevC.104.054610.

[39] I. Ciraldo et al. "Analysis of the one-neutron transfer reaction in ^{18}O+^{76}Se collisions at 275 MeV". In: *Phys. Rev. C* 105 (4 Apr. 2022), p. 044607. DOI: 10.1103/PhysRevC.105.044607.

[40] F. Cappuzzello et al. "Confirmation of Giant Pairing Vibration evidence in ^{12,13}C(^{18}O,^{16}O) ^{14,15}C reactions at 275 MeV". In: *European Physical Journal A* 57.1 (2021). cited By 1. DOI: 10.1140/epja/s10050-021-00345-7.

[41] A. Spatafora. "A full-comprehensive experimental and theoretical approach applied to the $^{12}C(^{18}O,^{18}F)^{12}B$ single charge-exchange reaction at 15.3 AMeV". In: *Il Nuovo Cimento C* 45 (2022), p. 131. DOI: 10.1393/ncc/i2022-22131-7.

[42] O. Sgouros et al. "One-proton transfer reaction for the ^{18}O +^{48} Ti system at 275 MeV". In: *Phys. Rev. C* 104 (3 Sept. 2021), p. 034617. DOI: 10.1103/PhysRevC.104.034617.

[43] G. A. Brischetto. "Data reduction of the ^{18}O + ^{48}Ti elastic and inelastic scattering at 275 MeV in the context of the NUMEN project". In: *Il Nuovo Cimento C* 45 (2022), p. 96. DOI: 10.1393/ncc/i2022-22096-5.

[44] H. Lenske et al. "Theory of Single Charge Exchange Heavy Ion Reactions". In: *Phys. Rev.* C98.4 (2018), p. 044620. DOI: 10.1103/PhysRevC.98.044620.

[45] H. Lenske. "Probing Double Beta-Decay by Heavy Ion Charge Exchange Reactions". In: *J. Phys.: Conf. Ser.* 1056 (July 2018), p. 012030. DOI: 10.1088/1742-6596/1056/1/012030.

[46] J. I. Bellone et al. "Two-step description of heavy ion double charge exchange reactions". In: *Physics Letters B* 807 (2020), p. 135528. ISSN: 0370-2693. DOI: 10.1016/j.physletb.2020.135528.

[47] J. A. Lay et al. “Double charge-exchange reactions and the effect of transfer”. In: *Journal of Physics: Conference Series* 1056 (July 2018), p. 012029. DOI: 10.1088/1742-6596/1056/1/012029.

[48] E. Santopinto et al. “Heavy-ion double-charge-exchange and its relation to neutrinoless double-β decay”. In: *Phys. Rev. C* 98 (6 Dec. 2018), p. 061601. DOI: 10.1103/PhysRevC.98.061601.

[49] C. Agodi and et al. In: *Universe* 7 (2021), p. 72. DOI: 10.3390/universe7030072.

2

The present MAGNEX facility

Contents

2.1 The scattering chamber **30**

2.2 The MAGNEX magnetic elements **34**

2.2.1 Trajectory reconstruction 36

2.3 The present Focal Plane Detector **38**

2.3.1 The gas tracker 39

2.3.2 The silicon stopping wall 42

2.3.3 Principle of operation 43

The study of Double Charge Exchange (DCE) nuclear reactions constitutes the heart of the NUMEN project as they represent a formidable tool to deduce data-driven information on the neutrinoless double beta ($0\nu\beta\beta$) decay Nuclear Matrix Elements (NMEs). The measurement of the extremely low cross-sections of such a kind of nuclear reactions represents an arduous challenge that requires sophisticated experimental tools and techniques. It is at the Laboratori Nazionali del Sud of the Istituto Nazionale di Fisica Nucleare (LNS-INFN) in Catania that the NUMEN project has found the infrastructures and the expertise needed to carry out its research activity in the last years. Indeed, therein the coexistence of the K800 Superconducting Cyclotron (SC) and of the MAGNEX large-acceptance magnetic spectrometer has created the appropriate conditions to perform high-sensitivity measurements of nuclear reactions, as it was demonstrated for the first time in Ref. [50] where differential cross-sections of few tens of nb/sr were measured.

As discussed in Subsect. 1.4.1, during the Phase 2 the NUMEN project has carried out at the LNS an experimental campaign on some of the nuclei relevant for the $0\nu\beta\beta$ decay. In each of these experiments, in addition to the DCE process, a network of direct reaction channels was measured, according to the multichannel approach described in Subsect. 1.4.2. Such a network involves elastic and inelastic scattering, one- and two-proton transfer reactions, one- and two-neutron transfer reactions, and single charge exchange reaction. In this chapter, the MAGNEX facility used for the Phase 2 experimental campaign is described. The MAGNEX spectrometer is a complex detection system made up of three main components: a scattering chamber, a quadrupole-dipole magnet pair, and a focal plane detector. For the sake of clarity, each component is discussed in a dedicated section in the following.

Since one of the main subjects of the present work is the analysis of the elastic and inelastic scattering generated in the $^{18}O + ^{48}Ti$ collision at 275 MeV incident energy (see Chapt. 3), the description of the MAGNEX facility is presented in relation to the experimental set-up adopted for this measurement.

2.1 The scattering chamber

The $^{18}O^{8+}$ beam used for the ^{18}O + ^{48}Ti experiment was accelerated by the SC [2] to 15.3 AMeV bombarding energy with a high energy resolution (1/1000) and low emittance ($\rightarrow 2\pi$ mm mr). It was delivered through the magnetic elements of the beam line to the MAGNEX scattering chamber, that is placed within the MAGNEX experimental hall. In order to unambiguosly define the measured kinematic variables, a proper definition of the laboratory reference frame must be given. The origin of such a reference frame is set as the object point of the MAGNEX spectrometer, while the corresponding axes are chosen in the following way: the y-axis is the spectrometer rotation axis (vertical direction); the z-axis is along the beam direction; the x-axis is fixed by the two previous definitions to allow a right-handed orthogonal system.

The target consisted in a 510 μg/cm^2 thick $^{48}TiO_2$ layer evaporated on a 216 μg/cm^2 thick aluminum backing, which was produced by the "Thin-films laboratory" of the LNS. To estimate the background contributions due to the oxygen target component, additional measurements were performed using a 284 μg/cm^2 thick WO_3 target evaporated on a 230 μg/cm^2 thick aluminum backing. The background due to the aluminum backing, present in both the $^{48}TiO_2$ and the WO_3 target, was measured by performing auxiliary runs with a 226 μg/cm^2 thick natural aluminum target. A picture of the targets used in the experiment is shown in Fig. 2.1. The targets thicknesses were deduced by measuring the energy loss of α-particles generated by a radioactive source, giving uncertainties of about $\mp 5\%$. The positioning of the target in the object point of the MAGNEX spectrometer is carried out by a steppermotor controlled by the slow control system, which moves the target ladder with sub-millimetric accuracy.

In the target ladder were also hosted an alumina (see Fig. 2.1), a quartz that emits visible light when hit by the beam. It has a central hole of 3 mm diameter, which was carefully positioned in the spectrometer object point. Thanks to a CCD camera placed inside the scattering chamber, it is possible to see the beam impact point on the alumina and, therefore, to tune the beam transport along the line in order to minimize the dimensions of the beam spot and to centre it with respect to the alumina hole.

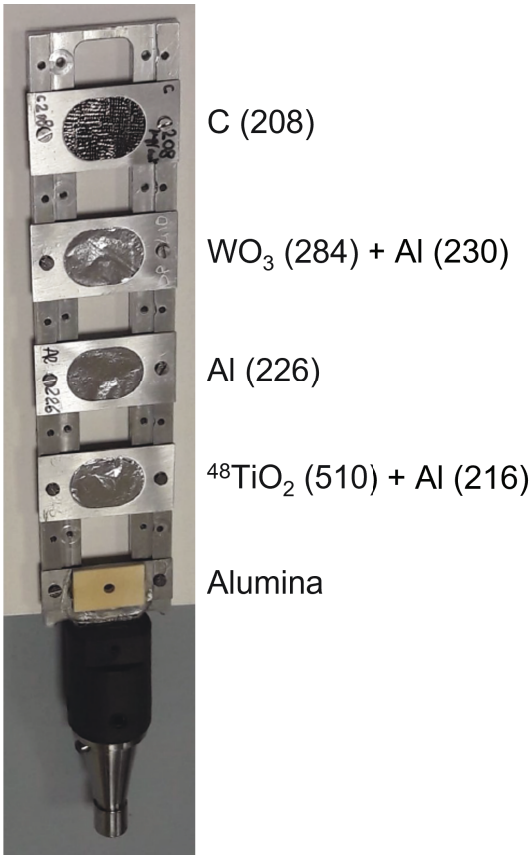

Figure 2.1: Target ladder: in parenthesis the thicknesses of the several targets are indicated in μg/cm^2.

A copper Faraday Cup (FC) with 0.8 cm entrance diameter and 3 cm depth was placed 15 cm downstream the target position (along the beam direction) to stop the beam and collect its total charge in each run, which is essential for the determination of absolute cross-sections. The FC was equipped with an electron suppressor, that was polarized at 200 V to ensure that all the electrons generated in the interaction between the beam ions and the copper material are collected. The beam current measured by the FC is converted into charge by a low-noise integrator [51], with an intrinsic accuracy better than 0.5% [3]. For each run, the integrated charge is saved in the memory of a latching scaler [52], that provides two charge measurements: one is independent from the busy signal of the acquisition system (Q_{raw}), the other is in coincidence with it (Q_{live}). The ratio between these two quantities defines the live time t_{live} of each experimental run.

Four copper slits downstream the target define the MAGNEX angular acceptance. They are accurately positioned by remotely controlled stepper motors, being the position measured through appropriate potentiometers [53]. The maximum MAGNEX angular acceptance is [5.16°; +6.13°] horizontal and [7.16°; +7.16°] vertical, corresponding to a total solid angle of $\Delta\Omega \rightarrow 50$ msr. A picture of the interior of the scattering chamber is shown in Fig. 2.2.a, where the four slits and the FC are clearly visibile.

A collimation system was mounted to limit the beam spot diameter to $\rightarrow 3$ mm at the target position and the beam angular divergence to 3 mrad. It consisted of a 2 mm diameter collimator followed by a 4 mm diameter antiscatterer placed 125 and 20 mm upstream the target, respectively.

An ancillary ΔE E telescope detector was placed in the scattering chamber. The ΔE layer was a 50 μm thick silicon (Si) detector biased at +10 V to measure the ions energy loss. The E stage was a thallium-doped cesium iodide crystal (CsI(Tl)) with dimensions of $15 \pm 15 \pm 5$ mm^3, where the ions were stopped producing a number of photons proportional to their residual energy. The photons were detected by a silicon photodiode polarized at 70 V. The telescope was placed at the same height of the object point at angle of 19.5° with respect to the beam direction. A small collimator was put in front of the monitor detector to reduce the rate of incident ions. In Fig. 2.2.b, a picture of the monitor detector and of the collimation system is reported.

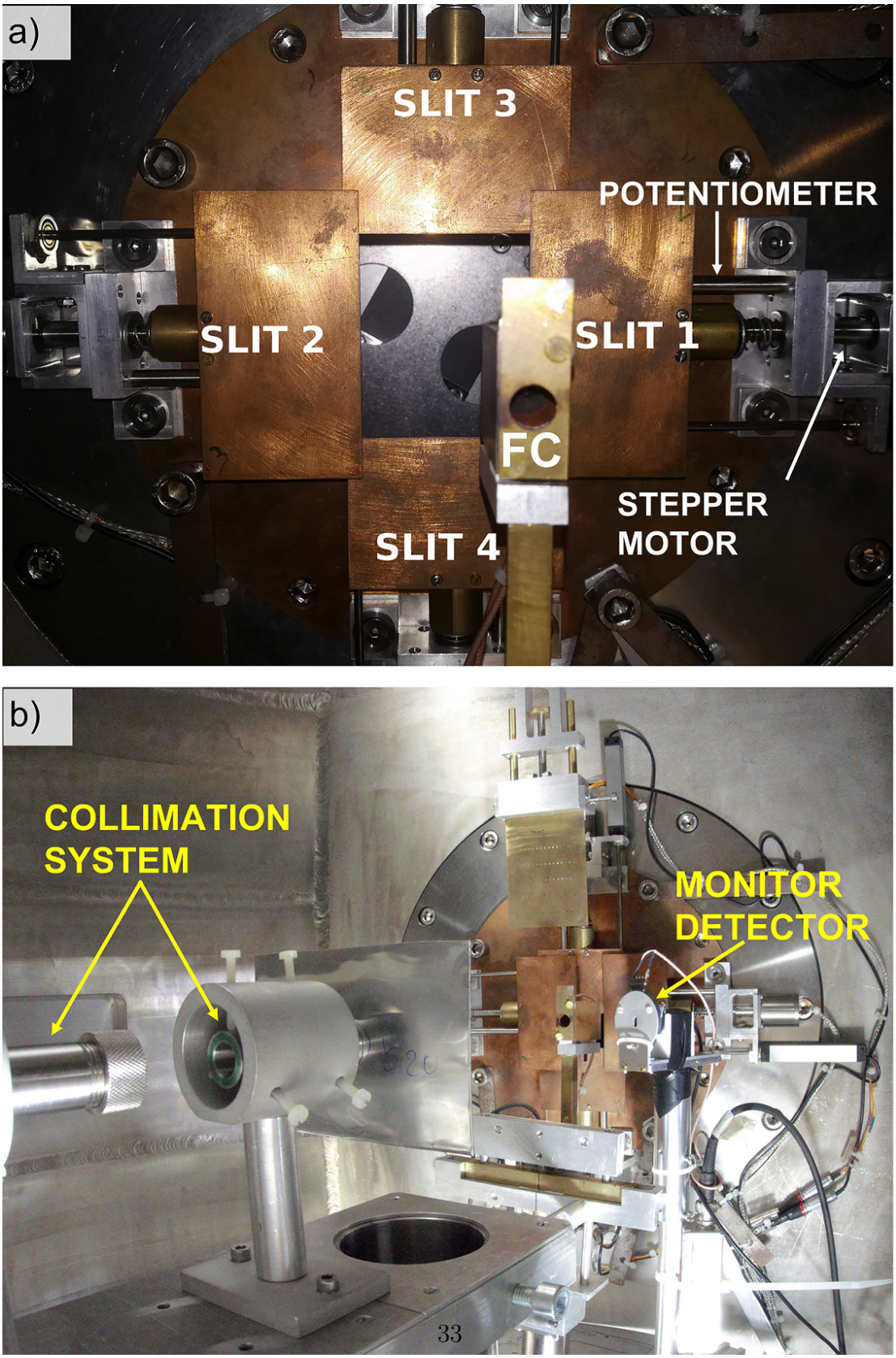

Figure 2.2: Interior of the scattering chamber. (a) The four slits that define the MAGNEX angular acceptance and the Faraday Cup (FC). (b) The collimation system and the monitor detector.

A careful alignment of all the mentioned item was carried out by using accurate optical instruments (theodolites and bubble-levels), ensuring an accuracy of about 0.1 mm. This is essential to control that the beam hits the target at the spectrometer object point and that the kinematic variables are well measured.

2.2 The MAGNEX magnetic elements

MAGNEX is a large-acceptance magnetic spectrometer [3], belonging to the family of the Quadrupole-Dipole (QD) spectrometers. It is composed by two large-aperture magnets: the quadrupole [54] and the 55° dipole [55]. The quadrupole magnet (Q) focuses the ejectiles in the vertical (non-dispersive) direction, while the dipole (D) provides the dispersion along the horizontal direction. In Fig. 2.3, a picture of the MAGNEX spectrometer and of its experimental hall are shown. The most important optical and magnetic properties of the MAGNEX spectrometer are listed in Table 2.1.

MAGNEX can rotate around its object point by moving on a rail (see Fig. 2.3.b). In this way, the angle (θ_{opt}) between the spectrometer optical axis and the beam direction can be set between 15° and 70°. The value of θ_{opt} is typically chosen according to the nuclear reaction under study, e.g. for the elastic scattering measurements discussed in this Thesis three angular ranges were explored where θ_{opt} was set, respectively, to 9°, 15°, and 21°. For each configuration, the angular acceptance is defined by positioning the horizontal and vertical slits inside the scattering chamber (see Fig. 2.2)

MAGNEX offers high performance in terms of mass (ΔA/A $\rightarrow$1/300)[56–58], angular ($\Delta\theta/\theta \rightarrow$0.2°) and energy resolution (ΔE/E $\rightarrow$1/1000). A key aspect that makes MAGNEX a unique device is the possibility to account for highly non linear optical aberrations by applying a sophisticated ray-reconstruction technique based on the differential algebra formalism. Since this characteristic is fundamental for the understanding of the MAGNEX operation, it will be discussed in detail in the next paragraph.

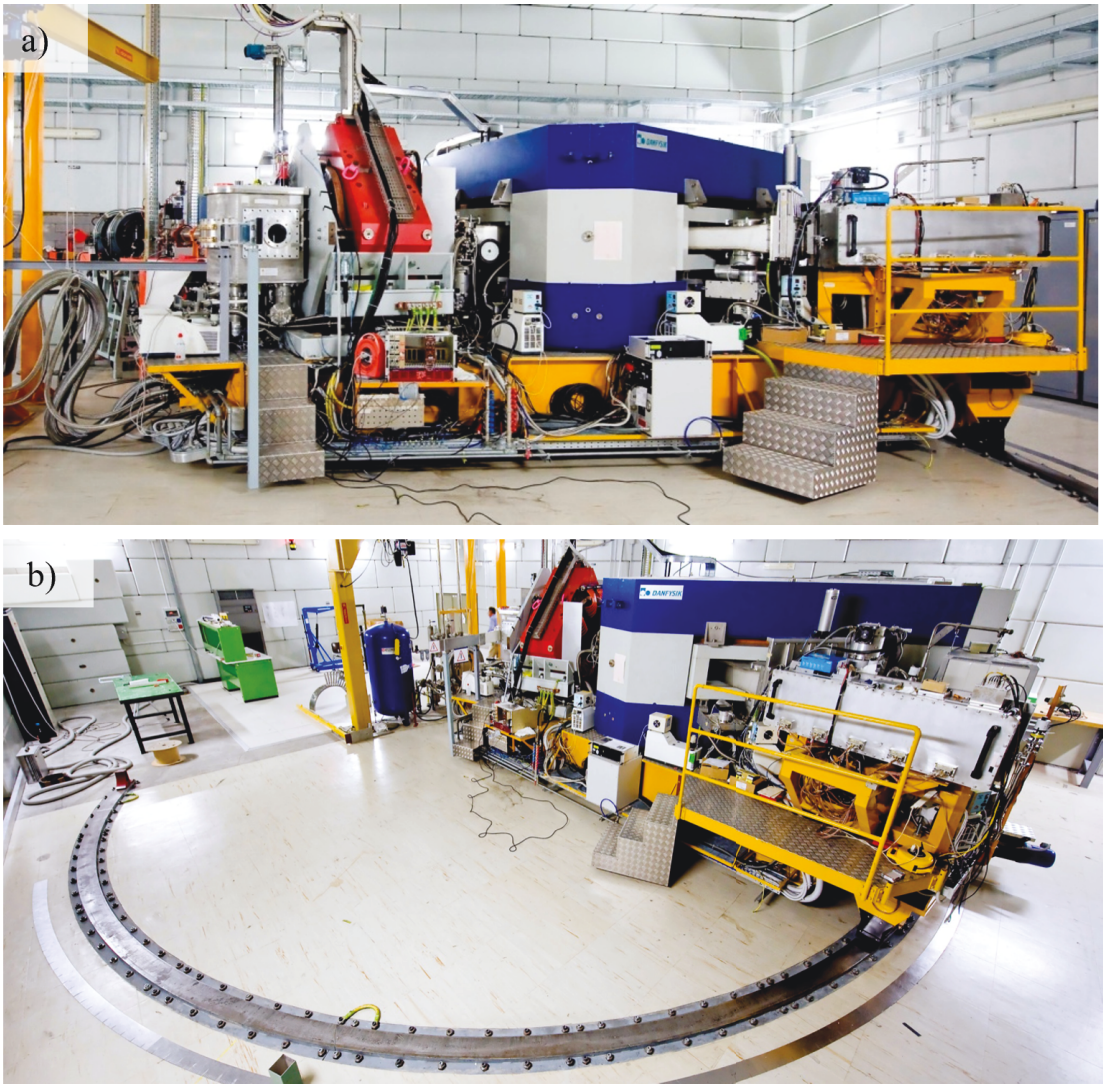

Figure 2.3: The MAGNEX magnetic spectrometer at the LNS-INFN in Catania. (a) From the left to the right: the scattering chamber, the quadrupole (red) magnet, the dipole (blue) magnet and the Focal Plane Detector chamber. (b) Panoramic view of the MAGNEX experimental hall.

Table 2.1: Main optical properties of the MAGNEX magnetic spectrometer (from Ref. [3]).

		Actual value
Optical properties	Maximum magnetic rigidity (Tm)	1.8
	Solid angle (msr)	50
	Horizontal angular acceptance (mrad)	-90, +110
	Vertical angular acceptance (mrad)	-123, +123
	Momentum acceptance (%)	-14, +10
	Central path length (cm)	596
	Momentum dispersion (cm/%)	3.68
	Focal plane rotation angle (deg)	59.2
	Focal plane length (cm)	92
	Focal plane height (cm)	20
Dipole parameters	Maximum Field (T)	1.15
	Bending angle (deg)	55
	Bending radius ρ (m)	1.60
	$\rho_{\min}$, $\rho_{\max}$ (m)	0.95, 2.35
Quadrupole parameters	Maximum field strength (T/m)	5
	Radius of aperture (cm)	20
	Effective length (cm)	58

2.2.1 Trajectory reconstruction

The motion of a charged particle through a spectrometer can be formally expressed as a phase-space map F that connects the initial phase-space vector P_i to the final phase-space one P_f, namely

$$F : P_i \propto P_f \tag{2.1}$$

The P_i and P_f vectors are respectively defined as $P_i \leq P_i(x_i, y_i, \theta_i, \phi_i, l_i, \delta_i)$ and $P_f \leq P_f(x_f, y_f, \theta_f, \phi_f, l_f, \delta_f)$, where x, y, θ, ϕ represent the horizontal and vertical positions and angles, respectively, of the particle with respect to the reference one; l is the difference in path length between the particle trajectory and the reference one; $\delta = (p \quad p_0)/p_0$ is the fractional momentum of the particle momentum p with respect to reference one p_0. Eq. 2.1 describes a non-linear transport relation, which depends on the specific magnetic field of the optical system. A more explicit

way to express Eq. 2.1 in terms of the measured observables is the following

$$\begin{aligned} x_f &= F_1(x_i, \theta_i, y_i, \phi_i, l_i, \delta_i) \\ \theta_f &= F_2(x_i, \theta_i, y_i, \phi_i, l_i, \delta_i) \\ y_f &= F_3(x_i, \theta_i, y_i, \phi_i, l_i, \delta_i) \\ \phi_f &= F_4(x_i, \theta_i, y_i, \phi_i, l_i, \delta_i) \\ l_f &= F_5(x_i, \theta_i, y_i, \phi_i, l_i, \delta_i) \\ \delta_f &= \delta_i \end{aligned} \tag{2.2}$$

For thin targets, the parameter l_i is practically constant, therefore it can be neglected in the following discussion. The last equation in 2.2 highlights the conservation of the momentum modulus in a static magnetic field in absence of energy absorbing materials. The previous equations can be expanded in Taylor series using the tensor notation as follows

$$\begin{aligned} q_j(f) &= \sum_k \frac{\partial q_j(f)}{\partial q_k(i)} q_k(i) + \sum_{k,l} \frac{\partial q_j(f)}{\partial q_k(i)} \frac{\partial q_j(f)}{\partial q_l(i)} q_k(i) q_l(i) + \dots \\ &= \sum_k R_{jk}\, q_k(i) + \sum_{k,l} T_{jkl}\, q_k(i) q_l(i) + \dots \end{aligned} \tag{2.3}$$

where $q_j(f)$ and $q_k(i)$ are the generic final and initial phase-space coordinates, while R_{jk} and T_{jkl} are the first and second order coefficients, respectively. The coefficients higher than the first order are usually referred to as aberrations, since they describe the deviations from the ideal first-order optical properties. The maximum order of the Taylor expansion is strictly related to the acceptance of the magnetic spectrometer; indeed, for small acceptance device the first order truncation is typically sufficient to describe the ions motion. In case of large acceptance spectrometers, higher order terms must be included (e.g. for the MAGNEX spectrometer, an expansion to the 10^{th} order is needed [59]).

The momentum vector at the target position can be determined by inverting Eq. 2.1, which can be formally expressed as

$$F^{-1} : P_f \propto P_i \tag{2.4}$$

The inversion problem implied in Eq. 2.4 can be opportunely reformulated in terms of the measured observables at the focal plane, which can be expressed in vector notation as $Q_f(x_f, y_f, \theta_f, \phi_f)$. Analogously, the reconstructed quantities can be denoted as $Q_i(y_i, \theta_i, \phi_i, \delta)$. Under this hypothesis, Eq. 2.4 can be rewritten as

$$G^{-1} : Q_f \propto Q_i \tag{2.5}$$

The ray-reconstruction procedure consists in determining and inverting the G operator or, equivalently, to solve for the G operator the transport equations analogous to 2.2. The stability and the accuracy of the solution are strongly dependent on the spectrometer acceptance, because, as stated above, high-order terms in the Taylor expansion of the transport equations are needed as the acceptance increases. A powerful tool to solve high-order transport problems is the COSY INFINITY software, which was developed at the Michigan State University using the differential algebra formalism [60]. The application of such an algorithm requires the precise description of the magnetic fields crossed by the particles [61, 62], the exact knowledge of the spectrometer geometry [59] and the accurate measurement of the phase-space vector Q_f at the focal plane. The accuracy level needed for all the mentioned items can be estimated by using sophisticated numerical simulations, as described in Ref. [63] for the MAGNEX case. The COSY INFINITY software requires also the accurate knowledge of the position of the beam spot at the target, as well as the precise location of the magnets and of the FPD. Therefore accurate measurements and alignments are performed, as discussed in the previous section, to obtain an efficient reconstruction of the momentum vector at the target position.

2.3 The present Focal Plane Detector

The Focal Plane Detector (FPD) is usually considered the heart of the modern large-acceptance magnetic spectrometers, since they have to provide an accurate three-dimensional tracking of the ions trajectory at the focal plane [64–67]. The MAGNEX FPD [56, 57] is an hybrid detection system composed by two main parts: a gas tracker, sensitive to position, direction and energy loss of the ions, and a silicon detector stopping wall, which measures the ions residual energy. For

the sake of clarity, we discuss each component in a dedicated section. A cartoon highlighting the MAGNEX FPD structure is illustrated in Fig. 2.4. The FPD entrance plane is not perpendicular to the spectrometer optical axis; instead, it is rotated by an angle $\theta_{tilt} = 59.2°$ with respect to a plane orthogonal to the optical axis in order to minimize the effect of the chromatic aberrations [59].

2.3.1 The gas tracker

The MAGNEX gas tracker is a proportional drift chamber with a total active volume of $1360 \pm 200 \pm 90$ mm^3. It is divided into six sections, each one constituting an independent position-sensitive proportional counter. The gas tracker is hosted in the vacuum chamber, which can be moved of ∓ 0.08 m along the optical axis direction to allow different focus condition. In Fig. 2.5.a, a picture of the vacuum chamber is shown. It is filled with isobutane gas (iC_4H_{10}) of 99.95% purity at a pressure typically of few tens of mbar (e.g. for the ^{18}O + ^{48}Ti experiment it was set at 15 mbar). The vacuum chamber is equipped with a system that continually flows the gas to maintain stable pressure operations and preserve the gas purity. The gas-filled vacuum chamber is separated from the high-vacuum region of the spectrometer by means of a 2.5 μm thick Mylar window (see Fig. 2.5.a), which is mechanically supported by a grid of twenty metallic wires with a diameter of 0.5 mm placed along the horizontal direction. The position of each wire is known with high precision and this allows to calibrate the vertical coordinate.

The gas tracker is composed by three different regions: the drift region, the multiplication stage and the induction region.

- The drift region is delimited by the cathode and the Frisch grid: the former is an aluminum plate typically biased at −1200 V, the latter is made up of ten gold-plated tungsten wires with 50 μm diameter placed at a distance of 5 mm one from another, typically biased a +300 V. A double partition grid composed by 41 couples of rings made of gold-plated wires delimits the active area of the tracker, making the drift electric field as uniform as possible and shielding it from the external field generated by the high voltages applied to the silicon detectors of the stopping wall.

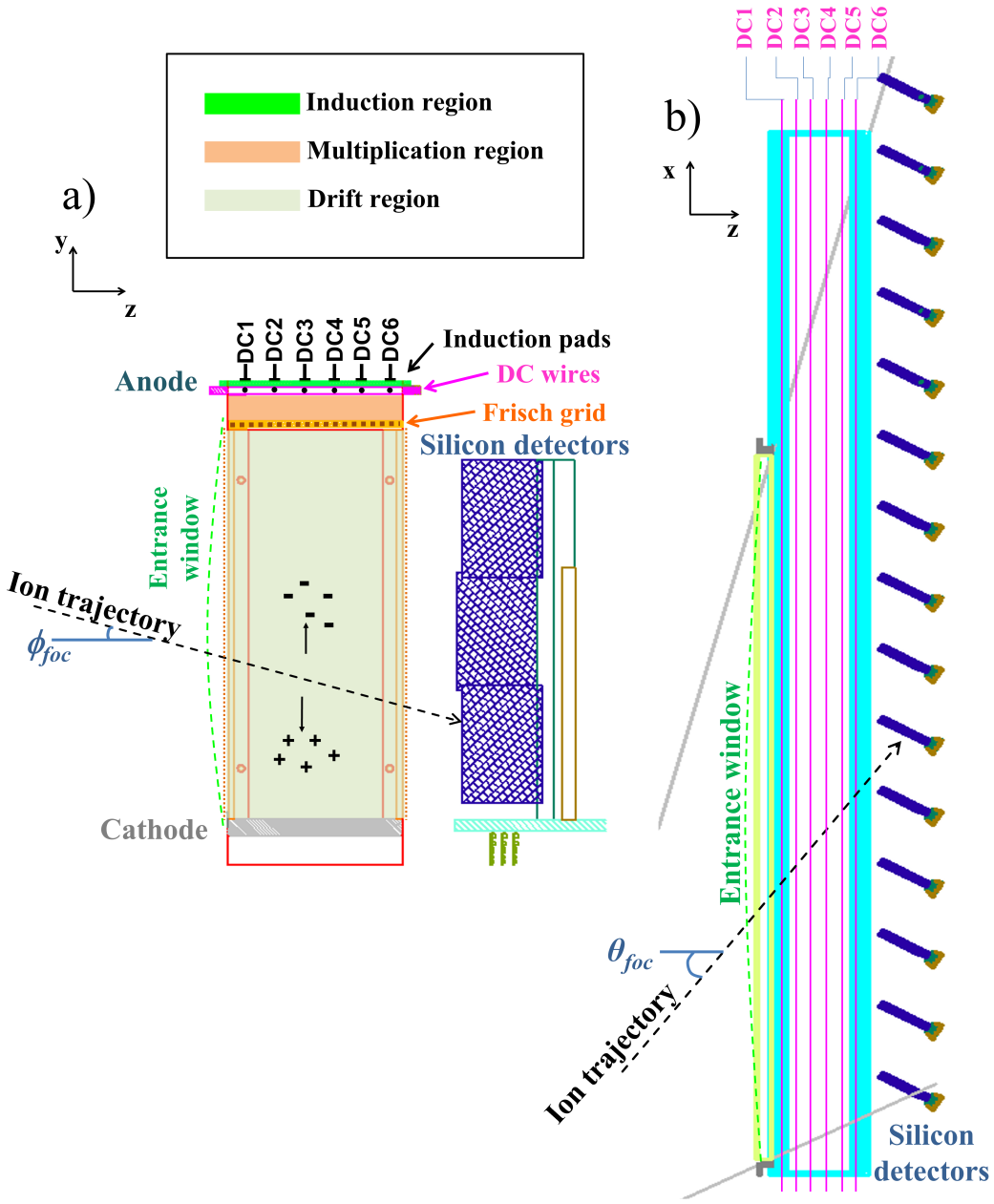

Figure 2.4: Schematic drawings of the MAGNEX FPD, showing the gas tracker and silicon stopping wall in: (a) lateral view (y-z plane) and (b) top view (x-z plane).

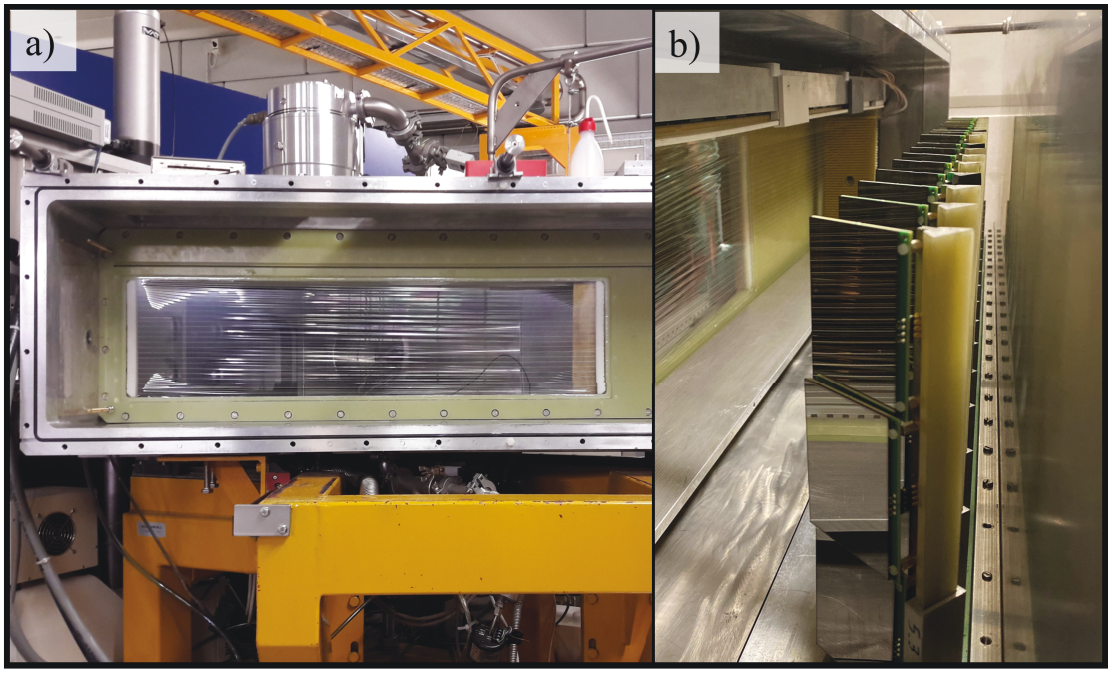

Figure 2.5: Picture of: (a) the vacuum chamber that hosts the gas tracker, opened on one side and showing the Mylar window; (b) the silicon detector columns. Figure from Ref. [31]

- The multiplication stage is 20 mm high and is delimited by the Frisch grid and the plane in which 10 proportional gold-plated tungsten wires lay. The proportional wires have a diameter of 50 μm each one and are biased at +650 V by a common power supply. They are subdivided among the six Drift Chambers DC_i, where $i = 1, \ldots, 6$, in the following way: DC_2 and DC_5 have just one multiplication wire each one, while the other DCs have two proportional wires. A sketch of the segmented anode highlighting the proportional wires positions is reported in Fig. 2.6. A partition grid is positioned on the border of the multiplication stage to reduce the effect due to non-uniformity of the electric field in this region.

- The induction region is delimited by the 10 multiplication wires plane and the anode. The latter is composed by a pad-segmented readout plane which are arranged in six longitudinal strips, one for each DC. The strips corresponding to DC_2 or DC_5 are 8 mm wide, while the others are 16 mm wide. Each strip is segmented in about 220 pads oriented along the spectrometer optical axis, i.e. at an angle equal to θ_{tilt}. A schematic view of the anodic board is illustrated in Fig. 2.6.

2.3.2 The silicon stopping wall

The silicon stopping wall is located downstream the gas tracker in the same vacuum chamber. No dead layer separates the tracker region from the silicon stopping wall, so that the latter is embedded in gas environment. The stopping wall is made of 57 silicon detectors arranged in 19 columns. A picture of the silicon stopping wall is shown in Fig. 2.5.b. The silicon detectors were manufactured by Micron Semiconductor Ltd. and belong to the model SX35. Each detector has rectangular shape, an active area of 50 $\pm$ 70 mm^2 and is 500 μm thick, enough to completely stop the ejectiles of interest produced in the ^{18}O + ^{48}Ti collision at 275 MeV. They are mounted orthogonally to optical axis of the spectrometer to minimize the effective dead layer. The minimum distance between the silicon detector and the gas tracker active volume is 15 mm, which is enough to avoid interference with the electric field within the tracker.

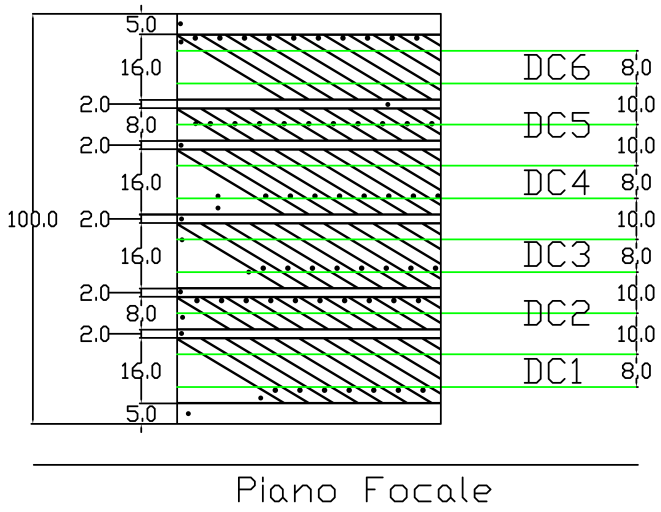

Figure 2.6: Scheme of the segmented anode (bottom view). The six anodic strips of corresponding to the six Drift Chambers DC_i are shown. Each strip is further segmented in pads (in gray) that are tilted of $\theta_{tilt} = 59.2°$. In green the positions of the proportional wires are shown. The sizes are expressed in mm. Figure from Ref. [57]

2.3.3 Principle of operation

An ejectile exiting from the dipole magnet crosses the Mylar window and enters in the drift region of the gas tracker. Therein, it generates a number of electron-ion pairs along its track. The electric field in the drift region of about 50 V/cm draws the positive ions to the cathode, while the electrons drift with almost constant velocity (about 5 cm/μs) towards the Frisch grid. Then, the primary electrons reach the multiplication stage, where they are accelerated by the strong electric field (reaching several kV/cm) produced by the proportional wires and generate the charge multiplication. Since the DCs operate in proportional regime, the total charge produced in the multiplication process is proportional to the primary charge. Therefore, a signal proportional to the energy loss of the ejectile is generated on the wire. Six independent energy loss measurements are acquired, one for each DC_i. The signals from the wires are shaped and amplified by charge-sensitive preamplifiers with a sensitivity of 200 mV/MeV (silicon equivalent). The output signals of the preamplifiers are fed to 16-channel MEGAMP modules designed at

INFN-Milano [68]. Each input channel of these modules produces two outputs: one is a shaped spectroscopic signal, which is sent to a peak-sensitive Analog to Digital Converter (ADC) to obtain the energy loss measurement (ΔE_i). The other output is a Constant Fraction Discriminator (CFD) logic signal, that is used as a STOP signal for the electron drift time measurement, as described in the following.

The electron avalanche generated in the multiplication process induces a charge on a number of pads just above the proportional wires. Such signals are preamplified and shaped by an analog multiplexed readout system based on GASSIPLEX chips [69]. The GASSIPLEX output is readout and digitally converted by a 100 MS/s Digitizer (CAEN model V1724) [70], that is controlled by a general purpose VME board (CAEN model V1495) [71]. The center of gravity of the charge distribution on the pads of a given DC_i is calculated by a specific algorithm. The six centers of gravity are then converted into six independent horizontal position measurements x_i, with $i = 1, \ldots, 6$. By fitting the six x_i with a straigth line, it is possible to obtain the horizontal coordinate (x_f) of the crossing point between the ejectile track and the focal plane, as well as the horizontal angle (θ_f) of the track.

Once crossed the gas tracker, the ejectile reaches the silicon detector stopping wall, where it deposits all its residual energy (E_{resid}). The silicon detectors signals are sent to charge preamplifiers similar to those used for the wires signals, but with sensitivity which can be set from 5 to 50 mV/MeV. The preamplified signals are fed to MEGAMP modules, which give spectroscopic and CFD outputs. The former are sent to peak-sensing ADCs to obtain the E_{resid} measurements of the ejectiles, the latter give multipurpose time signals for MAGNEX. The logic OR of the CFD signals provides the START signal for the electron drift time measurement (see explanation in the following), to trigger the data acquisition and to generate the gate windows for the ADCs. Since the overall dead layer are very thin, the energy threshold for the detection of ejectiles can be very low; with the thinnest Mylar window of 1.5 μm, it is of about 0.5 AMeV.

For each DC_i, a vertical position measurement of the track is determined by measuring the drift time of the primary electrons, which corresponds to the time interval between the START (silicon detectors) and the STOP (proportional

wires). The drift time is acquired with a standard Time to Amplitude Converter (TAC) plus ADC electronic chain. The drift time is converted into a vertical position by multiplying the former for the electron drift velocity, which can be considered as a constant since the tracker operates in electron velocity saturation regime. A total of six independent vertical position measurements y_i (where $i = 1, \ldots, 6$) is thus obtained. Analogously to the horizontal positions, a linear fit of the six y_i is performed, in order to determine the vertical coordinate (y_f) of the crossing point between the ejectile track and the focal plane, as well as the vertical angle (ϕ_f) of the track. A simplified scheme of the electronic chain and readout of the FPD signals is shown in Fig. 2.7.

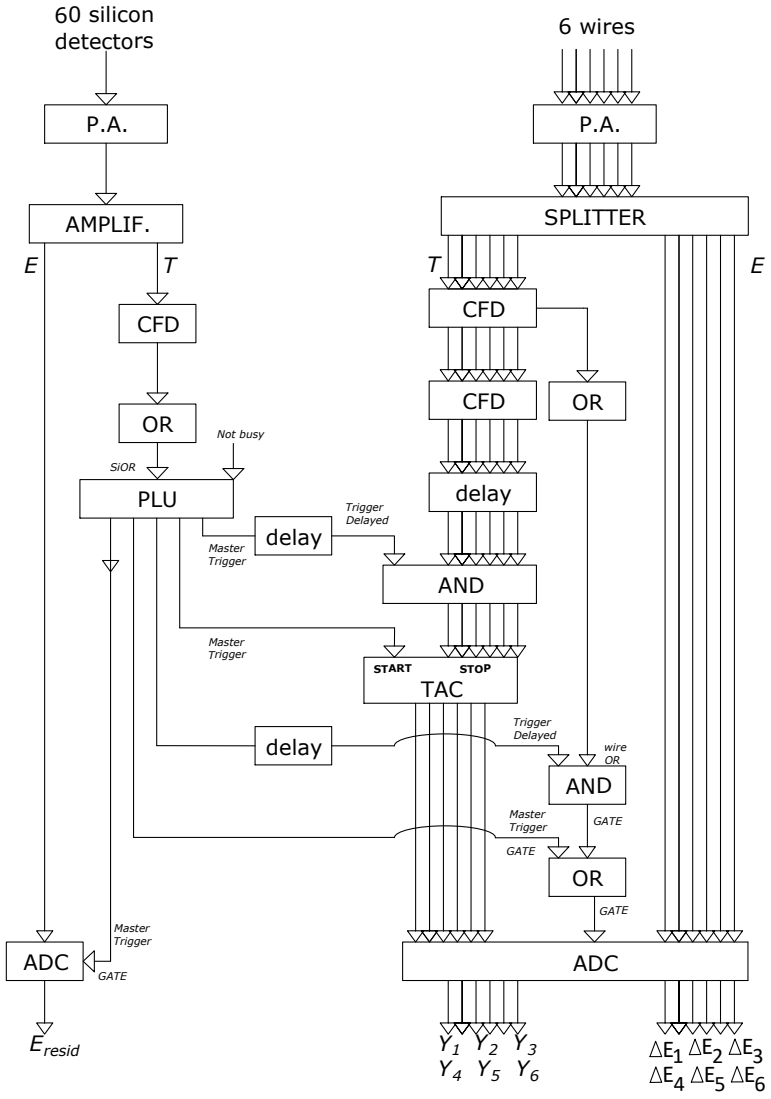

Figure 2.7: Scheme of the electronics and read-out of the detectors signals at the MAGNEX FPD.

Chapter References

[2] D. Rifuggiato, L. Calabretta, and G. Cuttone. "Cyclotrons and their applications. Proceedings, 17th International Conference, Cyclotrons 2004". In: *Part. Accel. Soc. Japan (2004) 541 p* (2004). Ed. by Akira Goto.

[3] F. Cappuzzello et al. "The MAGNEX spectrometer: results and perspectives". In: *Eur. Phys. J. A* 52.6 (2016), p. 167. DOI: 10.1140/epja/i2016-16167-1.

[31] A. Spatafora. "Experimental and theoretical multi-channel study of direct nuclear reactions: a tool to provide data driven information on neutrino-less double-beta decay". PhD thesis. Università degli studi di Catania, 2022.

[50] D. Pereira et al. "Nuclear rainbow in the 16O+27AL system: The role of couplings at energies far above the barrier". In: *Phys. Lett. B* 710.3 (2012), pp. 426–429. ISSN: 0370-2693. DOI: https://doi.org/10.1016/j.physletb.2012.03.032.

[51] USA ORTEC. *Digital Current Integrator mod. 439*. https://www.ortec-online.com/products/electronics/digital-current-integrator/439. Oct. 2021.

[52] Italy CAEN Viareggio. *32 channel Latching Scaler mod. v820*. https://www.caen.it/products/v830/. Oct. 2021.

[53] M. Cavallaro et al. "Transport efficiency in large acceptance spectrometers". In: *Nucl. Instrum. Meth. A* 637 (May 2011), pp. 77–87. DOI: 10.1016/j.nima.2011.01.078.

[54] A. Lazzaro et al. “Field measurement for large quadrupole magnets”. In: *Nuclear Instruments and Methods in Physics Research Section A: Accelerators, Spectrometers, Detectors and Associated Equipment* 591.2 (2008), pp. 394–405. ISSN: 0168-9002. DOI: https://doi.org/10.1016/j.nima.2008.02.103.

[55] A. Lazzaro et al. “Field measurement for large bending magnets”. In: *Nuclear Instruments and Methods in Physics Research Section A: Accelerators, Spectrometers, Detectors and Associated Equipment* 585.3 (2008), pp. 136–145. ISSN: 0168-9002. DOI: https://doi.org/10.1016/j.nima.2007.10.046.

[56] M. Cavallaro et al. “The low-pressure focal plane detector of the MAGNEX spectrometer”. In: *The European Physical Journal A* 48.5 (May 2012), p. 59. ISSN: 1434-601X. DOI: 10.1140/epja/i2012-12059-8.

[57] D. Torresi et al. “An upgraded focal plane detector for the MAGNEX spectrometer”. In: *Nuclear Instruments and Methods in Physics Research Section A: Accelerators, Spectrometers, Detectors and Associated Equipment* 989 (2021), p. 164918. ISSN: 0168-9002. DOI: https://doi.org/10.1016/j.nima.2020.164918.

[58] A. Badalà et al. “Trends in particle and nuclei identification techniques in nuclear physics experiments - *Nuovo Cimento accepted*”. In: *Nuovo Cimento C* (2022). DOI: 10.1007/s40766-021-00028-5.

[59] A. Cunsolo et al. “Ion optics for large-acceptance magnetic spectrometers: application to the MAGNEX spectrometer”. In: *Nuclear Instruments and Methods in Physics Research Section A: Accelerators, Spectrometers, Detectors and Associated Equipment* 484.1 (2002), pp. 56–83. ISSN: 0168-9002. DOI: https://doi.org/10.1016/S0168-9002(01)02004-6.

[60] K. Makino and M. Berz. “COSY INFINITY version 8”. In: *Nuclear Instruments and Methods in Physics Research Section A: Accelerators, Spectrometers, Detectors and Associated Equipment* 427.1 (1999), pp. 338–343. ISSN: 0168-9002. DOI: https://doi.org/10.1016/S0168-9002(98)01554-X.

[61] A. Lazzaro et al. “Field simulations for large dipole magnets”. In: *Nuclear Instruments and Methods in Physics Research Section A: Accelerators, Spectrometers, Detectors and Associated Equipment* 570.1 (2007), pp. 192–204. ISSN: 0168-9002. DOI: https://doi.org/10.1016/j.nima.2006.10.055.

[62] A. Lazzaro et al. “Field reconstruction in large aperture quadrupole magnets”. In: *Nuclear Instruments and Methods in Physics Research Section A: Accelerators, Spectrometers, Detectors and Associated Equipment* 602.2 (2009), pp. 494–500. ISSN: 0168-9002. DOI: https://doi.org/10.1016/j.nima.2009.01.019.

[63] A. Lazzaro. “The large acceptance and high resolution ray-tracing magnetic spectrometer MAGNEX”. PhD thesis. Università degli studi di Catania, 2002.

[64] A. Lazzaro et al. “Computational aspects of the trajectory reconstruction in the MAGNEX large acceptance spectrometer”. In: vol. 175. Cited by: 5. 2005, pp. 171–180.

[65] F. Cappuzzello, D. Carbone, and M. Cavallaro. “Measuring the ions momentum vector with a large acceptance magnetic spectrometer”. In: *Nucl. Instrum. Methods Phys. Res. A* 638.1 (2011), pp. 74–82. ISSN: 0168-9002. DOI: https://doi.org/10.1016/j.nima.2011.02.045.

[66] S. Pullanhiotan et al. “Performance of VAMOS for reactions near the Coulomb barrier”. In: *Nuclear Instruments and Methods in Physics Research Section A: Accelerators, Spectrometers, Detectors and Associated Equipment* 593.3 (2008), pp. 343–352. ISSN: 0168-9002. DOI: https://doi.org/10.1016/j.nima.2008.05.003.

[67] D. Montanari et al. “Response function of the magnetic spectrometer PRISMA”. In: *The European Physical Journal A* 47.1 (2011), p. 4. DOI: 10.1140/epja/i2011-11004-9.

[68] C. Boiano, A. Guglielmetti, and S. Riboldi. “A 16 channels multi detector pulse shape amplifier with serialized readout”. In: *2012 IEEE Nuclear*

Science Symposium and Medical Imaging Conference Record (NSS/MIC). 2012, pp. 865–867. DOI: 10.1109/NSSMIC.2012.6551228.

[69] M. Bordessoule et al. "A simplified read out for high-resolution linear gas detector". In: *Nuclear Instruments and Methods in Physics Research Section A: Accelerators, Spectrometers, Detectors and Associated Equipment* 390.1 (1997), pp. 79–85. ISSN: 0168-9002. DOI: https://doi.org/10.1016/S0168-9002(97)00352-5.

[70] Italy CAEN Viareggio. *8 Channel 14 bit 100 MS/s Digitizer mod. V1724*. https://www.caen.it/products/v1724/. Oct. 2021.

[71] Italy CAEN Viareggio. *General purpose vme board mod. v1495*. https://www.caen.it/products/v1495/. Oct. 2021.

3

The ^{18}O + ^{48}Ti elastic and inelastic scattering

Contents

3.1 Data reduction **52**
3.1.1 Calibration 53
3.1.2 Particle Identification 60
3.1.3 Final phase-space parameters 62
3.1.4 Application of the ray-reconstruction technique to the experimental data 63
3.1.5 Excitation energy spectrum 71
3.1.6 Cross section angular distribution 71
3.2 Determination of the Initial State Interaction **77**
3.2.1 Optical Potential 78
3.2.2 Optical Model results 80
3.2.3 Coupling to the inelastic scattering channels 82
3.2.4 The ^{18}O + ^{48}Ti scattering at 54 MeV 84

The multi-channel approach consists in a unitary description of a wide network of nuclear reactions that allows to put increasingly stringent constraints to the reaction and nuclear structure models adopted to describe the measured cross-sections. In this framework, the analysis of the elastic and inelastic scattering channels plays a fundamental role since it is the most powerful tool to access the Initial State Interaction (ISI) associated to the reaction of interest. The ISI describes the distortion of the incoming waves due to the optical potential, which is the main actor in all the reaction channels; indeed, it accounts for the mean field interaction between the two reaction partners. Therefore, the study of the elastic scattering is fundamental to access the average nucleus-nucleus potential. The analysis of the inelastic scattering allows to obtain valuable information on the nuclear deformations and on the role of couplings with the first low-lying excited states.

In the first part of this Chapter, the data reduction procedure performed for the ^{18}O and ^{48}Ti scattering at 275 MeV incident energy is described. The final goal of such a procedure is the determination of excitation energy spectra and cross-section angular distributions. In the second part, the theoretical analysis of the experimental data is presented. The Optical Model (OM), Distorted-Wave Born Approximation (DWBA) and Coupled Channels (CC) formalisms were used to perform the theoretical calculations, which were compared to the experimental data in order to probe the optical potential and the coupling effects.

3.1 Data reduction

The data reduction procedure is composed by several steps. First, an accurate calibration of the horizontal and vertical positions measured by the gas tracker is crucial, since these parameters are necessary for the ray-reconstruction procedure. Then, the Particle IDentification (PID) is performed, which allows the unambiguous selection of the reaction channel of interest. For the selected events, the final phase-space is studied. Monte Carlo simulations of the ejectiles motion inside the spectrometer are performed to tune the high-order transport matrix, which is inverted to access the momentum vector at the target point for each detected event.

Finally, the excitation energy spectra and the cross-section angular distributions are extracted. The data reduction of the ^{18}O + ^{48}Ti scattering at 275 MeV is discussed in Ref. [43]

3.1.1 Calibration

Since the the PID capabilities and the angular and energy resolution achievable in a typical MAGNEX experiment depend on the tracking performance of the FPD, an accurate calibration of the measurument of the horizontal and vertical coordinates of the ejectile tracks is essential. In the following paragraph a detailed description of the calibration procedure is given.

Horizontal positions and angles

As discussed in Subsect. 2.3.1, the present gas tracker is constituted by six drift chambers DC_i (where $i = 1, \ldots, 6$), each one providing an independent measurement of the horizontal coordinate x_i. The measurement depends on the response of the induction pads, which are calibrated in the following way: four pulses with different amplitudes (2, 5, 8, and 10 V) are produced by a precision pulse generator and sent onto the multiplication wires of a given DC_i. Therefore, for each pulse amplitude value, the same charge is generated in front of each anodic pad associated to that DC_i. Then, the distribution of the induced charge on each pad is built for each pulser signal. After choosing a pad as the reference one (`pad_ref`), for each pad (`pad_i`) the plot that correlates the response of `pad_i` to that of `pad_ref` to the different pulser signals is built. An example of such a plot is shown in Fig. 3.1. A linear fit is then performed in order to obtain a relative calibration of the different electronic channels of the anodic pads.

Once the relative calibration has been carried out, the horizontal position x_i can be deduced by determining the Center Of Gravity (COG) of the charge distribution induced on the pads by the avalanche electrons. To this aim, a specific algorithm has been developed [72], where the centroid $\bar{n}$ is calculated by weighting each pad number n_j with the charge q_j measured by such a pad, namely:

$$\bar{n} = \frac{\sum_j (q_j \quad b) n_j}{\tilde{Q}} \tag{3.1}$$

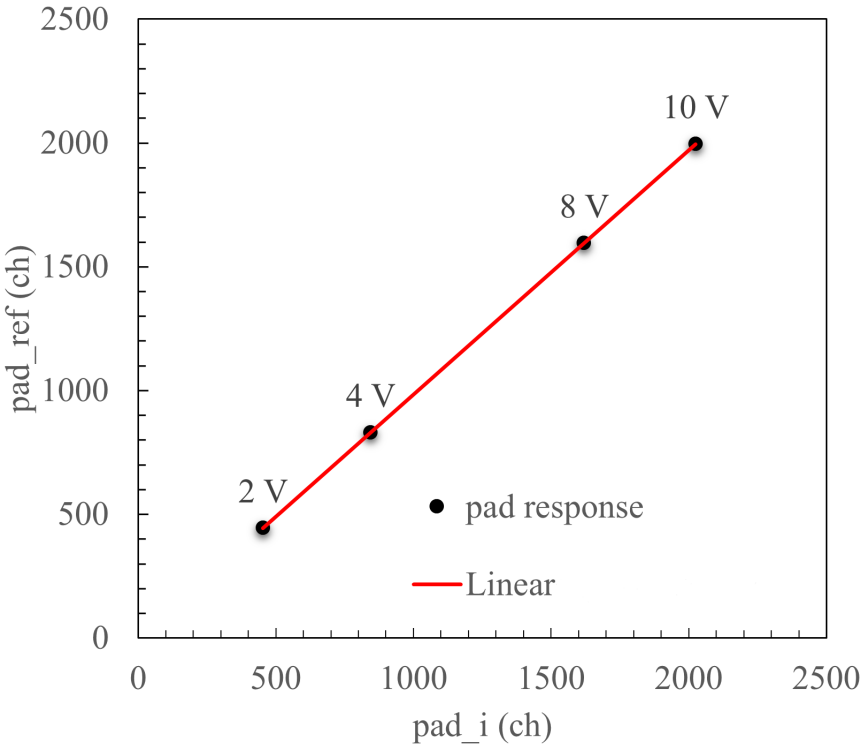

Figure 3.1: Linear correlation between the response of a pad (pad_i) with the response of a reference one (pad_ref). Each point corresponds to the pads response to the signal (2, 5, 8 and 10 V) generated by a pulse generator and sent onto the wires in the case of DC_3. Figure from Ref. [31].

, where

$$\tilde{Q} = \sum_{\{q_j > b\}} (q_j \quad b)$$

is the total induced charge and only the pads with signals above the threshold b (bias) are included in the summation. The key aspect of the COG algorithm is the careful choice of b, since this affects the quality and the stability of the measurement. The optimal value of b has been found to be proportional to the total charge $Q = \sum_j q_j$ measured by the entire strip of pads (see Subsect. 2.3.1), namely

$$b = kQ \tag{3.2}$$

where k can vary between 0.005 and 0.025 in standard FPD working conditions [72].

In order to analyse the charge distribution and test the quality of both the chosen thresholds and the calculated centroids, the standard deviation σ of the distributions is studied:

$$\sigma = \sqrt{\frac{\sum_j (n_j \quad \bar{n})^2 (q_j \quad b)}{\tilde{Q}}} \tag{3.3}$$

If the threshold is properly set, σ should range from 1 (in the case 3 pads above the threshold) to 5 (for 20 pads above the threshold). As described in Ref. [72], the σ is taken as the control parameter of a recursive algorithm that increases the bias level of a small quantity in each iteration, controlled by the i index

$$b_i = (k + 0.002i)Q \tag{3.4}$$

The iterations are repeated until the σ value becomes smaller than 5. Typically, the number of iterations required to obtain the correct bias level is smaller than 40. This algorithm allows to achieve an high efficiency ($\rightarrow 97\%$) in the number of centroids correctly determined and to recover about 40% of the events wrongly reconstructed with the standard COG algorithm.

In Fig. 3.2, three typical examples of charge distributions on row of induction pads are shown. In panel (a), an event characterized by a signal over a low

background level is illustrated. As can be seen, the initial b_i (green dashed line) does not exclude all the spurious signals. The recursive algorithm increases the threshold up to the optimal value (red solid line), thus allowing a better evaluation of the centroid and consequently the improvement of resolution in the position measurement. In panel (b) and (c), two other examples are shown. In the former, despite the high background level, the algorithm can recover the event by a proper setting of b_i. In the latter, a pile-up of the charge distributions of two different ions is present; therefore, for any b_i value, a $\sigma > 5$ is found and, then, the event is discarded.

After the determination of the COG of the electronic avalanche induced in the anodic pads, the horizontal position X_i of the ion track corresponding to DC_i is calculated using the formula:

$$x_i = \bar{n}_i \, d + h_i \tag{3.5}$$

, where d is the horizontal size of each pad (6 mm, within 0.01 mm tolerance) and h_i is the horizontal position of the crossing-point of the optical axis of the spectrometer with the symmetry plane of each DC_i, accurately determined by optical sights. The six horizontal positions x_i obtained in this way are used to reconstruct the projection of the ion trajectory onto the horizontal x-z plane. This is possible because the longitudinal positions z_i of the six DC_i are very accurately defined by mechanical construction (tolerance within 0.1 mm). It is worthwhile to remark that the z_i positions are measured with respect to the $z = 0$ locus corresponding to the MAGNEX focal plane. An example of correlation between the x_i and the z_i coordinates is shown in Fig. 3.3.a.

For each event, a linear fit is performed to extract the xf_fit and θ_{foc} parameters, namely the x position and the horizontal angle of the track at the focal plane. Both parameters are used as inputs for the ray-reconstruction technique discussed in Subsect. 2.2.1.

Vertical positions and angles

Six independent vertical coordinate y_i of the ejectile track are determined by measuring the drift time of the primary electrons moving towards the multiplication

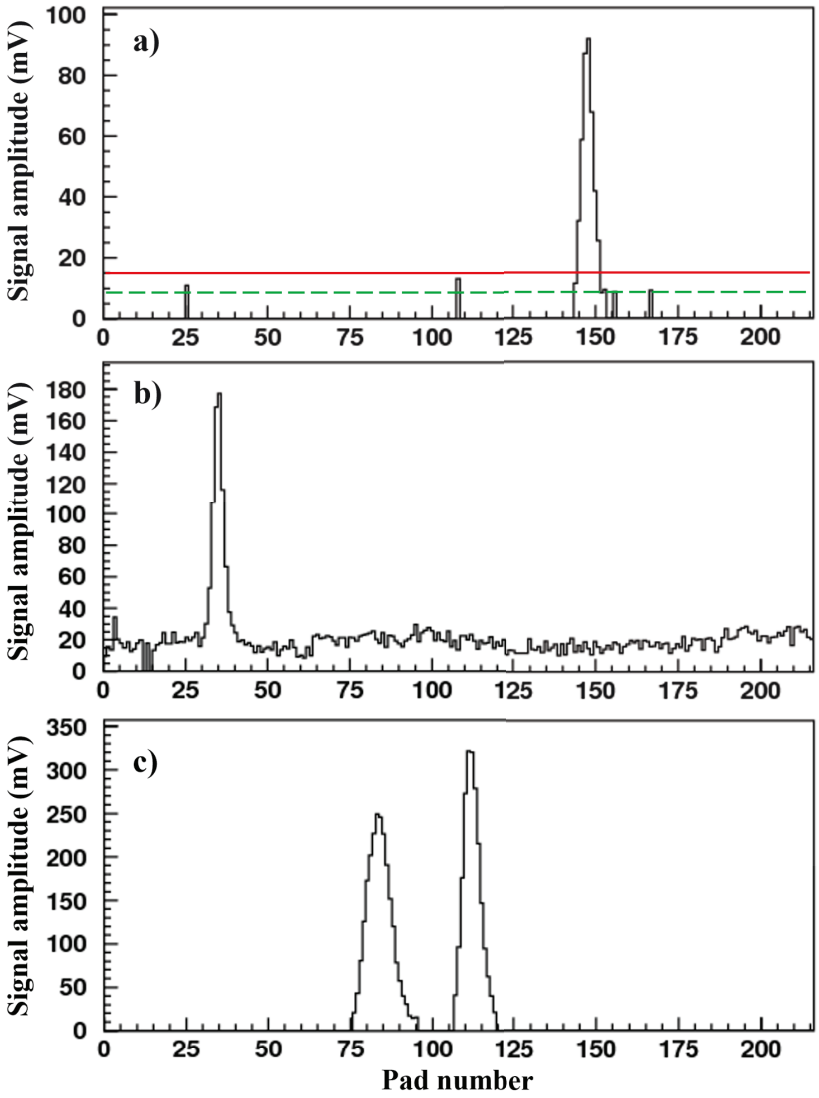

Figure 3.2: Examples of charge distributions on DC1: a) presence of spurious signals distant from the main avalanche. Threshold values obtained using the standard COG method and the optimized algorithm (green dashed and red solid line, respectively); b) time variation of the pedestal level above the stored values; c) two ions trajectories piling-up in the multiplexer. Figure from Ref. [72].

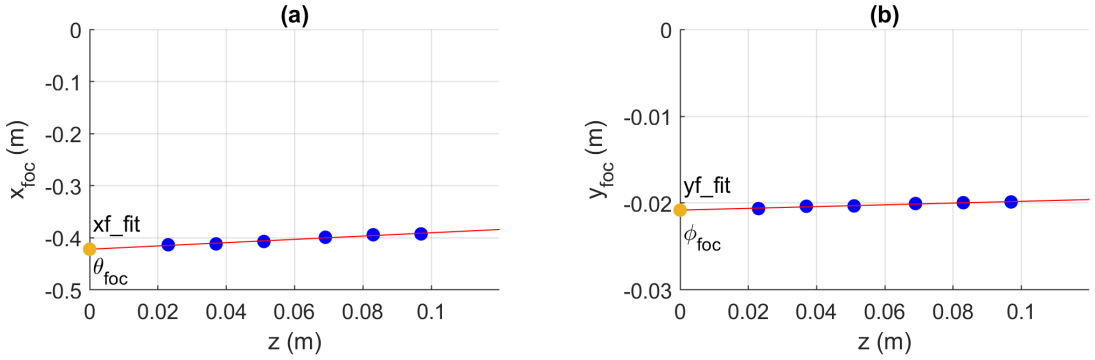

Figure 3.3: Ion track through the FPD. Blue and orange dots are the experimentally measured and the extrapolated positions of the ion, respectively. Red line is the implemented linear fit. (a) Track projection onto the x-z (horizontal) plane. (b) Track projection onto the y-z (vertical) plane. Figure from Ref. [31].

wires. The calibration of such y_i is performed by using mechanical constraints. In Fig. 3.4, the distribution of one of the y_i coordinate is shown for unidentified events measured by the FPD. In such a spectrum, 17 minima are clearly visible: they are due to the metallic wires used to support the thin Mylar window (see Subsect. 2.3.1) that block the ions impinging on them. The distance between two adjacent wires is accurately known (10 mm) and their altitude in the laboratory reference frame was measured in the alignment procedure. In Fig. 3.4, the correspondence between the position of the minima and the position of the wires is highlighted. Such a correspondence allows to perform the calibration of the vertical coordinate y_i.

The y_i parameters are used to determine the projection of the ion track onto the vertical y-z plane. A typical correlation plot of the y_i and z_i coordinates is shown in Fig. 3.3.b. A linear fit is performed to determine the yf_fit and ϕ_{foc}, where the former is the vertical position of the track at the focal plane, the latter is the corresponding vertical incident angle. Together with xf_fit and θ_{foc}, the yf_fit and ϕ_{foc} parameters complete the set of ingredients used for the ray-reconstruction.

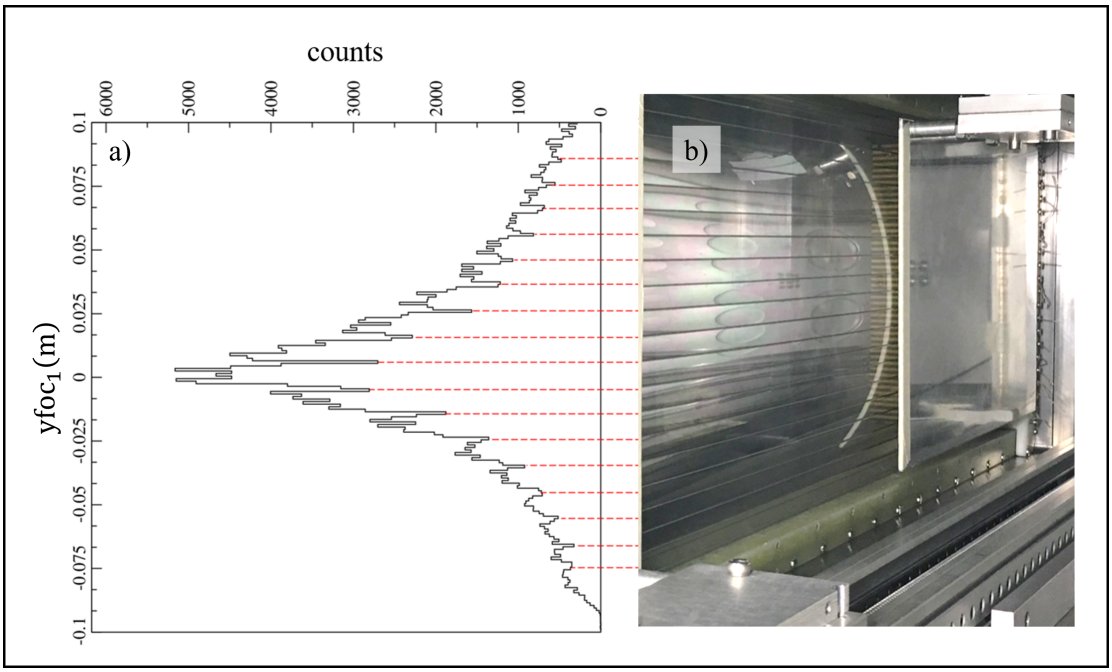

Figure 3.4: (a) y_1 distribution of unidentified events. The minima, indicated by the red dashed lines, correspond to the mechanical wires (see text) shown in panel (b).

3.1.2 Particle Identification

After the calibration procedure, the particle identification (PID) is performed. This step is essential to isolate the reaction channel of interest among all the reaction products generated in a nuclear collision. The PID strategy is developed in two phases, which are described in the following paragraphs. In this work, the focus of the PID procedure is the selection of the $^{18}O^{8+}$ ions.

Atomic number identification

The identification in atomic number (Z) of the ejectiles is accomplished with the standard $\Delta E \quad E$ method, which is derived from the well-known Bethe-Bloch formula [73, 74]. For the MAGNEX case, for each DC_i a ΔE_i is measured; therefore, the total energy loss (ΔE_{tot}) of the ion inside the gas tracker is given by the sum of the individual ΔE_i. The residual energy E_{resid} is measured by the silicon stopping detectors. A typical $\Delta E \quad E$ correlation plot for a single silicon detector is shown in Fig. 3.5.a. The ΔE_{tot}^{corr} parameter is the total energy loss in the gas corrected for the ion incident angle measured by the gas tracker. Indeed, the ejectiles travel different path lenghts in the gas according to their incident angle θ_{foc}. Such a correction removes the dependence on the path lenghts of the energy loss, taking into account also the rotation angle of the FPD ($\theta_{tilt} = 59.2°$). It is expressed by the following relation

$$\Delta E_{tot}^{corr} = \Delta E_{tot} \frac{\cos\theta_{foc}}{\cos\theta_{tilt}} \tag{3.6}$$

The energy calibration of E_{resid} and ΔE_{tot}^{corr} is not necessary, because they are used only for PID purposes*. As can be seen in Fig. 3.5.a, the atomic species between the beryllium and the fluorine are clearly distinguishable, thus allowing to select the oxygen ions with a graphical contour like the one drawn in the Figure.

*Actually the $E_{resid} \quad \Delta E_{tot}^{corr}$ correlation plots were studied during the commissioning of the MAGNEX FPD detector, where a careful calibration allowed to recognize all the loci as due to event associated to specific ions.

Since the FPD response pattern is known, it is not necessary to repeat the energy calibration for each experimental campaign, at least for the PID application.

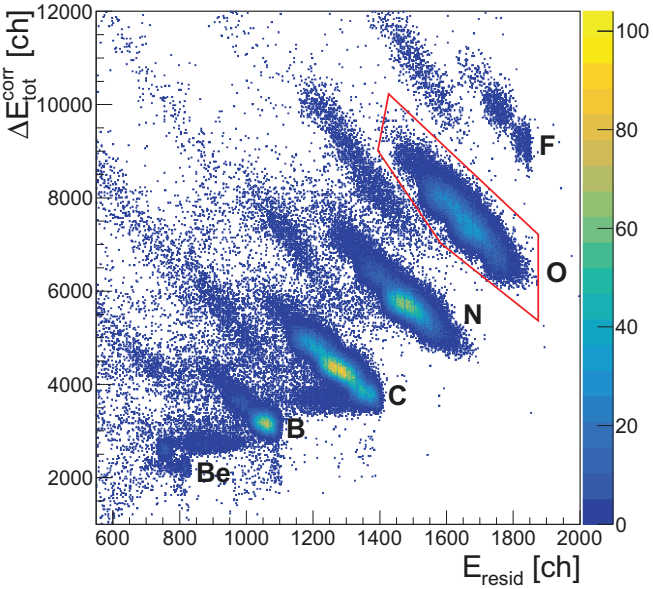

(a)

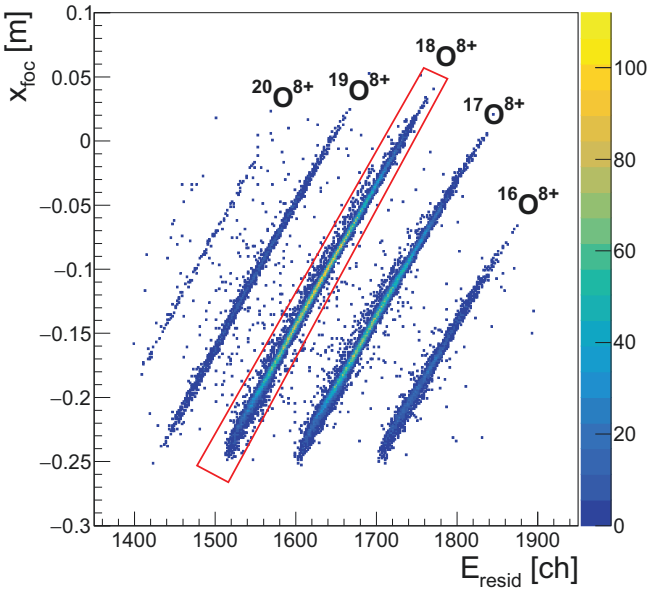

(b)

Figure 3.5: Typical ΔE_{tot}^{corr} E_{resid} plot for a single silicon detector at $\theta_{opt} = 15°$. (b) x_{foc} E_{resid} plot for the ions selected with the graphical cut in (a).

Mass and charge state identification

The $\Delta E \quad E$ plot illustrated in Fig. 3.5.a does not allow to discriminate between ions with the same atomic number Z and different mass number A. The selection of the $^{18}O^{8+}$ isotopes is performed by applying a special PID technique, described in detail in Ref. [75]. It exploits the properties of the Lorentz force: a particle with charge q and mass m in a magnetic field B orthogonal to its momentum p moves along a curved trajectory with radius ρ, according to the formula

$$B\rho = \frac{p}{q} \tag{3.7}$$

In non-relativistic approximation, the momentum p is connected to the kinetic energy E by the relation $p = \quad \overline{2mE}$. As the energy loss in the low-pressure conditions of the gas tracker is typically small, one can approximate E with E_{resid}. Since the curvature radius ρ is, to the first order of approximation, proportional to the horizontal position at the focal plane x_{foc}, Eq. 3.7 can be expressed as

$$x_{foc} \; / \; \frac{\overline{m}}{q} \sqrt{E_{resid}} \tag{3.8}$$

Therefore, in a $x_{foc} \quad E_{resid}$ correlation plot the events associated to the detected ions are distributed on different loci according to their mass-to-charge ratio ($\overline{m}/q$). This is confirmed in Fig. 3.5.b, where the oxygen ions selected with the graphical contour in Fig. 3.5 are plotted. As can be noticed, the high resolution of the silicon detectors determines a large separation between the several oxygen isotopes, thus allowing a clean identification of the $^{18}O^{8+}$ ions.

3.1.3 Final phase-space parameters

Once the identification procedure is completed, the analysis of the final phase-space parameters for the selected events is performed, in order to obtain information about the horizontal and vertical focusing and aberrations. As illustrative case, the $\theta_{foc} \quad xf\_fit$ correlation plot for the selected $^{18}O^{8+}$ ions at $\theta_{opt} = 15°$ is shown in Fig. 3.6.a. Since the FPD entrance face is rotated by an angle $\theta_{tilt} = 59.2°$ (corresponding to 1.033 rad) with respect to a plane perpendicular to

the optical axis, the measured θ_{foc} values are distributed around such an angle. The intense quasi-vertical loci correspond to elastic and inelastic scattering events. The deviation of the loci from a perfect vertical line depends on two factors: the kinematic effect (i.e. the dependence of the kinetic energy on the scattering angle in a two-body collision) and high-order aberrations in the horizontal phase-space.

In Fig. 3.6.b, the $yf\_fit \quad xf\_fit$ correlation plot for the same $^{18}O^{8+}$ identified events is shown. The *butterfly* shape, typical of the QD spectrometer like MAGNEX, is clearly visible. It points out that the trajectories are vertically focused only for a certain value of the ion magnetic rigidity.

3.1.4 Application of the ray-reconstruction technique to the experimental data

The trajectory reconstruction method was applied to the selected events in order to retrieve the ejectile momentum at the target, thus determining the scattering angle and the reaction Q-value. As will be shown in Subsect. 3.1.5 and 3.1.6, this information were used to deduce the excitation energy spectra and the cross-section angular distributions for the elastic and some inelastic transitions. The practical implementation of the ray-reconstruction technique is based on the comparison between the experimental data measured by the FPD and simulated ones generated by a specific Monte Carlo code. Such a code represents a model of the spectrometer response to the scrutinized reaction. Therefore, if the simulated data are compatible with the experimental one, the transport operator is well defined.

The ray-reconstruction procedure in composed by two main steps, which are discussed in the following paragraphs.

Direct transport map

As explained in Subsect. 2.2.1, the ray-reconstruction method consists in solving the Eq. 2.5, therefore determining the initial phase-space vector $Q_i \leq (\theta_i, y_i, \phi_i, \delta)$ starting from the final phase-space vector $Q_f \leq (x_f, y_f, \theta_f, \phi_f)$ and the inverted transport matrix G^{-1}.

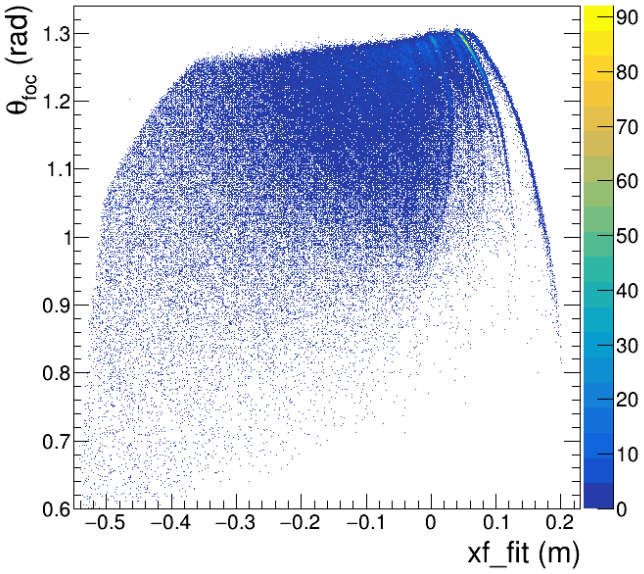

(a)

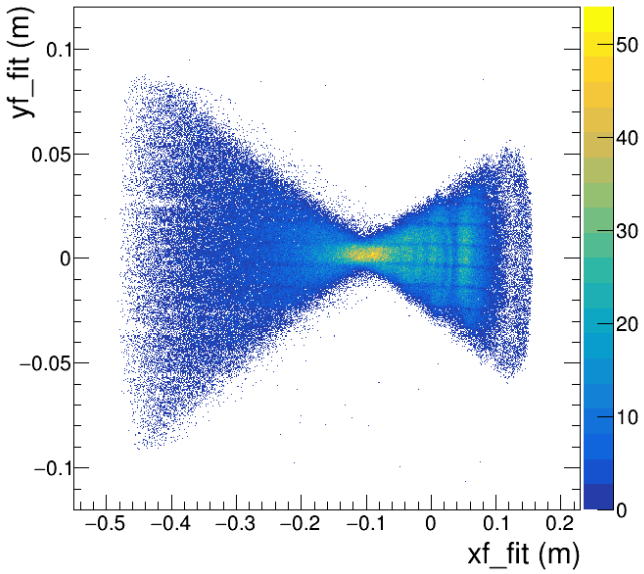

(b)

Figure 3.6: Final phase-space parameters for the selected $^{18}O^{8+}$ events belonging to the $^{18}O + ^{48}Ti$ scattering at 275 MeV incident energy and $\theta_{opt} = 15°$. In (a) and (b) the θ_{foc}-xf_fit and yf_fit-xf_fit correlation plots are shown, respectively.

The first step of the procedure is the construction of the direct transport map G, that describes the transformation of Q_i into Q_f. For MAGNEX, due to the large acceptance of the spectrometer, the G matrix is calculated up to the 10^{th} order [3]. This high-order transport problem is carried out by the COSY INFINITY software, which is based on the differential algebra formalism [60].

The COSY INFINITY input includes an accurate description of the spectrometer geometry, as well as the position and dimensions of the FPD. In addition, the value of the magnetic fields of the dipole and quadrupole are specified.

As mentioned, the quality of the direct transport matrix G produced by COSY INFINITY is tested by comparing the final phase-space observables (see Subsect. 3.1.3) of the experimental data with those of simulated events generated with a Monte Carlo-based algorithm. One of the input of such an algorithm is the ^{18}O beam energy value, which differs from the nominal one (E_{beam} = 275.4 MeV) due to the energy loss experienced by the ^{18}O ions crossing the target material before entering the spectrometer. The evaluation of the effective beam energy E_{eff} requires energy loss and kinematics calculations: the former were carried out with LISE++ [76], the latter with CATKIN [77]. It was assumed that the scattering process occurs on average in the middle of the target. The procedure followed to determine E_{eff} for the case of interest is the following (schematically reported in Fig. 3.7.a): crossing half of the TiO_2 layer, the ^{18}O projectile looses some energy and reaches the scattering point with kinetic energy E_1. Then, the kinematic calculation for the ^{18}O + ^{48}Ti elastic scattering at incident energy E_1 is performed, obtaining the ^{18}O ejectile with kinetic energy E_2 and scattering angle equal to spectrometer optical axis angle θ_{opt} (in the laboratory reference frame). Afterwards, the ejectile crosses the second half of the TiO_2 layer and the aluminum backing with an inclination θ_{opt}, emerging from the target with a kinetic energy E_3. The effective ^{18}O beam energy E_{eff} is thus determined as the initial kinetic energy that generates a ^{18}O ion elastically scattered with final energy E_3 and scattering angle θ_{opt}, without any energy loss. This "zero thickness" target model is sketched in Fig. 3.7.b. The Monte Carlo code takes into account also the excitation energies of the ejectiles and of the residual nuclei, thus allowing to simulate not only ground-to-ground state processes, but also transitions to excited states.

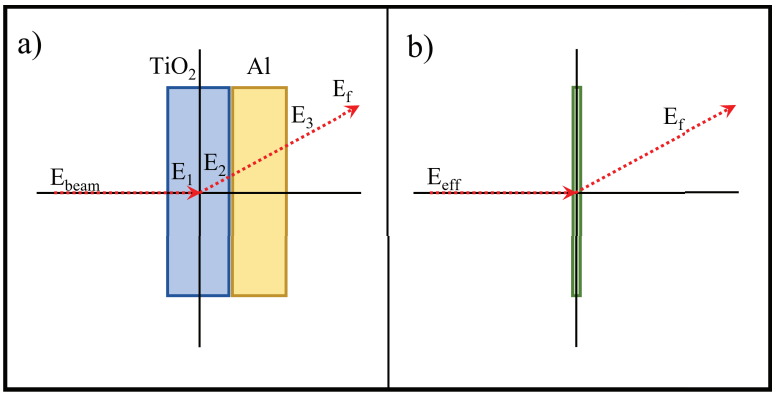

Figure 3.7: Sketches of the target and the projectile/ejectile energies involved in the nuclear reactions from the ^{18}O + ^{48}Ti collision at 275 MeV of incident energy. Panels (a) and (b) indicate the true scale geometry and the zero thickness hypothesis described in the text, respectively.

Four processes were simulated, corresponding to the scattering of a ^{18}O beam at incident energy E_{eff} onto different targets, i.e. ^{48}Ti, ^{184}W, ^{16}O and ^{27}Al. Regarding the ^{18}O + ^{48}Ti scattering, which is the focus of this analysis, both elastic scattering events and inelastic transitions to the low-lying excited states of projectile and target were included. To explore the spectrometer response in a wide range of accepted momenta, fictitious excited states with energy up to 20 MeV were also taken into account. For the other three simulated processes, only elastic scattering was considered.

The comparison between experimental (black points) and simulated (coloured points) data for $\theta_{opt} = 15°$ is shown in Figs. 3.8.a and 3.8.b for the x_{foc}-θ_{foc} and x_{foc}-y_{foc} representations of the final phase-space parameters, respectively. In the x_{foc}-θ_{foc} plot, it can be noticed that the loci corresponding to the scattering on the four target nuclei show different shapes. As mentioned, this is also due to the kinematical relation between the kinetic energy and the scattering angle of the ejectiles. The Monte Carlo simulations allowed to understand that the locus located at large x_{foc} values is owing to a tungsten contamination of the target, somehow expected due to the evaporation procedure in the target construction. The good matching between the experimental and simulated data for both the x_{foc} - θ_{foc} and x_{foc} - y_{foc} representations confirms the reliability of constructed direct transport operator modelling the spectrometer response.

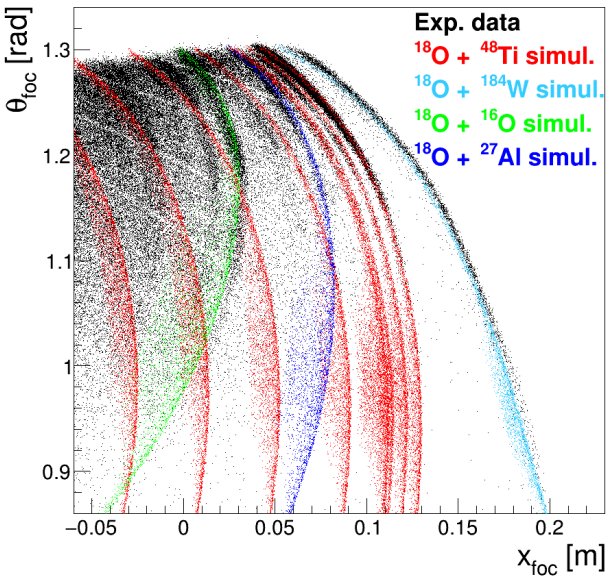

(a)

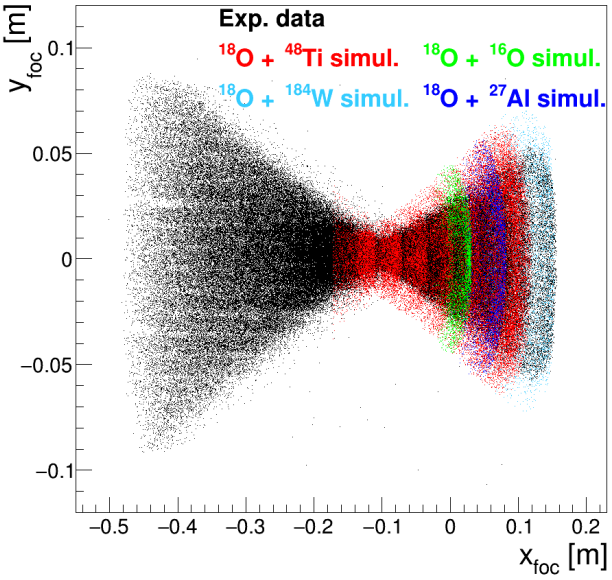

(b)

Figure 3.8: (a) Horizontal final phase-space representation in terms of the θ_{foc} x_{foc} parameters for both the experimental and simulated data at $\theta_{opt} = 15°$. (b) Vertical final phase-space representation in terms of the y_{foc} x_{foc} parameters for both the experimental and simulated data at $\theta_{opt} = 15°$. Figure from Ref. [43].

Inverse transport map and initial phase-space parameters

The COSY INFINITY software is able to invert the direct transport map and build the inverse transport operator G^{-1}, which allows to reconstruct the initial phase-space vector Q_i from the final phase-space one Q_f. The momentum vector at the target point is then accessed through the Q_i vector [65].

In Fig. 3.9, the correlation plot between the vertical ϕ_i and the horizontal θ_i initial angle is shown for $\theta_{opt} = 15°$. Although the reconstructed solid angle acceptance is consistent with the nominal one ($7° < \phi_i < 8°$ and $10° < \theta_i < 21°$), defined by the four slits in the MAGNEX scattering chamber (see Sect. 2.1), it does not show the ideal rectangular shape. This is due to an efficiency loss originated from a cut-off of the ejectile envelope due to the spectrometer vacuum vessels. It actually reduces the nominal solid angle acceptance to an effective value, which must be evaluated in order to determine the cross-section angular distributions [53]. The method used to calculate the effective solid angle acceptance is discussed in Subsect. 3.1.6.

The two quantities of interest are the scattering angle in the laboratory reference frame θ_{lab} and the Q-value of the reaction. The first one is obtained according the following relation:

$$\theta_{lab} = \arccos \frac{\cos\theta_{opt} \quad \sin\theta_{opt}\tan\theta_i}{\sqrt{1+\tan^2\theta_i+\tan^2\phi_i}} \tag{3.9}$$

From the reconstructed relative momentum δ, the kinetic energy of the ejectile is deduced and, consequently, the corresponding Q-values or, equivalently, the excitation energy E_x. The latter is determined from missing mass calculations based on relativistic energy and momentum conservation laws for binary reactions:

$$E_x = Q_0 \quad Q = Q_0 \quad K\left(1+\frac{M_e}{M_r}\right)+E_{beam}\left(1 \quad \frac{M_b}{M_r}\right)+2\frac{\overline{M_bM_e}}{M_r}\sqrt{E_{beam}K}\cos\theta_{lab} \tag{3.10}$$

where M_e, M_r, M_b are the ejectile, residual and beam nuclei masses, respectively, K is the kinetic energy of the ejectile (related to the δ parameter) and Q_0 is the ground-to-ground state Q-value for the considered nuclear reaction, which

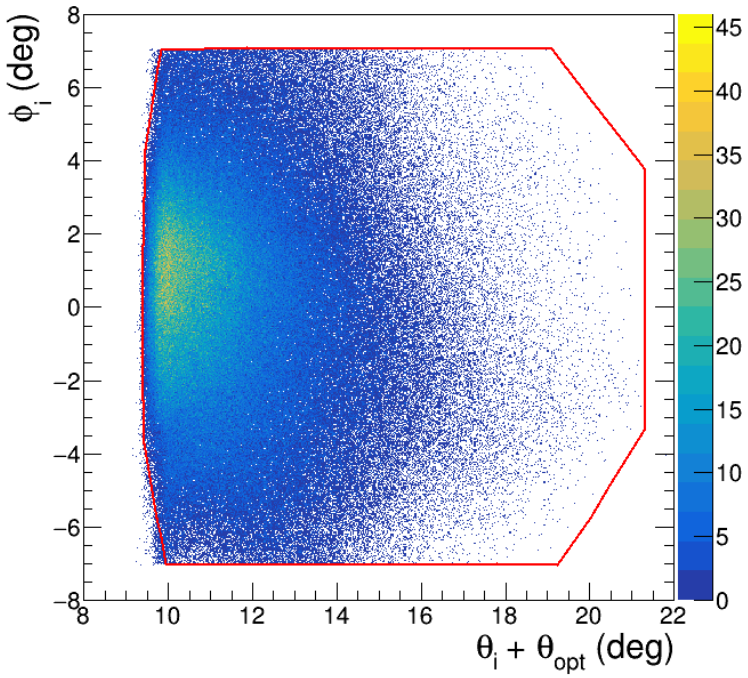

Figure 3.9: The ϕ_i vs. $\theta_i + \theta_{opt}$ correlation plot for the ^{18}O + ^{48}Ti scattering at 275 MeV incident energy and $\theta_{opt} = 15°$. The graphical contour indicates the effective solid angle acceptance of MAGNEX.

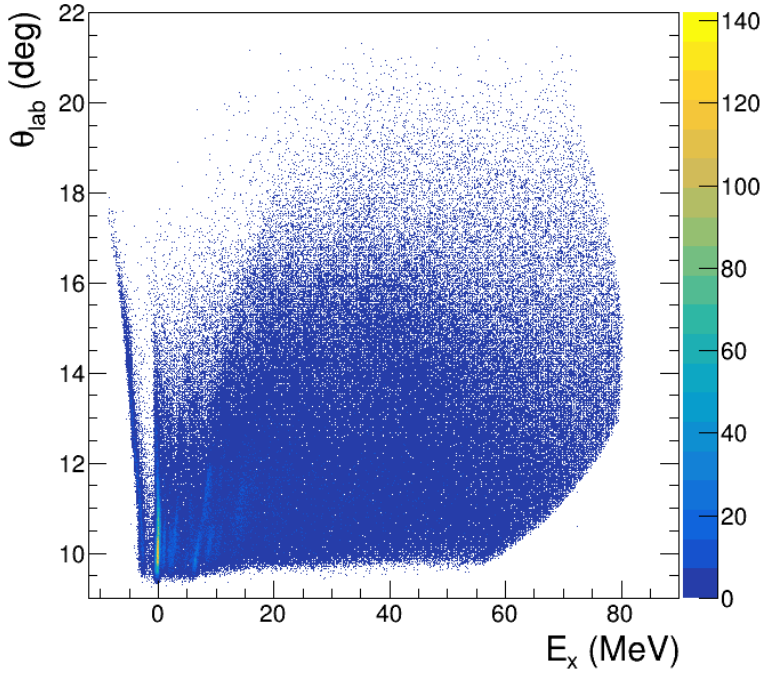

Figure 3.10: The θ_{lab} E_x correlation plot for the ^{18}O + ^{48}Ti scattering at 275 MeV incident energy and $\theta_{opt} = 15°$.

for the elastic scattering case is zero. The θ_{lab}-E_x correlation plot for $\theta_{opt} = 15°$ is shown in Fig. 3.10, where the vertical locus of the ^{18}O + ^{48}Ti elastic scattering is clearly visible at $E_x = 0$ MeV. Other vertical loci corresponding to inelastic transitions towards ^{18}O and ^{48}Ti excitated states are present. As expected, the excitation energy E_x does not depend on the scattering angle θ_{lab} for transitions populating ^{18}O and ^{48}Ti states. Some loci with non-vertical structure are also visible. They are due to the elastic scattering of ^{18}O projectiles on the oxygen component of the TiO_2 target and on the aluminum backing. Moreover, at negative E_x values it is possible to see the locus corresponding to the elastic scattering of ^{18}O onto the tungsten target contaminant. Since the E_x parameter was reconstructed using the two-body kinematics of the ^{18}O + ^{48}Ti system, the scattering onto a different target can not be vertical because it is characterized by another kinematics. Above 30 MeV excitation energy, an efficiency loss is present, due to the limited acceptance of the spectrometer [53].

3.1.5 Excitation energy spectrum

By projecting the θ_{lab}-E_x plot onto the E_x axis, the excitation energy spectrum of the ^{18}O + ^{48}Ti scattering at 275.4 MeV incident energy can be obtained. An example of such a spectrum for the angular range $11° < \theta_{lab} < 12°$ is shown in Fig. 3.11, where the most intense peak correspond to the ^{18}O + ^{48}Ti elastic scattering. The achieved energy resolution of $\rightarrow 0.5$ MeV Full-Width at Half Maximum (FWHM) was deduced by fitting the elastic peak with a Gaussian function. The peak at $\rightarrow$1 MeV is attributed to the inelastic transition to the 2_1^+ state of the ^{48}Ti at $E_x = 0.984$ MeV. The broad structure centered at about 2.2 MeV corresponds to the superposition of the 2_1^+ excited state of the ^{18}O at 1.982 MeV and three ^{48}Ti states: the 4_1^+ state at 2.296 MeV, the 2_2^+ state at 2.421 MeV, and a state of unknown spin-parity at 2.465 MeV. The structure centered at $\rightarrow$ 3.4 MeV was ascribed to the elastic scattering on the ^{27}Al backing of the target.

For each angular slice (typically with an angular step $\Delta\theta_{lab} = 0.3°$), a multiple-fit procedure of the excitation energy spectrum was carried out [32, 37, 38], taking into account the low-lying states of ^{18}O and ^{48}Ti, which are reported in Table 3.1.

The experimental yields of each transition was deduced assuming that the observed peaks may be described in terms of Gaussian functions. The width of each Gaussian peak was fixed according to the experimental energy resolution; for the inelastic transitions populating excited states of the ^{18}O, the Doppler broadening due to the in-flight γ-decay of the ejectiles was also taken into account. As an example, the result of the fit procedure on the excitation energy spectrum with $11° < \theta_{lab} < 12°$ is shown in Fig. 3.11.

3.1.6 Cross section angular distribution

It is well-known that the cross-section angular distribution in the laboratory reference frame $d\sigma/d\Omega_{lab}$ is experimentally defined as:

$$\frac{d\sigma}{d\Omega_{lab}} = \frac{N(\theta_{lab})}{N_t\, N_{beam}\, \epsilon(\theta_{lab})\, \Delta\Omega_{lab}} \tag{3.11}$$

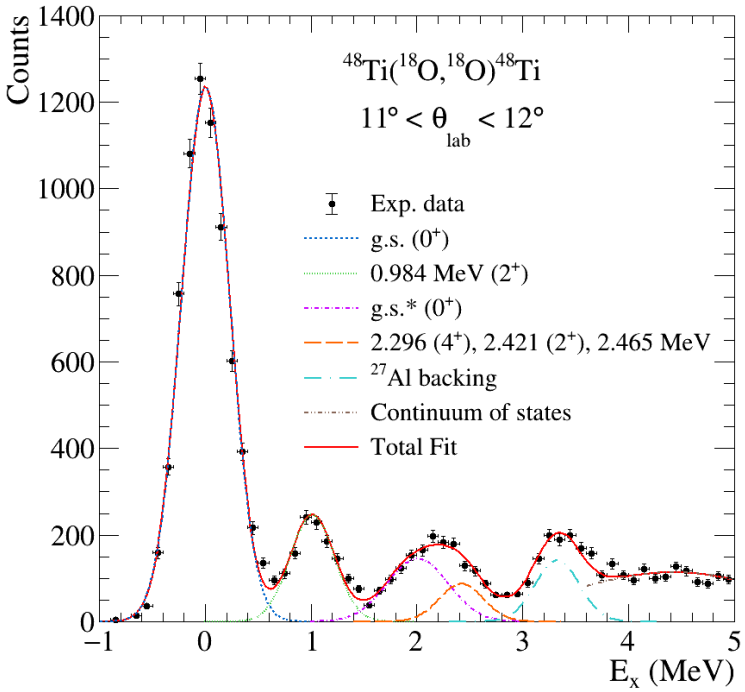

Figure 3.11: Excitation energy spectrum for the ^{18}O +^{48} Ti elastic and inelastic scattering at 275 MeV in the angular range $11° \sim \theta_{lab} < 12°$. The coloured lines show the result of the multiple-fit procedure and identify different states of projectile and target, as well as a structure due to the Al backing, as explained in the legend. The asterisk refers to the transition where the 2_1^+ excited state of the ^{18}O at 1.982 MeV is populated.

Table 3.1: Excitation energies (E_x) and spin-parity (J^+) of the low-lying states of ^{18}O and ^{48}Ti.

^{18}O		^{48}Ti	
E_x (MeV)	J^π	E_x (MeV)	J^π
0	0^+	0	0^+
1.982	2^+	0.984	2^+
3.555	4^+	2.296	4^+
3.634	0^+	2.421	2^+
3.920	2^+	2.465	
		2.997	0^+
		3.062	2^+

, where $N(\theta_{lab})$ is the number of counts acquired in the angular interval $\Delta\theta_{lab}$ centered on θ_{lab}; N_t, N_{beam} and $\epsilon(\theta_{lab})$ are the number of scattering centre in the target (in atoms/cm^2), the number of incident ^{18}O beam ions and the total detection and reconstruction efficiency at θ_{lab}, respectively; $\Delta\Omega_{lab}$ is the solid angle covered by the MAGNEX spectrometer for the $\Delta\theta_{lab}$ interval centered on θ_{lab}.

The number of incident ^{18}O ions N_{beam} is calculated from the total charge collected by the Faraday cup Q_{live}, where this quantity already takes into account the live time of the FPD (see Sect. 2.1). Since the ^{18}O ions in the beam are totally stripped (charge state 8^+), N_{beam} can be obtained as:

$$N_{beam} = \frac{Q_{live}}{8e} \tag{3.12}$$

, where e is the electron charge.

The number of scattering centers in the target per unit area N_{target} is given by the formula $N_{target} = sN_A/A$, where s is the target thickness (510 μg/cm^2 for the TiO_2 target), N_A is the Avogadro constant and A is the target mass number.

The efficiency $\epsilon(\theta_{lab})$ was evaluated considering the FPD detection efficiency

(88%) [56] and the reconstruction efficiency (ranging from 95% to 99% for the analyzed channel). The latter was calculated as the ratio between the well reconstructed events and the total identified events at the focal plane for each angular step.

The calculation of the solid angle $\Delta\Omega_{lab}$ requires a more detailed description, here presented. A representation of the spectrometer solid angle acceptance is shown in Fig. 3.12.a, where the circular rings, corresponding to the minimum and maximum horizontal angles accepted, are sketched. The nominal spectrometer solid angle acceptance, illustrated in Fig. 3.12.b with a green line, is delimited by the already described copper slits (see Sect. 2.1); however, the overall efficiency losses in the spectrometer correspond to an effective reduction of the solid angle, as explained in Ref. [53]. Therefore, the actual solid angle acceptance is deduced by drawing the contour of the θ_i-ϕ_i distribution of the reconstructed events (see Fig. 3.9). In Fig. 3.12.b, it is shown that the solid angle $\Delta\Omega$ (hatched region) is defined by the intersection between the circular ring with inner radius θ_{lab} $\Delta\theta_{lab}/2$ and outer radius $\theta_{lab} + \Delta\theta_{lab}/2$ and the above-mentioned graphical contour (red line). Each $\Delta\Omega$ was calculated by using a Monte Carlo method, according to the formula

$$\Delta\Omega = \lim_{N\to+\infty} \frac{N_{in}}{N} A \tag{3.13}$$

where N is the number of points generated with a uniform distribution in the rectangular area A defined by the green line, while N_{in} is the number of points inside the region delimited by the red line. The N number is typically large enough to ensure the statistical convergence.

The comparison between the experimental cross sections and the theoretical calculations is usually performed in the center-of-mass (c.m.) reference frame. The formula

$$\left.\frac{d\sigma}{d\Omega}\right|_{cm} = J \left.\frac{d\sigma}{d\Omega}\right|_{lab} \tag{3.14}$$

is used to convert the Eq. 3.11 from laboratory to c.m. reference frame. The quantity J is Jacobian operator defined as the ratio $\frac{d\Omega_{lab}}{d\Omega_{cm}}$ (see Ref. [78]).

In Fig. 3.13, the experimental cross-section angular distribution of the elastic scattering for the three explored angular settings are shown, which, as can be noticed, are in good agreement one another. It is worthwhile to remark that

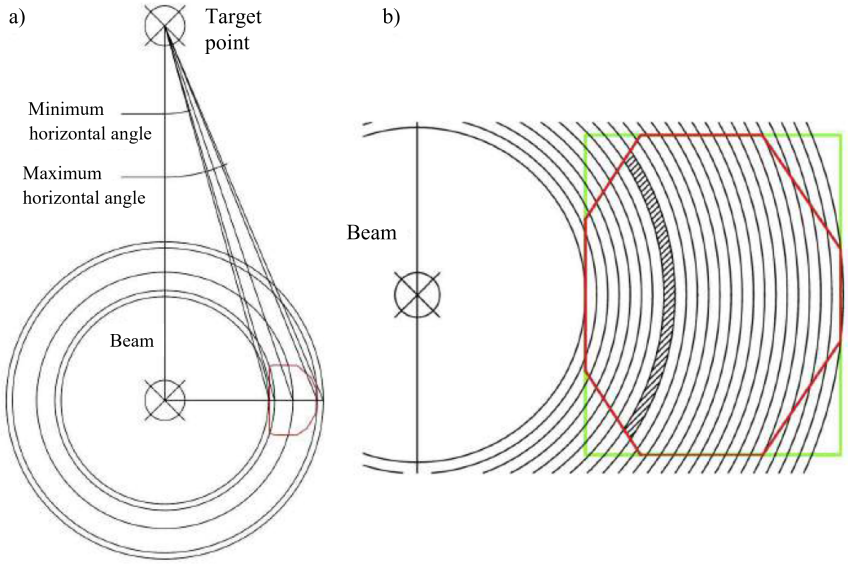

Figure 3.12: (a) Geometrical representation of the MAGNEX solid angle acceptance. (b) Differential solid angle evaluation: the nominal and the effective MAGNEX solid angle acceptance are shown with the green and red lines, respectively. The solid angle of a singular angular bin (hatched region) is defined by the intersection of the circular ring enclosed in the $(\theta_{lab} \quad \Delta\theta_{lab}/2;\ \theta_{lab} + \Delta\theta_{lab}/2)$ interval and the red contour.

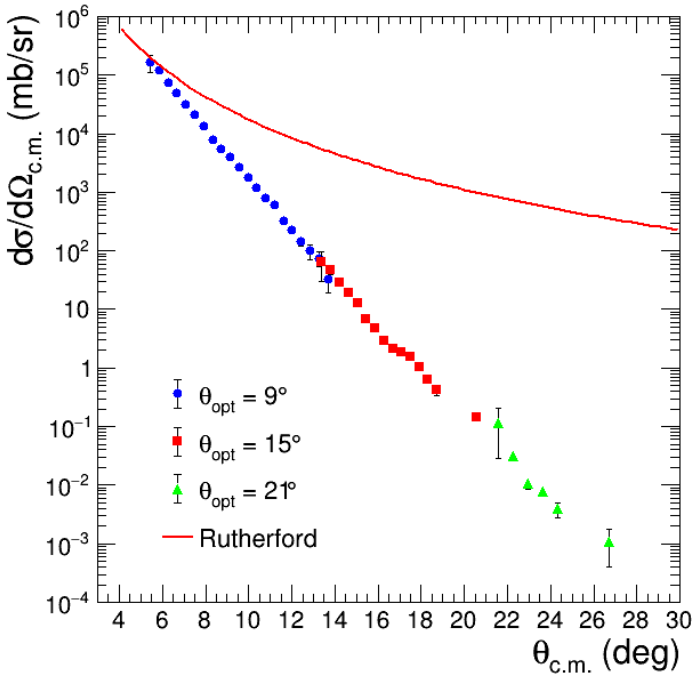

Figure 3.13: Cross-section angular distribution for the $^{18}O + ^{48}Ti$ elastic scattering at 275 MeV. The three explored angular ranges are highlighted with different colors and marker. The Rutherford differential cross-section is also shown (red line).

the measured elastic angular distribution varies of eight orders of magnitude in the overall angular range covered, which extending from 5° to 27° in the c.m. reference frame. The error bars include contributions from the statistical error, the fitting procedure, and the solid angle evaluation. The systematic error due to uncertainties in the measure of the total charge with the FC and in the evaluation of the target thickness was estimated to be less than 10% and it is not explicitly considered in the error bars, since it is common to all the experimental points. In Fig. 3.13, the Rutherford differential cross-section is also represented, which is given by the well-know analytic expression

$$\left.\frac{d\sigma}{d\Omega}\right|_{Ruth} = \left(\frac{Z_1 Z_2 \alpha \hbar c}{4E_{cm}}\right)^2 \frac{1}{\sin^4(\theta_{cm}/2)} \tag{3.15}$$

where Z_1 and Z_2 are the atomic number of projectile and target, respectively; α is the fine structure constant; $\hbar$ is the reduced Planck constant; c is the speed of light in the vacuum; E_{cm} and θ_{cm} are, respectively, the kinetic energy and the scattering angle in the c.m. reference frame. At forward angle, there is a good overlap between the experimental and the Rutherford angular distribution. Since the Rutherford scattering far dominates the outgoing flux at very forward angles in heavy-ion collisions, the above result reflects a small systematic error in the procedure adopted to extract the experimental cross-sections.

3.2 Determination of the Initial State Interaction

A theoretical description of the elastic and inelastic scattering experimental data is fundamental to deduce the Initial State Interaction (ISI) to be used in the multi-channel approach of the nuclear reactions network induced by the ^{18}O + ^{48}Ti collision at the same incident energy. The ISI is responsible for the distortion of the incoming waves, therefore it is essential to properly describe all the direct nuclear reaction channels. The theoretical calculations for the elastic and inelastic scattering were performed in the Optical Model (OM), Distorted Wave Born Approximation (DWBA) and Coupled-Channel (CC) formalisms. All the mentioned calculations were performed by using the FRESCO code [79].

3.2.1 Optical Potential

In the OM framework, the complicated many-body problem of the interaction between two nuclei is simplified into that of a particle in a non-local complex potential, called Optical Potential (OP) [80]. In many cases the OPs are taken to be local, where the non-locality effects are treated in terms of an energy dependence: they are usually referred to as local equivalent potentials [80]. The local equivalent OP $U_{opt}(r)$, which accounts for both the Coulomb and the nuclear interaction, may be written as the sum of a real $V(r)$ and an imaginary $W(r)$ part:

$$U_{opt}(r) = V(r) + i\,W(r) \tag{3.16}$$

where r is the distance between the centers of mass of two colliding nuclei. The real part of the OP accounts for the refraction of the incident waves; the imaginary term is introduced to describe the absorption of the incident waves leading to a loss of flux from the elastic process towards channels not explicitly included in the model space. In literature, several types of OP have been proposed; for example, as a consequence of the short range of the nuclear interaction, it may be described by a function with radial shape similar to the nuclear density one. Such phenomenological OPs are often parameterized in terms of Woods-Saxon functions for the nuclear part (e.g. [81–84]). This is the case of the Akyuz-Winther potential [85], widely used for the description of heavy-ion collisions (e.g. [37, 86–88]). The parameters entering in such a kind of OP are usually derived from wide systematics in mass and energy, but they are expected to reproduce the trend for specific systems only in average, often needing arbitrary scaling on the experimental data (e.g. [37]). For this reason, an OP based on microscopic approach, such as the double-folding [89], is preferable.

In the double-folding framework (e.g. [89–91]), the real part $V(r)$ of the nuclear potential is constructed as the integral of the nucleon-nucleon effective interaction $V_{NN}(r_{12}, E_N)$ weighted on the ground-state matter density distributions $\rho_1(\mathbf{r}_1)$ and $\rho_2(\mathbf{r}_2)$ of the projectile and the target, respectively [89]. It may be expressed as follows:

$$V(r) = \int\int d\mathbf{r}_1 d\mathbf{r}_2\, \rho_1(\mathbf{r}_1)\, \rho_2(\mathbf{r}_2)\, V_{NN}(r_{12}, E_N) \tag{3.17}$$

where $r_{12} = \mathbf{r}_1 + \mathbf{r}_2$, $\mathbf{r}_1$ and $\mathbf{r}_2$ represent the internal coordinates of the two nuclei, and E_N is the energy per nucleon in the c.m. reference frame.

In the present analysis, the adopted OP is the double-folding local equivalent São Paolo potential (SPP) V_{SPP} [92], which can be expressed as follows

$$V_{SPP}(r) = V(r)\, \mathrm{e}^{-\frac{4v^2}{c^2}} \tag{3.18}$$

where $V(r)$ is given by Eq. 3.17, v is the velocity between projectile and target and c is the speed of light. The exponential factor in Eq. 3.18 is called Pauli non-locality term. In this analysis, it was assumed to adopt the SPP for both the real and the imaginary parts of the OP, according to the formula

$$U_{opt}(r) = (N_R + iN_I)V_{SPP}(r) \tag{3.19}$$

where N_R and N_I are normalization factors for the real and imaginary parts, respectively. The adopted values for N_R and N_I derive from a wide systematics, where the SPP was used to describe experimental data [32, 33, 37, 53, 93–98]. Based on such a systematics, N_R is always set to 1, while the value of N_I depends on the coupling scheme adopted in the calculations. Indeed, as already mentioned, the imaginary term of the OP effectively accounts for the absorption to reaction channels and inelastic states not explicitly included in the coupling scheme. In the OM approach, where only the elastic channel is considered in the model space (for this reason it is also known as one-channel approximation), N_I is typically set to 0.78. The same holds also for the DWBA framework; instead, when the couplings to the inelastic transitions towards the main low-lying collective states are explicitly taken into account, the N_I value is typically decreased to about 0.6 [99].

The matter densities $\rho_j(\mathbf{r}_j)$ adopted in the double-folding procedure of the SPP are two-parameters (radius R and diffuseness a) Fermi-Dirac distributions and are assumed to be spherical. The radius and diffuseness adopted in the present analysis are taken from the systematic analysis of electron scattering data and Hartree-Fock-Bogoliubov calculations for a wide range of nuclei [92]. In the specific case of the ^{18}O, a diffuseness of 0.61 fm was assumed, which is larger than the

Table 3.2: Coefficient N_I of the imaginary part of the SPP, volume integral per nucleon for the real (J_R) and the imaginary (J_I) part of the SPP and total reaction cross section σ_R in the case of the OM/DWBA and CC calculations.

Theor. approach	N_I	J_R (MeV fm^3)	J_I (MeV fm^3)	σ_R (mb)
OM/DWBA	0.78	-346	-270	2571
CC	0.60	-346	-208	2498

value reported in the SPP systematics (0.56 fm). This assumption, explored in details in several publications [38, 100–104], accounts for the effects of the two paired valence neutrons bound to the ^{16}O core in the ^{18}O ground state. Some relevant properties of the adopted SPP, such as the volume integral per nucleon J and the total reaction cross section σ_R, are reported in Table 3.2.

3.2.2 Optical Model results

The comparison between the results of the OM calculations and the experimental elastic scattering angular distribution (both expressed in terms of their ratio with the Rutherford differential cross-section) is shown in Fig. 3.14. A representation in terms of the transferred momentum q, expressed as

$$q = \frac{2\sqrt{2\mu c^2 E_{c.m.}}}{\hbar c} \sin(\theta_{c.m.}/2) \tag{3.20}$$

where μ is the reduced mass for the system and $E_{c.m.}$ is the energy in the c.m. reference frame, is also given. Both the experimental data and the OM calculation show the typical Fresnel-like diffraction pattern, as expected for heavy-ion elastic scattering with energy above the Coulomb barrier (Sommerfeld parameter $\eta \rightarrow 7$). Up to the grazing angle ($\theta_{gr} \rightarrow 7.6°$ in the c.m. reference frame), the scattering is mainly driven by the Coulomb field. Beyond such angle, the nuclear part of the interaction potential becomes dominant, giving rise to strong absorption phenomena manifested as a sharp decrease of the elastic cross section. This characteristic fall-off of the elastic scattering angular distribution is usually interpreted in terms of the near-side scattering amplitudes [80]. The OM calculations are in good

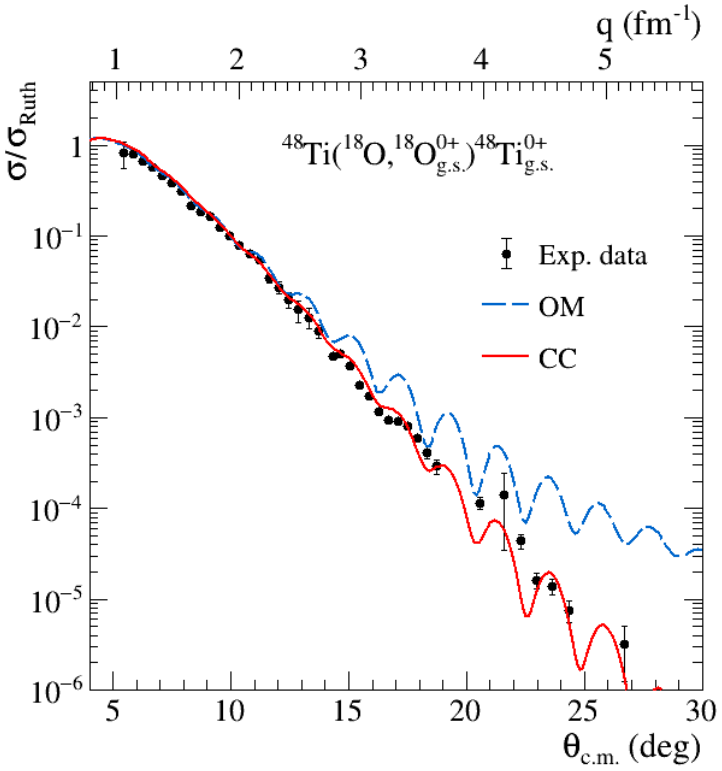

Figure 3.14: Experimental cross section angular distribution of the ^{18}O +^{48}Ti elastic scattering at 275 MeV incident energy in terms of the ratio with the Rutherford cross section. The theoretical calculations for the elastic transition in OM (blue dashed line) and CC (red solid line) are also shown. The theoretical curves are folded with the experimental angular resolution.

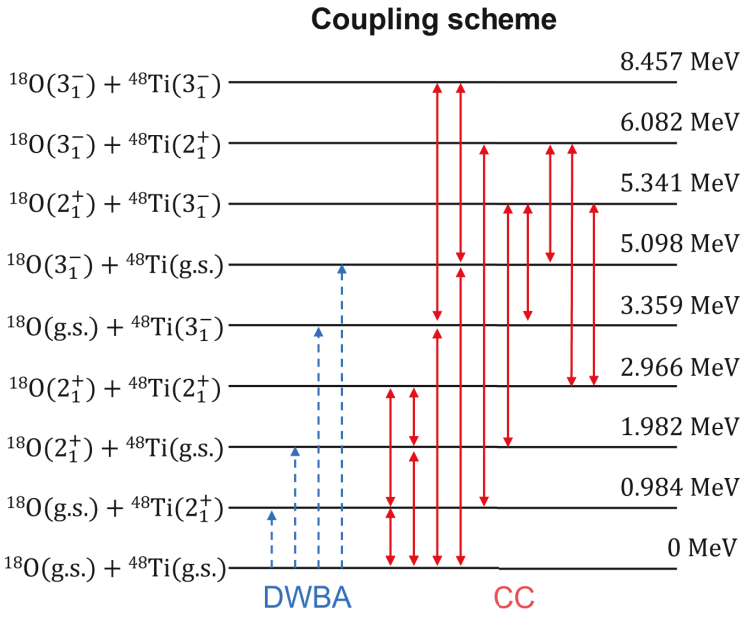

Figure 3.15: Coupling scheme adopted for the DWBA (blue dashed arrows) and CC (red solid arrows) theoretical calculations of the ^{18}O +^{48}Ti elastic and inelastic scattering at 275 MeV incident energy. On the right, the excitation energies of the considered states are reported.

agreement with the data up to $\theta_{c.m.} \rightarrow 13°$, which corresponds to a transferred momentum $q \rightarrow 2.5$ fm^{-1}. At larger q, the OM calculation overestimates the experimental data. The origin of such a discrepancy is ascribed to the fact that at larger momentum-transferred the cross sections of non-elastic channels become comparable with the elastic scattering one, so that the coupling effects must be taken into account for a better description of the data, as observed in similar analysis [32, 35, 37, 38, 97, 103]. To this extend, coupled channel calculations were performed.

3.2.3 Coupling to the inelastic scattering channels

In this analysis, the 2^+ and 3^- low-lying excited states of both projectile and target are included in the coupling scheme, as sketched in Fig. 3.15, and are described as collective excitations within the rotational model. They are treated in terms of quadrupole and octupole ($\lambda = 2, 3$) excitations of the deformed ^{18}O and ^{48}Ti

nuclei. The coupling potentials are derived from a multipole decomposition of the optical potential OP [80]. The Coulomb $V_C(r,\lambda)$ and nuclear $V_N(r,\lambda)$ coupling potentials for the λ-multipolarity are defined as follows:

$$V_C(r,\lambda) = M(E\lambda)\, e^2\, \frac{\overline{4\pi}}{2\lambda+1}\, r^{-\lambda-1} \tag{3.21a}$$

$$V_N(r,\lambda) = \quad \frac{\delta_\lambda}{\overline{4\pi}} \frac{dU_{opt}(r)}{dr}\,, \tag{3.21b}$$

in which $M(E\lambda)$ is the matrix element of the electric multipole operator $E\lambda$, e is the electron charge and δ_λ is the deformation length. The matrix element $M(E\lambda)$ in Eq. 3.21a can be related to the reduced transition probability $B(E\lambda; J \propto J')$ from the initial state J to the final one J' through the $E\lambda$ operator according to

$$M(E\lambda) = \mp\sqrt{(2J+1)B(E\lambda; J \propto J')} \tag{3.22}$$

As indicated in Ref. [79], the sign is the same as that of the intrinsic quadrupole moment (Q_0). The nuclear coupling potential $V_N(r,\lambda)$ is a complex deformed potential depending on the deformation length δ_λ. It is defined in the following way:

$$\delta_\lambda = \beta_\lambda R_V = \frac{4\pi}{3Ze} \frac{M(E\lambda)}{R_V^{\lambda-1}} \tag{3.23}$$

where β_λ is the deformation parameter for the 2^λ-transition, Z is the atomic number of the nucleus and R_V is the average radius of the SPP, expressed as

$$R_V = \frac{\int \mathrm{d}r\, 4\pi r^3\, V(r)}{\int \mathrm{d}r\, 4\pi r^2\, V(r)}\,. \tag{3.24}$$

The same prescriptions for the Coulomb and nuclear coupling potentials were recently adopted in Refs. [32, 38, 42, 103, 105]. The adopted values for the mentioned quantities are listed in Table 3.3.

The DWBA and CC calculations taking into account the low-lying inelastic transitions are shown in Fig. 3.15. In the DWBA approach the second order transitions to the $^{18}\mathrm{O}(2_1^+)$ + $^{48}\mathrm{Ti}(2_1^+)$ and $^{18}\mathrm{O}(3_1^-)$ + $^{48}\mathrm{Ti}(3_1^-)$ states are not

Table 3.3: Adopted values of average radius R_V of the SPP, reduced transition probability $B(E\lambda; J \propto J')$, reduced matrix element $M(E\lambda)$ and deformation length δ_λ adopted for $\lambda = 2, 3$ for the ^{18}O and ^{48}Ti nuclei.

	R_V (fm)	$B(E2; 0^+ \propto 2^+)$ (e^2b^2)	$M(E2)$ (e fm^2)	δ_2 (fm)	$B(E3; 0^+ \propto 3^-)$ (e^2b^3)	$M(E3)$ (e fm^3)	δ_3 (fm)
^{18}O	4.60	0.0043†	+6.56	+0.75	0.0013§	+35.36	+0.87
^{48}Ti		0.00720‡	+26.83	+1.11	0.0074§	+75.25	+0.77

†from Ref. [106]
§from Ref. [107]
‡from Ref. [108]

included because in such an approach only first-order processes are allowed†. For the same reason, the backflow to the elastic channel is not allowed in DWBA.

The experimental cross section angular distributions for the transition to the 2_1^+ excited state of the ^{48}Ti and for the structure centered at 2.2 MeV are shown in the top and in the bottom panel of Fig. 3.16, respectively, where they are compared to the DWBA and CC calculations. As can be observed, the CC approach provides a better description of the experimental data than the DWBA one, well reproducing the absolute value and the slope of both the experimental inelastic angular distributions. This is confirmed also for the elastic scattering case (see Fig. 3.14), where the CC calculations describe very well the experimental data in the overall explored angular range. The better agreement with the experimental data of the CC approach with respect to DWBA and OM is a clear sign of the importance of the couplings effect for the analyzed system, also observed in other systems at similar incident energies [37, 38, 50, 97].

3.2.4 The ^{18}O + ^{48}Ti scattering at 54 MeV

As a further test of the reliability of the approach described in this Thesis, a theoretical analysis of the experimental data reported in Ref. [83] by Essel et al., concerning the ^{18}O + ^{48}Ti system at 54 MeV incident energy, is performed.

†These transitions require a double excitation process of the target and projectile.

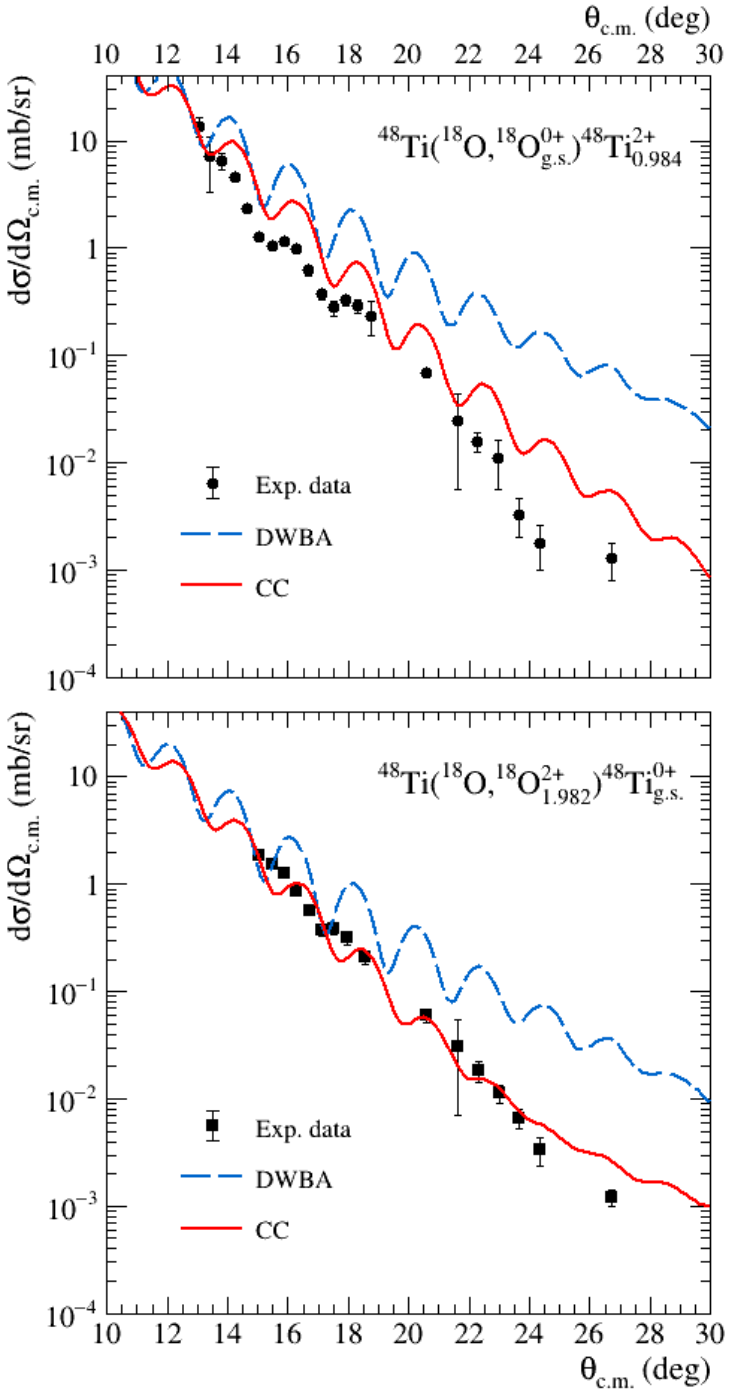

Figure 3.16: Experimental cross section angular distribution of the ^{18}O +^{48}Ti inelastic scattering to the 2_1^+ excited state of the ^{48}Ti (top panel) and of the structure centered at 2.2 MeV (bottom panel). The DWBA (blue dashed line) and CC (red solid line) theoretical calculations for both the inelastic channels are also shown. The theoretical curves are folded with the experimental angular resolution.

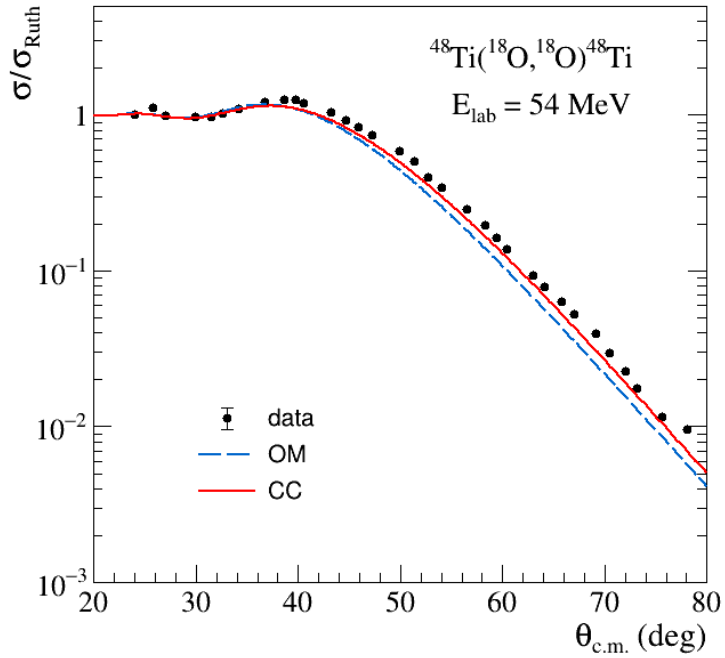

Figure 3.17: Experimental cross section angular distribution of ^{18}O +^{48}Ti elastic scattering at 54 MeV in terms of the ratio with the Rutherford cross section. The OM (blue dashed line) and CC (red solid line) theoretical calculations are also shown.

Here all the ingredients of the calculations are kept the same as discussed above, but the energy, which is obviously adapted to 54 MeV. The comparison between the experimental elastic angular distribution and the OM and CC calculations is shown in Fig. 3.17. The CC method describes better than the OM one the experimental data, characterized by the typical Fresnel-like pattern.

The angular distributions of the inelastic transitions populating the 2_1^+ states of ^{18}O and ^{48}Ti nuclei are also analysed. Both angular distributions are compared to my DWBA and CC calculations in Fig. 3.18. As can be noticed, for the inelastic transition toward the 2_1^+ state of the target, both approaches are in very good agreement with the experimental data; in particular, the DWBA result is compatible with the one reported in Ref. [83], where the parameters of the optical potential were deduced from a fit of the elastic scattering cross-section. Instead,

for the excitation of the 2_1^+ state of the projectile a discrepancy between the calculations and the experimental data is observed. Since the same disagreement is present also in Ref. [83], there is the suspect that it may be due to a problem in the reported experimental data.

For the three analyzed angular distributions, the calculations with and without the couplings (i.e. CC vs. OM for the elastic scattering process and CC vs. DWBA for the inelastic transitions) produce quite similar results. Therefore, it can be deduced that the coupling effects for collisions near the Coulomb barrier are less relevant.

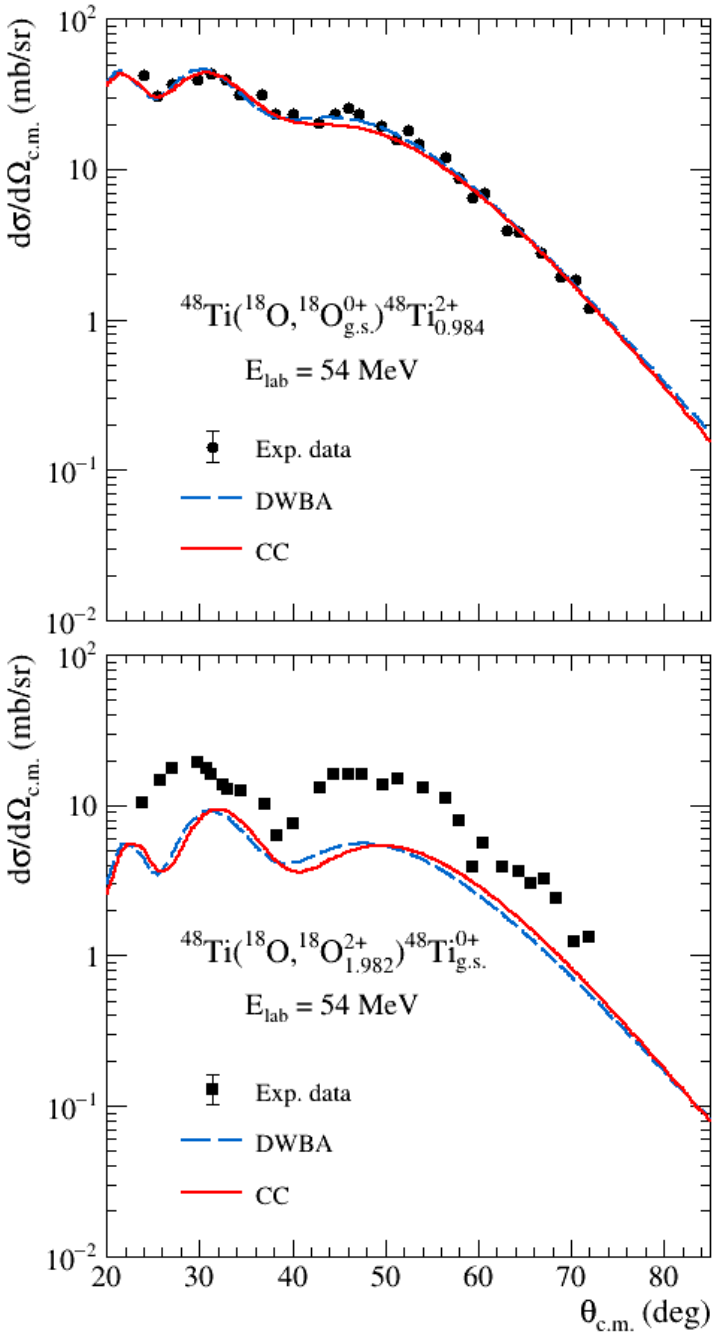

Figure 3.18: Angular distributions of differential cross-section for the inelastic transitions towards the 2_1^+ state of (top panel) target and (bottom panel) projectile induced by the ^{18}O + ^{48}Ti collision at 54 MeV. The DWBA (blue dashed line) and CC (red solid line) calculations are also shown.

Chapter References

[3] F. Cappuzzello et al. "The MAGNEX spectrometer: results and perspectives". In: *Eur. Phys. J. A* 52.6 (2016), p. 167. DOI: 10.1140/epja/i2016-16167-1.

[31] A. Spatafora. "Experimental and theoretical multi-channel study of direct nuclear reactions: a tool to provide data driven information on neutrino-less double-beta decay". PhD thesis. Università degli studi di Catania, 2022.

[32] D. Carbone et al. "Initial state interaction for the ^{20}Ne + ^{130}Te and ^{18}O + ^{116}Sn systems at 15.3 AMeV from elastic and inelastic scattering measurements". In: *Universe* 7.3 (2021). cited By 1. DOI: 10.3390/universe7030058.

[33] D. Carbone et al. "Analysis of two-nucleon transfer reactions in the ^{20}Ne + ^{116}Cd system at 306 MeV". In: *Physical Review C* 102.4 (2020). cited By 6. DOI: 10.1103/PhysRevC.102.044606.

[35] S. Burrello et al. "Multichannel experimental and theoretical constraints for the ^{116}Cd(^{20}Ne,^{20} F)^{116}In charge exchange reaction at 306 MeV". In: *Phys. Rev. C* 105 (2 Feb. 2022), p. 024616. DOI: 10.1103/PhysRevC.105.024616.

[37] A. Spatafora et al. "^{20}Ne+^{76}Ge elastic and inelastic scattering at 306 MeV". In: *Phys. Rev. C* 100 (3 Sept. 2019), p. 034620. DOI: 10.1103/PhysRevC.100.034620.

[38] L. La Fauci et al. "^{18}O +^{76} Se elastic and inelastic scattering at 275 MeV". In: *Phys. Rev. C* 104 (5 Nov. 2021), p. 054610. DOI: 10.1103/PhysRevC.104.054610.

[42] O. Sgouros et al. “One-proton transfer reaction for the ^{18}O +^{48} Ti system at 275 MeV”. In: *Phys. Rev. C* 104 (3 Sept. 2021), p. 034617. DOI: 10.1103/PhysRevC.104.034617.

[43] G. A. Brischetto. “Data reduction of the ^{18}O + ^{48}Ti elastic and inelastic scattering at 275 MeV in the context of the NUMEN project”. In: *Il Nuovo Cimento C* 45 (2022), p. 96. DOI: 10.1393/ncc/i2022-22096-5.

[50] D. Pereira et al. “Nuclear rainbow in the 16O+27AL system: The role of couplings at energies far above the barrier”. In: *Phys. Lett. B* 710.3 (2012), pp. 426–429. ISSN: 0370-2693. DOI: https://doi.org/10.1016/j.physletb.2012.03.032.

[53] M. Cavallaro et al. “Transport efficiency in large acceptance spectrometers”. In: *Nucl. Instrum. Meth. A* 637 (May 2011), pp. 77–87. DOI: 10.1016/j.nima.2011.01.078.

[56] M. Cavallaro et al. “The low-pressure focal plane detector of the MAGNEX spectrometer”. In: *The European Physical Journal A* 48.5 (May 2012), p. 59. ISSN: 1434-601X. DOI: 10.1140/epja/i2012-12059-8.

[60] K. Makino and M. Berz. “COSY INFINITY version 8”. In: *Nuclear Instruments and Methods in Physics Research Section A: Accelerators, Spectrometers, Detectors and Associated Equipment* 427.1 (1999), pp. 338–343. ISSN: 0168-9002. DOI: https://doi.org/10.1016/S0168-9002(98)01554-X.

[65] F. Cappuzzello, D. Carbone, and M. Cavallaro. “Measuring the ions momentum vector with a large acceptance magnetic spectrometer”. In: *Nucl. Instrum. Methods Phys. Res. A* 638.1 (2011), pp. 74–82. ISSN: 0168-9002. DOI: https://doi.org/10.1016/j.nima.2011.02.045.

[72] D. Carbone, F. Cappuzzello, and M. Cavallaro. “Universal algorithm for the analysis of charge distributions in segmented electrodes of gas detectors”. In: *The European Physical Journal A* 48.5 (May 2012), p. 60. ISSN: 1434-601X. DOI: 10.1140/epja/i2012-12060-3.

[73] W.R. Leo. *Techniques for Nuclear and Particle Physics Experiments: A How-to Approach*. Springer, 1994. ISBN: 978-3-642-57920-2.

[74] G. F. Knoll. *Radiation Detection and Measurement, 3rd ed.* 3rd edition. New York: John Wiley and Sons, 2000. ISBN: 978-0-471-07338-3.

[75] F. Cappuzzello et al. "A particle identification technique for large acceptance spectrometers". In: *Nucl. Instrum. Meth.* A621.1-3 (2010), pp. 419–423. DOI: 10.1016/j.nima.2010.05.027.

[76] O.B. Tarasov and D. Bazin. "LISE++: Radioactive beam production with in-flight separators". In: *Nuclear Instruments and Methods in Physics Research Section B: Beam Interactions with Materials and Atoms* 266.19 (2008). Proceedings of the XVth International Conference on Electromagnetic Isotope Separators and Techniques Related to their Applications, pp. 4657–4664. ISSN: 0168-583X. DOI: https://doi.org/10.1016/j.nimb.2008.05.110.

[77] W.N. Catford. "CATKIN". In: *University of Surrey* (2005).

[78] Gary L. Catchen, Javed Husain, and Richard N. Zare. "Scattering kinematics: Transformation of differential cross sections between two moving frames". In: *The Journal of Chemical Physics* 69.4 (1978), pp. 1737–1741. DOI: 10.1063/1.436749.

[79] I. J. Thompson. "Coupled reaction channels calculations in nuclear physics". In: *Comput. Phys. Rep.* 7.4 (1988), pp. 167–212. ISSN: 0167-7977. DOI: https://doi.org/10.1016/0167-7977(88)90005-6.

[80] G. R. Satchler. *Direct nuclear reactions.* Vol. 68. Int. series of monographs on physics. Oxford, UK: Clarendon Press, 1983. ISBN: 9780198512691.

[81] T. Udagawa, T. Tamura, and B. T. Kim. "Simultaneous analyses of elastic scattering and fusion cross sections for the ^{32}S + ^{58,64}Ni systems at energies near the Coulomb barrier". In: *Phys. Rev. C* 39 (5 May 1989), pp. 1840–1844. DOI: 10.1103/PhysRevC.39.1840.

[82] W. Henning et al. "Optical-model potential in single-nucleon-transfer reactions induced by heavy ions". In: *Phys. Rev. C* 15 (1 Jan. 1977), pp. 292–302. DOI: 10.1103/PhysRevC.15.292.

[83] H. Essel et al. “Inelastic scattering of ^{18}O and ^{17}O ions from medium-weight nuclei”. In: *Phys. Rev. C* 19 (6 June 1979), pp. 2224–2236. DOI: 10.1103/PhysRevC.19.2224.

[84] E. Vardaci et al. “Study of the threshold anomaly effect in the reaction ^{7}Li + ^{208}Pb at energies around the Coulomb barrier”. In: *European Physical Journal A* 57.3 (2021). DOI: 10.1140/epja/s10050-021-00400-3.

[85] R.O. Akyuz and A. Winther. “Nuclear structure and heavy ion reactions”. In: *Proc. Enrico Fermi Int. School of Physics*. Ed. by R. A. Broglia, C. H. Dasso, and R. Ricci. Amsterdam: North-Holland, 1979.

[86] K.-S. Choi et al. “Coupled-channels analyses for ^{9,11}Li + ^{208}Pb fusion reactions with multi-neutron transfer couplings”. In: *Physics Letters B* 780 (2018), pp. 455–460. ISSN: 0370-2693. DOI: https://doi.org/10.1016/j.physletb.2018.03.049.

[87] K. Cheng and C. Xu. “Systematic investigation of “hindrance” in heavy-ion fusion reactions at deep sub-barrier energies”. In: *Nuclear Physics A* 992 (2019), p. 121642. ISSN: 0375-9474. DOI: https://doi.org/10.1016/j.nuclphysa.2019.121642.

[88] C. H. Dasso and G. Pollarolo. “Investigating the nucleus-nucleus potential at very short distances”. In: *Phys. Rev. C* 68 (5 Nov. 2003), p. 054604. DOI: 10.1103/PhysRevC.68.054604.

[89] G.R. Satchler and W.G. Love. “Folding model potentials from realistic interactions for heavy-ion scattering”. In: *Phys. Rep.* 55.3 (1979), pp. 183–254. ISSN: 0370-1573. DOI: https://doi.org/10.1016/0370-1573(79)90081-4.

[90] Dao T. Khoa and G.R. Satchler. “Generalized folding model for elastic and inelastic nucleus–nucleus scattering using realistic density dependent nucleon–nucleon interaction”. In: *Nuclear Physics A* 668.1 (2000), pp. 3–41. ISSN: 0375-9474. DOI: https://doi.org/10.1016/S0375-9474(99)00680-6.

[91] Dao T. Khoa, G. R. Satchler, and W. von Oertzen. "Nuclear incompressibility and density dependent NN interactions in the folding model for nucleus-nucleus potentials". In: *Phys. Rev. C* 56 (2 Aug. 1997), pp. 954–969. DOI: 10.1103/PhysRevC.56.954.

[92] L. C. Chamon et al. "Toward a global description of the nucleus-nucleus interaction". In: *Phys. Rev.* C66 (2002), p. 014610. DOI: 10.1103/PhysRevC.66.014610.

[93] D. Carbone et al. "Microscopic cluster model for the description of new experimental results on the ^{13}C(^{18}O,^{16}O)^{15}C two-neutron transfer at 84 MeV incident energy". In: *Phys. Rev.* C95.3 (2017), p. 034603. DOI: 10.1103/PhysRevC.95.034603.

[94] B. Paes et al. "Long-range versus short-range correlations in the two-neutron transfer reaction ^{64}Ni(^{18}O,^{16}O)^{66}Ni". In: *Phys. Rev.* C96.4 (2017), p. 044612. DOI: 10.1103/PhysRevC.96.044612.

[95] M.J. Ermamatov et al. "Two-neutron transfer analysis of the ^{16}O (^{18}O, ^{16}O) ^{18}O reaction". In: *Phys. Rev.* C94.2 (2016), p. 024610. DOI: 10.1103/PhysRevC.94.024610.

[96] M. J. Ermamatov et al. "Comprehensive analysis of high-lying states in ^{18}O populated with (t,p) and (^{18}O,^{16}O) reactions". In: *Phys. Rev.* C96.4 (2017), p. 044603. DOI: 10.1103/PhysRevC.96.044603.

[97] V.A.B. Zagatto et al. "Important role of projectile excitation in ^{16}O + ^{60}Ni and ^{16}O + ^{27}Al scattering at intermediate energies". In: *Phys. Rev. C* 97 (May 2018), p. 054608. DOI: 10.1103/PhysRevC.97.054608.

[98] E. N. Cardozo et al. "Competition between direct and sequential two-neutron transfers in the ^{18}O +^{28} Si collision at 84 MeV". In: *Phys. Rev. C* 97 (6 June 2018), p. 064611. DOI: 10.1103/PhysRevC.97.064611.

[99] D. Pereira et al. "An imaginary potential with universal normalization for dissipative processes in heavy-ion reactions". In: *Phys. Lett. B* 670.4 (2009), pp. 330–335. ISSN: 0370-2693. DOI: https://doi.org/10.1016/j.physletb.2008.10.066.

[100] E. Crema et al. “Near-barrier quasielastic scattering as a sensitive tool to derive nuclear matter diffuseness”. In: *Phys. Rev. C* 84 (2 Aug. 2011), p. 024601. DOI: 10.1103/PhysRevC.84.024601.

[101] E. Crema et al. “Reaction mechanisms of the ^{18}O +^{63} Cu system at near-barrier energies”. In: *Phys. Rev. C* 98 (4 Oct. 2018), p. 044614. DOI: 10.1103/PhysRevC.98.044614.

[102] L. M. Fonseca et al. “Elastic and inelastic scattering of ^{16}O on ^{27}Al and ^{28}Si at 240 MeV”. In: *Phys. Rev. C* 100 (1 July 2019), p. 014604. DOI: 10.1103/PhysRevC.100.014604.

[103] M. Cavallaro et al. “A Constrained Analysis of the ^{40}Ca(^{18}O,^{18}F)^{40}K Direct Charge Exchange Reaction Mechanism at 275 MeV”. In: *Frontiers in Astronomy and Space Sciences* 8 (2021), p. 61. DOI: 10.3389/fspas.2021.659815.

[104] J.L. Ferreira et al. “Analysis of two-proton transfer in the ^{40}Ca (^{18}O, ^{20}Ne) ^{38}Ar reaction at 270 MeV incident energy”. In: *Physical Review C* 103.5 (2021). cited By 0. DOI: 10.1103/PhysRevC.103.054604.

[105] S. Calabrese et al. “^{18}O-induced single-nucleon transfer reactions on ^{40}Ca at 15.3A MeV within a multichannel analysis”. In: *Phys. Rev. C* 104 (6 Dec. 2021), p. 064609. DOI: 10.1103/PhysRevC.104.064609.

[106] B. Pritychenko et al. “Tables of E2 Transition Probabilities from the first 2^+ States in Even-Even Nuclei”. In: *Atom. Data Nucl. Data Tabl.* 107 (2016), pp. 1–139. DOI: 10.1016/j.adt.2015.10.001,10.1016/j.adt.2016.08.002.

[107] T. Kibedi and R. H. Spear. “Reduced electric-octupole transition probabilities, B(E3;$0^+ \propto 3^-$) - an update”. In: *Atomic Data and Nuclear Data Tables* 80.1 (2002), pp. 35–82. ISSN: 0092-640X. DOI: https://doi.org/10.1006/adnd.2001.0871.

[108] S. Raman, C. W. Nestor, and P. Tikkanen. “Transition probability from the ground to the first-excited 2+ state of even-even nuclides”. In: *Atomic Data and Nuclear Data Tables* 78.1 (2001), pp. 1–128. ISSN: 0092-640X. DOI: https://doi.org/10.1006/adnd.2001.0858.

4

The future MAGNEX focal plane detector

Contents

4.1 The gas tracker **97**
4.1.1 The drift region 99
4.1.2 The electron multiplication stage 99
4.1.3 The readout anode 100
4.1.4 The working principle 101
4.2 The wall of SiC-CsI(Tl) telescope detectors **102**
4.2.1 The silicon carbide ΔE detectors 104
4.2.2 The cesium iodide E detectors 108
4.3 Concept validation and commissioning **109**

The Double Charge Exchange (DCE) reactions are characterized by very low cross-sections, that are typically of the order of few tens of nb. In order to mea-

sure such a kind of reactions with significant statistics, a major upgrade of the K800 Superconducting Cyclotron and of the MAGNEX facility at the Laboratori Nazionali del Sud of the Istituto Nazionale di Fisica Nucleare (INFN-LNS) is ongoing with the aim of increasing the beam intensities on target up to three orders of magnitude, reaching a maximum value of 10^{13} particle-per-second (pps). Such a high intensity requires a radical change of the technologies used for the beam extraction and transport, for the target production and cooling, and for the detection of the ejectiles [4, 49, 109]. Regarding the latter, a full restyling of the Focal Plane Detector (FPD) of the MAGNEX spectrometer is foreseen, since neither the present gas tracker nor the silicon stopping wall (see Chapt. 2) are able to withstand the expected high particle rates. In particular, due to the intrinsic slowness of the response of the multiplication wires, the present gas tracker can tolerate rates up to few tens of Hz/cm, very far from the 30 kHz/cm expected at the end of the upgrade [56, 57]. Therefore, a new gas tracker based on Multi-layer THick Gas Electron Multipliers (M-THGEMs) [110] has been designed. However, in the present tracker the multiplication wires are also employed to measure the ions energy loss in the gas, an information used to perform the identification in atomic number of the ejectiles (see Subsect. 3.1.2). As a consequence, in the new MAGNEX FPD a dedicated detection system for the Particle IDentification (PID) must be included. Such a system consists of a wall of solid-state telescopes with the first stage based on a thin silicon carbide (SiC) detector, followed by a thallium-doped cesium iodide (CsI(Tl)) scintillator crystal as stopping detector.

In this chapter, a description of the new gas tracker and of the PID wall for the upgrade of the MAGNEX FPD is presented, paying particular attention to the reasons that guided the design. The NUMEN collaboration has carried out extensive test campaigns on suitable prototypes of the high performance detectors adopted for the new FPD. The results of some tests on the SiC-CsI(Tl) telescopes are reported in this chapter, while the characterization tests performed on a reduced-size prototype of the new gas tracker will be discussed in detail in Chapt. 6. Together with the test activity, the NUMEN collaboration developed dedicated simulations of the response of the gas tracker and of the PID wall to the ejectiles of interest: the former are briefly presented in this chapter, the latter are described thoroughly in Chapt. 5.

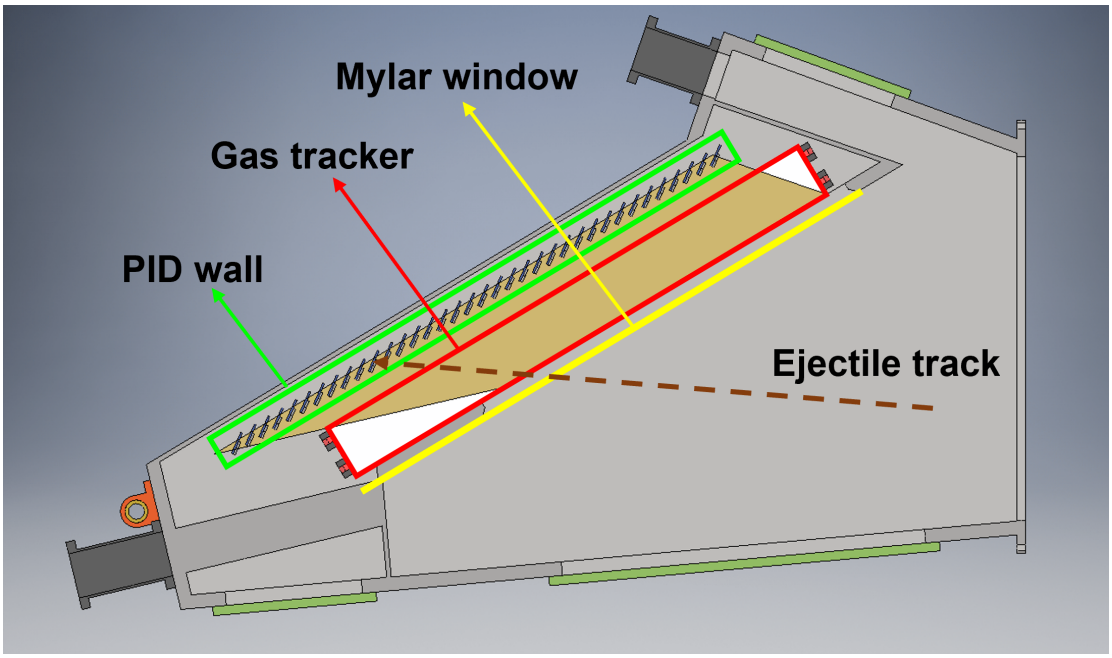

Figure 4.1: CAD Drawing of MAGNEX FPD. The Mylar window (yellow), the gas tracker (red) and the PID wall (green) are highlighted.

The upgraded FPD will be hosted in a vacuum chamber specifically designed. Similarly to the present apparatus, the new FPD is filled with isobutane at typical pressure of few tens of mbar. A Mylar window with a thickness of few μm is used to contain the gas within the FPD region, minimizing the material crossed by the ions before entering the FPD. A Computer-Aided Design (CAD) drawing of the new vacuum chamber is illustrated in Fig. 4.1, where the gas tracker, the PID wall and the Mylar window are highlighted.

4.1 The gas tracker

As discussed in Subsect. 2.2.1, the ray-reconstruction technique used to determine the momentum vector at the target position requires an accurate measurement of four phase-space parameters of the ejectiles at the focal plane, i.e. the horizontal (x_{foc}) and vertical (y_{foc}) positions, and the horizontal (θ_{foc}) and vertical (ϕ_{foc}) angles. Moreover, a good resolution of such parameters is fundamental for the particle identification capability of the experimental apparatus. Therefore,

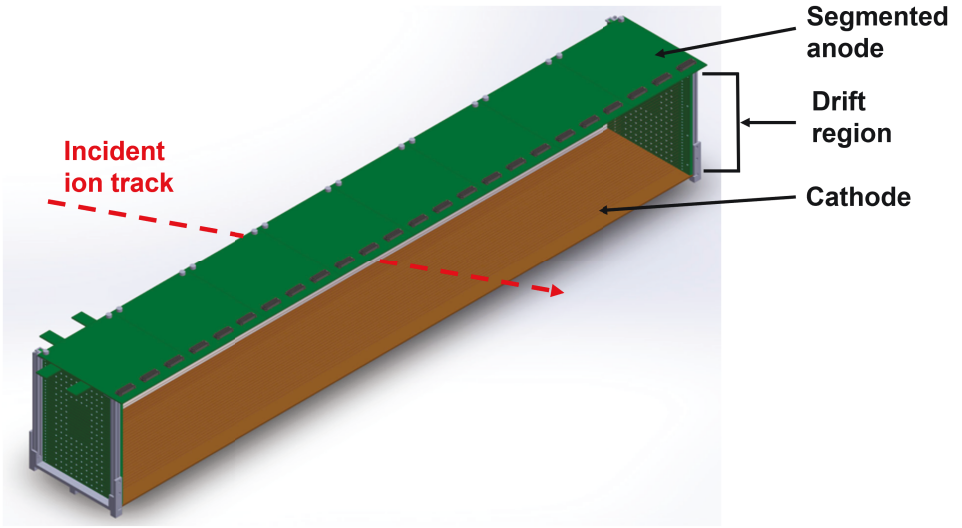

Figure 4.2: Drawing of the new gas tracker for the MAGNEX FPD. Figure from Ref. [111].

the new FPD tracking system must ensure performances comparable with those offered by the present gas tracker, namely a resolution better than 0.6 mm full width at half maximum (FWHM) in both x_{foc} and y_{foc}, and 5 mrad FWHM in θ_{foc} and ϕ_{foc} [56]. In addition, it must cope with the expected high rate of particles (up to $\rightarrow$30 kHz/cm), managing to disentagle the track of each detected ion. The structure of the new gas tracker consists of three main parts:

- a drift region, which corresponds to the active volume of the detector;
- a stage for the multiplication of primary electrons;
- a pad-segmented readout anode.

A sketch of the new gas tracker is illustrated in Fig. 4.2. The different parts and the working principle of the gas tracker are described in the following in dedicated subsections. Resembling the present FPD, the gas employed is pure isobutane (iC_4H_{10}), which is a fast gas also acting as a quencher thus being suitable for operations with heavy ions at low pressure. The working pressure is in the range 10-100 mbar, with the specific value to be set depending on the experiment.

4.1.1 The drift region

The drift region is delimited between the cathode and the electron multiplication element, extending for a total height of 150 mm. A uniform electric field is applied across this region with a typical value of 50 V/cm. A partition grid, composed by gold-plated tungsten wires connecting the two lateral walls, ensures the uniformity of the electric field, protecting the drift region from possible distortions due to the high-voltage biasing of the SiC detectors in the PID wall.

4.1.2 The electron multiplication stage

The electron multiplication stage is the element that mostly differentiates the new tracker from the present one. Indeed, in the latter the multiplication technology is based on 50 μm diameter multiplication wires, which can at most stand with incident ions rates of few tens of Hz/cm. The reason of this limitation depends on the sizable length of the wires (1.35 m) and on the long drift time of the positive ions moving from the wires to the Frisch grid (a few ms). The wire technology is therefore not suitable to work with the high intensity beams needed by the NUMEN project. Among the devices able to bear with high particle rates, Micro Pattern Gaseous Detectors (MPGDs) represents one of the most interesting options, because they can provide large sensitive area detectors with high spatial resolution, operational stability and radiation hardness [112]. One kind of MPGD very appealing for the upgrade of the MAGNEX FPD is the Multi-layer THick Gas Electron Multiplier (M-THGEM), which is a stack of several THGEM elements assembled together in a single device [110]. THGEMs [113, 114] are one of the most recent developments in the field of MPGDs, featuring a structure similar to the Gas Electron Multiplier (GEM) [115] but thicker and with a larger hole diameter *. A single THGEM foil is usually composed by an insulator substrate (e.g. ceramic, FR-4, Kapton, etc.) with a thickness of some tenths of millimeter coated on both side with metallic material (typically copper). A small rim ($\rightarrow$0.1 mm) is chemically etched around the holes on both the metallic surfaces. The most

*The typical hole diameter for GEMs is of the order of tens of μm, while for THGEMs it is of hundreds of μm. The THGEM tested for this Thesis and adopted for the future MAGNEX FPD has a hole diameter of 300 μm (see Table 6.1)

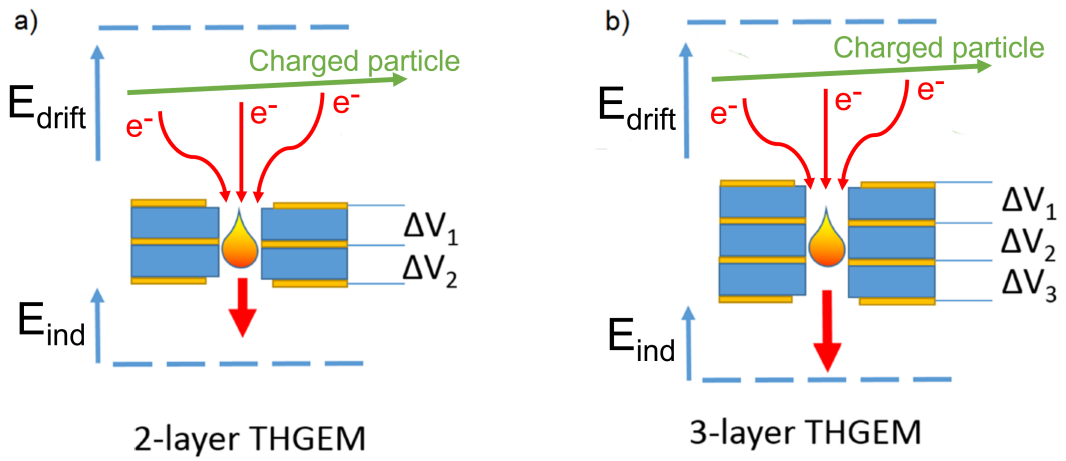

Figure 4.3: Schematic drawing of (a) two- and (b) three-layer M-THGEM device. Figure from Ref. [110].

common M-THGEM types are two- and three-layer structures, whose schematic drawings are shown in Fig. 4.3. M-THGEMs are fabricated using the standard multi-layer printed-circuit-board (PCB) technique, which consists in mechanically drilling the layers of metallic and insulating material laminated together. By applying voltage between the M-THGEM electrodes, an intense electric field is generated inside the holes. The gas avalanche process occurs along the successive THGEM layers and it is well confined within the holes. Thus, each hole can be considered as an indipendent electron multiplication device. M-THGEMs can provide high gas gain (of the order of 10^6 10^7 with single-photoelectrons), a rate capability up to 10^8 Hz/cm^2, sub-millimeter position resolution and time resolution of a few ns. In addition, M-THGEMs are a reliable solution for all applications that require to operate with gas at low pressure [116–118]. For the future gas tracker of the MAGNEX FPD, it was chosen to use a single three-layer M-THGEM foil of large area (1200 $\pm$ 107 mm^2).

4.1.3 The readout anode

The readout anode is composed by four modules which are mounted side-by-side. Each module is segmented in five rows, arranged along the spectrometer dispersive direction. The distance between two consecutive rows is of 10 mm. Each row is

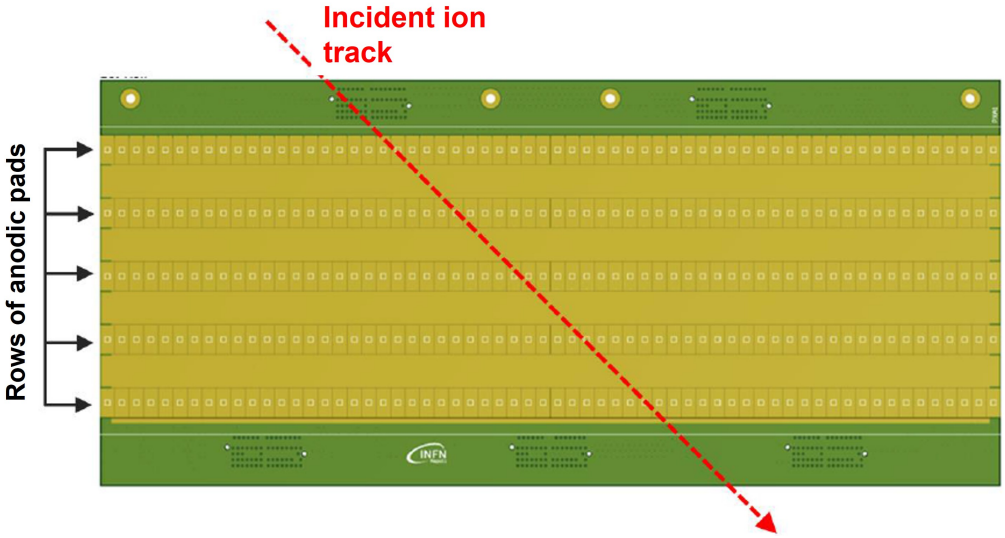

Figure 4.4: CAD drawing of one of the module of the anode for the new gas tracker. Figure from Ref. [111].

subdivided in 240 pads of 5± 10 mm^2. A sketch of one module of the anode is shown in Fig. 4.4. The anode structure allows to sample the incident ion track in five different points, as will be explained in the following. Each pad is connected to a preamplifier and then to a digitizer.

4.1.4 The working principle

An incident ion, after crossing the Mylar window, enters the drift region, where it ionizes the gas, producing primary electrons and ions. The uniform electric field applied across the drift volume drives the electrons with constant velocity towards the M-THGEM holes. Therein, the gas avalanche process occurs due to the strong electric field. The avalanche electrons are then directed towards the segmented anode, where they are collected by different pads. Each pad produces a signal proportional to the collected charge, thus for each row a charge distribution is measured. By calculating the center of gravity of such a charge distribution, an horizontal coordinate is determined. Since each row is indendent one from another, five different horizontal positions are measured. A linear fit of the five horizontal coordinates allows to reconstruct the projection of the particle trajectory onto the horizontal plane and the horizontal angle. Each pad also produces

a time signal related to the electron drift time in the gas. Knowing the electron drift velocity ($\rightarrow 5$ cm/μs), the time difference between the SiC detectors signal when a ion is detected and the pad signals generated by the tracker can be converted into a vertical position measurement. Therefore, for each row a vertical coordinate is determined. By a linear fit of the five indipendent vertical coordinates, the projection of the track onto the focal plane and the vertical angle are reconstructed. Thus, it is possible to extract the full 3D trajectory; in particular, the impact point (x_{foc}, y_{foc}) and the horizontal and vertical angles $(\theta_{foc}, \phi_{foc})$ at the focal plane are determined.

4.2 The wall of SiC-CsI(Tl) telescope detectors

In the study of nuclear reactions induced by heavy-ions, the identification in atomic number (Z), mass number (A) and charge (q) of the reaction products is fundamental to select the reaction channel of interest. As discussed in Subsect. 3.1.2, in the present MAGNEX FPD the atomic number identification is performed via the standard ΔE E_{resid} technique, where ΔE is the energy loss in the gas, which is measured by the multiplication wires working in proportional regime. As highlighted in the previous section, in the new FPD gas tracker the multiplication wires will be substituted by a M-THGEM device, that is not conceived to provide accurate information on the energy loss of charged particles. This implies a reduction of the overall PID capabilities of the experimental apparatus. Moreover, the large area (50 ± 70 mm^2) silicon detectors constituting the present ion stopping wall are not able to cope with the high rates of heavy ions foreseen for the NUMEN experiments. Therefore, the PID must be performed by a dedicated wall of telescope detectors placed downstream the gas tracker. The fundamental requirement that the new PID system must satisfy is the unambiguous identification of the ions in the region of oxygen (O), fluorine (F) and neon (Ne) [4, 109]. In addition, it must have the following characteristics:

- high radiation hardness, since the expected overall heavy-ion fluency will be of the order of 10^{11} ions/(cm^2 yr);
- energy resolution good enough to allow the unambiguous identification of

the ejectiles of interest, typically having $10 < A < 25$ and $4 < Z < 12$. Moreover, the energy resolution must be good enough to achieve the required sensitivity in the cross-section measurements, which is limited by the spurious events that fall inside the identification selection conditions;

- a time resolution better than 5 ns to perform an accurate drift time measurement, necessary for the reconstruction of the vertical coordinate and angle. In addition, the time resolution must be sufficient to allow the Time Of Flight (TOF) measurement with a resolution better than 2-3 ns;
- the granularity must be sufficient to keep the double-hit probability below the 3%. For this reason, telescopes with an area of 15 $\pm$ 15 mm^2 were chosen;
- the detectors must be thick enough to stop the ejectiles of interest in a wide dynamical range of incident energies (15-60 AMeV);
- the detectors must be easily built, assembled and handled, as well as having a reasonable price.

The use of telescope detectors is very common in nuclear physics [119–121]. A single telescope is typically composed by two elements: a thin detector, which is crossed by the ion, and a thick detector, where the ion stops. The former is usually referred to as ΔE stage, while the latter is called stopping detector. This system allows the ion identification because the correlation between the energy loss ΔE in the first stage and the residual energy (E_{resid}) deposited in the second one is a function of the Z of the incident ion, according to the Bethe-Bloch formula [74]. The telescopes chosen for the NUMEN project consist of a silicon carbide (SiC) detector as ΔE stage and a tallium-doped cesium iodide (CsI(Tl)) inorganic scintillator as stopping detector [4]. The sensitive area of both the detectors is of 15 $\pm$ 15 mm^2, with 0.2 mm dead space between adjacent telescopes. The SiC detector has a total thickness of 110 μm, subdivided in 100 μm of active volume and 10 μm of inert substrate. The CsI(Tl) scintillator is 5 mm thick and its lateral surface is covered with a white reflector consisting in a 0.2 mm thick epoxy resin (EPOTEK 301-1) layer. The light produced in the scintillator is read by a

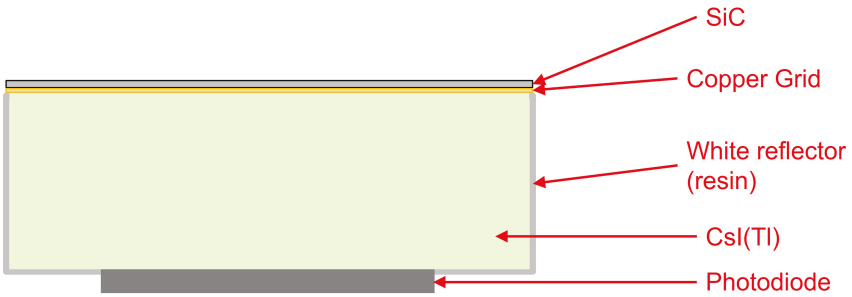

Figure 4.5: Sketch of a SiC-CsI(Tl) telescope for the PID wall of the MAGNEX FPD. Figure from Ref. [4].

Hamamatsu S3590 photodiode of 10 ± 10 mm^2 active area [122]. A scheme of the SiC-CsI(Tl) telescope is reported in Fig. 4.5. In Figs. 4.6.a and 4.6.b, the pictures of a SiC detector and a photodiode are shown, respectively.

The PID wall is composed by 36 towers, each one housing 20 SiC-CsI(Tl) telescopes, for a total number of 720 telescopes. The 20 CsI(Tl) crystals constituting a tower are contained in a single element, called tile. In Fig. 4.6.c, a picture of a CsI(Tl) tile is shown. A schematic drawing illustrating the structure of a tower is reported in Fig. 4.7. A PCB board hosts the photodiodes on top of which the CsI(Tl) crystals are glued. The SiC detector are glued on a copper grid placed on top of the CsI(Tl) tile. The signals are collected and sent to the front-end electronics by means of a Samtec connector on the top of each tower. The towers are rotated of 35° around the vertical axis, in order to minimize the path length differences inside the detectors. To avoid any loss of efficiency along the spectrometer dispersive direction, the towers are arranged in order to have an overlap of $\rightarrow 2$ mm, which corresponds to a distance of 4 mm between two consecutive towers. With this geometry, the 36 towers extend over a total width of 1260 mm, thus covering the full projection of the MAGNEX focal plane onto the PID wall plane. A scheme of the full PID wall is shown in Fig. 4.8.

4.2.1 The silicon carbide ΔE detectors

In the last years, silicon carbide (SiC) is being considered a state-of-the-art technology for the production of radiation detectors. Many efforts are devoted to develop and study innovative detection system based on SiC. Today, also thanks

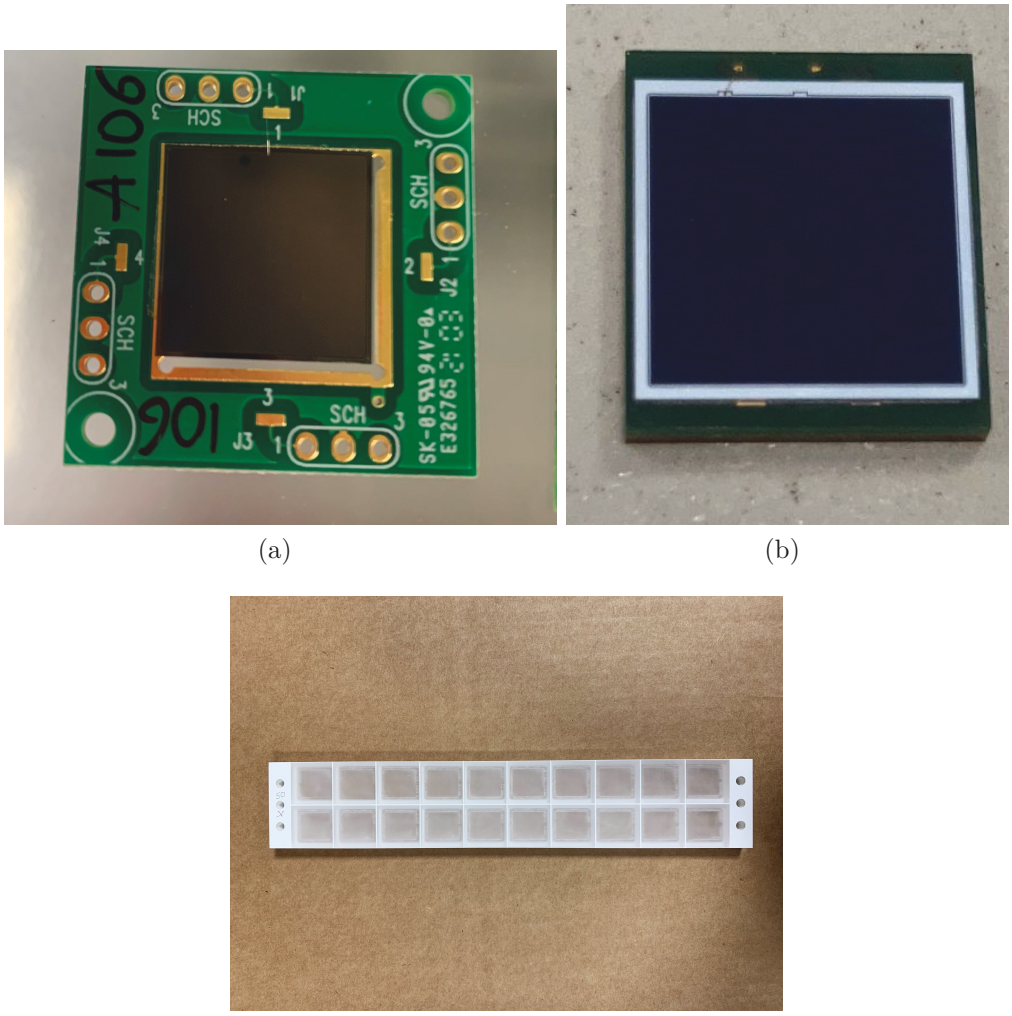

(a) (b)

(c)

Figure 4.6: Pictures of: (a) the SiC detector, (b) the Hamamatsu S3590 photodiode, (c) the CsI(Tl) tile housing 20 crystals.

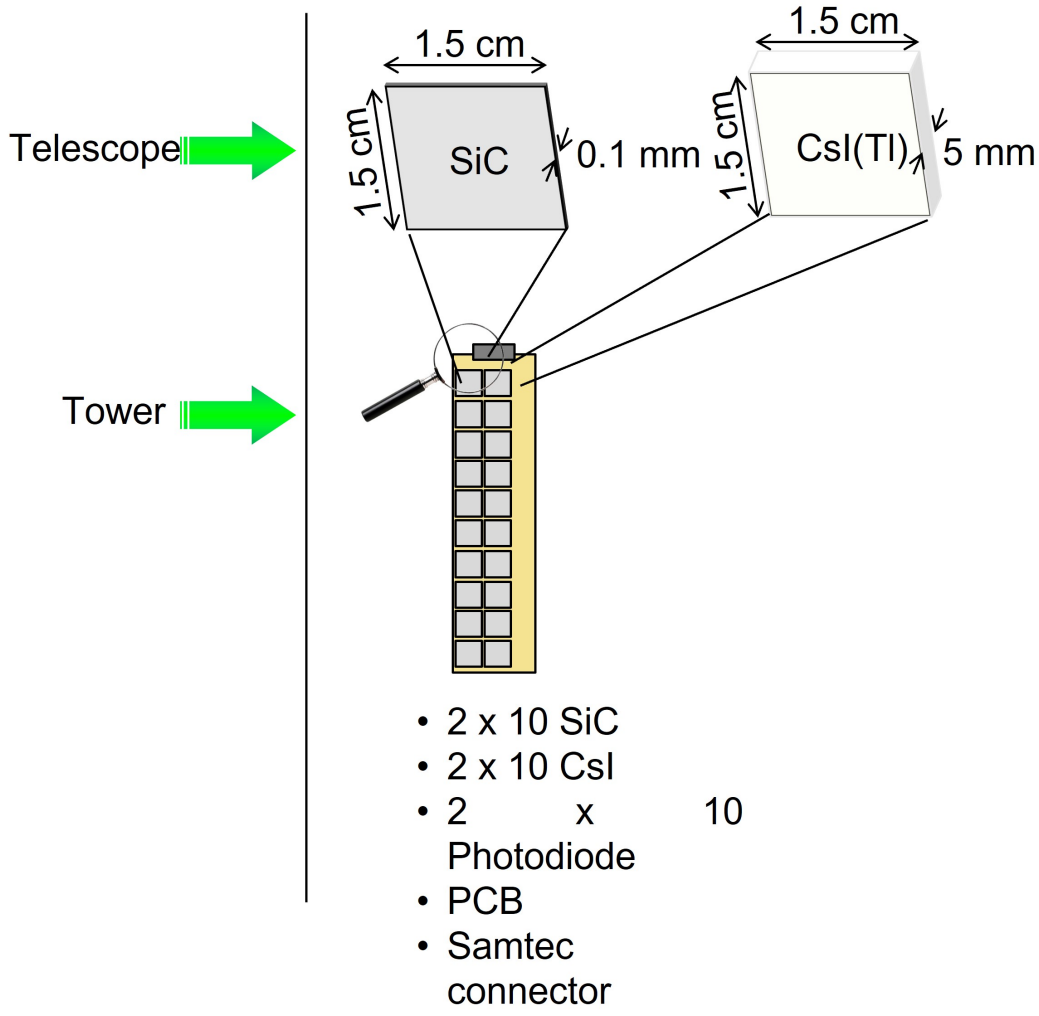

Figure 4.7: Drawing of a *tower* for the PID wall of the MAGNEX FPD. Each tower is composed by 20 SiC-CsI(Tl) telescopes. Figure from Ref. [4].

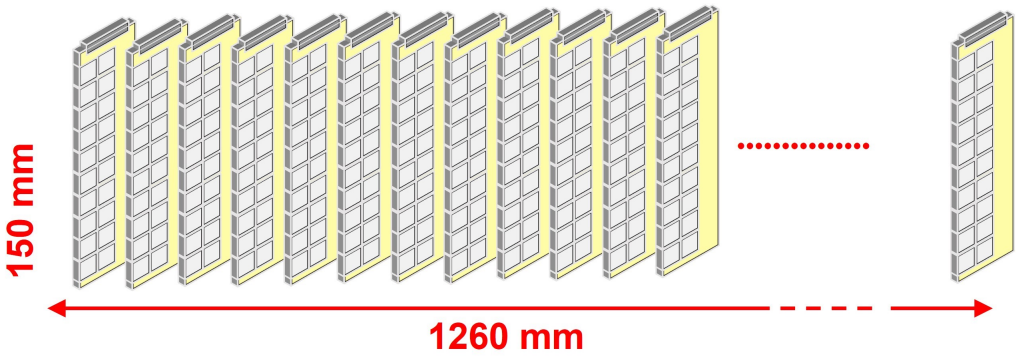

Figure 4.8: Sketch of the PID wall of the MAGNEX FPD. Figure from Ref. [4].

to the R&D activity carried out by the SiCILIA project [123], it represents a valid alternative to silicon (Si) for applications requiring a high radiation hardness. As the usual solid-state devices, SiC detectors are based on a p-n type junction, which is reverse biased to extend the depletion region and to improve the charge collection efficiency. When a charged particle crosses the detector, it looses energy generating electron-hole pairs, which are separated by the electric field and collected at electrodes producing a current pulse proportional to the energy deposited.

A comparison of the main physical properties of SiC and Si is reported in Table 4.1. SiC is a semiconductor with an energy bandgap of 3.23 eV, almost three times the Si one. This implies that the number of electron-hole pairs produced by a particle with a certain energy is almost three times larger in Si (bandgap 1.12 eV) than in SiC; thus, SiC-based detectors give a lower signal amplitude with respect to Si-based ones. The lower number of electron-hole pairs could also imply a worse energy resolution, however the large bandgap of SiC entails a significant reduction of the thermal noise, thus guaranteeing a good signal-to-noise ratio. Recent results with radioactive sources and heavy-ion beams demonstrate energy ($< 1\%$) and time (< 1 ns) resolutions for SiC detectors, comparable with those obtained with Si ones [124].

The high robustness of SiC against radiation is due to its wide bandgap and the strength of its chemical bonds; indeed, when a charged particle crosses a detector, besides ionizing and exciting the atoms in the medium, it can generate the onset of

Table 4.1: Comparison between the silicon carbide (SiC) and the silicon (Si) main properties.

Properties	**SiC**	**Si**
E_{gap} (eV)	3.23	1.12
$E_{breakdown}$ (V/cm)	3-4 $\pm 10^6$	3 $\pm 10^5$
Electron mobility (cm^2 V^{-1} s^{-1})	800	1450
Hole mobility (cm^2 V^{-1} s^{-1})	115	450
$v_{saturation}$ (cm/s)	2 $\pm 10^7$	8 $\pm 10^5$
Atomic number	14/6	14
Electron-hole creation energy (eV)	7.6-8.4	3.6
Density (g/cm^3)	3.22	2.33
Displacement energy (eV)	30-40	13-15

interstitials, vacancies and more complex structures in the crystal lattice. These defects can introduce new energy levels in the forbidden band, which alter the original properties of the semiconductor; in particular, the principal macroscopic effects are: the increase of the leakage current; the change of the depletion voltage; the reduction of the charge collection efficiency, because the defects act as traps for the charge carriers. Since SiC has a high displacement energy (average energy required to displace an atom, see Table 4.1), the probability to create defects in the crystal lattice is strongly reduced. For this reason, SiC is very robust against radiation, thus matching one of the main requirements of NUMEN for the PID wall detectors [125].

4.2.2 The cesium iodide E detectors

Scintillation detectors are among the most common devices for the detection of particles. Their working principle is the following: a charge particle crossing the scintillator excites the atoms or the molecules of the material, which then de-excite emitting photons. The light produced is proportional to the energy deposited and it is collected and transformed into electrical signal by specific

devices, as photomultipliers or photodiodes. Since the average energy required to produce a photon is about 30 times larger than the one needed to generate an electron-hole pair, the typical energy resolution of scintillators is worse than that of semiconductor detectors.

Many materials can produce scintillation light, characterized by different light yield (i.e. the number of photon produced per unit of energy deposited), linearity (i.e. the proportionality relationship between the light yield and the energy deposited) and decay time (i.e. the time between the energy deposit and the photon emission). One of the most widespread material is the CsI(Tl) (density 4.51 g/cm^3): thanks to its high light yield ($\rightarrow$ 32000 photons/MeV for α-particles at 5.4 MeV [126, 127]) and malleability, it is largely used in many experiments of both nuclear and high-energy physics to build detectors for charged particles or gamma-rays. The radiation hardness of CsI(Tl) has been investigated in several publications, where it shows a high robustness [128, 129]. Moreover, it can guarantee an energy resolution around 2% FWHM for the ion species at the energies of interest. Therefore, CsI(Tl) is a reliable solution for the NUMEN project.

4.3 Concept validation and commissioning

As mentioned in the previous sections, the upgrade of the MAGNEX facility towards high intensity beams requires the use of state-of-the-art technologies, in some cases developed by the NUMEN project. For this reason, the adopted solutions have been extensively studied and tested under realistic conditions to verify if the required performances in terms of resolution, rate capability, radiation tolerance, etc. are obtained.

Gas tracker

Regarding the new gas tracker, a reduced-size prototype was designed and built. It was tested with a radioactive α-source and ion beams to characterize its response in terms of several parameters: drift region voltage, M-THGEM voltage, currents, discharge voltages, gas pressure, incident particle rate, etc. Valuable information as the gas gain and the ion backflow were extracted. Since the characterization

tests of the prototype are specific topics of this Thesis, they are described in detail in Chapt. 6.

Together with the test activity, the tracker features have been studied and optimized by means of dedicated simulations implemented with Garfield++ toolkit [130]. This code allows to follow the transport of electrons and ions in the gas under the electric field maps built with the finite-elements software COMSOL Multiphysics [131]. Such a simulation was used to compare the detector behavior using different hole patterns of the M-THGEM, evaluating relevant parameters like the electron collection efficiency (i.e. the fraction of primary electrons reaching the M-THGEM holes) and the extraction coefficient (i.e. the fraction of secondary electrons collected at anode). Moreover, the achievable gain and ion backflow using different gas mixtures (such as Ar-CO_2 70%-30%, Ar-CO_2 90%-10%, CF_4) were investigated. The simulation activity is still ongoing to evaluate the detector behavior with others MPGD devices (such as the Multi-Mesh THGEM [132]) and with different hole structures (e.g. with or without the rim).

SiC detectors radiation hardness

For what concerns the SiC detector, the NUMEN project performed a dedicated test to evaluate its radiation hardness capability by irradiating the device with an ^{16}O beam at 25 MeV. The response of the SiC detector was compared to the one of a Si device in terms of energy resolution and charge collection efficiency at increasing values of ion fluence. As a result, the Si detector started to deteriorate at 10^9 ions/cm^2 and was completely broken after 10^{10} ions/cm^2. Instead, the SiC detector only showed a reduction of the charge collection efficiency down to the 20% after 10^{13} ions/cm^2. After a one-day annealing at room temperature, it was restored up to the 45%. Regarding the energy resolution of the SiC detector, the initial value of 0.3 MeV FWHM worsened to 0.7 MeV after the irradiation with 10^{13} ions/cm^2, but after the annealing procedure it was almost completely restored.

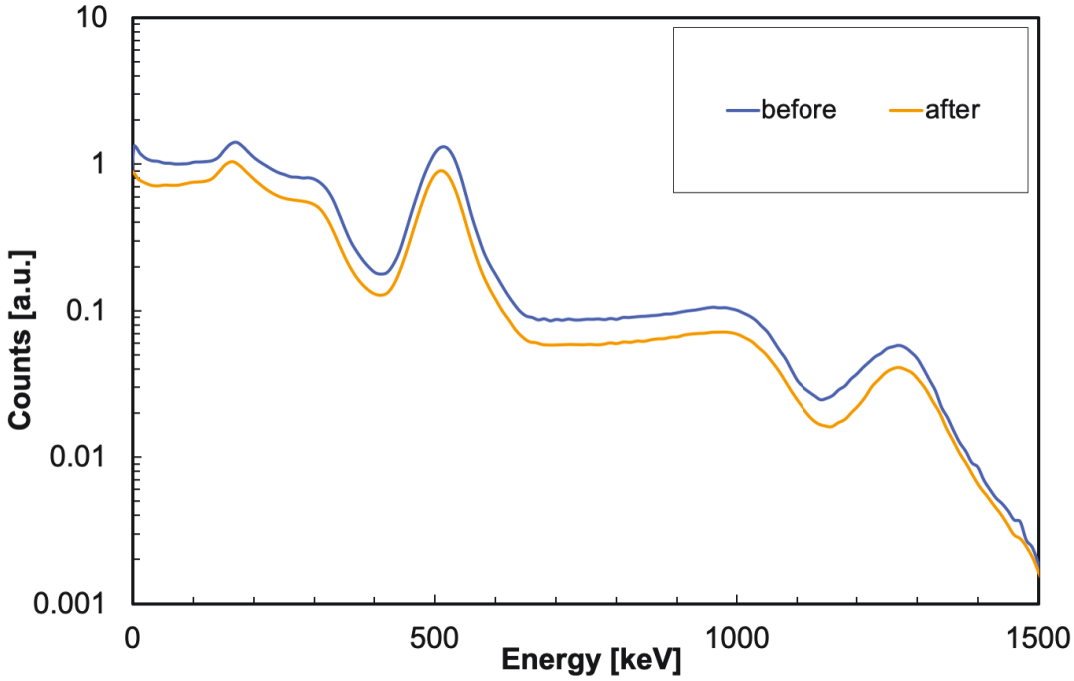

Figure 4.9: Energy spectrum measured with a CsI(Tl) scintillator before (blue) and after (orange) a dose equivalent to several years of NUMEN experiments.

CsI(Tl) detectors radiation hardness

The radiation robustness of the CsI(Tl) was investigated in a specific test, where a 1 ± 1 cm^2 crystal was irradiated with a ^{14}N beam at 62.5 AMeV. An energy spectrum was measured with a beam intensity of 10^4 pps; then, the crystal was irradiated with $\rightarrow 10^{12}$ ions; finally, the same energy spectrum was produced reducing the beam intensity again to 10^4 pps. The comparison between the energy spectra before and after the irradiaton is shown in Fig. 4.9, where it is evident that neither centroids drift nor resolution loss were observed. This means that the CsI(Tl) scintillators of the PID wall should perfectly work for several years of NUMEN experiments.

PID performances of the SiC-CsI(Tl) telescope

The identification capabilities of the SiC-CsI(Tl) telescope were tested in realistic conditions by using an ^{18}O beam at 15.4 AMeV impinging on a ^{76}Se target. The telescope was placed inside the MAGNEX scattering chamber (see Sect. 2.1) and located 20 cm downstream the target at an angle of 15° with respect to the beam direction. In Fig. 4.10, the obtained ΔE E_{resid} correlation plot is shown, where the E_{resid} observable is expressed in terms of the light output of the scintillator. The nine atomic species between Be and Mg were detected, thus exploring the whole region of interest for the NUMEN experiments. The corresponding experimental loci are clearly separated, giving an atomic number resolution ΔZ of $\rightarrow$0.16 FWHM. It should be pointed out that the light output of the CsI(Tl) scintillator is proportional to the deposited energy, but it depends on Z and A; therefore, a calibration is needed to obtain the correct energy scaling between the detected ions.

Tracker and PID: selection of the reaction channel of interest

The test just described allowed to get precious information about the atomic number identification capability of the SiC-CsI(Tl) telescopes, but for the NUMEN purposes also the discrimination performance in terms of mass number A has to be investigated. Thus, a specific test in which a SiC-CsI(Tl) telescope was coupled with MAGNEX was performed. Indeed, as described in Subsect. 3.1.2, the mass identification technique used in MAGNEX exploits the properties of the Lorentz force: according to Eq. 3.8, by correlating the horizontal coordinate at the focal plane (x_{foc}) with E_{resid}, a separation of the ejectiles according to their mass-to-charge ratio ($\overline{m}/q$) can be obtained. The test was performed with a ^{20}Ne beam at 20 AMeV directed onto a thin ^{12}C target. The MAGNEX optical axis was set a 10° with respect to the beam direction. A SiC-CsI(Tl) telescope was placed at the silicon stopping wall (see Subsect. 2.3.2), in a position similar to the one that will be occupied in the PID wall. The telescope was used to obtain the ΔE E_{resid} matrix, while the x_{foc} measurement was performed by the present gas tracker. The obtained ΔE E_{resid} correlation plot is shown in Fig. 4.11.a, where the loci of the detected ions appear well separated. The spectrum

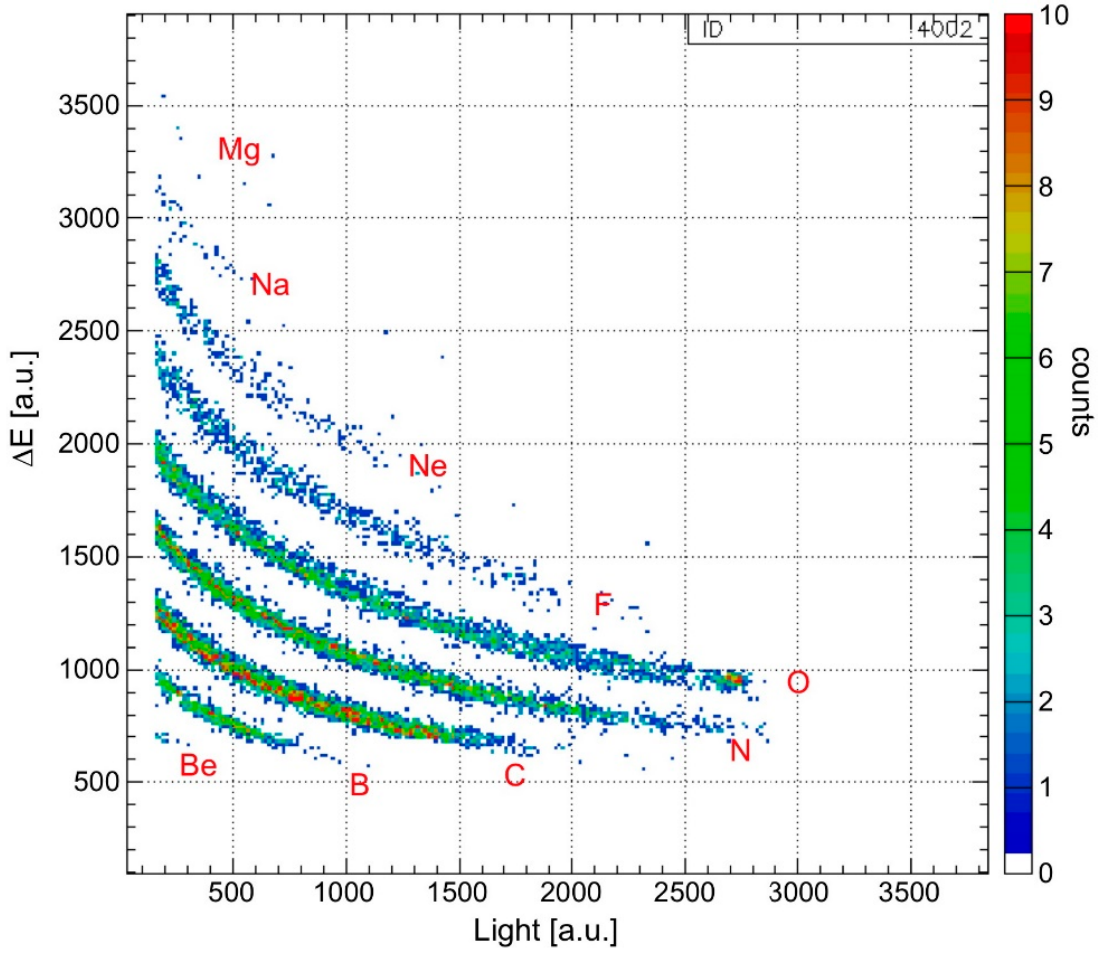

Figure 4.10: ΔE E_{resid} correlation plot measured with a SiC-CsI(Tl) telescope placed in the MAGNEX scattering chamber. Figure from Ref. [109].

was linearized and projected onto the ΔE axis, giving the distribution of the ejectiles as a function of their atomic number Z reported in Fig. 4.11.b. The atomic number distribution shows a $\Delta Z/Z$ of $\rightarrow 4.1\%$ FWHM for the ensemble of the detected oxygen ejectiles. After selecting the oxygen ions on the $\Delta E \quad E_{resid}$ plot with a graphical cut, the $x_{foc} \quad E_{resid}$ correlation plot was produced for only the selected ions. The resulting spectrum, reported in Fig. 4.12.a, shows the presence of three oxygen isotopes, i.e. $^{16}O^{8+}$, $^{17}O^{8+}$, and $^{18}O^{8+}$. Another linearization and projection procedure was performed to obtain the distribution of oxygen ions as a function of their mass number A, that is shown in Fig. 4.12.b. The resulting mass number resolution $\Delta A/A$ is of $\rightarrow 2.1\%$ FWHM, which, together with the obtained $\Delta Z/Z$ resolution, is sufficient to clearly identify the ejectiles of interest for the NUMEN project.

A specific simulation of the PID wall has been implemented and developed using the Geant4 toolkit. Since such a simulation is one of the main topics of my PhD activity, it is thoroughly discussed in Chapt. 5.

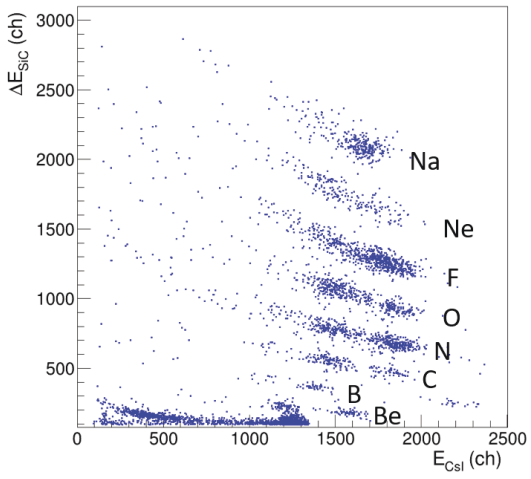

(a)

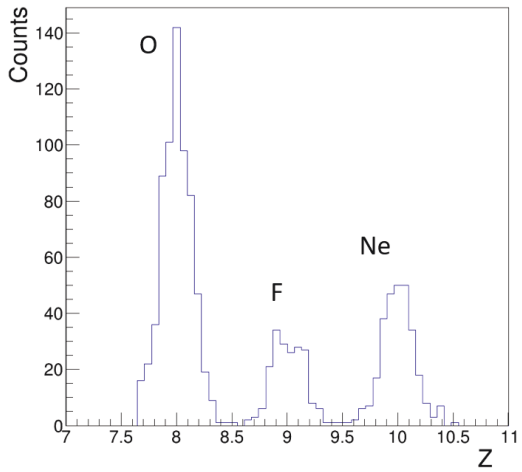

(b)

Figure 4.11: (a) The ΔE E_{resid} correlation plot measured with the SiC-CsI(Tl) telescope placed in the silicon stopping wall. (b) Distribution of the ejectiles close to oxygen as a function of their atomic number Z. Figure from Ref. [109].

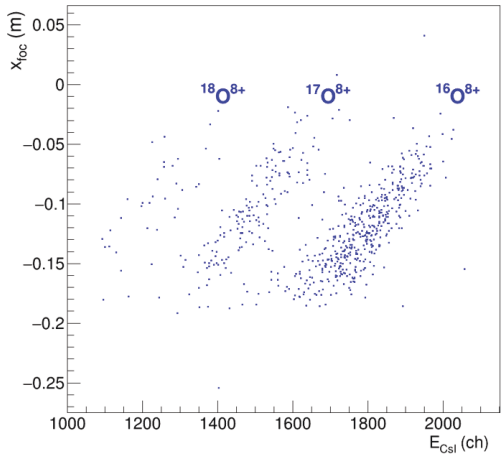

(a)

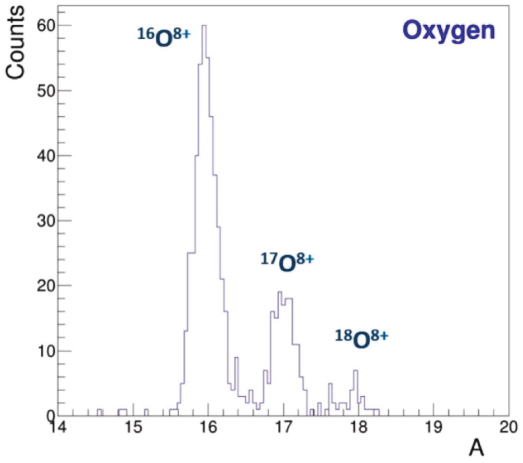

(b)

Figure 4.12: (a) The x_{foc} E_{resid} correlation plot for oxygen ions selected in the plot in Fig. 4.11.a. (b) Distribution of oxygen ejectiles as a function of their mass number A. Figure from Ref. [109].

Chapter References

[4] F. Cappuzzello et al. "The NUMEN Technical Design Report". In: *International Journal of Modern Physics A* 36 (2021), p. 2130018. DOI: 10.1142/S0217751X21300180.

[49] C. Agodi and et al. In: *Universe* 7 (2021), p. 72. DOI: 10.3390/universe7030072.

[56] M. Cavallaro et al. "The low-pressure focal plane detector of the MAGNEX spectrometer". In: *The European Physical Journal A* 48.5 (May 2012), p. 59. ISSN: 1434-601X. DOI: 10.1140/epja/i2012-12059-8.

[57] D. Torresi et al. "An upgraded focal plane detector for the MAGNEX spectrometer". In: *Nuclear Instruments and Methods in Physics Research Section A: Accelerators, Spectrometers, Detectors and Associated Equipment* 989 (2021), p. 164918. ISSN: 0168-9002. DOI: https://doi.org/10.1016/j.nima.2020.164918.

[74] G. F. Knoll. *Radiation Detection and Measurement, 3rd ed.* 3rd edition. New York: John Wiley and Sons, 2000. ISBN: 978-0-471-07338-3.

[109] P. Finocchiaro et al. "The NUMEN Heavy Ion Multidetector for a Complementary Approach to the Neutrinoless Double Beta Decay". In: *Universe* 6.9 (2020). ISSN: 2218-1997. DOI: 10.3390/universe6090129.

[110] M. Cortesi et al. "Multi-layer thick gas electron multiplier (M-THGEM): A new MPGD structure for high-gain operation at low-pressure". In: *Rev. Sci. Instrum.* 88 (2017), p. 013303. DOI: https://doi.org/10.1063/1.4974333.

[111] F. Cappuzzello et al. “The NUMEN Project: An Update of the Facility Toward the Future Experimental Campaigns”. In: *Front. Astron. Space Sci.* 8 (2021), p. 668587. DOI: https://doi.org/10.3389/fspas.2021.668587.

[112] F. Sauli and A. Sharma. “MICROPATTERN GASEOUS DETECTORS”. In: *Annual Review of Nuclear and Particle Science* 49.1 (1999), pp. 341–388. DOI: 10.1146/annurev.nucl.49.1.341.

[113] R. Chechik et al. “Thick GEM-like hole multipliers: properties and possible applications”. In: *Nucl. Instrum. Meth. A* 535 (2004), pp. 303–308. DOI: https://doi.org/10.1016/j.nima.2004.07.138.

[114] A. Breskin et al. “A concise review on thgem detectors”. In: *Nucl. Instrum. Meth. A* 598 (2009), pp. 107–111. DOI: https://doi.org/10.1016/j.nima.2008.08.062.

[115] F. Sauli. “The gas electron multiplier (gem): Operating principles and applications”. In: *Nucl. Instrum. Meth. A* 805 (2016), pp. 2–24. DOI: https://doi.org/10.1016/j.nima.2015.07.060.

[116] C. Shalem et al. “Advances in thick gemlike gaseous electron multipliers part II: Low-pressure operation”. In: *Nucl. Instrum. Meth. A* 558 (2006), pp. 468–474. DOI: https://doi.org/10.1016/j.nima.2005.12.219.

[117] Y. Ayyad et al. “CO2 operation of an active target detector readout based on THGEM”. In: *J. Instrum.* 12 (2017), p. 06003. DOI: https://doi.org/10.1088/1748-0221/12/06/P06003.

[118] M. Cortesi et al. “Development of a novel MPGD-based drift chamber for the NSCL/FRIB S800 spectrometer”. In: *J. Instrum.* 15 (2020), p. 03025. DOI: 10.1088/1748-0221/15/03/p03025.

[119] J. Pouthas et al. “INDRA, a 4-pi charged product detection array at GANIL”. In: *Nuclear Instruments and Methods in Physics Research Section A: Accelerators, Spectrometers, Detectors and Associated Equipment* 357.2 (1995), pp. 418–442. ISSN: 0168-9002. DOI: https://doi.org/10.1016/0168-9002(94)01543-0.

[120] S. Aiello et al. “The Chimera Facility at LNS”. In: *AIP Conference Proceedings* 495.1 (1999), pp. 353–354. DOI: 10.1063/1.1301817.

[121] R. Bougault and et. al. “The FAZIA project in Europe: R&D phase”. In: *The European Physical Journal A* 50.47 (2). DOI: 10.1140/epja/i2014-14047-4.

[122] Hamamatsu Products. https://www.hamamatsu.com/eu/en/product/type/S3590-08/. 2022.

[123] S. Tudisco et al. “SiCILIA—Silicon Carbide Detectors for Intense Luminosity Investigations and Applications”. In: *Sensors* 18.7 (2018), p. 2289. DOI: 10.3390/s18072289.

[124] S. Tudisco et al. “” In: *(in preparation)* ().

[125] A. Muoio et al. “Silicon carbide detectors study for NUMEN project”. In: *EPJ Web of Conferences* 117 (2016), p. 10006. DOI: 10.1051/epjconf/201611710006.

[126] A. Pappalardo et al. “An imaging technique for detection and absolute calibration of scintillation light”. In: *Review of Scientific Instruments* 81 (2010), p. 033308. DOI: 10.1063/1.3360931.

[127] A. Pappalardo et al. “Erratum: An imaging technique for detection and absolute calibration of scintillation light”. In: *Review of Scientific Instruments* 82 (2011), p. 049903. DOI: 10.1063/1.3579512.

[128] D.M. Beylin et al. “Study of the radiation hardness of CsI(Tl) scintillation crystals”. In: *Nuclear Instruments and Methods in Physics Research Section A: Accelerators, Spectrometers, Detectors and Associated Equipment* 541.3 (2005), pp. 501–515. ISSN: 0168-9002. DOI: https://doi.org/10.1016/j.nima.2004.11.023.

[129] M. Kobayashi and S. Sakuragi. “Radiation damage of CsI(Tl) crystals above 103 rad”. In: *Nuclear Instruments and Methods in Physics Research Section A: Accelerators, Spectrometers, Detectors and Associated Equipment* 254.2 (1987), pp. 275–280. ISSN: 0168-9002. DOI: https://doi.org/10.1016/0168-9002(87)90675-9.

[130] H. Schindler. *Garfield++*. https://garfieldpp.web.cern.ch/garfieldpp/. 2022.

[131] COMSOL Multiphysics. *COMSOL AB, Stockholm, Sweden, v. 5.4*. https://www.comsol.it. 2018.

[132] R. de Olivera and M. Cortesi. "First performance evaluation of a Multi-layer Thick Gaseous Electron Multiplier with in-built electrode meshes—MM-THGEM". In: *J. Instrum.* 13 (2018), p. 06019. DOI: 10.1088/1748-0221/13/06/p06019.

5

The simulation tool of the future Focal Plane Detector

Contents

5.1 The Geant4 toolkit **123**
5.1.1 Geant4 structure 123
5.2 Main aspects of the FPD simulation tool **124**
5.2.1 The first part of the simulation tool: COSY INFINITY 125
5.2.2 The second part of the simulation tool: the Geant4 application 127
5.3 Results **134**
5.3.1 The elastic scattering of ^{20}Ne as examplifying case . . 135
5.3.2 Study of the towers rotation angle 137
5.3.3 Proposal of a particle identification strategy 137
5.3.4 Ionization processes in the gas tracker 142

In the modern physics experiments, numerical simulations play a role of ever-increasing importance; in particular, the use of Monte Carlo techniques [133] allows to tackle complex problems otherwise difficult to solve. Indeed, thanks to the

outstanding development of computer and simulation softwares, today it is possible to develop large-scale, accurate and comprehensive Monte Carlo simulations of detectors and particle interactions in matter.

One of the main results of this work is the implementation and development of a simulation tool, based on Monte Carlo methods, of the future Focal Plane Detector (FPD) of the MAGNEX magnetic spectrometer (see Chapt. 4). In the previous version of such a tool, it was possible to simulate only one silicon carbide-cesium iodide (SiC-CsI) telescope detector. The new version, developed for this Thesis, provides an accurate representation of the future FPD, including both the gas tracker and the full wall of SiC-CsI telescopes, as well as passive volumes, such as the Mylar window and the mechanical supports. The main goal of the simulation tool is to give a reliable prediction of the FPD response to the events of interest for the NUMEN project. This tool was used in the design phase to optimize the layout and the arrangement of the detectors, allowing to establish the best geometrical configuration of the experimental apparatus. For example, in this Thesis the rotation angle of the towers constituting the wall of telescopes was studied and optimized. Moreover, as will be shown in the following, the tool permits to evaluate the Particle IDentification (PID) performance of the full detection system. This is of high relevance for NUMEN, since the meauserement of double charge exchange reactions imposes stringent requirements on the PID capabilities (see Sect. 4.2). A detailed characterization of the main sources of contamination to the events of interest will be performed, thus allowing to evaluate the sensitivity of the future FPD. The simulation tool will be also used to calculate the efficiency of the experimental apparatus, which is a fundamental information to determine absolute cross-sections. In the operative phase of the future FPD, the Monte Carlo simulations will support the data analysis and provide valuable information to the interpretion of the experimental data. For all these reasons, the development of the simulation tool is a key aspect for the future FPD.

In this chapter, the simulation tool of the future MAGNEX FPD is described. As it will be shown, it is composed by two interconnected parts: one is based on the COSY INFINITY software [60], the other is a specific Geant4 [134–136] application. Thus, a brief introduction to the Geant4 toolkit is given. Then, the main results obtained with the such a tool are presented; in particular, the study

about the optimization of the towers rotation angle and a proposal of a particle identification strategy are discussed.

5.1 The Geant4 toolkit

The simulation software Geant4 (GEometry ANd Tracking) [134–136] was born in 1974 at CERN in Geneva to simulate the interaction of high energy elementary particles with detectors. In the first version, it was possible to simulate only simple geometrical shape and a limited number of particles. In 1982 GEANT3 was released, which was based on the FORTRAN language. It was strongly superior than its predecessor; indeed, it allowed to simulate experiments of increasing size and complexity, as well as the transport of high energy beams. However, the code had a very complex structure, hard to understand and manage for external users. In 1998, thanks to the collaboration of more than 40 international institutes, a new project was released, called Geant4. It is entirely based on C++, thus taking advantage of all the potentialities offered by an object-oriented language, such as modularity and compactness. The code is open-source and twice per year an updated version is released.

Today, Geant4 allows to simulate the interaction of all the known particles with matter, in a wide energy range spanning from eV to TeV. Thanks to its flexibility, a large number of experiments takes advantage of this software, encompassing high-energy physics, nuclear physics, medical physics and astrophysics.

Since the documentation about Geant4 is ample and detailed*, in the following only the aspects useful to the understanding of the simulation tool here presented are described.

5.1.1 Geant4 structure

The Geant4 toolkit consists of a collection of C++ libraries that must be included by the user to write his specific application. Geant4 is based on *classes*, that can be developed independently one from another, giving a modular structure to the software. The classes are conceived to be easily customized and extended, following the philosophy typical of the object-oriented paradigm. Indeed, thanks to

*See, for example, www.geant4.org.

an approach based on *polymorphism* and *inheritance* the user is allowed to create classes derived from other classes and to provide an alternative implementation of the functions contained in a class, respectively. In Geant4 there is a large number of classes, each one corresponding to a different aspect of a typical physics experiment (e.g. the detector geometry, the source features, etc.) Three classes have to be implemented and instantiated mandatorily:

- the class dedicated to the definition of geometry and materials of the experimental setup;
- the class devoted to the primary particle generation;
- the class dedicated to the definition of particles, physics processes and cut-off for the production of secondary particles.

The implementation of other classes is not mandatory and can be carried out according to the specific requirements of the user. It is worthwhile to remark that in the Monte Carlo codes the propagation of particles is performed in steps of finite length. There are Geant4 classes that allow to manage the simulation at various stages; for example, at the beginning and/or at the end of processing the track of a particle, etc. For the application described in this Thesis, it was particularly important to implement the *user hook* (called `G4UserSteppingAction`) that allows to retrieve the information at the end of each step of the particle track. Such information are contained in the `G4Step` class. For this work, the relevant information were the position and the energy deposit at every step. As will be discussed in the following, this aspect was very important to describe the edge effects of the detectors.

5.2 Main aspects of the FPD simulation tool

The simulation tool discussed in this Thesis describes the interaction of the ions relevant for the NUMEN project with the future FPD designed for the upgrade of the MAGNEX magnetic spectrometer. As explained in Chapt. 4, the new FPD will consist of a gas tracker and a wall of telescopes based on thin silicon carbide (SiC) detectors and cesium iodide (CsI) scintillators. A fundamental aspect of

the simulation tool is that it is composed by two parts that operate in an interconnected way. The first part accounts for the transport of the ions through the magnetic elements of MAGNEX. This task is carried out by the COSY INFINITY software, which is capable to simulate the trajectory of each ion, as explained in Chapt. 2. The second part, that is dedicated to the simulation of the interaction of the particles with the gas tracker and the wall of SiC-CsI telescopes, is accomplished by a specific Geant4 application.

5.2.1 The first part of the simulation tool: COSY INFINITY

In order to have a reliable simulation of the response of the future FPD, it is crucial to take into account the optical transport of the ions since MAGNEX introduces a correlation between the kinetic energy and the horizontal position at the focal plane of the particles. Indeed, in a magnetic spectrometer ions travel along different trajectories according to their magnetic rigidity $B\rho$. To first order in the transport operator, ions with the same magnetic rigidity reach the same position on the focal plane, while ions with different magnetic rigidity arrive in different positions. A pictorial representation of this situation is reported in Fig. 5.1, where a GEANT simulation of different trajectories accepted by MAGNEX is shown. To the first order of approximation, the correlation between the kinetic energy and the horizontal position at the focal plane is given by Eq. 3.8. Moreover, the reaction kinematics implies a further correlation between the kinetic energy and the scattering angle of the ejectile. Both these correlations are characterized by non-linear effects, particularly important for MAGNEX because of its large acceptance in solid angle (→50 msr) and momentum (+10%, 14%). Since it is hard to implement such distortions directly in the Geant4 application, we decided to exploit the COSY INFINITY program [60], that is already developed and optimised for this aim. The input parameter of COSY INFINITY, relevant for the undestanding of the simulation tool, are:

- beam energy;
- projectile, target, ejectile and residual nuclues;
- excitation energy of ejectile and/or residual nucleus;

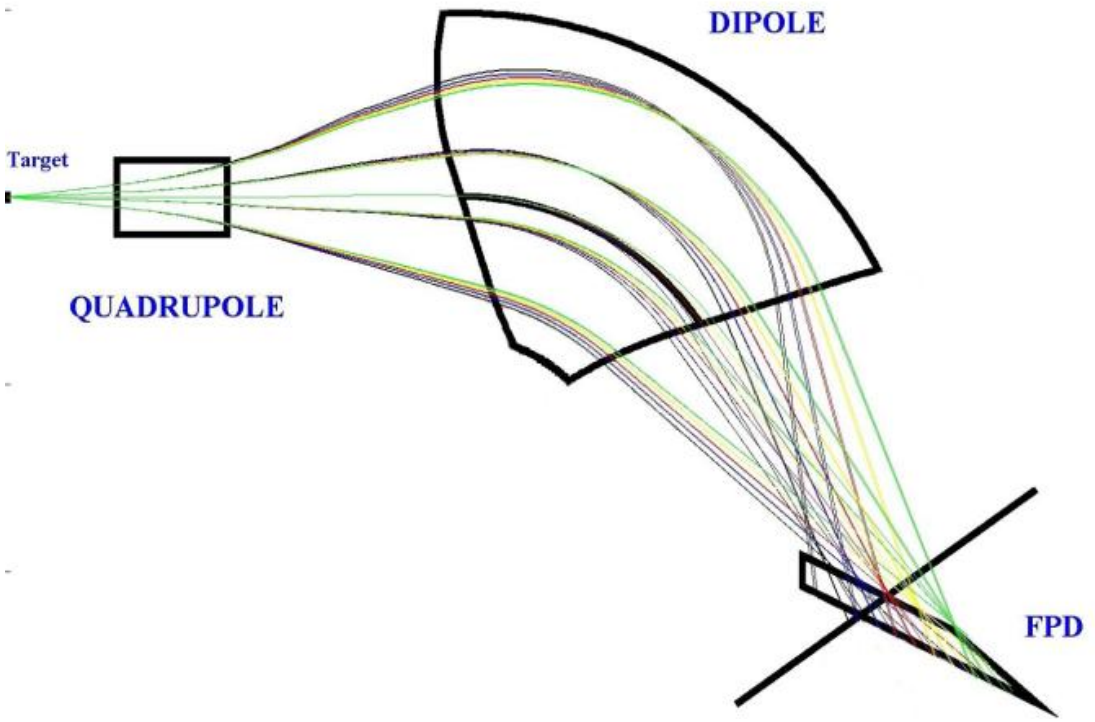

Figure 5.1: GEANT simulation of the MAGNEX magnetic spectrometer: trajectories with different colors correspond to different kinetic energies. Figure from Ref. [3].

- reference magnetic rigidity;
- angle of the spectrometer optical axis.

Given such parameters, the COSY INFINITY algorithms calculate the reaction kinematics and the initial phase space. Then, they determine the high-order transport matrix and reconstruct the ejectile trajectories up to the focal plane. The software produces an output file containing the values of several relevant observables of the ejectile at the MAGNEX focal plane, e.g. the kinetic energy E, the horizontal and vertical coordinates (x_{foc}, y_{foc}) and the horizontal and vertical angles (θ_{foc}, ϕ_{foc}) of its track. The interconnection between COSY INFINITY and the Geant4 application consists in the fact that the latter takes as input the output of the former for the event generation. In other words, the initial kinetic energy, position and direction of each primary particle are directly derived from COSY INFINITY.

For this Thesis, the collision of a ^{20}Ne beam onto a ^{76}Ge target was considered, except when explicitly mentioned. The reason of this choice is that the ^{20}Ne + ^{76}Ge system is one of major interest for NUMEN. Indeed, it has been already investigated in a dedicated experiment at 306 MeV bombarding energy during the Phase 2 of the project [37]. The incident energy chosen for this work is 700 MeV, which represents an intermediate value between the minimum and the maximum beam energy available after the upgrade of the superconducting cyclotron at the Laboratori Nazionali del Sud. Excitation energy ranging up to 70 MeV with a uniform distribution were simulated, thus spanning a wide portion of the FPD. The reference magnetic rigidity of MAGNEX was set to 2 Tm. The spectrometer optical axis was fixed at an angle of 3°, according to the value typically adopted in the MAGNEX setup to perform the measurement of double charge exchange reactions.

5.2.2 The second part of the simulation tool: the Geant4 application

This subsection is devoted to the description of the Geant4 application specifically developed for the simulation of the future FPD of the MAGNEX spectrometer. For the sake of clarity, it is organized in paragraphs that focus on the key features

of the application. The Geant4 version used for this work is the 11.0, released in December 2021.

Geometry and material of the experimental apparatus

The experimental apparatus described in the Geant4 application consists of two main parts: the gas tracker and the wall of SiC-CsI telescopes. A snapshot of the FPD simulation is illustrated in Fig. 5.2.a. The gas tracker is a parallelepiped of 1200 $\pm$ 107 $\pm$ 150 mm^3, according to the dimensions of the future detector (see Sect. 4.1). The entrance face of the tracker is placed 1.9 cm downstream the MAGNEX focal plane, where the primary particles are generated.

The SiC-CsI wall is composed by 36 modules (called *towers*), each one constituted by 20 telescopes. Each telescope includes three elements:

- the SiC active volume, which accounts for the sensitive region of the detector. It has a surface of 15.4 $\pm$ 15.4 mm^2 and a thickness of 100 μm.
- the SiC dead substrate, that represents the inert layer of the detector. Its surface has the same extension as the one of the SiC active volume, but its thickness is of 10 μm.
- the CsI crystal, which has dimensions of 15 $\pm$ 15 $\pm$ 5 mm^3.

A sketch of a telescope is reported in Fig. 5.2.b. Each CsI crystal is embedded in a epoxy resin (EPOTEK 301-1) matrix which covers only the lateral surfaces of the scintillator, leaving opened its entrance and exit faces, as shown in Fig. 5.2.c. A 0.5 mm thick copper grid is placed between the SiC detectors and the CsI crystals. It constitutes the mechanical support where the SiC devices will be mounted.

Each tower of the PID wall is rotated around the vertical direction of an angle θ_{tilt}, which was one of the parameter studied for this work. Since it is essential to have no dead space along the dispersive (horizontal) direction, the distance d between two adjacent towers was chosen in order to have an overlap of 2 mm. The SiC-CsI wall is located at a minimum distance of 15 mm with respect to the exit face of the gas tracker. The Geant4 application includes the Mylar window which in the real apparatus separates the high-vacuum region from the vacuum

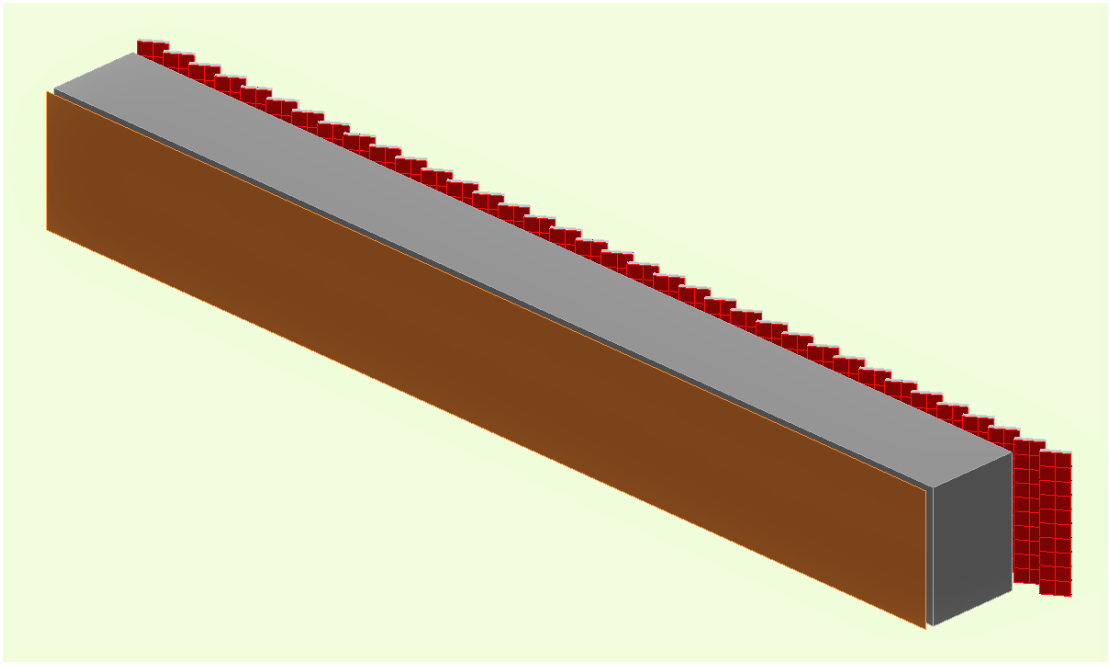

(a)

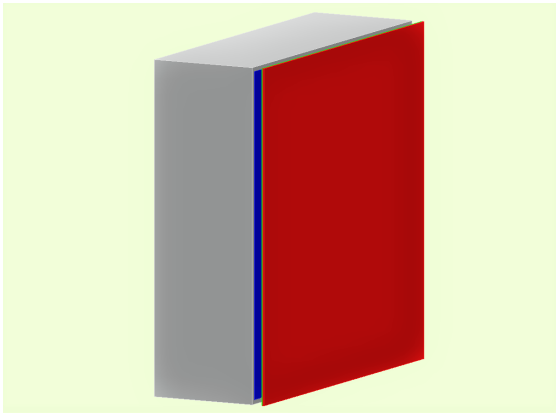

(b)

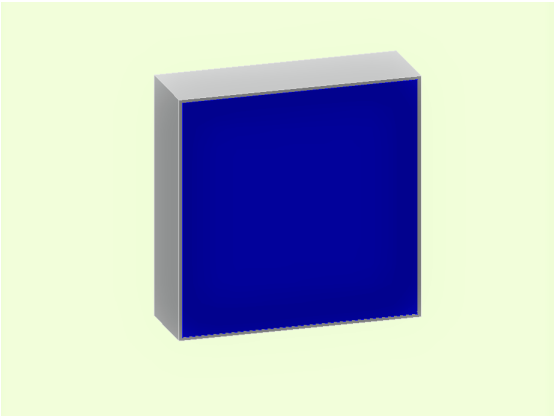

(c)

Figure 5.2: Snapshots from the Geant4 application. (a) The Focal Plane Detector: the Mylar window (orange), the gas tracker (grey) and the SiC-CsI wall are shown. (b) A telescope detector: the SiC active volume (red), the CsI crystal (blue) and the epoxy resin (light grey) are visible. The SiC dead substrate (green) behind the SiC active volume is barely distinguishable. (c) Details of the CsI scintillator: the CsI crystal (blue) is embedded in the epoxy resin (light grey).

chamber (see Chapt. 4). It has an area of 1200 ± 150 mm^2 and a thickness of 2.5 μm. The whole simulated region downstream the Mylar window is filled with isobutane (iC_4H_{10}) at a pressure of 30 mbar, that is a typical value adopted for the NUMEN experiments.

Generation of primary particles

In a Geant4 simulation the parameters that typically must be defined to generate an event are the type, the initial kinetic energy, the initial position, and the initial direction of the primary particle. As explained in Subsect. 5.2.1, for the application here described such parameters are taken from the output file of the COSY INFINITY software. The primary particles are generated at the focal plane of MAGNEX, which is located 1 cm upstream the Mylar window. The simulated ejectiles are isotopes of O, F, Ne, which are the ions of interest for NUMEN.

Physics processes

In order to get a realistic response of the detectors, it is crucial to choose appropriately the physics processes to be included in the simulation. The Geant4 toolkit provides several *physics lists*, each one adopting different physics processes and models, but it gives also the possibility to the user to construct his own physics list. For the studies described in this Thesis, the `Shielding` list was chosen, which is offered by Geant4. It accounts for the electromagnetic and hadronic interactions, as well as the decay of excited nuclei and the radioactive decay. The electromagnetic interaction is the most important one in the ion-detector interaction at the energies of interest for NUMEN; indeed, it is the foundation of the PID techniques based on the energy loss of the ions in the detector matter. The hadronic interactions allow to simulate elastic and inelastic scattering process and nuclear reactions.

One of the fundamental choice of the Geant4 simulations are cut-off parameters; indeed, it is possible to define a range production cut: ionization electrons and bremsstrahlung gammas which have a range below the threshold are not explicitely generated, but their energy is considered as a local energy deposit. If the default value of the range (1 mm) is maintened, a large number of electrons is

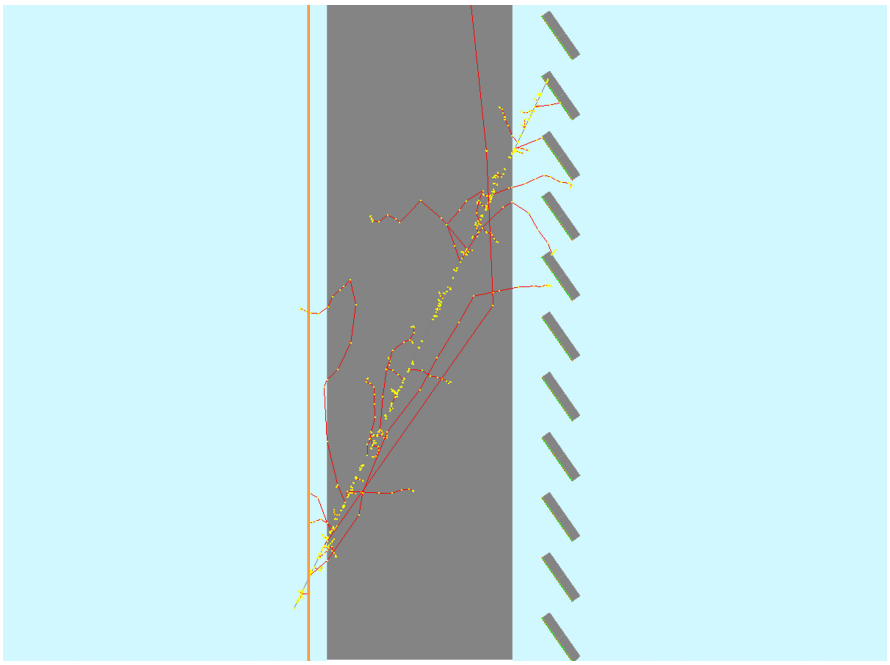

Figure 5.3: Simulation of a ^{20}Ne ion at 700 MeV kinetic energy crossing the Mylar window (orange) and the gas tracker (grey) and stopping in a telescope. The ion track is clearly recognizable. The yellow points represent the enery releases in the gas, while the red lines are the trajectories of primary electrons with energies above the production threshold.

produced in the isobutane, as can be seen in Fig. 5.3. Such electrons are usually referred to as δ-rays. Some of these electrons can have energy of the order of keV, thus producing further ionization in the gas. Since the detailed simulation of the electromagnetic showers is not necessary to evaluate the PID performance of the future FPD, a large cut-off threshold (1 km) was set to save computing resources. However, as will be shown in Subsect. 5.3.4, the information about the production position of the secondary electrons can be useful for the softwares that simulates the signal formation of the gas tracker (see Sect. 4.3). Therefore, for some specific simulations the default value of the range was used.

The Geant4 output

As anticipated in Sect. 5.1.1, a custom user class derived from the Geant4 interface `G4UserSteppingAction` was defined in order to retrieve and store the position and

the energy deposit of the ion at every step. All the energy deposits are recorded, either in a detector (tracker, SiC active volume, CsI crystal) or in a insensitive volume (SiC dead substrate, Mylar window, resin, etc.). The Geant4 output includes an identification number that unambiguosly determines the volume where the energy deposit occurred. This information is written in the output file of the Geant4 application, that is a ROOT [137] file containing a TTree. In such a file, also the parameters read from the output file of COSY INFINITY and used to generate the primary particles are stored.

Post-processing of the Geant4 output

The output of the Geant4 application is processed with a dedicated ROOT macro, developed for this work, that allows to account for the edge effect of the SiC detectors; indeed, because of the production process, such detectors present an outer edge totally insensitive and an intermediate region partially active. In the former the charge generated by the primary particle is not collected at all, in the latter it is partially collected. Both the totally inert and the partially active regions have a width of about 100 μm. In the ROOT macro, the edge effect are introduced by weighting each energy deposit with a response function defined in the following way:

- in the active region it is equal to 1;
- in the partially active zone it linearly decreases from 1 to 0;
- in the totally insensitive edge it is equal to 0.

For this reason, it is fundamental to store at every step the coordinate of each energy release.

Moreover, since the output of the Monte Carlo simulation consists in the position/deposit of the individual energy releases by charged particles, the macro reconstructs the total energy release in each simulated volume and, in particular, in the gas tracker, in the SiC detector and in the CsI crystal. It is worth to note that the Geant4 simulation accounts only for the intrinsic statistical fluctuations in the process of energy loss of the incident ion in matter. Then, in order to reproduce the energy resolution typical of the detectors, the energy loss is smeared

by sampling each energy deposit with a gaussian distribution g, whose expression is given by

$$g(E, E_0, \sigma) = \frac{1}{\sqrt{2\pi\sigma^2}} \exp\left[\frac{(E \quad E_0)^2}{2\sigma^2} \right] \tag{5.1}$$

where E_0 is the original value of the energy deposit, E is the energy value after the sampling and σ is the standard deviation. Given the mean value E_0, the σ must be determined in such a way that the energy resolution obtained from the simulation is comparable with the experimental one. The energy resolution is typically expressed as the quadratic sum of a term corresponding to the statistical fluctuations of the number of the charge carriers (proportional to $E^{-1/2}$) and a term due to electronic noise (proportional to E^{-1}) [74]. Since the σ can be related to the energy resolution R through the formula

$$R = \frac{\text{FWHM}}{E} = \frac{2.35\,\sigma}{E} \tag{5.2}$$

where FWHM is the full width at half maximum of the distribution, in the ROOT macro it has been parameterized in the following way

$$\sigma = \sqrt{a + b\,E} \tag{5.3}$$

where a and b are constants. In the square root in 5.3, the first term accounts for the electronic noise, while the second one represents the statistical fluctuations of the number of charge carriers or scintillation photons, respectively for the SiC detector and the CsI scintillator. For the SiC detector, the a and b parameters were obtained by fitting the energy resolution values reported in literature for α-particles at 5.486 MeV and for ^{16}O ions at 26 MeV, respectively equal to 0.8% and 1.2% FWHM [123, 124]. In this way, an energy resolution of about 1.2% FWHM for ^{20}O at 25 MeV was obtained. A similar procedure was applied to the CsI scintillator, determining an energy resolution of about 2% FWHM for ^{20}O at 650 MeV [138].

It is important to remark that the Geant4 application developed for this work gives as output the energy deposit and not the light output. Therefore, in order to have a realistic simulation of the CsI response, a specific algorithm in the macro

converts the energy deposited (E_{CsI}) in the crystal into light output (L). It is well known that for scintillators the relation between the energy deposited by the incident ion and the light output is non-linear due to quenching effects that reduce the scintillation yield [139]. The quenching depends not only on the energy release (E_{CsI}), but also on the atomic (Z) and mass (A) number of the incident ion. Among the several parameterizations of the scintillator response reported in literature, the one proposed by Horn et al. in Ref. [140] was adopted. The light output is then expressed as

$$L = a_1 \left\{ E_{CsI} \quad a_2 \, A \, Z^2 \ln \left| \frac{E_{CsI} + a_2 \, A \, Z^2}{a_2 \, A \, Z^2} \right| \right\} \tag{5.4}$$

where a_1 and a_2 are constants, equal to 8.145 and 0.326, respectively. The light output was scaled by a factor $N \rightarrow$32000 photons/MeV experimentally determined for α-particles from radioactive source [126, 127]. Then, the number of scintillation photons n_{phot} produced in the crystal is given by the following formula

$$n_{phot} = N \times L(W, Z, A) \tag{5.5}$$

5.3 Results

In this section, the results obtained with the simulation tool implemented and developed for this Thesis are presented. First, the case of the ^{20}Ne + ^{197}Au elastic scattering at 700 MeV incident energy is discussed as an example, in order to describe some features which are common to all the ΔE E correlation plots that will be illustrated. Then, the simulations devoted to the study of two possible rotation angles of the PID wall towers are illustrated. Afterward, a proposal of PID procedure is applied to the simulated data in order to evaluate the overall PID capabilites of the full FPD. As will be shown in Subsect. 5.3.3, such a procedure resembles the one discussed in Subsect. 3.1.2. Finally, the representation of 10 simulated trajectories in the gas tracker is reported.

5.3.1 The elastic scattering of ^{20}Ne as examplifying case

The elastic scattering of a ^{20}Ne beam at 700 MeV incident energy onto a ^{197}Au target was simulated. The towers were rotated with an angle $\theta_{tilt} = 35°$. The resulting ΔE_{SiC}^{corr} E_{CsI} correlation plot observed by a SiC-CsI(Tl) telescope of the PID wall is reported in Fig. 5.4, where it can be noticed that the locus of events corresponding to ^{20}Ne is well defined. The ΔE_{SiC}^{corr} variable represents the energy loss in the SiC detector (ΔE_{SiC}) corrected for the different effective thickness crossed by particles incoming with different angles [3], according to the formula:

$$\Delta E_{SiC}^{corr} = \Delta E_{SiC} \cos(\theta_{foc} \quad \theta_{tilt}) \tag{5.6}$$

where θ_{foc} is the horizontal angle of the incident ion track. Three kinds of degraded events are visible in Fig. 5.4:

- events with E_{CsI} value in agreement with the expected one ($\rightarrow$630 MeV), but with ΔE_{SiC}^{corr} value smaller than the expected one ($\rightarrow$45 MeV). These events are due to incident ions impinging on the partially active region of the SiC detector, thus only a fraction of the energy released is collected;

- events with a $\Delta E_{SiC}^{corr} \rightarrow$45 MeV, but with $E_{CsI} <$ 630 MeV. These events are generated by ions that, due to their incident angle, do not stop in the CsI crystal. Therefore, only a part of the residual energy is deposited in the scintillator;

- events located along the Bethe-Bloch curve. These events are due to ions that cross a detector upstream, losing a part of their initial kinetic energies, and then hit the selected telescope.

The spurious events are one of the main source of background in the PID, because they could pollute the locus of a different ion, thus being assigned to a wrong atomic number Z. This aspect can be critical in the study of rare processes such as the double charge exchange reactions. Moreover, such degraded events constitute a loss of detection efficiency which has to be minimized.

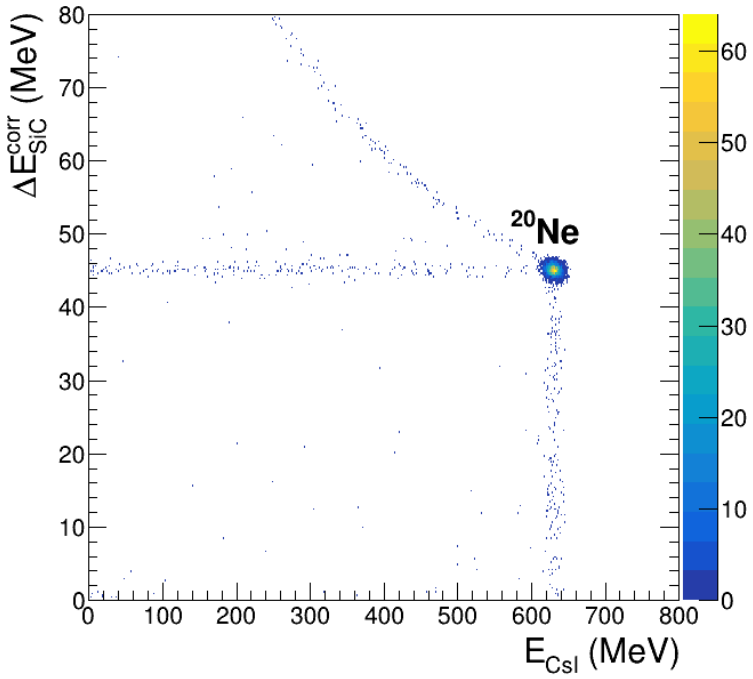

Figure 5.4: A typical ΔE_{SiC}^{corr} E_{CsI} correlation plot for a single SiC-CsI(Tl) telescope. The ^{20}Ne + ^{197}Au elastic scattering at 700 MeV bombarding energy was simulated.

5.3.2 Study of the towers rotation angle

The simulation of the entire PID wall allows to analyze and optimize the mechanical configurations of the towers. For this Thesis, a study of the optimal rotation angle of the towers was conducted by performing two dedicated simulations, where θ_{tilt} was set to 0° and 35°, respectively. For both cases, the collision of a ^{20}Ne beam at 700 MeV incident energy onto a ^{76}Ge target was simulated, as described in Subsect. 5.2.1, where the setup of MAGNEX is reported. The simulated ejectiles are ^{19}O, ^{20}O, ^{21}O, ^{19}F, ^{20}F, and ^{20}Ne, which are some of the ions of interest for NUMEN in the study of the above-mentioned collision. For each ejectile, one million of events were generated. The ΔE_{SiC}^{corr} E_{CsI} plot for $\theta_{tilt} = 0°$ is shown in Fig. 5.5.a, where it is evident that the loci of the different ions are not separated. This is a consequence of the wide range of horizontal angles at the FPD ($40° < \theta_{foc} < 70°$) that the ions can have due to the MAGNEX large angular acceptance (200 mr) and the horizontal magnification (-2.7) [3]; indeed, when $\theta_{tilt} = 0°$ the trajectories at 40° and 70° cross very different thicknesses of the SiC detector, thus losing quite diverse amount of energy.

In Fig. 5.5.b, the ΔE_{SiC}^{corr} E_{CsI} matrix for $\theta_{tilt} = 35°$ is shown. In this case, the separation between ions with different atomic number Z is good. By comparing the Figs. 5.5.a and 5.5.b, it is evident the mechanical arrangement with $\theta_{tilt} = 0°$ is not suitable for the MAGNEX FPD, since it does not allow to perform the identification in atomic number of the ejectiles.

5.3.3 Proposal of a particle identification strategy

The preliminary step in the PID procedure is the calibration of the output signals of the detectors; indeed, before the calibration such signals are expressed in channels. For the aims of the study here described, the quantities that have to be calibrated are the signals corresponding to the energy loss in the SiC detector (ΔE_{SiC}) and to the light output of the CsI scintillator (here expressed in number of scintillation photons n_{phot}). From the experimental point of view, such a calibration can be performed by measuring the elastic scattering of different ion beams. Fixed the kinematics, in the elastic scattering process the kinetic energy of the ejectile is completely determined; therefore, one can calculate the energy

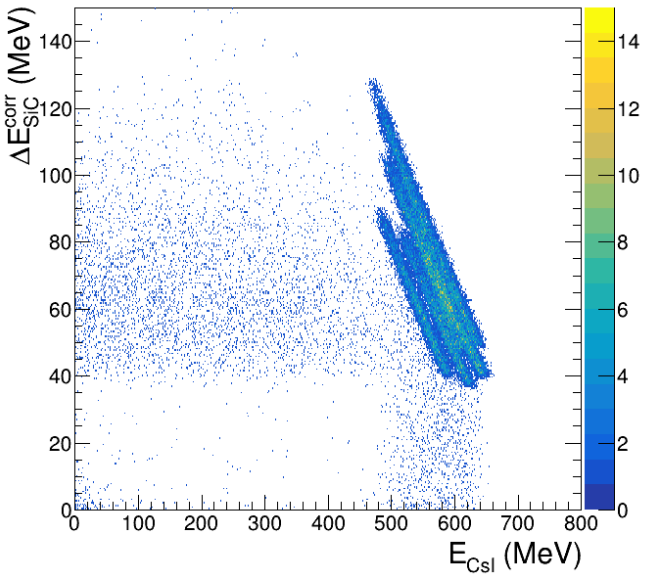

(a)

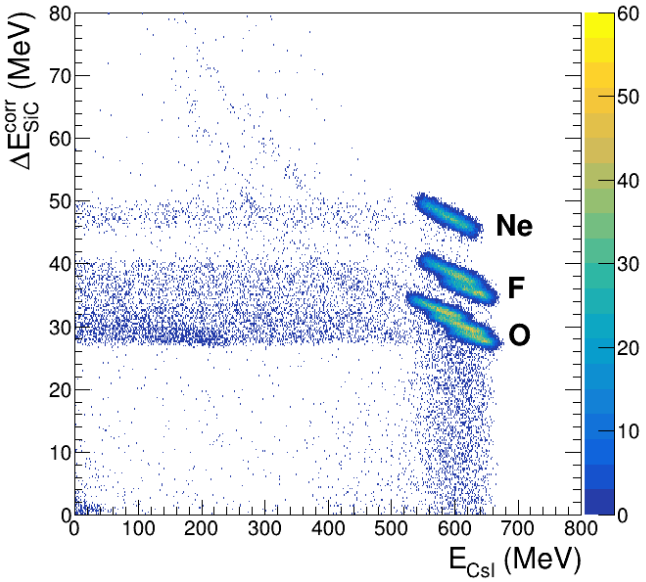

(b)

Figure 5.5: The typical ΔE_{SiC}^{corr} E_{CsI} correlation plots of a single SiC-CsI(Tl) telescope for (a) $\theta_{tilt} = 0°$ and (b) $\theta_{tilt} = 35°$.

release in the SiC detector and the residual deposited in the CsI scintillator by using dedicated softwares (such as LISE++ or SRIM) or Monte Carlo simulations. In this way, a correspondence between ADC channels and energy can be obtained. Since the ions of interest for NUMEN are in the region of O, F and Ne, beams suitable for the calibration procedure are ^{18}O, ^{19}F and ^{20}Ne, which are available at LNS. For this reason, a dedicated simulation was performed considering the elastic scattering of the above-mentioned beams at 700 MeV onto a ^{197}Au target. The resulting ΔE_{SiC}^{corr} n_{phot} correlation plot is reported in Fig. 5.6.a, while in Figs. 5.6.b and 5.6.c the corresponding ΔE_{SiC}^{corr} and n_{phot} spectra are shown, respectively. By comparing the position of the centroids in the experimental and in the simulated ΔE_{SiC}^{corr} histograms, the calibration of the energy loss spectrum is obtained. Similarly, the residual energy spectrum can be calibrated.

Once the energy calibration procedure is completed, it is possible to attribute the right atomic number to each experimental locus in the ΔE_{SiC}^{corr} n_{phot} matrix, since for each atomic species the corresponding energy loss and residual energy can be evaluated. In order to implement a PID technique, the collision between a ^{20}Ne beam onto a ^{76}Ge target at 700 MeV was considered. Since the NUMEN project is mainly interested in studying the DCE cross sections, in this PID procedure the focus is on the identification of the $^{20}O^{8+}$ ions. The other simulated ejectiles are ^{19}O, ^{21}O, ^{19}F, ^{20}F, and ^{20}Ne. Such ions were chosen because they represent the principal sources of background in the study of DCE reactions induced by a ^{20}Ne beam. All ejectiles were simulated with charge state 8^+ and, for each ion, one million events were generated. For each ejectile, an excitation energy up to 70 MeV with a uniform distribution was considered. In Fig. 5.7.a, the resulting ΔE_{SiC}^{corr} n_{phot} plot for one of the telescope of the PID wall is illustrated. As can be noticed, there is a good separation between the loci of ejectiles with different atomic number Z, thus satisfying one of the main requirements for the PID wall, consisting in the unambiguous identification of the the ions in the region of O, F and Ne. As mentioned in Subsect. 5.3.1, the degraded events can represent a source of contamination for the identification of the oxygen ions. By comparing Figs. 5.7.a and 3.5.a, it is evident the imrovement of the ΔE resolution, due to the fact that the SiC detector has a better intrinsic energy resolution than the proportional chamber.

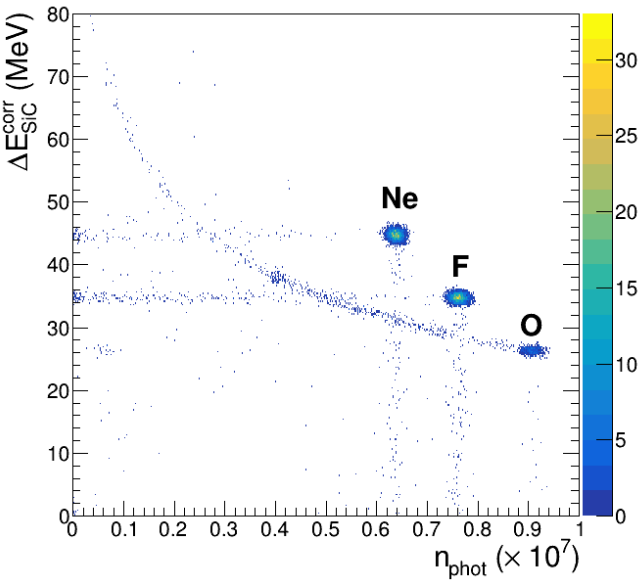

(a)

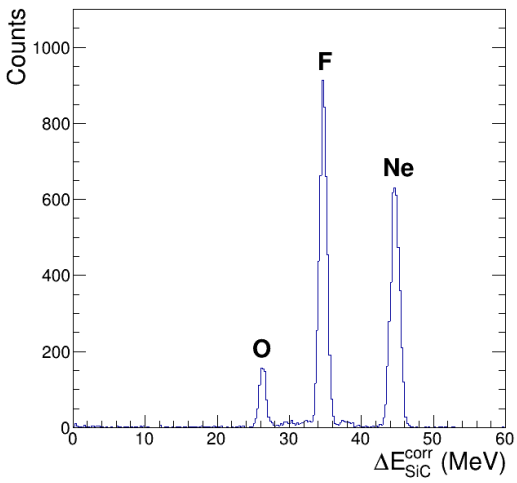

(b)

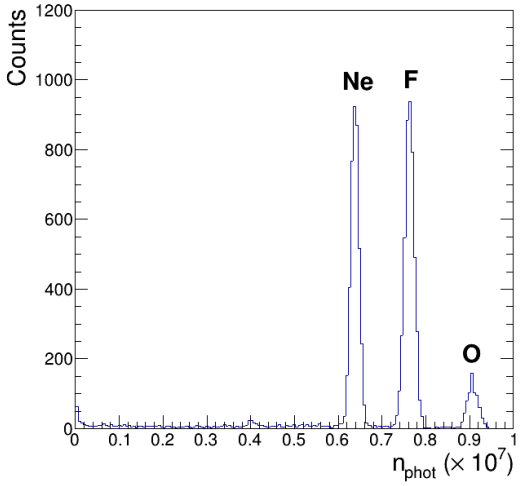

(c)

Figure 5.6: The elastic scattering of ^{18}O, ^{19}F and ^{20}Ne onto a ^{197}Au target at 700 MeV bombarding energy: (a) a typical ΔE^{corr}_{SiC} n_{phot} correlation plot for a single SiC-CsI(Tl) telescope is shown. The corresponding ΔE^{corr}_{SiC} and n_{phot} spectra are illustrated in (b) and (c), respectively.

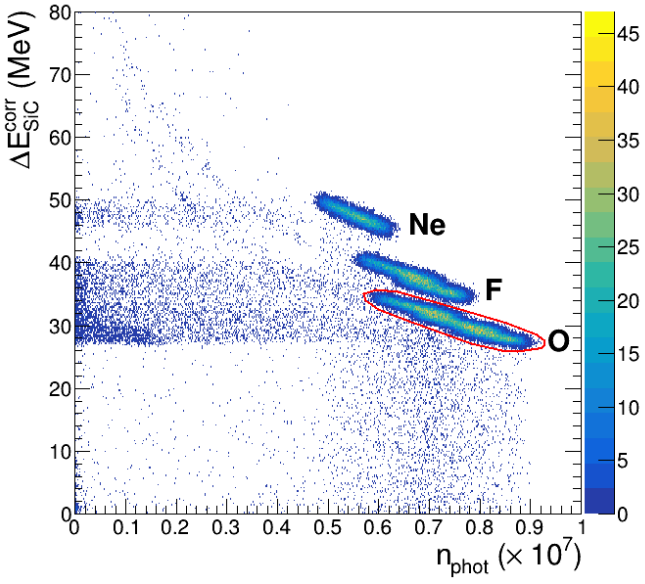

(a)

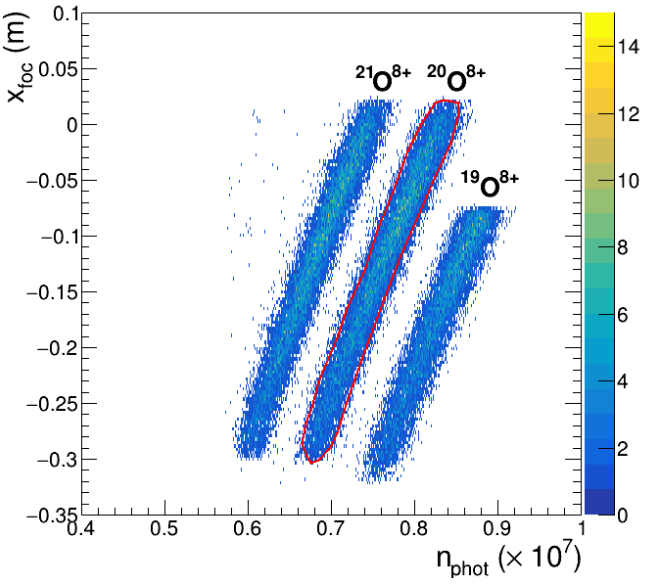

(b)

Figure 5.7: The identification procedure of the $^{20}O^{8+}$ ejectiles: (a) a typical ΔE_{SiC}^{corr} n_{phot} matrix for a single SiC-CsI(Tl) telescope. The graphical cut to select the oxygen ions is reported. (b) A typical x_{foc} n_{phot} correlation plot for a single SiC-CsI(Tl) telescope for the oxygen ions selected with the graphical cut shown in (a). The graphical cut to select the $^{20}O^{8+}$ isotopes is also represented.

The PID can be performed by applying a procedure similar to the one described in Subsect. 3.1.2, which consists in the combined use of two techniques: the ΔE E method for the Z identification and a technique based on the Lorentz force to discriminate the ions according to their mass-to-charge ratio ($\overline{m}/q$). Therefore, the oxygen ions were selected with a graphical contour as the one shown in Fig. 5.7.a. Then, the selected events were plotted in the represention in which the horizontal coordinates of the ejectiles at the focal plane (x_{foc}) are correlated with their residual energy (here expressed in n_{phot}). The resulting matrix is shown in Fig. 5.7.b, where the simulated oxygen isotopes ($^{19}O^{8+}$, $^{20}O^{8+}$, $^{21}O^{8+}$) are well distinguishable. As expected, the comparison between Figs. 5.7.b and 3.5.b highlights the worsening of the resolution in the residual energy measurement; the CsI scintillator has a typical energy resolution poorer than the Si detector by a factor of 4-5. Nevertheless, an effective identification of the ejectiles of interest is still possible: for example, the $^{20}O^{8+}$ ions can be easily selected with a graphical contour as the one shown in Fig. 5.7.b.

It is worthwhile to remark that in Figs. 5.7.a and 5.7.b the spectra were plotted without any condition on the horizontal angle θ_{foc} of the ejectiles. A further improvements of the PID performance can be obtained by analyzing the ΔE^{corr}_{SiC} n_{phot} correlation matrix in ranges of θ_{foc}. For example, if the ΔE^{corr}_{SiC} n_{phot} matrix of Fig. 5.7.a is plotted under the condition $45.8° < \theta_{foc} < 57.3°$, one obtains the result shown in Fig. 5.8.a, where the same graphical contour as in Fig. 5.7.a is drawn for comparison. In this case, the loci with different atomic numbers are more distinguishable and, in addition, there is a separation between the different isotopes. Therefore, together with the atomic number discrimination, a coarse mass identification could be performed even in the ΔE^{corr}_{SiC} n_{phot} matrix. If a more refined mass identification is needed, it is still possible to use the x_{foc} n_{phot} represention (see Fig. 5.8.b). Thus, the analysis of different ranges of θ_{foc} improves the overall PID quality.

5.3.4 Ionization processes in the gas tracker

As described in Subsect. 5.2.2, the Monte Carlo simulation stores the position and the deposit of the individual energy releases (called *hits*) inside each volume.

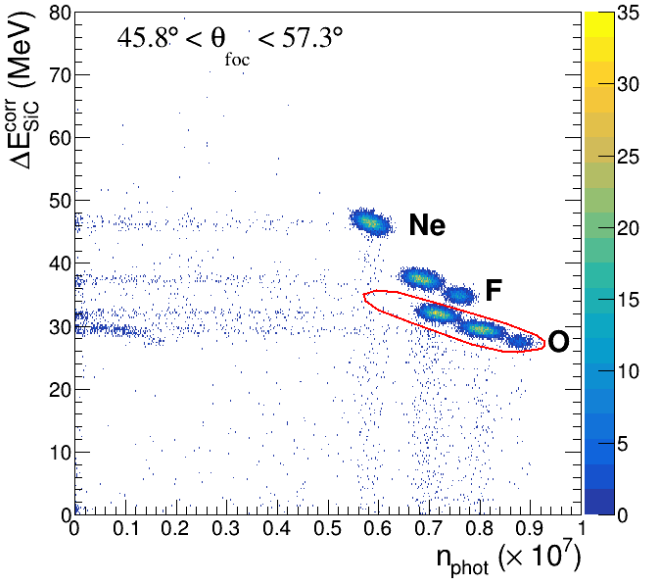

(a)

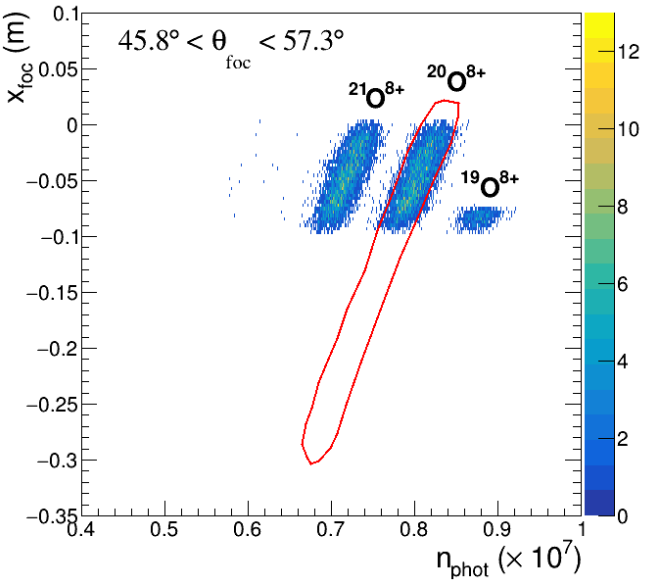

(b)

Figure 5.8: (a) ΔE_{SiC}^{corr} n_{phot} matrix of Fig. 5.7.a under the condition $45.8° < \theta_{foc} < 57.3°$. (b) x_{foc} n_{phot} correlation plot of Fig. 5.7.b under the identical condition on θ_{foc}. The same graphical contours as in Fig. 5.7 are reported.

In particular, this information allows to reconstruct the ionization processes produced in the interaction between the ejectiles and the isobutane within the gas tracker. In Fig. 5.9, the simulation of 10 tracks of ^{20}Ne ions at 700 MeV kinetic energy in the gas tracker is shown. As expected, a ^{20}Ne ion generates a high ionization density along its path. Moreover, energy deposits far away from the ion trajectories can be noticed: they are due to δ-rays, which can travel a significant distance from their origin point and produce further ionization. In Fig. 5.9.b and 5.9.c the projection of the trajectories onto the horizontal (x-z) and vertical (y-z) plane are illustrated, respectively. As can be seen, a wide range of horizontal angles is spanned ($[+40°; +70°]$), while the vertical angles are in the interval $[\ \ 2°; +2°]$ according to the MAGNEX optical properties.

The storing of the individual hits in the gas tracker allows to evaluate the number and the position of the secondary electrons. This information is being used as input by the softwares that simulate the gas avalanche process in the M-THGEM, the charge collection in the pad-segmented anode and the digitization of the signals (see Sects. 4.1 and 4.3). Thus, the Monte Carlo simulation developed for this work serves as critical input for the softwares downstream and it is fundamental to simulate the electronic response of the detectors and the data stream, including detectors response time and pile-up.

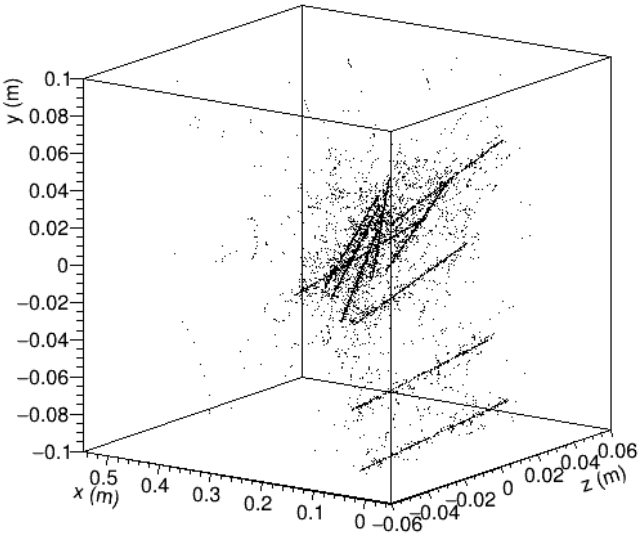

(a)

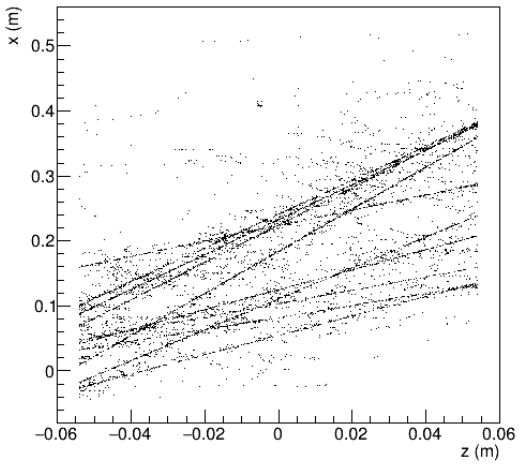

(b)

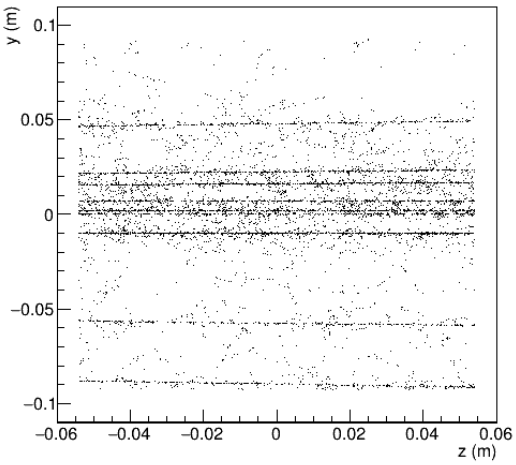

(c)

Figure 5.9: Simulation of 10 trajectories of ^{20}Ne ions at 700 MeV kinetic energy in the gas tracker: in (a) the full 3D tracks are shown; in (b) and (c) the projections of the tracks onto the x-z and the y-z planes are shown, respectively. Each point corresponds to an energy release in the gas. The points far away from the ions trajectories are due δ-rays.

Chapter References

[3] F. Cappuzzello et al. “The MAGNEX spectrometer: results and perspectives”. In: *Eur. Phys. J. A* 52.6 (2016), p. 167. DOI: 10.1140/epja/i2016-16167-1.

[37] A. Spatafora et al. “^{20}Ne+^{76}Ge elastic and inelastic scattering at 306 MeV”. In: *Phys. Rev. C* 100 (3 Sept. 2019), p. 034620. DOI: 10.1103/PhysRevC.100.034620.

[60] K. Makino and M. Berz. “COSY INFINITY version 8”. In: *Nuclear Instruments and Methods in Physics Research Section A: Accelerators, Spectrometers, Detectors and Associated Equipment* 427.1 (1999), pp. 338–343. ISSN: 0168-9002. DOI: https://doi.org/10.1016/S0168-9002(98)01554-X.

[74] G. F. Knoll. *Radiation Detection and Measurement, 3rd ed.* 3rd edition. New York: John Wiley and Sons, 2000. ISBN: 978-0-471-07338-3.

[123] S. Tudisco et al. “SiCILIA—Silicon Carbide Detectors for Intense Luminosity Investigations and Applications”. In: *Sensors* 18.7 (2018), p. 2289. DOI: 10.3390/s18072289.

[124] S. Tudisco et al. “” In: *(in preparation)* ().

[126] A. Pappalardo et al. “An imaging technique for detection and absolute calibration of scintillation light”. In: *Review of Scientific Instruments* 81 (2010), p. 033308. DOI: 10.1063/1.3360931.

[127] A. Pappalardo et al. “Erratum: An imaging technique for detection and absolute calibration of scintillation light”. In: *Review of Scientific Instruments* 82 (2011), p. 049903. DOI: 10.1063/1.3579512.

[133] N. Metropolis and S. Ulam. "The Monte Carlo method". In: *Journal of the American Statistical Association* 44 (1949), pp. 335–341. DOI: 10.1080/01621459.1949.10483310.

[134] S. Agostinelli et al. "Geant4—a simulation toolkit". In: *Nuclear Instruments and Methods in Physics Research Section A: Accelerators, Spectrometers, Detectors and Associated Equipment* 506.3 (2003), pp. 250–303. ISSN: 0168-9002. DOI: https://doi.org/10.1016/S0168-9002(03)01368-8.

[135] J. Allison et al. "Geant4 developments and applications". In: *IEEE Transactions on Nuclear Science* 53.1 (2006), pp. 270–278. DOI: 10.1109/TNS.2006.869826.

[136] J. Allison et al. "Recent developments in Geant4". In: *Nuclear Instruments and Methods in Physics Research Section A: Accelerators, Spectrometers, Detectors and Associated Equipment* 835 (2016), pp. 186–225. ISSN: 0168-9002. DOI: https://doi.org/10.1016/j.nima.2016.06.125.

[137] R. Brun and F. Rademakers. "ROOT — An object oriented data analysis framework". In: *Nuclear Instruments and Methods in Physics Research Section A: Accelerators, Spectrometers, Detectors and Associated Equipment* 389.1 (1997). New Computing Techniques in Physics Research V, pp. 81–86. ISSN: 0168-9002. DOI: https://doi.org/10.1016/S0168-9002(97)00048-X.

[138] G. Prete et al. "The Use of CsI(Tl) Scintillators with Photodiode Read-Out in Heavy Ion Experiments". In: *IEEE Transactions on Nuclear Science* 34.1 (1987), pp. 423–426. DOI: 10.1109/TNS.1987.4337376.

[139] J. B. Birks. *The Theory and Practice of Scintillation Counting*. Pergamon Press, 1964. ISBN: 978-0-08-010472-0. DOI: https://doi.org/10.1016/C2013-0-01791-4.

[140] D. Horn et al. "The mass dependence of CsI(Tl) scintillation response to heavy ions". In: *Nuclear Instruments and Methods in Physics Research Section A: Accelerators, Spectrometers, Detectors and Associated Equipment* 320.1 (1992), pp. 273–276. ISSN: 0168-9002. DOI: https://doi.org/10.1016/0168-9002(92)90785-3.

6

The characterization of the gas tracker prototype

Contents

6.1 The gas tracker prototype **149**
6.2 Layout of the M-THGEM **149**
6.3 The characterization test set-up **156**
6.4 Current-voltage characterization of the gas tracker prototype **158**
6.4.1 Current-induction voltage characterization 161
6.4.2 Current-drift voltage characterization 164
6.4.3 Current-THGEM voltage characterization 166
6.4.4 Gain 166
6.4.5 Ion backflow 169
6.4.6 Rate characterization 172
6.5 Track reconstruction test **174**
6.5.1 Charge distribution and arrival time measurement . . 174
6.5.2 Horizontal and vertical angles reconstruction 175
6.6 Conclusions **178**

In order to check if a gas tracker based on M-THGEM can satisfy the challenging requirements presented in Chapt. 4, a reduced-size prototype was built. This chapter is dedicated to the description of the characterization tests of the prototype, in which the currents flowing across the detector electrodes were measured as a function of the biasing voltages, gas pressure and particle rate. These tests allow to evaluate two important quantities: the gain and the ion backflow. More detailed information about the characterization tests are discussed in Ref. [141]. In the last part of this chapter, the first test on the track reconstruction capability of the prototype is described. The results of the measurements of charge distribution and drift time are reported, together with the determination of the track horizontal and vertical angle.

6.1 The gas tracker prototype

The gas tracker prototype is a drift chamber having an active volume of $107 \pm 107 \pm 185$ mm^3 (see Fig. 6.1). It was designed to have a smaller lateral extension than the final MAGNEX gas tracker, which will have dimensions of $1200 \pm 107 \pm 150$ mm^3. The prototype height is larger than 150 mm for the final detector, since the decision of reducing it was taken after the prototype construction, based on budget limitations. In the tests described in the following the detector worked with isobutane gas (iC_4H_{10}) of 99.95% purity at pressure typically between 10 and 40 mbar. The structure and the working principle of the prototype corresponds to those described in Sect. 4.1. The only exception involves the segmented, position-sensitive anode, which in the tests here presented was replaced by a single anode plate of 107 ± 107 mm^2 to collect the full avalanche charges in a single pad.

6.2 Layout of the M-THGEM

The characterization tests described in this Thesis involved two different M-THGEM [110, 116–118, 132] layouts: both of them are three-layer M-THGEMs and have an area of 107 ± 107 mm^2, but they present different hole patterns, as can be seen in Fig. 6.2. The first type (ROW M-THGEM, ROW in the following) is characterized by just five equidistant rows of holes, which are parallel to the

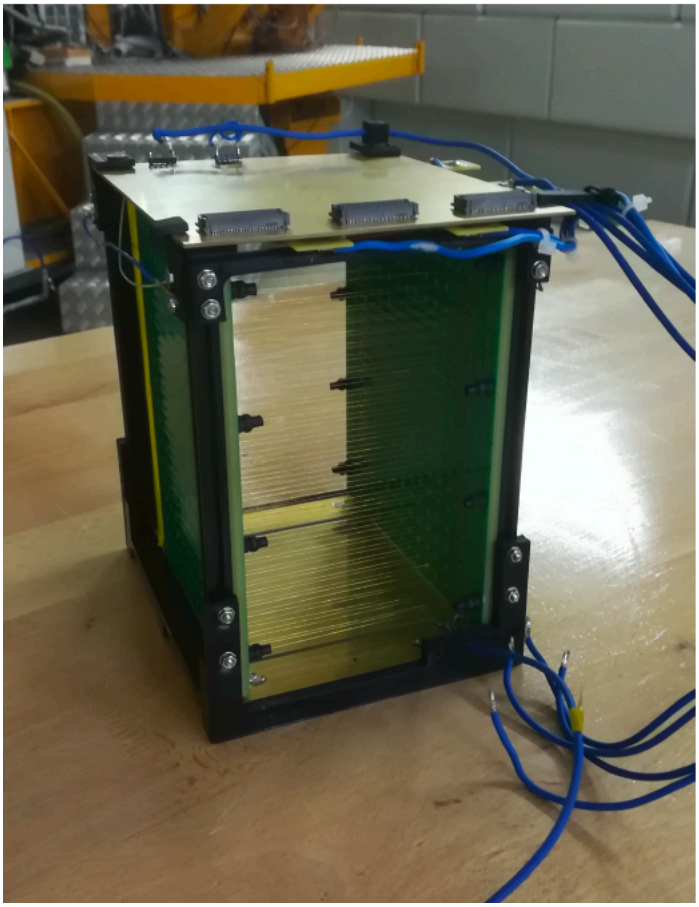

Figure 6.1: Picture of the gas tracker prototype.

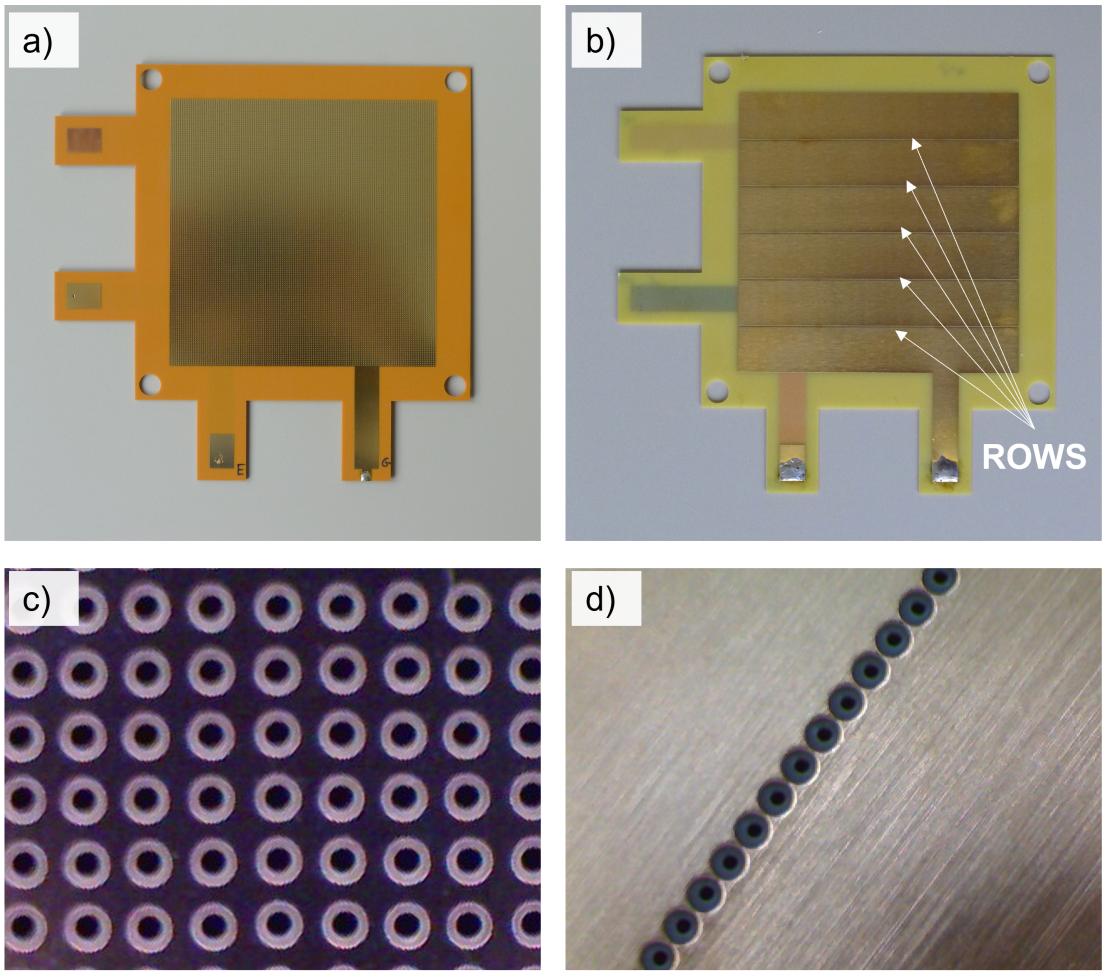

Figure 6.2: Pictures of the two types of M-THGEMs: (a) the FULL M-THGEM and (b) the ROW M-THGEM. In (c) and (d) are shown a magnification of a small area of the FULL M-THGEM and of the ROW M-THGEM, respectively.

Table 6.1: Main characteristics of the two types of tested M-THGEM foils.

	FULL M-THGEM	**ROW M-THGEM**
Substrate material	Ceramic SD103K	PCB
Finish board thickness (mm)	1.37	1.28
Dimension (mm^2)	107 ± 107	107 ± 107
Rim size (mm)	0.1	0.2
Number of holes	20449	715
Hole diameter (mm)	0.30	0.280
Hole pitch (mm)	0.75	0.75

entrance and exit surfaces of the detector (see Fig. 6.2.b). Each row is composed by 143 holes with a diameter of 0.30 mm and a pitch of 0.75 mm (see Fig. 6.2.d). The distance between two hole rows is of 18 mm. ROW was fabricated by Zener s.r.l. and is made of three layers of PCB (0.40 mm thick), each one coated with copper (0.020 mm thick), resulting in a total thickness of 1.28 mm.

In the second type (FULL M-THGEM, FULL from now on) the holes are present over the whole active area and are arranged in a square pattern (the holes are placed at the vertices of a square, as shown in Fig. 6.2.c). The holes present a diameter of 0.30 mm and a pitch of 0.75 mm. FULL was manufactured by Shenzhen HeLeeX Analytical Instrument Co. Ltd. and consists of alternate layers of ceramic SD103K (0.422 mm thick) and copper (0.026 mm thick) for a total thickness of 1.37 mm. The main characteristics of the two M-THGEM foils are summarized in Table 6.1.

ROW was designed to work with an anode segmented in strips orthogonal to the hole rows, as sketched in Fig. 6.3 and described in Ref. [4]. In this case, each row of holes of the M-THGEM defines one z coordinate. Just the electrons produced in correspondence of each row are multiplied and can induce a signal in the segmented stripped anode. Therefore, in our case the track is sampled at five different z coordinates. If the anodic strip size is large enough, for each hole row just one strip is fired, which corresponds to the crossing point between the ion

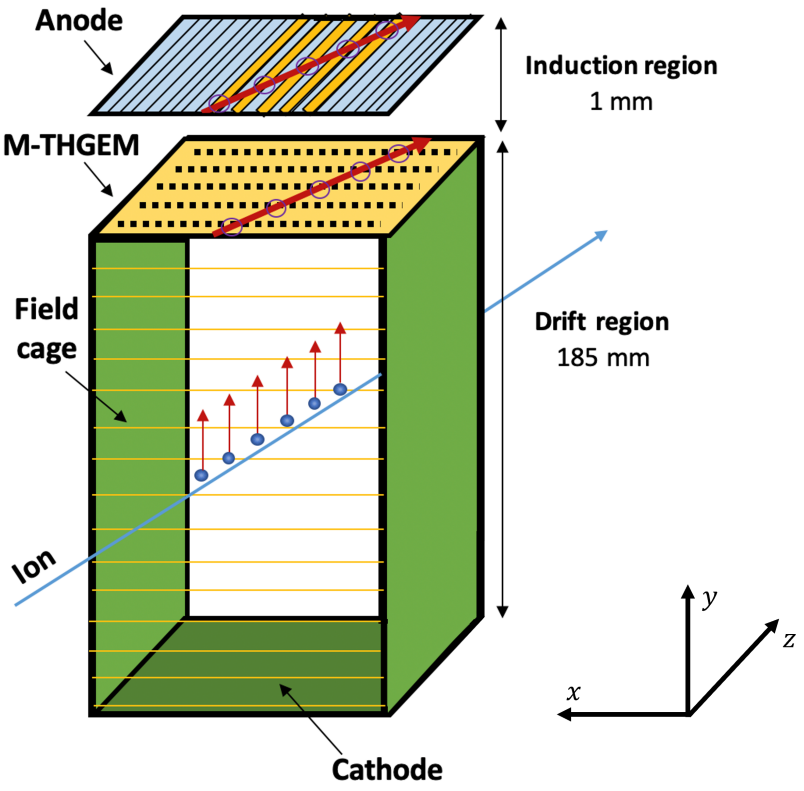

Figure 6.3: Schematic drawing of the gas tracker prototype illustrating the operation principles.

track and a M-THGEM row. The fired strip defines a x coordinate. Therefore, in our case an ideal track with an angle $\theta \neq 0$ on the x-z plane generates signals on a total of five strips, providing five (x,z) pairs. As will be shown in Sect. 6.5, in the real situation not just a single strip but rather a group of adjacent strips is hit owing to the broadening of the electronic cloud. The electrons produced by the incident ion have different arrival time on the strips depending on the vertical position they are produced. Therefore, it is possible to determine the y coordinate by measuring the time of the strip signals. Thus, the setup based on ROW and stripped anode could allow to reconstruct the full 3D track of the incident ion without measuring the charge distribution but just acquiring the strips hit-map, resulting in a fast, cheap and easier approach for signal transmission. A drawback of this setup is that the x position resolution is limited by the size of the anodic strips. Moreover, ambiguities on the track reconstruction for trajectories parallel to the anodic strips could appear. On the other hand, a more standard setup based on FULL coupled with an anode segmented in pads distributed in the x-z plane, as the one described in Ref. [111], overcomes the above-mentioned problems.

The different hole geometries of the two M-THGEM foils strongly affects the shape of the electric field, especially close to the M-THGEM surface. For both types of M-THGEM foils, calculations of the electric field in the detector using the finite-elements software COMSOL Multiphysics [131] have been performed. In Fig. 6.4 the electric field lines for the two cases are shown. The electrical configuration of the detector adopted in these calculations is: 800 V potential difference across the drift region, 200 V across each M-THGEM layer, and 50 V across the induction region. In both cases it is evident that far from the holes the electric field is quite uniform, while close to the M-THGEM plate the electric field lines focus inside the holes. Due to the focusing effect, the bending of the field lines occurs in an area that is much larger for ROW compared to FULL. The amount of field lines that end up on the M-THGEM bottom electrode explains the lower electron collection efficiency in the ROW. This behavior has a significant impact on the electronic transparency, that results smaller for ROW and larger for FULL, as will be shown in Sect. 6.4.

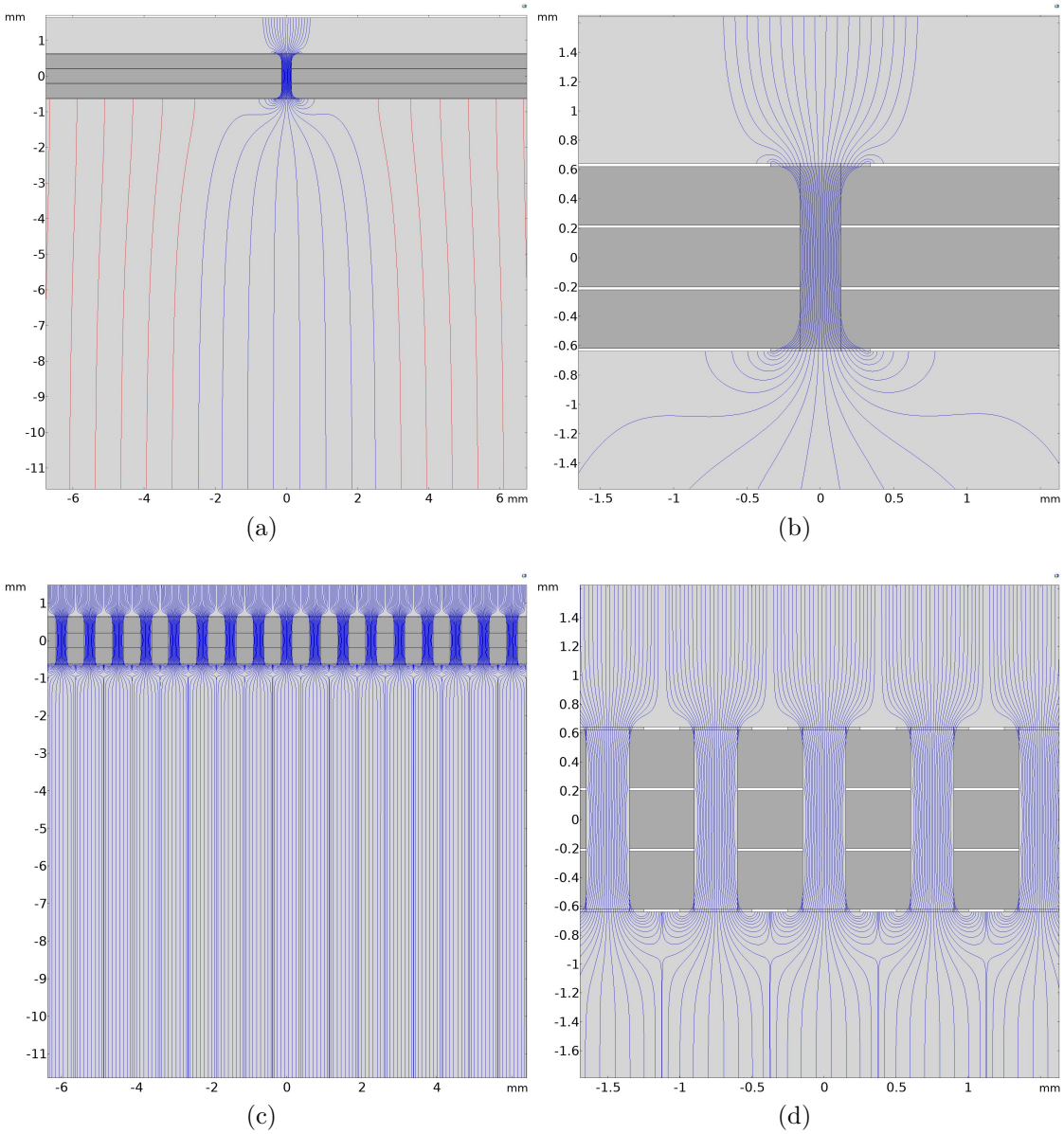

Figure 6.4: Electric field in the region of the holes for ROW a), b) and for FULL c), d) obtained with COMSOL Multiphysics software. The blue field lines start from a plane parallel to the M-THGEM foils placed in the middle of the central hole, while the red field lines in a) originate from the cathode.

6.3 The characterization test set-up

The characterization tests of the tracker prototype were carried out at LNS-INFN (Catania, Italy) at the TEBE (TEst BEnch) facility, whose schematic drawing is shown in Fig. 6.5. TEBE is an equipped beam line mainly devoted to tests and characterization of detectors for the NUMEN project. Two vacuum chambers are arranged along the beam line: the first is the scattering chamber, which is equipped with a movable target holder that can house many targets. The second chamber (detector chamber) is rotated at 30° with respect to the beam direction and can be filled with gas. It is isolated from the scattering chamber by a 2.5 μm thick Mylar window, which is thick enough to withstand a pressure difference of more than 100 mbar and thin enough to minimize the energy and angular straggling, even for low energy heavy-ion beams. The detector chamber hosts the tracker prototype and, during normal operation, is filled with 99.95% pure isobutane at pressure ranging from 10 to 40 mbar. A typical gas flow rate of 130 sccm (standard cubic centimeter per minute) is constantly maintained and controlled by a mass flow controller.

In the tests, a ^{241}Am radioactive α-particle source with a nominal activity of 52 kBq was placed inside the detector chamber, in front of the tracker prototype. The source was collimated in order to reduce the incident particle rate on the detector to about 200 Hz. A remote-controlled shutter was placed in front of the source to prevent α-particles from reaching the detector in between two experimental runs or whenever needed.

The characterization activity also included in-beam tests, in order to explore detector response to heavy-ion beams at different rates. An $^{18}O^{8+}$ beam at 270 MeV incident energy was delivered by the LNS Superconducting Cyclotron with intensities, measured by two Faraday cups located upstream and downstream of the target, ranging from 100 to 900 pA. Two gold targets with thicknesses of 0.97 and 9.6 mg/cm^2, respectively, were used as additional element to change the rate of particles scattered to the detector from a few tens of pps up to over 3 kpps.

A 16 channel high-voltage power supply (CAEN SY5527 mainframe with A1515 board + A1015G adapter [142]), specifically designed for powering multiple GEM detectors, was used to supply the required voltages.

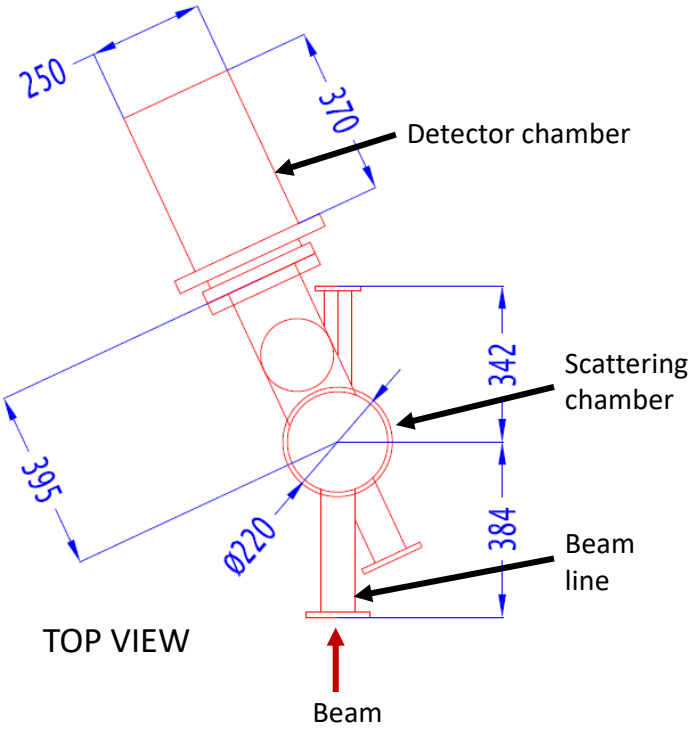

Figure 6.5: Top-view drawing of the TEBE facility at INFN-LNS.

The currents induced on the different electrodes of the tracker were measured by PICO, a high voltage (0 - 1000 V) seven-channel picoammeter, designed and assembled at INFN - Napoli (Italy). PICO was designed to act as fast monitor of the voltage and current of the triple-GEM detector for the CMS experiment [143], but it can be implemented as a general purpose device for other applications with micro-pattern gaseous detectors. The picoammeter hosts 7 ADCs (24bit) and is capable of measuring voltage with a precision better than 10 mV and current with a precision of about 15 pA for the [16; 4] μA full-scale range and about 2 nA for the [0.8; 0.2] mA full-scale range. In particular, in our tests the current on the bottom electrode of the M-THGEM (I_{bot}, see Sect. 6.4) is typically measured in the low precision scale, while the other currents have values compatible with the high precision one. A detailed scheme of the electrical connection between CAEN SY5527 and PICO is illustrated in Fig. 6.6.

6.4 Current-voltage characterization of the gas tracker prototype

This section presents the results of the current-voltage characterization and the gain and ion backflow measurements for different voltages and different gas pressures configurations.

A schematic electrical diagram of the detector is shown in Fig. 6.7. The currents flowing through the detector electrodes are:

- I_{an}, fraction of the avalanche electrons that are transferred to the readout anode and contribute to the detected signals;
- I_{top}, fraction of the avalanche electrons and ions (see Sect. 6.4.1) collected onto the M-THGEM top electrode;
- I_{bot}, fraction of the avalanche ions collected onto the M-THGEM bottom electrode;
- I_{cath}, fraction of the avalanche ions that flow back to the cathode through the drift region.

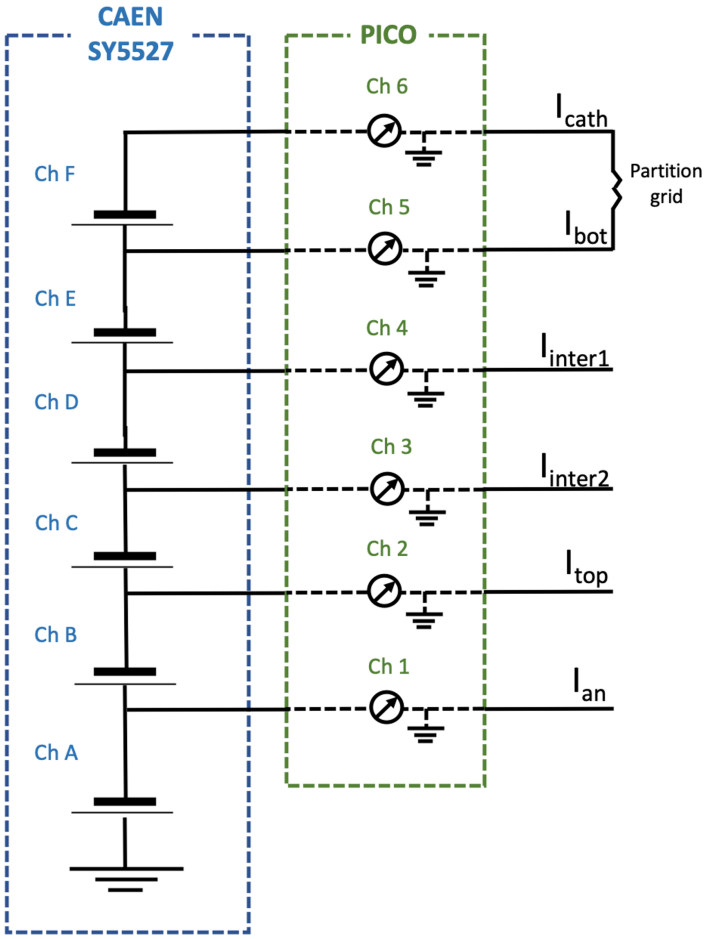

Figure 6.6: Scheme of the biasing and measuring systems based on CAEN SY5527 and PICO.

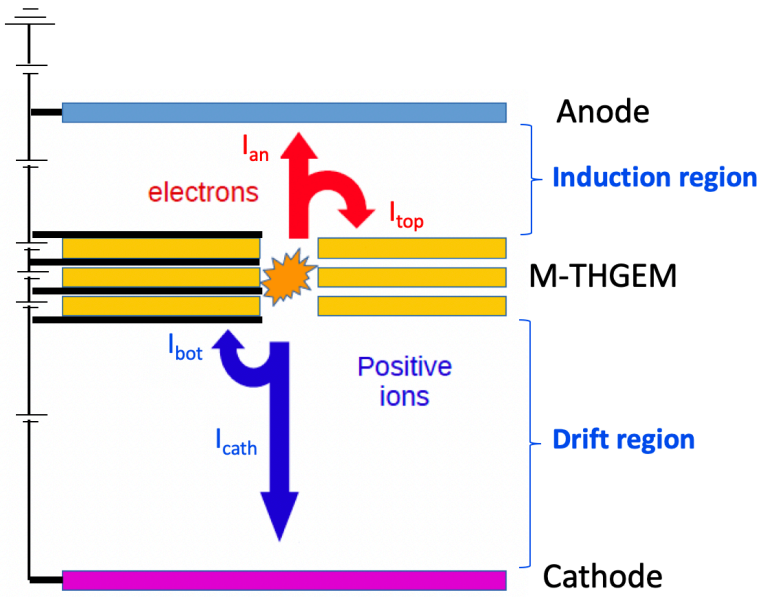

Figure 6.7: Biasing scheme of the detector with an illustration of the measured currents.

When no beam or α-particles cross the detector, the dark current measured by PICO is the parasitic current due to the ohmic resistance of the M-THGEM insulator substrate, sandwiched between the electrodes at different potential. Due to the partition grid, a typical current of few μA is measured by the cathode (I_{cath}) and bottom (I_{bot}) electrodes. The currents collected by the intermediate M-THGEM electrodes (not indicated in Fig. 6.7) are in most of the cases below the precision of the picoammeter and will not be discussed in the following. In the present tests the anode was biased at 20 V.

In the measurements with α-particle source or ^{18}O beam, for each electrical configuration, a run of about 200 s was performed. During the first 80 s the shutter in front of the source was closed, in the next 100 s it was opened and finally for the last 20 s it was closed again. The net current induced on each electrode was extracted as the difference between the average current measured with closed and open shutter. The error on the net current was obtained in the following way. First, the error on the average current with closed shutter (ΔI_{closed}) was calculated as the quadratic sum of the statistical contribution and the precision of the picoammeter. The same procedure was applied to deduce the

error on the average current with open shutter (ΔI_{open}). Then, the total error assigned to each point is the quadratic sum of ΔI_{closed} and ΔI_{open}. This method allows to measure currents due only to the charged particles crossing the detector; any contribution from dark currents circulating in the detector and/or possible bias in the picoammeter current measurements are removed. Possible sources of systematic errors are due to electronic noise, change in temperature and pressure and stability of the bias supply. During the runs the gas temperature and the pressure were within 1°C and 0.5 mbar, respectively. The total systematic error, estimated by comparing the measurements performed in the same experimental conditions, is at most 10%. An example of the currents measured in a single run as a function of time is shown in Fig. 6.8. In the explored experimental conditions a good long-term gain stability is observed, which is a sign of negligible charging up of the insulator substrate.

The currents have been measured, varying four parameters that affect the behavior of the detector, namely:

- the gas pressure;
- the voltage difference applied to the induction region (V_{ind});
- the voltage difference applied across a single THGEM layer (V_{THGEM}), which was the same for all the three layers of the M-THGEM except when explicitly mentioned;
- the voltage difference applied to the drift region (V_{drift}).

Each current-voltage characterization was obtained changing only one parameter at a time and keeping fixed all the others. In the figures shown in this section, the error bar of the measured points is always included, if not visible it is because it is smaller than the marker size.

6.4.1 Current-induction voltage characterization

Since the V_{ind} voltage determines the electric field in the induction region, it impacts on the efficiency of extracting the avalanche electrons from the M-THGEM holes and collecting them onto the readout anode.

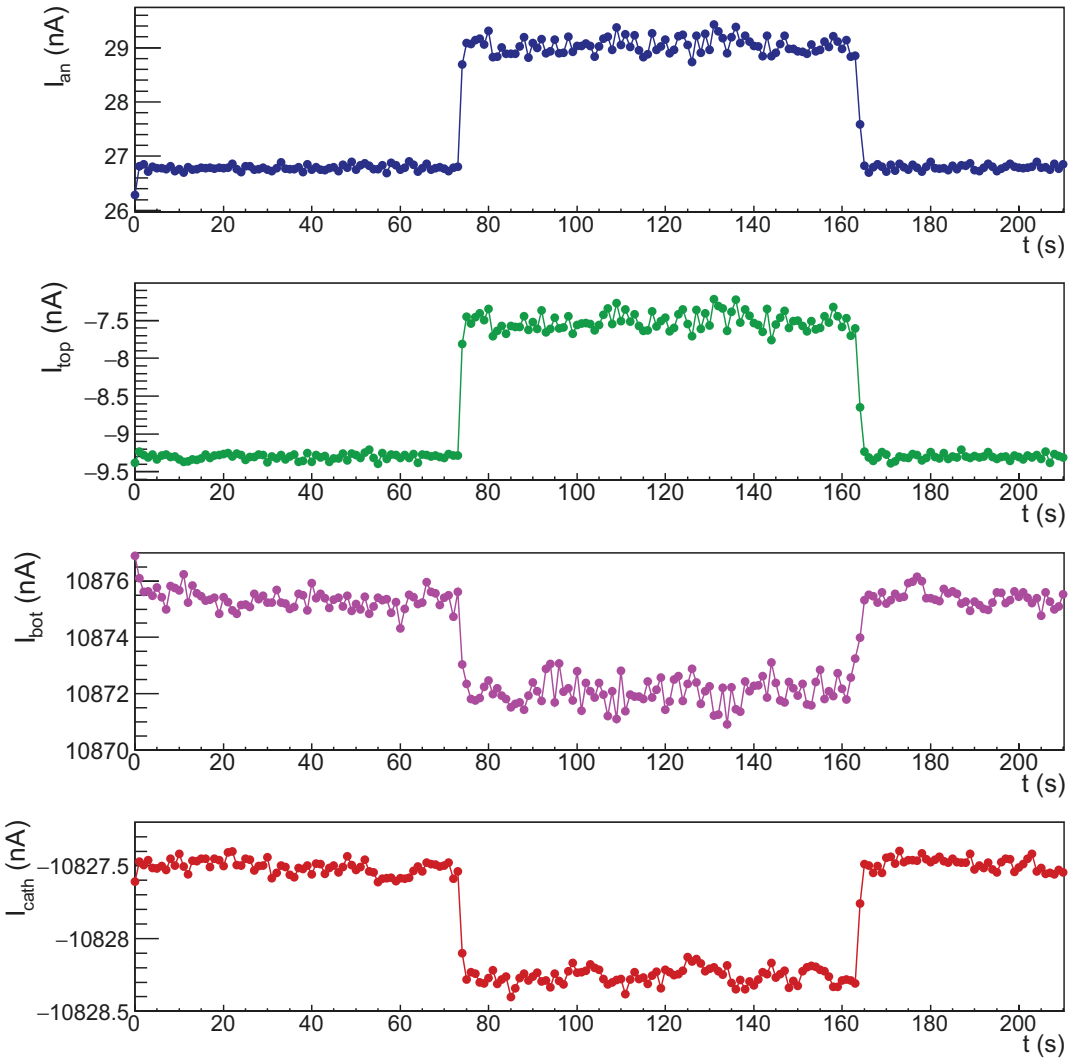

Figure 6.8: Measured currents as a function of time in a typical run. From the top to the bottom of the figure, the current of anode, top layer of the M-THGEM, bottom layer of the M-THGEM and cathode electrodes are shown. The two abrupt changes in the current at $\rightarrow$80 and $\rightarrow$160 s correspond to the opening and closure of the shutter in front the α-particle source, respectively. The measurement was performed with $P = 30$ mbar, $V_{ind} = 40$ V, $V_{THGEM} = 200$ V, and $V_{drift} = 1000$ V.

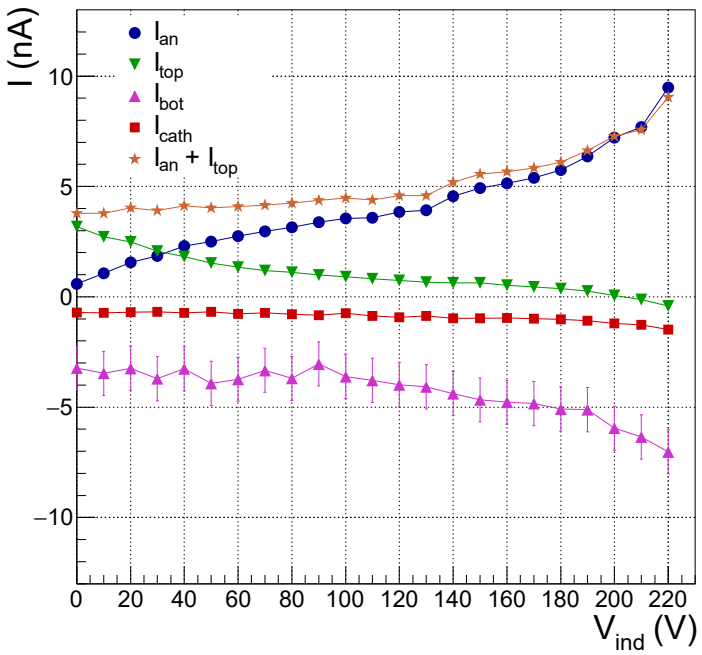

Figure 6.9: Current-induction voltage characterization for FULL at $P = 30$ mbar, $V_{THGEM} = 220$ V and $V_{drift} = 1000$ V.

The characterization of the measured currents as a function of V_{ind} was performed by fixing the gas pressure, V_{THGEM} and V_{drift} and changing V_{ind} in steps of 10 or 20 V from 0 V up to the discharge value. Different configurations of V_{THGEM}, V_{drift} and pressure were used, as listed in Table A.1.

Since a similar behavior is observed for all the electrical configurations and pressures studied, as well as for both FULL and ROW, in Fig. 6.9 the characterization of V_{ind} for $P = 30$ mbar, $V_{THGEM} = 220$ V and $V_{drift} = 1000$ V for FULL is shown as exemplifying case. The main feature of the plot is that as V_{ind} increases, the magnitude of I_{an} increases, whilst I_{top} decreases. Therefore the value of V_{ind} modulates the ratio I_{an}/I_{top}. The sum of the currents read on top of the M-THGEM and anode electrodes ($I_{top} + I_{an}$), that is the total negative charge (TNC) produced by the M-THGEM, is also shown in the figure. Up to about 140 V, the TNC is approximately constant, while for values larger than 140 V it starts to increase. This indicates that, up to 140 V, the stronger the electric field

in the induction region, the larger the fraction of secondary electrons collected by the anode and the lower the fraction of the electrons hitting the top electrode. For V_{ind} larger than 140 V, the rise of the TNC can be explained considering that the electric field in the induction region becomes strong enough to produce charge multiplication. It can be estimated that the maximum gain obtained in the induction region in these electrical conditions is of a factor 2. For higher values of V_{ind}, I_{top} becomes negative. In this condition the amount of the positive ions produced in the induction region and collected by the top of the M-THGEM is larger than the electrons collected by the same electrode. For the FULL with this electrical and pressure configuration an operational value of about $V_{ind} = 120$ V allows that a large fraction of the electrons is collected on the anode and the multiplication is mainly confined inside the M-THGEM channels.

6.4.2 Current-drift voltage characterization

The study of the V_{drift} current-voltage characterization was performed varying the V_{drift} value from 0 V up to the discharge value. A summary of the different configurations explored during the tests is given in Table A.2.

For the FULL the anodic current is almost completely flat and no variation with V_{drift} is evident for all the configurations explored. An example of the behavior is shown in Fig. 6.10 (top).

The ROW behaves in a very different way. A typical plot is shown in Fig. 6.10 (bottom). As V_{drift} increases the anodic current increases reaching a maximum, after this value the current decreases. For small V_{drift} values (less than $\rightarrow$100 V), most of the primary electrons are lost because of recombination effects. Increasing V_{drift}, a larger number of primary electrons reaches the multiplication stage resulting in an increment of the anodic current. Assuming the same electric field in the M-THGEM hole, a larger drift velocity results in a large defocusing of the electrons. Thus, more field lines ends up on the M-THGEM bottom surface, with a decrease of collection efficiency. The behavior of the anodic current for higher V_{drift} values has also been observed in other GEM-based detectors [144, 145].

The different behavior of the two kinds of M-THGEMs has important consequences on the operation of the detector. In fact the strong dependence of the

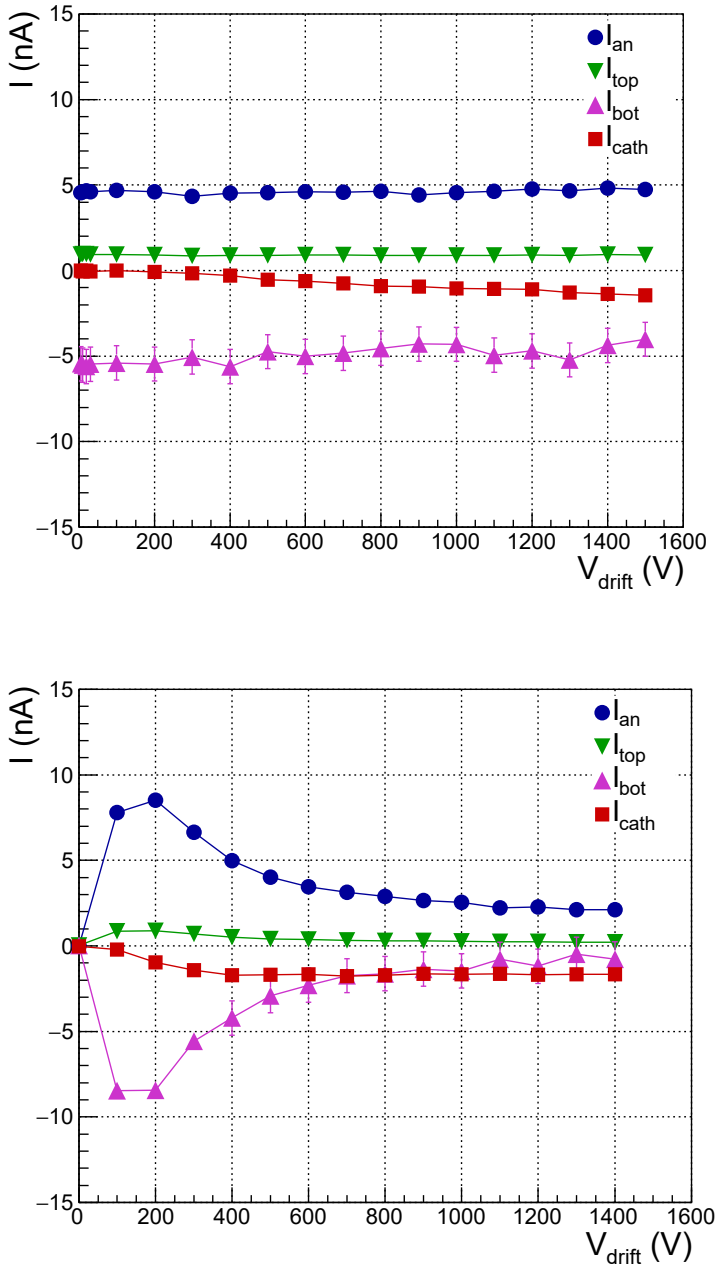

Figure 6.10: Current-drift voltage characterization for FULL at P = 30 mbar, V_{ind} = 70 V and V_{THGEM} = 240 V (top) and for ROW at P = 30 mbar, V_{ind} = 120 V and V_{THGEM} = 220 V (bottom).

anodic current with V_{drift} makes the gain of ROW very sensitive to any variation of V_{drift}, on the contrary the behavior of FULL is not affected by change of V_{drift} in a wide range of values.

6.4.3 Current-THGEM voltage characterization

Similarly to the previous cases, the V_{THGEM} current-voltage characterization was studied at fixed values of gas pressure, V_{ind}, V_{drift} and changing V_{THGEM} at steps of 5 or 10 V from the minimum value for which currents are measurable up to the discharge value. A list of the different configurations explored in the tests is given in Table A.3. As an example, the curve for the ROW at a pressure of $P = 10$ mbar is shown in Fig. 6.11. The measured currents increase exponentially with V_{THGEM}, as expected. For V_{THGEM} larger than 180 V, one observes for I_{cath} and I_{bot} a deviation from the exponential behavior due to a different charge sharing between cathode and bottom of the M-THGEM. A possible explanation of the slight deviation of I_{an} from the exponential behavior is the gas gain saturation inside the holes generated by space charge effects. A similar behavior is observed both for ROW and FULL in all the electrical configurations and pressures investigated.

6.4.4 Gain

The gain of the M-THGEM-based gas detector is here defined as the ratio between the sum of the measured I_{an} and I_{top} currents and the charge of primary electrons per unit of time (I_e):

$$G = \frac{I_{an} + I_{top}}{I_e} \tag{6.1}$$

I_e was estimated from the number of α-particles emitted by the source that enter the detector or the number of scattered ^{18}O ions reaching the detector per unit of time, and calculating the energy loss of the particles inside the active volume of the detector using the LISE++ tool [146]. Dividing the energy loss (ΔE) by the isobutane mean ionization energy (23 eV), the number of primary electron-ion pairs (N_{prim}) can be deduced. The obtained values of ΔE and N_{prim} are listed in Table 6.2 for different pressures and for both α-particle and ^{18}O ion.

As a general observation, the ROW has a lower signal to the readout compared

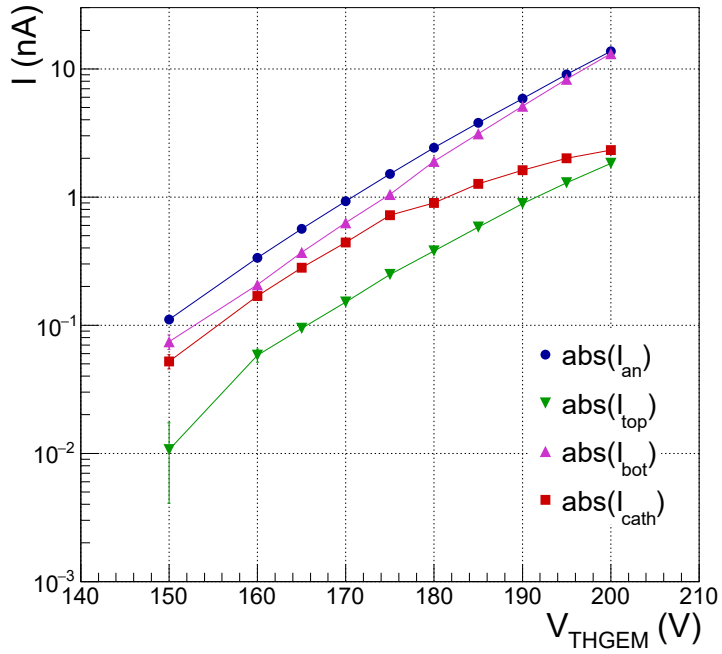

Figure 6.11: Current-THGEM voltage characterization for ROW at $P = 10$ mbar, $V_{ind} = 50$ V, and $V_{drift} = 200$ V. The absolute values of the measured currents are plotted.

Table 6.2: Values of energy loss (ΔE) evaluated with LISE++ and corresponding number of primary electron-ion pairs (N_{prim}) for both α-particle and ^{18}O ion at different gas pressures (P).

Ion	P (mbar)	ΔE (keV)	N_{prim}
α	10	314	13650
α	20	646	28100
α	30	1000	43500
^{18}O	20	1185	51500

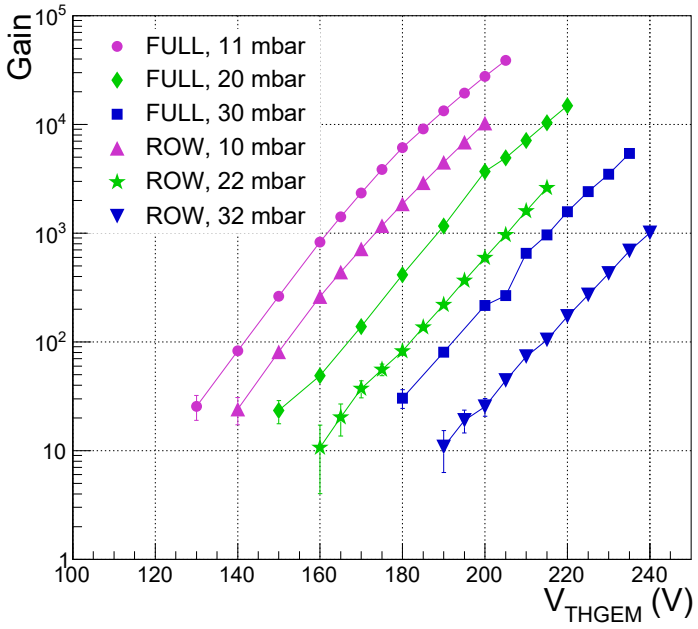

Figure 6.12: Gain as a function of V_{THGEM} for different configurations listed in Table A.3.

to the FULL because of its lower electron collection efficiency due to the hole layout, as discussed in Sect. 6.1.

The gain as a function of V_{THGEM} for different pressures for both ROW and FULL is shown in Fig. 6.12. The maximum achievable gain was defined by the onset of the discharges. One can see that, as expected, the measured gain exponentially increases as a function of V_{THGEM} for all the explored electrical configurations. A high electron multiplication was achieved also at very low pressure of 11 mbar. A maximum gain value of 4 ± 10^4 is reached at 11 mbar. These values are in agreement with those measured for similar detectors [110, 118, 132]. The decrease of the maximum achievable gain with pressure can be explained in terms of discharge when reaching Raether's limit. In fact, this latter defines the maximum number of electrons in a single avalanche (about 10^7 - 10^8). Thus, if the pressure increases, the number of primary electrons rises as well and the Raether's limit is reached at a lower gain.

In Fig. 6.13, a comparison between gains obtained with the α-particle source

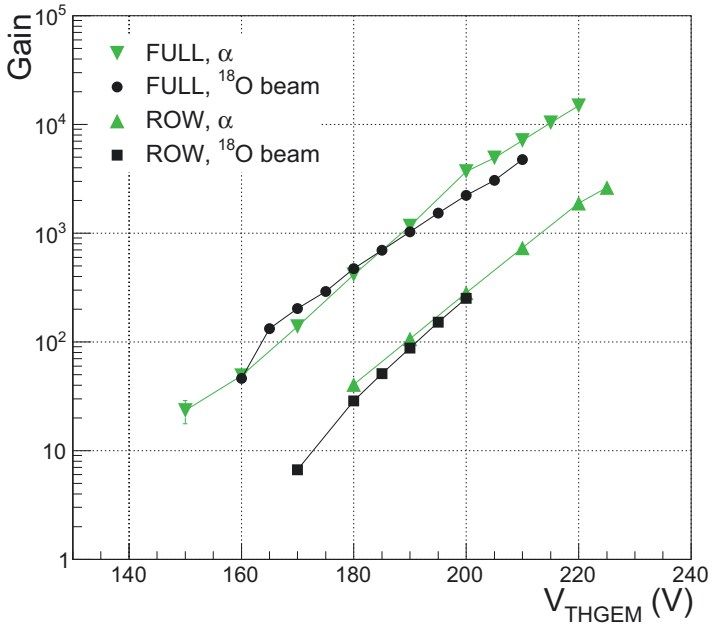

Figure 6.13: Gain for ROW and FULL as a function of V_{THGEM} for ^{18}O beam data (black) and α-particle source data (green) at $P = 20$ mbar. See Table A.3 for electrical configurations.

and the ^{18}O beam for both the M-THGEM types is shown. There is no significant difference between the gains obtained for the two particle species.

6.4.5 Ion backflow

The positive ions emerging from the multiplication region are mainly collected on the bottom surface of the M-THGEM whilst a part of them drift back to the cathode. The presence of such a spatial charge in the drift volume can induce severe distortions of the electric field in the drift region that may affect the position resolution and the drift time of the electrons [147, 148].

The Ion BackFlow (IBF) is the fraction of positive ions reaching the cathode and it is usually defined as the ratio between the current at the cathode (I_{cath}), and the sum of I_{cath} and I_{bot}. In our case I_{bot} is measured with a lower precision than the other currents (see Sect. 6.3), therefore we decided to use an alternative definition of IBF as the ratio between I_{cath} and sum of negative currents $I_{an} + I_{top}$:

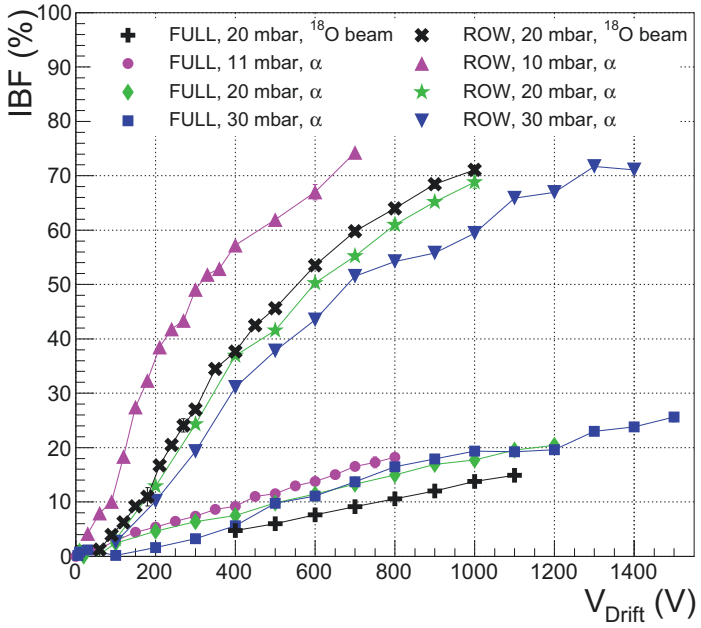

Figure 6.14: IBF for the ROW and FULL as a function of V_{drift} for different gas pressures, using ^{18}O beam and α-particle source. See Table A.2 for electrical configurations.

$$IBF = \left| \frac{I_{cath}}{I_{an} + I_{top}} \right| \tag{6.2}$$

This definition relies on the fact that the total positive charge ($I_{cath} + I_{bot}$) must be equal to the total negative charge ($I_{an} + I_{top}$) and on the experimental check that the relation: $I_{cath} + I_{bot} = I_{an} + I_{top}$ holds within the experimental error.

In Fig. 6.14 the behavior of the IBF as a function of V_{drift} for FULL and ROW using α-particle source and ^{18}O ion beam is shown. As expected, the IBF presents an increasing monotonic behavior with V_{drift}. The ROW detector systematically shows a larger IBF than the FULL one. In particular, the FULL detector reaches a maximum value of about 25%, to be compared with a maximum IBF of about 75% for the ROW one. This means that for electronic signals on the anode of same amplitude the ROW suffers from a larger IBF.

In Fig. 6.15 the IBF as a function of the gain for FULL and ROW is compared. The main feature is that IBF has a monotonic trend that decreases with increasing

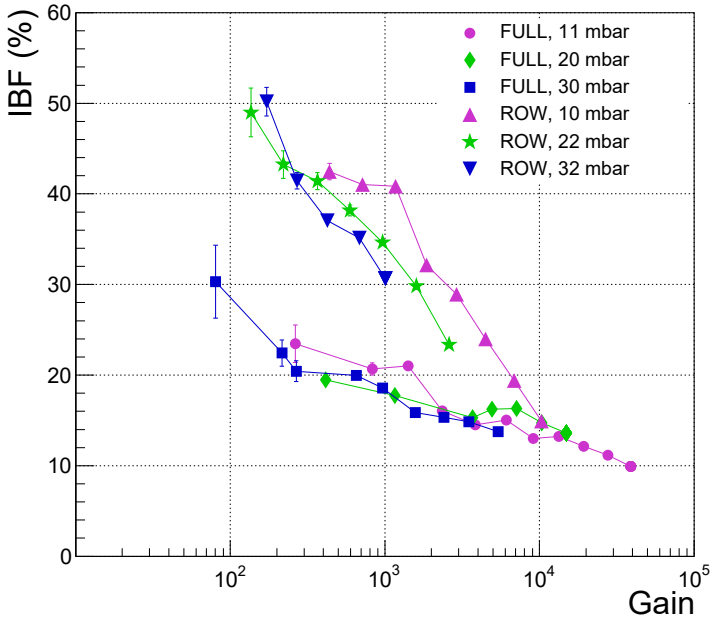

Figure 6.15: IBF for different gas pressures as a function of the gain for α-particle source data. See Table A.3 for electrical configurations.

gain. Such a behavior is in agreement with what is present in literature, see for example [110, 132]. In particular, for the FULL, an almost constant IBF of about 10% seems to be reached at sufficiently high gain (above 10^3).

In all the above discussed tests the three layers of the M-THGEM foil were set at the same bias (symmetric bias configuration). The asymmetric M-THGEM configuration was also studied, i.e. configuration where the three layers are set at different voltages, in order to investigate possible effects on the IBF. The tests were performed with the FULL at $P = 10$ mbar, $V_{drift} = 600$ V, $V_{ind} = 70$ V. For the sake of clarity, V_{TH1}, V_{TH2}, and V_{TH3} are defined as the voltage difference across the top, middle and bottom layers of the M-THGEM, respectively. In Fig. 6.16 the symmetric configuration (magenta curve), obtained varying $V_{TH1} = V_{TH2} = V_{TH3}$ between 120 and 210 V, is compared with two asymmetric configurations (blue and green curves). The first asymmetric configuration (green line) is obtained keeping V_{TH3} to a fixed value of 200 V and increasing V_{TH1} and V_{TH2} from 150 to 190 V (discharge value), maintaining $V_{TH1} = V_{TH2}$. The second asymmetric

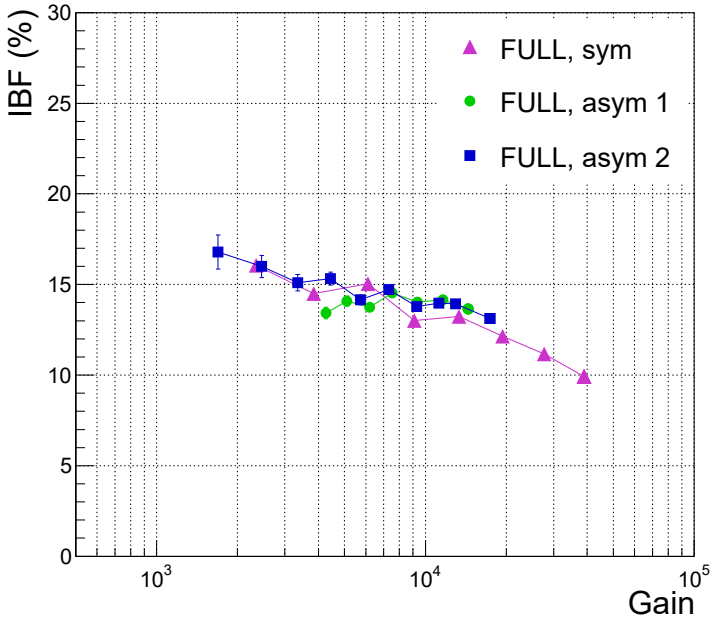

Figure 6.16: IBF as a function of the gain for one symmetric and two asymmetric configurations for the FULL at $P = 10$ mbar, $V_{ind} = 70$ V and $V_{drift} = 600$ V. Sym: $V_{TH1} = V_{TH2} = V_{TH3} = 120$ - 210 V; Asym 1: $V_{TH1} = V_{TH2} = 150$ - 190 V, $V_{TH3} = 200$ V; Asym 2: $V_{TH1} = 200$ V, $V_{TH2} = V_{TH3} = 150$ - 195 V.

configuration (blue line) is obtained keeping fixed V_{TH1} at 200 V and varying V_{TH2} and V_{TH3} from 150 to 195 V (discharge value) under the condition $V_{TH2} = V_{TH3}$. The three configurations do not show significant differences, therefore one can conclude that the IBF depends on the total gain of the M-THGEM and not on how it is shared among the three THGEM layers.

6.4.6 Rate characterization

The effects of the incident particle rate on the M-THGEM response were investigated by using the products of scattering of a ^{18}O beam on Au targets. Different rates on the detector ranging from 10 pps to about 3 kpps were obtained using a combination of different beam intensities and target thicknesses. Since the detector covers a wide horizontal angle ($\approx 15°$) respect to the scattering center, the rate of incident particles was not uniform along the detector width but was chang-

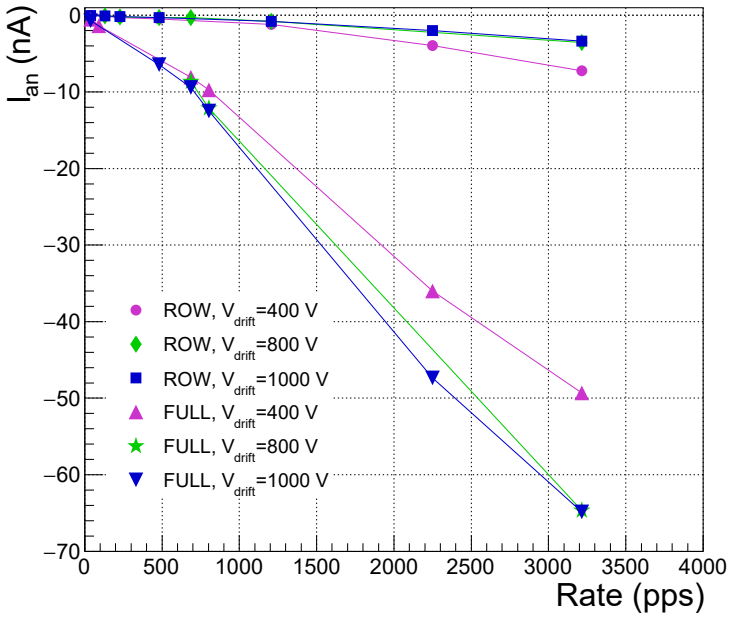

Figure 6.17: Anodic current as a function of the rate of incident particles for the FULL (circles) and ROW (squares) at $P = 20$ mbar, $V_{ind} = 50$ V and $V_{THGEM} = 190$ V for ROW and $V_{ind} = 100$ V and $V_{THGEM} = 205$ V for FULL, at $V_{drift} = 400$ V (magenta), 800 V (green) and 1000 V (blue). The data were obtained with ^{18}O beam and α-particle source.

ing of more than two orders of magnitude from one edge to the other, reaching a maximum value of about 300 pps/cm. The rate here reported is the total rate in the detector. In Fig. 6.17 the plot of the anodic current as a function of the rate at $P = 20$ mbar is shown. For each M-THGEM, three different V_{drift} values were investigated, keeping the other voltages fixed. As shown in Sect. 6.4.5, the IBF is strongly dependent on V_{drift}. Therefore, possible effects in the detector response due to spatial charge should be stronger at low V_{drift}. The behavior of the anodic current as a function of the particle rate is compatible with a linear one for all the curves. Therefore, no relevant effects of the rate on the response of the detector are observed up to a rate of about 3 kpps for all the explored values of V_{drift} and for both FULL and ROW geometries.

6.5 Track reconstruction test

In order to study the track reconstruction capability of the gas tracker prototype equipped with the ROW, a dedicated test was carried out in July 2020. A setup similar to the one described in Sect. 6.3 for the current-voltage characterization was adopted; indeed, the same power supply module, α-particle source and shutter were used. The ^{241}Am source was placed at about 15 mm in front of the prototype active volume, with an average horizontal angle of about 20°. In this test, also the first version of the electronic system for the final tracker was used. It consisted of a 64-channel charge-sensitive preamplifier (CAEN model A1429) [149] and a 64-channel, 125 MS/s, 16-bit Waveform Digitizer (CAEN model V2740) [150]. The electronic chain was the following: the signal from a strip of the segmented anode was fed to the A1429 preamplifier through a passive adapter; the preamplifier output signal was directly sent to the V2740 digitizer. In this test a single digitizer module and a single preamplifier were employed, so that only 64 strips out of 192 were connected to the electronics, corresponding to a sensitive region of about 48 mm in the horizontal direction. The working conditions were $P = 10$ mbar, $V_{ind} = 50$ V, $V_{THGEM} = 190$ V and $V_{drift} = 600$ V.

The reconstruction procedure of the 3D track can be divided in two steps: in the first, the horizontal angle (θ) is calculated by means of an algorithm that determines the charge distribution of the secondary electrons on the anodic strips; in the second, the vertical angle (ϕ) is deduced from the arrival time of the electrons on the strips. The detailed procedure is described in the following.

6.5.1 Charge distribution and arrival time measurement

Since the ROW M-THGEM used in this test has five rows of multiplication holes, when an α-particle goes through the tracker, it produces a charge distribution on the anodic strips that could have at most five peaks, depending on the track horizontal angle. The charge induced on each strip by a typical α-particle track is shown in Fig. 6.18a. The five-peaks structure is evident and each peak exhibits a well-defined bell shape. The separation between two adjacent peaks is directly correlated to the alpha particle horizontal angle: the larger is the θ angle, the more distant are the peaks. In the limit case of an α-particle trajectory parallel

to the strips, the five peaks would join into a single peak.

For the same track, the electron arrival time measured by each strip is shown in Fig. 6.18b. The arrival times Δt are evaluated with respect to the time measured by the first fired strip (in this case, the strip n. 71). The behavior of the arrival times is related to the vertical angle: a decreasing trend is associated with a positive value, while an increasing one corresponds to a negative value. Moreover, the slope of the time distribution is correlated to the vertical angle magnitude, so that a horizontal line would correspond to $\phi = 0°$.

6.5.2 Horizontal and vertical angles reconstruction

To evaluate the track horizontal angle, a fitting procedure of the charge distribution is performed with a function model consisting in the sum of five gaussian functions. The initial parameters are determined by fitting each peak with a single gaussian function. In Fig. 6.18a an example of multiple-fit is shown. Each centroid pinpoints a horizontal position, so that five horizontal coordinates x_i ($i = 1, \ldots, 5$) are determined. The θ angle is obtained as the slope of the straight-line fit to the x_i coordinates against the longitudinal positions z_i of the hole rows, whose measured values are 18, 36, 54, 72, and 90 mm, respectively.

Since the main focus of this test was the challenging measurement of the horizontal coordinates and angle with the novel ROW-based prototype, no additional detector was added to provide the start signal and, therefore, to measure the electron drift time in a standard way. In any case, by the measurement of the difference of the electron arrival times on the strips Δt, it was possible to extract the vertical angle ϕ of the α-particle trajectory.

The spectra of the reconstructed ϕ and θ angles for only the events with five peaks in the charge distribution are shown in Fig. 6.19a and 6.19b, respectively. The ϕ distribution is centered near 0°, as expected from a source placed at almost half the tracker height. The θ distribution extends from 19° to 27° and has its maximum at about 23°, in good agreement with the geometrical conditions of the experimental setup.

A rough estimate of the track reconstruction accuracy of the prototype can be obtained by calculating the difference between a measured horizontal coordinate

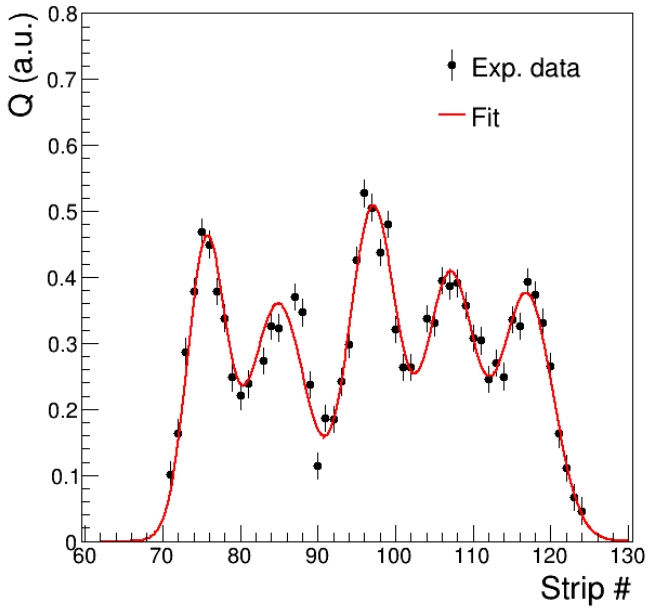

(a)

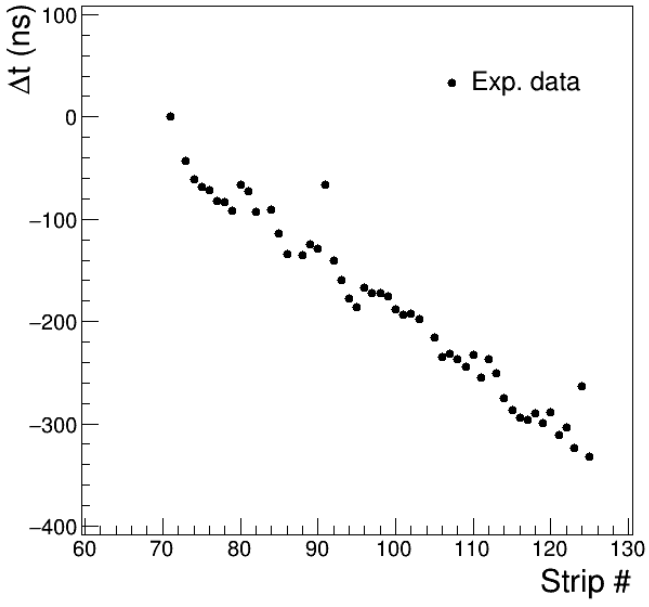

(b)

Figure 6.18: Signals generated on the strip-segmented anode by a typical α-particle track: (a) The charge induced on each strip. The five-gaussian fit function is also shown. (b) The arrival time measured by each strip with respect to the first one fired.

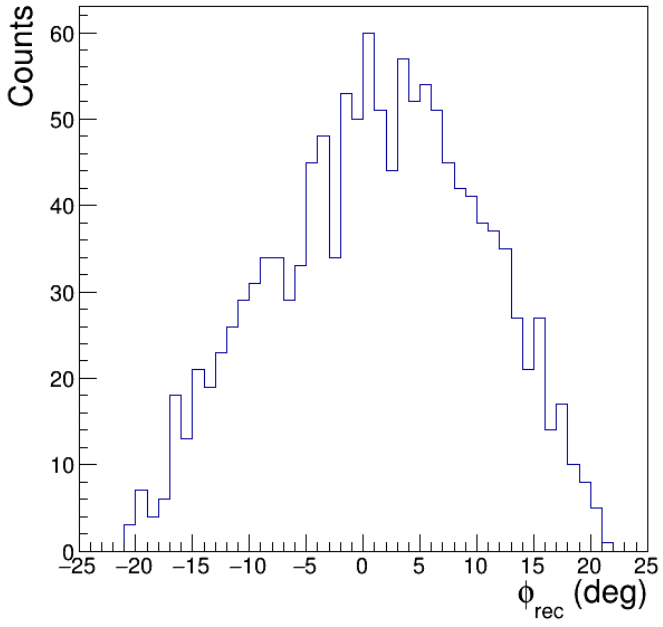

(a)

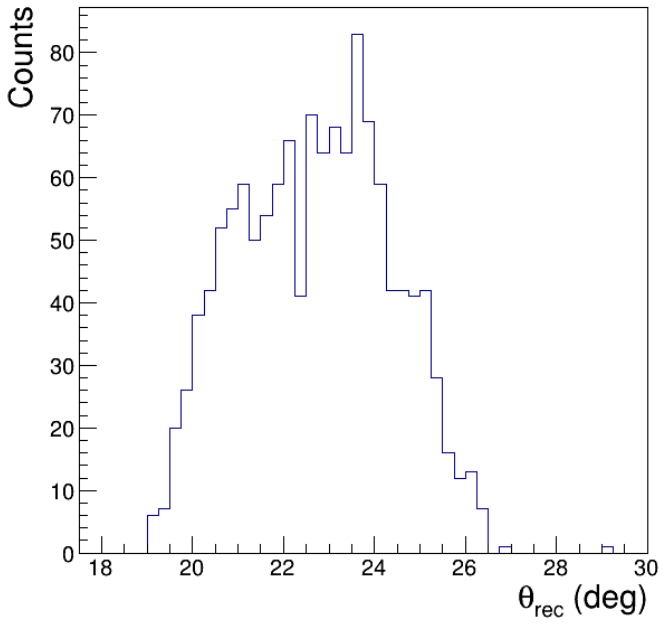

(b)

Figure 6.19: Distribution of the (a) vertical and (b) horizontal reconstructed angles.

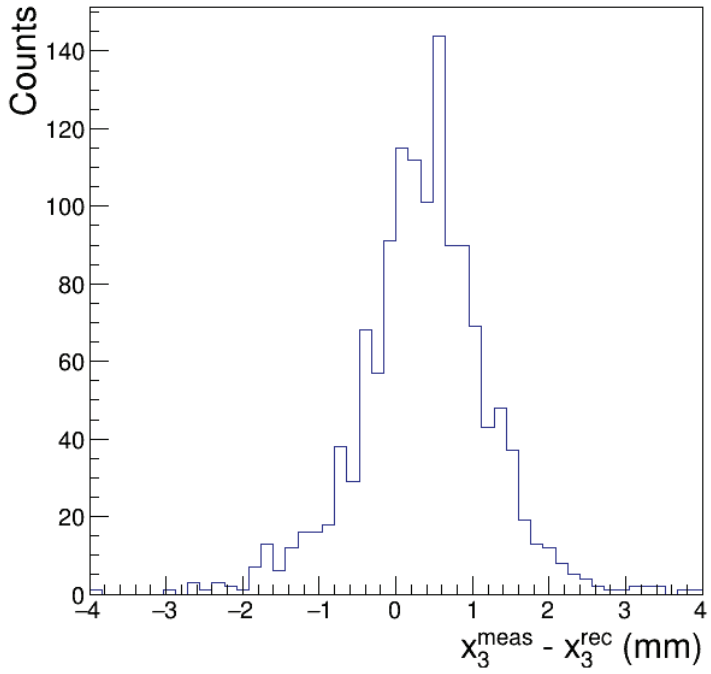

Figure 6.20: Difference between the measured third horizontal coordinate (x_3^{meas}) and the same coordinate reconstructed from the fit on the other four horizontal positions (x_3^{rec}).

and the corresponding one reconstructed from the linear fit on the other four horizontal positions. In Fig. 6.20 this difference is shown taking into consideration the third horizontal coordinate. The centroid of the distribution is situated at about 350 μm, thus indicating a sub-millimetric accuracy. The resolution of the track reconstruction can be evaluated through the FWHM of the distribution, which is $\delta x \rightarrow 1.5$ mm.

6.6 Conclusions

The tests performed for this Thesis allow to compare the performances of the FULL- and ROW-based detectors. In particular, the track reconstruction test showed that a position resolution $\delta x \rightarrow 1.5$ mm can be achieved with a ROW-based prototype and a strip-segmented anode. Such a result does not match the

NUMEN requirement of a sub-millimetric position resolution for the ion track measurement. Moreover, the ROW is more unstable, has a less uniform electric field and a larger ion backflow with respect to the FULL. For these reasons, the results described in this chapter led the NUMEN collaboration to adopt the FULL layout for the M-THGEM of the final FPD gas tracker.

Chapter References

[4] F. Cappuzzello et al. “The NUMEN Technical Design Report”. In: *International Journal of Modern Physics A* 36 (2021), p. 2130018. DOI: 10.1142/S0217751X21300180.

[110] M. Cortesi et al. “Multi-layer thick gas electron multiplier (M-THGEM): A new MPGD structure for high-gain operation at low-pressure”. In: *Rev. Sci. Instrum.* 88 (2017), p. 013303. DOI: https://doi.org/10.1063/1.4974333.

[111] F. Cappuzzello et al. “The NUMEN Project: An Update of the Facility Toward the Future Experimental Campaigns”. In: *Front. Astron. Space Sci.* 8 (2021), p. 668587. DOI: https://doi.org/10.3389/fspas.2021.668587.

[116] C. Shalem et al. “Advances in thick gemlike gaseous electron multipliers part II: Low-pressure operation”. In: *Nucl. Instrum. Meth. A* 558 (2006), pp. 468–474. DOI: https://doi.org/10.1016/j.nima.2005.12.219.

[117] Y. Ayyad et al. “CO2 operation of an active target detector readout based on THGEM”. In: *J. Instrum.* 12 (2017), p. 06003. DOI: https://doi.org/10.1088/1748-0221/12/06/P06003.

[118] M. Cortesi et al. “Development of a novel MPGD-based drift chamber for the NSCL/FRIB S800 spectrometer”. In: *J. Instrum.* 15 (2020), p. 03025. DOI: 10.1088/1748-0221/15/03/p03025.

[131] COMSOL Multiphysics. *COMSOL AB, Stockholm, Sweden, v. 5.4*. https://www.comsol.it. 2018.

[132] R. de Olivera and M. Cortesi. “First performance evaluation of a Multilayer Thick Gaseous Electron Multiplier with in-built electrode meshes—MM-THGEM”. In: *J. Instrum.* 13 (2018), p. 06019. DOI: 10.1088/1748-0221/13/06/p06019.

[141] I. Ciraldo and G. A. Brischetto et al. “Characterization of a gas detector prototype based on Thick-GEM fir the MAGNEX focal plane detector”. In: *Nuclear Instruments and Methods in Physics Research Section A: Accelerators, Spectrometers, Detectors and Associated Equipment* 1048 (2023), p. 167893. DOI: https://doi.org/10.1016/j.nima.2022.167893.

[142] CAEN. *Universal Multichannel Power Supply System SY5527*. https://www.caen.it/products/sy5527/. 2021.

[143] M. Abbas and et al. “Performance of a triple-GEM demonstrator in pp collisions at the CMS detector”. In: *J. Instrum.* 16 (2021), p. 11014. DOI: 10.1088/1748-0221/16/11/p11014.

[144] S. Bachmann et al. “Charge amplification and transfer processes in the gas electron multiplier”. In: *Nucl. Instrum. Meth. A* 438.2 (1999), pp. 376–408. ISSN: 0168-9002. DOI: https://doi.org/10.1016/S0168-9002(99)00820-7.

[145] R. Bellazzini and et al. “A two-stage, high gain micro-strip detector”. In: *Nucl. Instrum. Meth. A* 425 (1999), p. 218. DOI: https://doi.org/10.1016/S0168-9002(98)01356-4.

[146] O.B. Tarasov and D. Bazin. “LISE++: Exotic beam production with fragment separators and their design”. In: *Nucl. Instrum. Meth. B* 376 (2016). Proceedings of the XVIIth International Conference on Electromagnetic Isotope Separators and Related Topics (EMIS2015), Grand Rapids, MI, U.S.A., 11-15 May 2015, pp. 185–187. ISSN: 0168-583X. DOI: https://doi.org/10.1016/j.nimb.2016.03.021.

[147] F. Sauli, S. Kappler, and L. Ropelewski. “Electron collection and ion feedback in GEM-based detectors”. In: *IEEE Trans. Nucl. Sci.* 50.4 II (2003), pp. 803–808. DOI: 10.1109/TNS.2003.814543.

[148] F. Sauli, L. Ropelewski, and P. Everaerts. “Ion feedback suppression in time projection chambers”. In: *Nucl. Instrum. Meth. A* 560.2 (2006), pp. 269–277. ISSN: 0168-9002. DOI: https://doi.org/10.1016/j.nima.2005.12.239.

[149] CAEN. *64 Channel charge sensitive preamplifier A1429*. https://www.caen.it/products/a1429/. 2021.

[150] CAEN. *64 Channel 16 bit 125 MS/s Digitizer V2740*. https://www.caen.it/products/v2740/. 2021.

Conclusions

The NUMEN project has promoted an upgrade towards high intensity beams of the K800 Superconducting Cyclotron and the MAGNEX magnetic spectrometer, installed at the Laboratori Nazionali del Sud of the Istituto Nazionale di Fisica Nucleare (INFN-LNS). The upgrade of MAGNEX involves a radical change of the Focal Plane Detector (FPD). Indeed the present gas tracker, based on multiplication wires, will be replaced by a tracking system using Multi-layer THGEM, while the present silicon detectors stopping wall will be replaced by a wall of $\Delta E \quad E$ telescope detectors, devoted to the Particle IDentification (PID). In this framework, an intense R&D activity was performed, that required the realization of extensive tests and simulations of the detectors. In particular, for this Thesis a Monte Carlo simulation tool including both the future gas tracker and the PID wall was developed and implemented. The development of such a tool is very important for the NUMEN project for several reasons: firstly, it supports the design of the FPD, optimizing the layout and technical specifications of the detectors and reducing economic and man-power demands. Secondly, it gives a realistic prediction of the response of the future FPD to the events of interest, allowing to evaluate the PID performance and the sensitivity of the detection system.

In this work, the simulation tool was used to optimize the rotation angle θ_{tilt} of the towers of telescopes which constitute the PID wall. This parameter is highly impactive on the overall FPD project, as it controls the number of telescopes necessary to cover the explored phase-space, the PID capability, the detection sensitivity and the background level. Two simulations were performed, where θ_{tilt} was set to 0° and 35°, respectively. In both cases the collision ^{20}Ne + ^{76}Ge at 700 MeV incident energy was considered and several ejectiles were simulated (^{19}O, ^{20}O,

^{21}O, ^{19}F, ^{20}F, and ^{20}Ne). In the ΔE_{SiC}^{corr} E_{CsI} correlation plot corresponding to $\theta_{tilt} = 0°$ the loci of the different ejectiles are not separated, thus not allowing the PID. Instead, for $\theta_{tilt} = 35°$ the ΔE_{SiC}^{corr} E_{CsI} plot shows a good separation between the loci of ions with different atomic number Z. By comparing the results of the two simulations, it is evident that the configuration with $\theta_{tilt} = 0°$ does not satisfy the NUMEN requirements. As a result, the NUMEN collaboration has adopted the solution at $\theta_{tilt} = 35°$ [4].

The simulation tool was also used to develop a PID technique strategy, which is composed by the following steps: first, a calibration procedure of the ΔE_{SiC}^{corr} and n_{phot} quantities was simulated; second, the oxygen ions were selected with a graphical contour in the ΔE_{SiC}^{corr} n_{phot} correlation plot. The selected ions were plotted in the x_{foc} n_{phot} representation, where the oxygen isotopes are separated according to their $\overline{m}/q$ ratio. A clear identification of the ion of interest (^{20}O) was obtained. Moreover, the overall PID quality can be further improved if the same PID procedure is carried out in ranges of θ_{foc}. Therefore, the Monte Carlo simulations performed for this Thesis allowed to study to PID performance of the future FPD, showing that the SiC-CsI telescopes can provide a good separation in atomic number of the ions in the region of O, F and Ne. In addition, a clear mass number identification can be obtained in the x_{foc} n_{phot} representation once the selection of the atomic number is performed.

Part of the activity I have been involved in for the characterization tests of the prototype of gas tracker for the future FPD was presented in this work. Two three-layer M-THGEMs with different hole pattern layouts were used as electron multiplication device: the FULL, where the holes fill the whole active area, and the ROW, which has five rows of holes parallel to the entrance and exit face of the detector. The tests were performed to study the main characteristics of the detector, varying the voltages across the tracker regions (drift, THGEM, induction), the gas pressure and the rate of incident heavy ions. They were performed using an ^{18}O beam at 270 MeV and a ^{241}Am α-particle source. The gain and ion backflow of the prototype, for both M-THGEM layouts, were determined. A maximum gain of 4 ± 10^4 was obtained in stable conditions at a pressure of 11 mbar with isobutane gas. For the FULL-based detector, the minimum ion backflow achieved was 10%, while for the ROW it reached much higher values. Such large

ion backflow for the ROW do not affect the detector response at the maximum explored rate of about 3 kpps (300 pps/cm). However, the track reconstruction test showed that, with the ROW-based prototype and a strip-segmented anode, a position resolution of $\rightarrow 1.5$ mm can be achieved. This result is not compliant with the NUMEN request to have a sub-millimetric position resolution in the measurement of the ion track. In addition, the better performances of the FULL with the respect to the ROW in terms of electron transparency, electric field uniformity, stability and ion backflow lead to the conclusion that, for the NUMEN purposes, the FULL geometry is prefereable. As a result of these studies, the NUMEN collaboration has adopted the FULL-based M-THGEM solution [4].

In this Thesis, the elastic and inelastic scattering of the ^{18}O + ^{48}Ti system at 275 MeV incident energy were studied for the first time. Such a study had two main purposes: on the one hand the analysis of experimental data gave me the possibility to understand the MAGNEX response to real events and the significance of the typical parameters and correlation plots used in the data reduction procedure. This was fundamental to the development of the mentioned simulation tool and to the correct interpretation of the simulated data, which were compared to the experimental one. On the other hand, the theoretical analysis of the ^{18}O + ^{48}Ti elastic and inelastic scattering is crucial for the multi-channel description of the full reaction network. Indeed, the analysis of the elastic and inelastic channels allows to determine the average nucleus-nucleus potential of the two colliding partners and to evaluate the role of the couplings with the low-lying collective excited states. Both these ingredients constitute the initial state interaction, which plays an essential role for the theoretical analysis of the complete ensemble of the direct nuclear reactions induced in the projectile-target collision.

The large acceptance of MAGNEX allowed to explore a wide range of transferred momenta in only three angular settings. The elastic transition and the one towards to the 2_1^+ excited state at 0.984 MeV of ^{48}Ti appear as isolated peaks, thanks to the high energy resolution ($\rightarrow 0.5$ MeV FWHM) achieved in the excitation energy spectra. A broad structure centered at about 2.2 MeV is ascribed to the superposition of the 2_1^+ excited state of the ^{18}O at 1.982 MeV and three ^{48}Ti states: the 4_1^+ state at 2.296 MeV, the 2_2^+ state at 2.421 MeV, and a state of unknown spin-parity at 2.465 MeV. The cross-section angular distributions were obtained

for the elastic scattering, the inelastic transition to the 2_1^+ state of ^{48}Ti and for the structure containing the inelastic scattering to the 2_1^+ state of ^{18}O.

The experimental results were compared with cross-section calculations performed with the FRESCO code. The double folding São Paolo potential (SPP) was adopted as the optical potential and the couplings with the low-lying collective excited states of projectile and target were treated in terms of deformed Coulomb and nuclear potentials. The theoretical calculations were performed in Optical Model (OM), Distorted-Wave Born Approximation (DWBA) and Coupled Channel (CC) framework. The OM calculations fail to reproduce the elastic scattering experimental data at large transferred momenta. A good description of the data is obtained with the CC approach over the full explored angular range. Such a result highlights the importance of the couplings with the 2^+ and 3^- low-lying collective states of projectile and target at 15 MeV/u incident energy, i.e. far above the Coulomb barrier. This is also confirmed by the analysis of the mentioned inelastic transitions, where the CC calculations reproduce the experimental data better than the DWBA ones.

The reliability of the approach was further tested by performing a theoretical analysis of experimental data reported in literature about the same scattering but at 54 MeV incident energy. For the elastic transition, both the OM and CC calculations give a good description of the data. A similar result is valid also for the inelastic transition to the 2_1^+ excited state of ^{48}Ti, where DWBA and CC formalisms well reproduce the data, showing a much less pronounced role of the couplings at energies (3 MeV/u) close to the Coulomb barrier. Instead, for the inelastic transition to the 2_1^+ excited state of ^{18}O both DWBA and CC show a discrepancy with the data. Since a similar result is found also in the original paper, such a discrepancy may be due to a problem in the data.

The result of these studies is the extraction of the initial state interaction and of the proper coupling scheme for the ^{18}O + ^{48}Ti system, which are crucial for the analysis of all the direct reactions induced in the projectile-target collision. Such a system is of interest for the study of the ^{48}Ti – ^{48}Ca transition, which is relevant for the $0\nu\beta\beta$ decay of the ^{48}Ca nucleus.

A

Electrical configurations and gas pressures explored for the characterization tests of the prototype

Table A.1: Values of pressure (P), V_{THGEM} and V_{drift} adopted for the study of V_{ind} for ROW and FULL M-THGEM with α-particle source.

M-THGEM	P (mbar)	V_{ind} range (V)	V_{THGEM} (V)	V_{drift} (V)
ROW	20	0 - 110	220	800
ROW	20	0 - 130	210	800
ROW	30	0 - 110	240	800
ROW	42	0 - 170	260	700
FULL	11	0 - 150	170	600
FULL	11	0 - 60	170	800
FULL	11	0 - 60	180	800
FULL	20	0 - 200	200	1000
FULL	30	0 - 220	200	1000
FULL	30	0 - 220	220	1000
FULL	30	0 - 220	230	1000

Table A.2: Values of pressure (P), V_{ind} and V_{THGEM} adopted for the study of V_{drift} for ROW and FULL M-THGEM.

Ion	M-THGEM	P (mbar)	V_{ind} (V)	V_{THGEM} (V)	V_{drift} range (V)	Fig.
α	ROW	10	50	180	0 - 800	6.14
α	ROW	20	80	210	100 - 1000	6.14
^{18}O	ROW	20	50	190	30 - 1000	6.14
α	ROW	30	70	240	0 - 1400	6.14
α	ROW	30	70	230	0 - 1400	
α	FULL	9	50	160	200 - 600	
α	FULL	11	70	190	0 - 800	6.14
α	FULL	11	70	170	600 - 850	
α	FULL	20	100	205	100 - 1200	6.14
^{18}O	FULL	20	100	205	400 - 1100	6.14
α	FULL	30	120	220	0 - 1500	6.14

Table A.3: Values of pressure (P), V_{ind} and V_{drift} adopted for the study of V_{THGEM} for ROW and FULL M-THGEM.

Ion	M-THGEM	P (mbar)	V_{ind} (V)	V_{THGEM} range (V)	V_{drift} (V)	Fig.
α	ROW	10	50	140 - 205	200	6.12,6.15
α	ROW	21	50	180 - 225	800	6.13
^{18}O	ROW	20	50	165 - 205	800	6.13
α	ROW	22	80	120 - 220	300	6.12,6.15
α	ROW	30	70	180 - 240	800	
α	ROW	32	70	170 - 245	400	6.12,6.15
α	ROW	42	80	220 - 270	700	
α	FULL	9	50	130 - 210	400	
α	FULL	11	70	120 - 210	600	6.12,6.15,6.16
α	FULL	11	70	V_{TH3} = 200, $V_{TH1,2}$ = 150 - 190	600	6.16
α	FULL	11	70	V_{TH1} = 200, $V_{TH2,3}$ = 150 - 195	600	6.16
α	FULL	20	100	150 - 215	1000	6.12,6.13,6.15
^{18}O	FULL	20	100	160 - 210	1000	6.13
α	FULL	30	120	180 - 235	1000	6.12,6.15